

Lattice Boltzmann Methods for Microswimmers in Complex Environments

Von der Fakultät Mathematik und Physik der Universität Stuttgart zur
Erlangung der Würde eines Doktors der Naturwissenschaften (Dr. rer. nat.)
genehmigte Abhandlung

Vorgelegt von
Michael Johannes Kuron
aus Mannheim

Hauptberichter:	Prof. Dr. Christian Holm
Mitberichter:	Prof. Dr. Udo Seifert
Mitberichter:	Dr. Joost de Graaf
Tag der mündlichen Prüfung:	19. Oktober 2021

Institut für Computerphysik der Universität Stuttgart

2021

Contents

Abstract	7
Publications	11
1 Introduction	13
1.1 Active matter	14
1.1.1 Wet and dry active matter	14
1.1.2 Swimming at low Reynolds numbers	15
1.1.3 Biological microswimmers	16
1.1.4 Artificial microswimmers	17
1.1.5 Pairwise and collective interactions	18
1.2 Modeling of active matter	19
1.2.1 Explicit-particle methods	21
1.2.2 Continuum fluid methods with resolved propulsion .	21
1.2.3 Continuum fluid methods with effective propulsion .	22
1.2.4 Explicit fluid methods	23
1.2.5 Continuum fluid methods with point-coupled swimmers	23
1.2.6 Active Brownian particles	23
1.2.7 Continuum active matter	24
1.3 Scope of this thesis	24
2 Theoretical background	27
2.1 Fluid dynamics	27
2.1.1 Navier-Stokes equations	27
2.1.2 Incompressible Navier-Stokes equations	29
2.1.3 Stokes equations	29
2.1.4 Generalized Stokes equations	30
2.1.5 Viscoelastic fluids: Oldroyd-B	31
2.2 Electrokinetic equations	32
2.2.1 Diffusion-advection-migration processes	32
2.2.2 Poisson-Boltzmann theory	34
2.2.3 Diffusion-reaction processes	35
2.3 Boundary conditions	37
2.3.1 Boundary conditions for fluid dynamics	37

2.3.2	Boundary conditions for electrokinetics	38
2.4	Squirmers	38
2.5	Dimensionless numbers	41
3	Semi-analytic methods	45
3.1	Oseen tensor	45
3.2	Hydrodynamic mode decomposition	46
3.3	Method of reflections	46
3.3.1	Reflection at a flat wall	48
3.3.2	Reflection at a sphere	48
3.4	Faxén’s laws	51
3.5	Integrating the squirmer’s trajectory	52
3.6	Electrostatic Green’s function and multipoles	58
4	Computational methods	61
4.1	Lattice Boltzmann	61
4.2	Finite volume method	65
4.2.1	Discretization	65
4.2.2	Stability improvements	68
4.2.3	Finite volume Oldroyd-B	69
4.2.4	Lattice electrokinetics	72
4.2.5	Chemical reactions	74
4.3	Fast Fourier electrostatics	74
4.3.1	Charge monopoles	75
4.3.2	Charge dipoles	76
4.4	Moving boundaries	76
4.4.1	Moving-boundary lattice Boltzmann	77
4.4.2	Moving-boundary electrokinetics	78
4.4.3	Moving-boundary Oldroyd-B	84
4.5	Implementation	85
5	A lattice Boltzmann model for squirmers	87
5.1	Model and methods	89
5.2	Validation	90
5.2.1	Squirmers in bulk	90
5.2.2	Impact of resolution	90
5.2.3	Interaction between two squirmers	96
5.2.4	Squirmer in a cylindrical channel	96
5.3	Summary	98

6	Hydrodynamic mobility reversal of squirmers near flat and curved surfaces	103
6.1	Model and methods	106
6.2	Characterization	108
6.2.1	Trajectories	108
6.2.2	Interpreting the bound states	111
6.3	Stability analysis using lubrication theory	114
6.4	Results	115
6.4.1	Effects of obstacle size	115
6.4.2	Effects of short-range repulsion	119
6.4.3	Effects of higher-order hydrodynamic modes	119
6.4.4	Swimming inside a cavity	122
6.4.5	Accounting for the near field	127
6.5	Summary	127
7	An extensible lattice Boltzmann method for viscoelastic flows	131
7.1	Model and methods	132
7.1.1	Background on viscoelastic lattice Boltzmann	133
7.1.2	Implementation	134
7.2	Validation and results	134
7.2.1	Time-dependent Poiseuille flow	134
7.2.2	Steady shear flow	139
7.2.3	Lid-driven cavity	139
7.2.4	Four-roll mill	143
7.2.5	Sedimenting sphere	145
7.2.6	Two-sphere snowman	149
7.2.7	Squirmer	151
7.3	Summary	155
8	Moving charged particles in lattice Boltzmann-based electrokinetics	157
8.1	Model and methods	160
8.2	Validation	160
8.2.1	Electrophoresis of a single colloid	160
8.2.2	Electrophoresis of a colloidal suspension	165
8.3	Summary	167
9	Summary and outlook	171
	Bibliography	175

Contents

Acknowledgments	217
Zusammenfassung	219
Erklärung	225

Abstract

This dissertation introduces, validates, and applies various models for the study of microswimmers, predominantly focusing on the development of lattice algorithms. The models are applicable to biological swimmers like bacteria, but also to artificial ones propelled via chemical reactions. The unifying theme is a complex fluidic environment, ranging from Newtonian single-component fluids, to electrolyte solutions, to viscoelastic media flowing through arbitrary geometries. A particular focus is placed on resolving each swimmer's surface since the propulsion, or phoresis, originates from a small layer of fluid around it. Resolving the propulsion mechanism is necessary to accurately study hydrodynamic interactions with obstacles and other swimmers. It is also a prerequisite for the study of taxis, that is, alignment with an external field such as a nutrient gradient. Similarly, phoretic interactions can be investigated, like when a swimmer senses and avoids the trail where another swimmer has already depleted the fuel.

Resolving the propulsion poses a challenge because it significantly increases the required computational effort. Methods like multi-particle collision dynamics (MPCD) or finite element method (FEM) have previously been used for this purpose, but suffer from unphysical effects or are not efficient enough to simulate transient behavior. This open problem is addressed by the new computational methods developed in this thesis. We design them to be sufficiently generic to also be applied to other types of fluids and even to areas of soft matter physics beyond active matter. The methods are based on lattice Boltzmann (LB), which is well-suited for time-dependent problems involving complex boundary conditions. Ionic solutes and viscoelastic stresses are considered via the finite volume (FV) method, which is ideal for the study of problems based on conservation laws. Novel moving boundary schemes permit resolving the swimmers on the lattice without re-meshing as they move. A sub-grid scheme is employed to smoothen out artifacts when lattice cells are converted between fluid and solid. A simple analytic far-field model is also used in this thesis to understand mobility reversal of simple swimmers at obstacles — a behavior that had previously been observed, but not explained solely in terms of hydrodynamics.

The development of these lattice methods allowed me and my collaborators to address open questions in literature, leading to four main results, each

of which is each presented in a separate chapter. The first result is for a squirmer, a simple yet instructive model for microswimmers, which employs an effective slip velocity on the surface of a sphere to describe self-propulsion. Solving for the flow around the squirmer using the LB method is relatively straightforward, but requires an unexpectedly fine grid resolution to capture the physical flow fields and behaviors with adequate precision. The accuracy of the LB model is demonstrated using four basic hydrodynamic tests, two for the far-field flow, and two that require the near field to be accurately resolved, which LB is capable of doing down to the grid resolution. Excellent agreement with results obtained using other hydrodynamic solvers in the same geometries is found, and the minimum resolution required to achieve this reproduction is identified.

The second topic was inspired by an unexpected mobility reversal observed in some of the LB squirmer simulations. Self-propelled particles have been experimentally shown to orbit spherical obstacles and move along planar walls. A theoretical and numerical investigation of this behavior is performed for a squirmer interacting with flat and curved surfaces. The hydrodynamics are approximated by means of the method of reflections, which is accurate in the far field; the LB solver is used to confirm that the far-field predictions remain valid when also accounting for near-field flows. The far-field model predicts three distinct behaviors: orbiting/sliding, scattering, and hovering, with orbiting being favored for lower curvature as in the experimental literature. Surprisingly, the far-field calculations also predict backward orbiting/sliding for sufficiently strong pushers. This is caused by fluid recirculation in the gap between the squirmer and the obstacle leading to strong forces opposing forward motion. The effect can be attributed to the quadrupolar mode of the squirmer. These results provide insight into a possible mechanism of mobility reversal mediated solely through hydrodynamic interactions with a surface.

The third main subject concerns viscoelastic fluids. This makes it applicable to many biological fluids, which have elastic properties in addition to the dissipative properties found in Newtonian fluids. Examples include the loss of time-reversibility due to memory, as well as a coupling between translation and rotation. Computational models can help us understand viscoelastic flow, but are often limited in how they deal with complex flow geometries and suspended particles. Some incorporate unphysical additional terms into the constitutive equations; others require the stress to be known at boundaries, which is not a priori possible for arbitrarily-shaped fixed and moving boundary conditions. The LB solver for Oldroyd-B fluids introduced in this thesis avoids these shortcomings, making it ideally suited for the simulation of confined colloidal suspensions. The method is validated using several

standard rheological setups: transient Poiseuille flow, steady shear flow, the lid-driven cavity, and the four-roll mill. Additionally, a single sedimenting colloid is studied to verify the new moving boundary scheme, also finding good agreement with literature. Translation-rotation coupling, an important property of viscoelastic media, is demonstrated for two rigidly-connected spheres. This snowman-like object is spun by an externally-applied torque, leading to linear motion only in viscoelastic fluids. The squirmer is again used, showing the applicability of the method to microswimmers, but also encountering the limitations of Oldroyd-B. Oldroyd-B becomes unphysical for elastic relaxation times beyond a certain limit. However, we have designed our approach such that it is easy to extend the algorithm to other constitutive equations, like Giesekus or FENE-P, which do not suffer from this problem.

The fourth topic deals with colloids suspended in electrolyte solutions, introducing a moving boundary scheme similar to the one for the viscoelastic fluids. The motion of ionic solutes and charged particles under the influence of an electric field and the ensuing hydrodynamic flow of the underlying solvent are ubiquitous in soft matter physics. The solute and flow are described by a coupled set of differential equations, collectively referred to as the electrokinetic equations; the boundary conditions define the specific problem being considered. A lattice-based method for solving this system of equations has previously been introduced based on a coupled LB-lattice electrokinetics (EK) scheme, but did not allow for particle coupling. The key ingredients of the new moving boundary method are mass and charge conservation for the solute species and a partial-volume smoothing of the solute fluxes to minimize discretization artifacts. The algorithm's effectiveness is demonstrated by simulating the electrophoresis of charged spheres in an external field. For a single sphere this is compared to the equivalent electro-osmotic (co-moving) problem, where the former's instantaneous velocity is found to lie within 2% of the latter's steady-state value and the temporal artifacts of the discretization are of the same magnitude.

The field of active matter research has changed significantly since I started working on this thesis in the year 2016. Development and understanding of the propulsion and behavior of artificial microswimmers had been one of the major research questions occupying the active matter community for the preceding decade. My work on electrokinetics was aimed at contributing to this line of research, while also being relevant to the fields of catalysis and bioreactive flows. A comprehensive answer to the open questions on self-diffusiophoretic and self-electrophoretic propulsion has yet to be reached, with the main obstacle appearing to be insufficient understanding of the chemical reactions involved. Even before research of artificial microswimmers

started, it was realized that much of the larger-scale behavior of swimmers is universal across different kinds of propulsion. Significant insight into microswimming could thus be obtained irrespective of these details, for example by looking at their swarming behavior or their interaction with surfaces. As a result, my own interest has shifted toward simpler models, aligning with a longer-standing trend in the community. Nevertheless, electrokinetics remains relevant in active matter because chemical propulsion leads to emergent phenomena that are not universal or not captured by the simpler models. More recently, the focus of the community has shifted to biological, bio-compatible, and bio-inspired swimmers, to which my work on squirmers connects. Research into such swimmers has more medical relevance and delivers direct insight into biology. As a consequence, viscoelastic fluids have seen a surge of interest due to their prevalence in nature. Their more complex rheology facilitated new kinds of swimmer behavior, for example because it allows swimmers to evade the scallop theorem. The combination of the computational methods for viscoelasticity, electrolytes, and chemical reactions I give in this thesis will provide a valuable tool for the study of biological and man-made microswimmers across a wide range of fluid environments.

Publications

This thesis is based on my following peer-reviewed publications:

- M. Kuron, G. Rempfer, F. Schornbaum, M. Bauer, C. Godenschwager, C. Holm, and J. de Graaf, “Moving charged particles in lattice Boltzmann-based electrokinetics”, *Journal of Chemical Physics* **145**, 214102 (2016),
- M. Kuron, P. Stärk, C. Burkard, J. de Graaf, and C. Holm, “A lattice Boltzmann model for squirmers”, *Journal of Chemical Physics* **150**, 144110 (2019),
- M. Kuron, P. Stärk, C. Holm, and J. de Graaf, “Hydrodynamic mobility reversal of squirmers near flat and curved surfaces”, *Soft Matter* **15**, 5908 (2019),
- M. Kuron, C. Stewart, J. de Graaf, and C. Holm, “An extensible lattice Boltzmann method for viscoelastic flows: complex and moving boundaries in Oldroyd-B fluids”, *European Physical Journal E* **44**, 1 (2021).

Parts of these are reproduced verbatim in this thesis without further citation. In the same way, the thesis reproduces some of my contributions to:

- M. Kuron, P. Kreissl, and C. Holm, “Toward Understanding of Self-Electrophoretic Propulsion under Realistic Conditions: From Bulk Reactions to Confinement Effects”, *Accounts of Chemical Research* **51**, 2998 (2018),
- I. Tischler, F. Weik, R. Kaufmann, M. Kuron, R. Weeber, and C. Holm, “A thermalized electrokinetics model including stochastic reactions suitable for multiscale simulations of reaction-advection-diffusion systems”, *ChemRxiv preprint*, 10.33774/chemrxiv-2021-39nhv (2021).

My further publications are not immediately relevant to this thesis:

- M. Kuron and A. Arnold, “Role of geometrical shape in like-charge attraction of DNA”, *European Physical Journal E* **38**, 20 (2015),

- F. Weik, R. Weeber, K. Szuttor, K. Breitsprecher, J. de Graaf, M. Kuron, J. Landsgesell, H. Menke, D. Sean, and C. Holm, “ESPResSo 4.0 – an extensible software package for simulating soft matter systems”, *European Physical Journal Special Topics* **227**, 1789 (2019),
- M. Bauer, S. Eibl, C. Godenschwager, N. Kohl, M. Kuron, C. Rettinger, F. Schornbaum, C. Schwarzmeier, D. Thönnnes, H. Köstler, and U. Rüde, “waLBerla: A block-structured high-performance framework for multi-physics simulations”, *Computers & Mathematics with Applications* **81**, 478 (2021).

1 Introduction

Microswimmers have fascinated people ever since bacteria were first seen under a microscope [10, 11]. Only after the development of microhydrodynamics nearly three centuries later, physicists have been able to describe and come to appreciate the unique challenges that a microorganism’s environment poses on its motion [12, 13]. The term ‘microhydrodynamics’ was coined by Batchelor, who gave a review of its early days in reference 14. It was noticed that swimming at such scales works completely differently from what a human swimmer might be accustomed to [15–19]: more akin to attempting to swim through honey or a tangle of rope than through a pool of water. Theoretical models [20, 21] were developed to abstract the complexities of biology into simple mathematics.

The field gained traction once it was realized that artificial microswimmers could have a plethora of applications in engineering and medicine [22–24]. After the groundbreaking experiments of Paxton et al. [25], whose bimetallic nanorods propel by catalytically decomposing hydrogen peroxide, soon followed by Howse et al. [26] with catalyst-covered non-conductive microspheres, dozens of other groups devised their own microswimmers that swam in all kinds of environments [27–29]. Collective effects previously only known from macroscopic scales, like turbulence [30, 31] or flocking [32], were also observed. New propulsion schemes were developed faster than theoretical understanding could be gained on how efficient they are or why they work at all [33–36]. Some people even argued that a natural microswimmer like *Escherichia coli*, combined with the tools of modern genetics, would provide a simpler, more well-controlled model and yield more insight into microswimming than any of its artificial counterparts [37].

It is difficult and time-consuming to explore a high-dimensional parameter space in experiments, and not all relevant quantities may be directly measurable. A bottom-up model can be constructed to help here once the relevant physical phenomena — like diffusion, hydrodynamics, or heat conductivity — have been identified. The defining property of a bottom-up model is that it contains only physical parameters — such as diffusion coefficients, viscosity, or heat capacity — and no modeling parameters like surface potentials or effective charges. Such a model can give a more detailed picture of what is happening in the experiment and permits selectively switching on and

off aspects like electrostatics or hydrodynamics to determine their relative importance. It might also be employed to optimize a propulsion method for efficiency or speed in a specific environment. Analytic theory can often only solve these models for simple systems or in rough approximation, but gives mathematical expressions that fully answer a question for a wide range of parameters. The power of computer simulations, on the other hand, lies in their ability to deal with complex many-body problems and arbitrary boundary conditions. As a result, theoretical and computational approaches often go hand-in-hand to further the understanding of microswimmers and, in fact, many other fields of physics.

The present chapter will give an overview of active matter and different modeling approaches for it. This shall set the stage for the rest of this thesis.

1.1 Active matter

There are two defining qualities to active matter. Firstly, it must convert energy, either stored internally or harvested from the environment, into useful work. This work is often in the form of motion, but biological active matter also expends a significant amount of energy on upkeep and reproduction of its organism. Secondly, it must possess some kind of asymmetry, e.g. in shape or surface features, that determines the direction of the motion. Spontaneous symmetry breaking is also sufficient [38, 39]. External fields are not allowed to be used to break symmetry under this definition, but their non-directional presence may be used as a convenient energy source [40]. The energy turnover on the single-particle level makes active systems inherently non-equilibrium, which prohibits the use of common terms and methods from thermodynamics. Some equilibrium concepts have successfully been extended for non-equilibrium purposes in active matter [41, 42], and active matter has become an important application and driver [43, 44] of the emerging field of non-equilibrium thermodynamics.

1.1.1 Wet and dry active matter

Active matter can generally be divided into two classes: ‘dry’ and ‘wet’ [45]. The former includes systems where particle momentum is fully dissipated into a rigid substrate, such as a surface or porous medium [46]. The latter encompasses systems where interactions mediated by a fluid play a role [47, 48]. Dense suspensions of active particles are an intermediate case, but can often be considered ‘dry’: while they involve a fluid, thermal fluctuations and steric interactions with neighboring particles typically prevail over any

hydrodynamic interactions [49]. This is not always the case, however, and hydrodynamics might suppress effects predicted by ‘dry’ models [50].

‘Dry’ active matter can exhibit fascinating phenomena such as flocking [51]. Vicsek et al. [52] considered self-propelled particles with constant speed and an alignment interaction and were the first to recognize that there is a phase transition between a disordered and an ordered state. Competition of directional motion and stochastic reorientation, together with short-range pairwise repulsion, gives rise to motility-induced phase separation (MIPS), where particles cluster into an ordered state when directionality dominates and disperse into a disordered state when noise dominates [53–55]. Descriptions in terms of thermodynamics have recently been developed [56, 57]. Some other classic soft matter systems also have active analogues. Active gels consist of cross-linked filaments where the activity stems from attached proteins [58, 59]. Active nematics resemble liquid crystals, but the activity of the constituent particles leads to turbulence and dynamic topological defects [60, 61].

‘Wet’ active matter systems are significantly more complex because they involve more than just the swimmers and their containers. Now the mass, heat, and momentum transport of a fluid may affect the dynamics of the swimmers. Molecules of substances much smaller than the swimmers may be dissolved in the fluid. Long-ranged interactions between swimmers, e.g. through electrostatics [62, 63] or hydrodynamics [64–66], may become relevant as they are no longer screened by the dense packing. In the case of electrostatics, dissolved salt can serve as an alternative screening agent, however some electrostatic potentials due to chemical reactions may not be screenable [35]. Some important functionality of biological microswimmers is due to hydrodynamics [47, 67]: certain sperm swim faster together [68] or accumulate at surfaces [69], and bacteria can attach to surfaces [70]. Use of microswimmers as microfluidic mixing devices has also been demonstrated [71, 72]. Hydrodynamics can have profound effects even on systems typically considered ‘dry’ [73, 74], but cases where effects attributed to hydrodynamics [75] turned out to only be modeling artifacts [65] have also been reported.

1.1.2 Swimming at low Reynolds numbers

Compared to what we know about swimming in a macroscopic world, the hydrodynamics of small length scales poses a major challenge for swimming. The Reynolds number, which will be formally introduced in section 2.5, is significantly less than unity here. This means that the fluid’s dissipative friction dominates and inertial effects are negligible. As a result of this, the Navier-Stokes equations, which govern flow, reduce to the time-independent

Stokes equations as will be shown in section 2.1.3. The lack of time-dependence means that only an asymmetric swimming stroke can lead to net motion. In a symmetric (or reciprocal) stroke, even if forward and backward stroke were carried out at different speeds, both strokes would cover the exact same distance. This was originally described by Taylor [15–17] and later popularized by Purcell [19], who stated that swimming like a scallop — by opening slowly and closing quickly to squirt out water — is ill-suited for moving through the microscopic world.

For this reason, evolution has come up with a variety of specialized propulsion methods for biological microorganisms. Similarly, scientists have to resort to certain tricks to make man-made microswimmers actually swim. These will be covered in the sections below. Additionally, it is worth noting that Purcell’s theorem is only valid under precisely the conditions given: as soon as any symmetry is broken, swimming is possible even by reciprocal motion [76]. Flows in viscoelastic fluids, which have memory, are not time-reversible [77, 78]. Small amounts of inertia of the fluid [79] or the swimmer [80, 81] can also break time-reversibility. Spatial symmetry can be broken by the hydrodynamic interaction with other swimmers [82] or with surfaces [83].

1.1.3 Biological microswimmers

The most prominent microswimmers are bacteria. They typically propel mechanically by beating or turning one or more flagella, which are hair-like appendages of lengths similar to the bacterium itself. Each flagellum is attached to a motor protein, which converts chemical energy into rotational motion [84, 85]. Such bacteria are classified by the number and positioning of their flagella [86]: one or more may be anchored in one spot or at opposite ends of the bacterium, or the entire surface of the bacterium might be covered with flagella.

Flagella alone may be sufficient for directed motion, but not for the choice of direction to follow a specific purpose. The bacterium needs to be able to influence its direction of swimming, e.g. in response to a gradient in nutrient concentration, viscosity, or temperature that it senses. This is called “taxis”, or for the specific examples, “chemotaxis”, “viscotaxis”, and “thermotaxis”. One approach to this is employed by *Escherichia coli* and is called “run and tumble” [85]: Depending on the direction in which the motor protein turns, the helical flagella either bundle together or unbundle. When the flagella are bundled together, their rotation propels the bacterium forward in a corkscrew fashion. When the bacterium needs to reorient, it changes

the motor direction to unbundle the flagella until rotational diffusion has reoriented it to its new preferred direction.

Other biological microswimmers include sperm, algae such as *Chlamydomonas reinhardtii* or *Volvox*, and microorganisms like *Paramecium*. They employ similar kinds of mechanical propulsion, even if the precise details of the motor and beating pattern differ and the appendages might be called “cilia” or “filaments” [29]. In the case of the algae, an additional kind of taxis becomes relevant, namely phototaxis, as swimming toward light is favorable for photosynthesis [87]. Even some enzymes may be considered swimmers as they perform phoresis [88, 89].

Most biologically relevant fluids are more complex than water. Examples include ovary fluids, through which sperm swim [90, 91]; stomach mucus, through which *Helicobacter pylori* burrows [92]; the biofilms formed by some bacteria [93]; and blood, in which *Trypanosoma* live [94]. All of these fluids possess internal structure, which means that they might necessitate specialized swimming modes or can even enable swimming by strokes that do not yield net propulsion in Newtonian media. The non-Newtonian rheology of blood is shear-thinning, while the other fluids are viscoelastic.

1.1.4 Artificial microswimmers

Millions of years of evolution have endowed even single-celled microorganisms with enough complexity that arguably they cannot serve as minimal model microswimmers. While much of this complexity is unrelated to the process of swimming itself, the non-swimming and swimming functions are entwined, for example via shape changes or the metabolism. Furthermore, some examples listed in the previous section are highly pathogenic and thus not suitable for use in many laboratories. As a result, various kinds of artificial microswimmers have been developed. Mechanical propulsion like for the natural microswimmers still poses a significant engineering challenge, so with the exception of some swimmers with propulsion resembling that of sperm [95, 96], most work has focused on chemically-propelled microswimmers, some of which we will detail in the following. A further advantage of this is that taxis can be built directly into the propulsion scheme [97, 98], whereas microorganisms typically have distinct sensing and propulsion organs [99].

Bimetallic nanorods and microspheres were among the first artificial chemical microswimmers as mentioned at the beginning of this chapter [25, 100]. They consist of a catalytic and an inert metal, for example platinum and gold. The catalyst enables the decomposition of a fuel, typically hydrogen peroxide into water and oxygen. This is a redox reaction, where the conduction of electrons across the bimetal plays a role [101]. The

propulsion is commonly understood to be self-electrophoretic in nature [102]: the swimmer is charged and the reaction creates an inhomogeneous charge distribution around the swimmer, so it moves in this self-generated field [103]. A crucial aspect here is the large difference in diffusivity of the various solute ions [104]. The full chemistry of the catalytic process is unfortunately not yet known; it has been speculated that intermediate reaction products play a significant role [35], but simpler models without these have also been highly successful at explaining experimental observations [101].

Janus swimmers are colloids partially coated with a catalyst, often platinum on silica [26, 105]. They operate on the same hydrogen peroxide-decomposition reaction as above, but the isolating properties of the colloid seemed to rule out that this is the same propulsion method. Propulsion here was first attributed to self-diffusiophoresis [106–108], where the inhomogeneous distribution of neutral reaction products and their short-ranged interaction with the swimmer’s surface lead to motion. It was later argued that there is a self-electrophoretic component to the propulsion as well due to intermediate reaction products [34–36, 109] and that inhomogeneous reaction rates due to inhomogeneous catalyst coating thickness play a role [36].

Many other swimmer propulsion methods have been realized in experiments. For extensive reviews, see references 27–29. These include self-thermophoresis [40, 110, 111], bubble propulsion [112], propulsion by differences in surface tension via the Marangoni effect [113, 114], and propulsion by Quincke rotation [115, 116].

1.1.5 Pairwise and collective interactions

So far, we have only discussed active matter on the single-swimmer level. This might suffice for many applications, e.g. drug delivery [117] or micromixing [118], but some of microswimmers’ most interesting properties stem from their interactions with each other [64–66]. Long-ranged interactions in soft matter are generally hydrodynamic or electrostatic, which are relevant here for ‘wet’ and for charged active matter, respectively. Short-ranged interactions also play a role, e.g. the repulsion on close contact that prevents overlap of two swimmers, and are the primary interactions found in ‘dry’ active matter. A different kind of interaction is unique to active matter: the phoretic interaction. In this case, one swimmer’s phoresis affects another swimmer’s taxis or ability to phorese. For example, a chemophoretic bacterium’s consumption of nutrient might cause another bacterium to perform taxis away from it or slow down that bacterium’s chemophoresis. This kind of effect has been directly observed in an experiment where oil droplets

self-propel through a surfactant solution and leave behind a trail of filled micelles, which other droplets then avoid until the trail has dispersed [114].

The combination of all these interactions may lead to collective effects that span large groups of swimmers or even an entire population [29]. This can either be in the form of self-organization [119–127] or as cooperative behavior [68, 128, 129], where swimmers together achieve something that a single one could not achieve. Such behavior can resemble turbulence [30, 31] — a phenomenon well-known in high-Reynolds fluid dynamics but with a completely different underlying cause — and flocking [32] similar to how large groups of birds or fish behave. This kind of collective behavior is currently one of the most actively researched areas of active matter.

1.2 Modeling of active matter

The level of detail on which microswimmers need to be modeled depends on the phenomena one intends to study. It is generally not possible to consider every atom in the system: for analytic theory, the atoms’ discrete nature is highly inconvenient, while for computation, the sheer number of atoms is intractable. Fortunately this amount of detail is usually not necessary. The first question to answer before picking a modeling approach is whether the fluid plays a role. This mirrors the ‘wet’ vs. ‘dry’ discussion of section 1.1.1. This is followed by questions about what resolution is required (the collective of swimmers, the swimmer, the swimmer’s surface, the fluid’s structure) and whether the details of the propulsion method matter, as illustrated by the decision tree in figure 1.1.

Microswimmers, being on the order of 10^{-8} m to 10^{-4} m [27], are not subject to quantum effects, only their surface chemistry might be. Even the influence of thermal fluctuations at this length scale is often negligible. Water and many other fluids consist of molecules much smaller than that, so they may be described by continuum equations, e.g. for mass and momentum, to which the microswimmers only act as boundary conditions. Solutes suspended in the fluid, like ions or polymers, are usually also much smaller than the swimmers, so these too may be described by continuum equations, e.g. for concentration or orientation. Note that there are exceptions: for example, some viscoelastic liquids contain polymers with effective sizes on the order of or larger than typical microswimmers [130], in which case the polymers need to be modeled at the same level as the microswimmer. There are even situations in which the swimmers themselves can be considered implicitly via continuum equations.

Each of these modeling approaches will be briefly discussed in the rest of

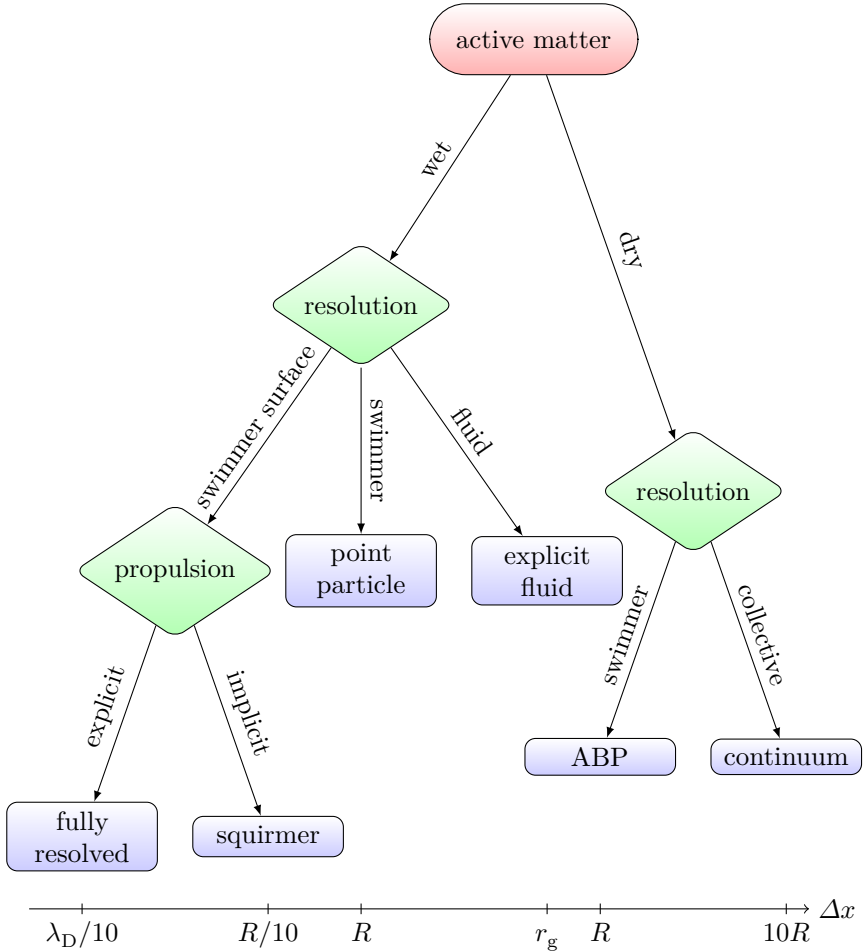


Figure 1.1: Decision tree for the choice of a modeling approach for microswimmers. The scale bar at the bottom indicates the finest length scale resolved — like the size of a lattice cell, the physical radius of a particle modeled as point-like, or the smallest physical features incorporated into an analytic model. R is the radius of an individual swimmer, λ_D is a characteristic interaction length scale (like the Debye length in an electrolyte solution, see section 2.2.2), and r_g is the structure size of the fluid (like the radius of gyration of the polymers in a polymer solution).

this section, but the thesis as a whole will focus on the surface-resolved ones. We start with the most detailed and then move to the coarser, more abstract models. For each model, it will be mentioned what kind of phenomena can be studied with it and what its limitations are.

1.2.1 Explicit-particle methods

The simplest models describe the microswimmers and their surrounding fluid as particles. This is generally done in a molecular dynamics (MD) or Monte Carlo (MC) simulation, where trajectories or thermodynamic states are calculated from particle-particle interactions. The main modeling assumptions lie in these interactions. In an atomistic simulation, these could come from first principles, but due to the large number of atoms involved, coarse-grained simulations are typically used. There, each particle represents entire molecules, monomers, clusters of fluid molecules, or even entire swimmers, so effective interactions need to be used.

Experimentally measurable parameters such as diffusion coefficients, reaction rates, and colloid sizes can be used to inform simulation parameters, but there is generally no trivial parameter mapping. For this reason, explicit-particle methods are not often used directly for active matter [131].

1.2.2 Continuum fluid methods with resolved propulsion

The highest-level models that are compatible with phoretic interactions of the swimmers are those that explicitly consider the swimmers' propulsion. Generally, this means resolving the swimmer's surface, e.g. the bacterium's flagella or the Janus colloid's surface coating profile. The fluid is treated as a continuum, usually by the Navier-Stokes equations (see section 2.1.3) or a viscoelastic model (see section 2.1.5). Other relevant fields, such as temperature, concentration of various solutes, etc. may be included and similarly evolved by continuum equations. The main requirement here is that fluid molecules and any solutes are significantly smaller than the swimmer. Most model parameters — like diffusion coefficients, reaction rates, or viscosity — can be measured in experiments, so this can be considered a bottom-up model. The main modeling choice is which equations and fields to include. The microswimmers serve as boundary conditions to these equations.

The limitations of this approach are mostly due to computational effort. In addition to resolving the swimmer's surface, all field gradients need to be resolved. For self-electrophoresis, this poses a problem when the electric double layer (see section 2.2.2) is thin compared to the swimmer's

size, as in high-salt environment or for nanoswimmers. In the case of self-diffusiophoresis, the relevant interactions take place on atomistic length scales [106, 107], which cannot reasonably be resolved in a continuum model. Thus it is common practice to introduce effective surface charges and surface slip velocities on the swimmer [132–134], which defeats the bottom-up nature of this modeling approach and makes it difficult to include phoretic interactions in the model.

These continuum models have successfully been applied to single artificial swimmers [101, 102, 135, 136] and for the interactions of several swimmers [137, 138], but simulations involving the collective effects of thousands of swimmers are just barely possible given today’s computing capabilities [134]. The finite element method (FEM) [136, 139, 140], finite volume (FV) method [141], boundary element method (BEM) [135], and boundary integral method (BIM) [138] are commonly used for modeling on this scale, but are primarily suited to steady states and not to the calculation of trajectories, due to the cost of re-meshing. Lattice Boltzmann (LB) and multi-particle collision dynamics (MPCD) are thus a more natural choice for the simulation of transient behavior, and the work of chapter 8 takes a step in that direction. That chapter’s introduction also draws a comparison between available simulation methods and mentions some of their applications beyond the field of active matter. MPCD is comparable to LB in terms of computational effort, but for the systems considered here, its unphysical compressibility and inherent thermal fluctuations are a disadvantage. Another method worth mentioning is dissipative particle dynamics (DPD), whose use has mostly been superseded by MPCD because its model parameters do not easily translate into rheological quantities like viscosity. LB and MPCD have successfully been applied to mechanical propulsion by flagella [142–145], but these simulations are simpler because they do not involve any non-hydrodynamic effects. DPD has been applied to chemical swimmers [146] and self-thermophoretic swimmers [147], but proved computationally too inefficient as it required a resolution that would more readily put it into section 1.2.1.

1.2.3 Continuum fluid methods with effective propulsion

Compared to section 1.2.2, effective-propulsion models eliminate the details of the propulsion method and resort to purely hydrodynamic descriptions [148–153], usually by the squirmer model [20, 21], which will be formally introduced in section 2.4. The squirmer parameters may be chosen based on the specific propulsion method of the swimmer [154–156]. This eliminates a significant part of the computational effort, but also eliminates any phoretic

interactions from the model. The reduction in complexity enables scaling up to systems where collective effects across many swimmers play a role [65, 75, 129, 157–160]. The simulations in chapters 5 and 7 fall into this category, and these chapters will draw a more detailed comparison between available computational methods.

Further simplification is possible by only considering the far field [161–164]. In this case, the equations may simplify to the point where they are analytically tractable [165–167], but this comes at the price of a loss of accuracy in the hydrodynamic interactions over small distances. Despite this simplification, the predictive power of such far-field models is astonishing, as seen, for example, with the calculations performed in chapter 6. That chapter’s introduction will also give a broader perspective on hydrodynamic far-field models.

1.2.4 Explicit fluid methods

The continuum fluid methods of sections 1.2.2 and 1.2.3 cannot deal with fluids composed of molecules that are not small compared to the swimmer. The most prominent example of this is swimming in polymeric solutions [168, 169]. In this case, the solvent can be modeled as before, but the polymers are considered in an MD fashion and coupled to the fluid.

1.2.5 Continuum fluid methods with point-coupled swimmers

The continuum fluid methods of sections 1.2.2 and 1.2.3 resolve the swimmer to study interactions between multiple swimmers at high precision. If that is not required, swimmers can be considered as point forces acting on the fluid [73, 170, 171]. This decreases the required resolution by an order of magnitude and thus enables the study of systems involving millions of swimmers on a single computer [73, 171].

1.2.6 Active Brownian particles

The active Brownian particle (ABP) model is a coarse-grained MD model with a prescribed velocity for each particle, hard-core repulsion between particles, and thermal fluctuations that randomly reorient particles [172–174]. In stark contrast to the models discussed so far, it does not involve a fluid and is thus not momentum-conserving, which makes it suited for ‘dry’ active matter. With the swimmers only represented by an effective velocity and rotational diffusivity, phoretic interactions are obviously not represented

either. Due to its simplicity and high computational efficiency, the ABP model can easily be applied to systems involving millions of swimmers [175]. The run-and-tumble particle (RTP) model is conceptually similar to the ABP model, tumbling at discrete times instead of exhibiting continuous rotational diffusion [176].

1.2.7 Continuum active matter

The coarsest active matter models are those where the individual swimmers are not resolved, but rather considered as a continuous medium with local properties like density and orientation. The time evolution is described by a Fokker-Planck equation that incorporates any interactions of a swimmer with other swimmers and with its environment into effective interactions, making it a mean-field approximation. The Fokker-Planck equation is a stochastic differential equation, which makes the approach well-suited for Brownian diffusion processes.

This kind of continuum method has been applied to microswimmers both with hydrodynamics [177–181] and without [182–185]. Comparable methods have been applied to active nematics [186–189], where the nematics and their activity are included into the hydrodynamic equations, and to ABPs [190], where continuum equations for their density distribution are obtained. Continuum methods are well suited to study collective effects, as long as these are agnostic to the details of the swimmers’ interactions. Hydrodynamic interactions are dealt with in a significantly simplified way, and phoretic interactions are usually not considered. For this reason, they are mostly suited to ‘dry’ active matter.

1.3 Scope of this thesis

Recapitulating this brief overview, we have seen that many different methods for modeling exist, covering various scales and levels of detail. The rest of this thesis focuses on those methods with resolved propulsion and high computational efficiency. Such methods are adapted for new purposes and applied to sample problems. In the near future, this will allow for simulations that incorporate enough detail to calculate phoretic interactions between individual swimmers, yet are scalable enough to handle numbers of swimmers that were previously only accessible to ‘dry’ simulations.

Chapter 2 will introduce in detail the theoretical background for the later chapters. Chapters 3 and 4 will follow with the computational and analytic methods used. In chapter 5, a hydrodynamic model microswimmer will be

studied using a surface-resolved fluid dynamics method. This is followed up by chapter 6, which uses a much simpler analytic far-field model to efficiently shed light on a specific class of trajectories discovered in chapter 5. Chapter 7 introduces and validates a computational model for studying surface-resolved microswimmers in viscoelastic fluids. Chapter 8 takes a comparable approach for colloids in electrolyte solutions as a basis for a propulsion-resolved model, and finds a solution to the additional complications stemming from highly inhomogeneous ion distributions. Finally, chapter 9 will summarize this work and give an outlook on worthwhile future directions of research.

2 Theoretical background

This chapter introduces the equations underlying the relevant flow and transport phenomena. We start out with the Navier-Stokes and Stokes equations for hydrodynamics in sections 2.1.1 to 2.1.4 and extend them to a viscoelastic Oldroyd-B fluid in section 2.1.5. Next, the electrokinetic equations that describe the diffusion, advection and migration of ions in solution are introduced in section 2.2. All of these equations describe bulk behavior, to which section 2.3 provides the relevant boundary conditions. While electrokinetics can be used to propel a microswimmer, we also introduce a simple and purely hydrodynamic far-field model microswimmer in section 2.4. The final section, section 2.5, list all dimensionless numbers relevant to the physical problems discussed in this thesis. In terms of notation, bold symbols denote vectors $(\mathbf{Z})_i = Z_i$ and bold sans-serif symbols denote tensors $(\mathbf{Z})_{ij} = Z_{ij}$.

2.1 Fluid dynamics

The dynamics of a fluid can be derived by assuming that mass and momentum are conserved. For the fluids considered in this thesis, incompressibility and the irrelevance of inertia may be assumed to further simplify the resulting equations.

2.1.1 Navier-Stokes equations

Let us consider the fluid in a small volume V_0 and with density ρ . Any change of the mass inside this small volume is due to flow with velocity \mathbf{u} through ∂V_0 , the control volume's surface. This may be expressed as

$$\frac{\partial}{\partial t} \int_{V_0} \rho(\mathbf{r}, t) d^d r = - \int_{\partial V_0} \rho(\mathbf{r}, t) \mathbf{u}(\mathbf{r}, t) \cdot \hat{\mathbf{n}} d^{d-1} r, \quad (2.1)$$

with d the number of spatial dimensions and $\hat{\mathbf{n}}$ the surface normal vector. The surface integral may be transformed into a volume integral using Gauß's

2 Theoretical background

divergence theorem to obtain

$$\frac{\partial}{\partial t} \int_{V_0} \rho(\mathbf{r}, t) d^d r = - \int_{V_0} \nabla \cdot (\rho(\mathbf{r}, t) \mathbf{u}(\mathbf{r}, t)) d^d r. \quad (2.2)$$

This expression holds for arbitrary V_0 , so the mass conservation law may also be written in differential form,

$$\frac{\partial}{\partial t} \rho(\mathbf{r}, t) + \nabla \cdot (\rho(\mathbf{r}, t) \mathbf{u}(\mathbf{r}, t)) = 0. \quad (2.3)$$

This expression is often referred to as continuity equation for the fluid.

A similar approach may be taken to momentum conservation. Momentum inside the small volume may change due to momentum flowing through the surface, due to forces acting on the volume, and due to forces acting across the surface:

$$\begin{aligned} \frac{\partial}{\partial t} \int_{V_0} \rho(\mathbf{r}, t) \mathbf{u}(\mathbf{r}, t) d^d r &= - \int_{\partial V_0} \rho(\mathbf{r}, t) \mathbf{u}(\mathbf{r}, t) (\mathbf{u}(\mathbf{r}, t) \cdot \hat{\mathbf{n}}) d^{d-1} r \\ &\quad + \int_{V_0} \mathbf{F}(\mathbf{r}, t) d^d r + \int_{\partial V_0} \boldsymbol{\sigma}(\mathbf{r}, t) \hat{\mathbf{n}} d^{d-1} r. \end{aligned} \quad (2.4)$$

Note that the surface force is written in terms of a stress $\boldsymbol{\sigma}$. Again, the divergence theorem may be applied,

$$\begin{aligned} \frac{\partial}{\partial t} \int_{V_0} \rho(\mathbf{r}, t) \mathbf{u}(\mathbf{r}, t) d^d r &= - \int_{V_0} \nabla \cdot (\rho(\mathbf{r}, t) \mathbf{u}(\mathbf{r}, t) \otimes \mathbf{u}(\mathbf{r}, t)) d^d r \\ &\quad + \int_{V_0} \mathbf{F}(\mathbf{r}, t) d^d r + \int_{V_0} \nabla \cdot \boldsymbol{\sigma}(\mathbf{r}, t) d^d r, \end{aligned} \quad (2.5)$$

and the differential momentum conservation law may thus be expressed as

$$\frac{\partial}{\partial t} \rho(\mathbf{r}, t) \mathbf{u}(\mathbf{r}, t) + \nabla \cdot (\rho(\mathbf{r}, t) \mathbf{u}(\mathbf{r}, t) \otimes \mathbf{u}(\mathbf{r}, t)) = \mathbf{F}(\mathbf{r}, t) + \nabla \cdot \boldsymbol{\sigma}(\mathbf{r}, t). \quad (2.6)$$

Here, \otimes is the tensor product and $\nabla \cdot$ now operates in a tensorial fashion. To avoid ambiguity in the meaning of these symbols, component notation will be used in the following.

A Newtonian fluid's stress $\boldsymbol{\sigma}$ consists of a viscous stress $\boldsymbol{\epsilon}$ and a pressure p :

$$\sigma_{ij}(\mathbf{r}, t) = \epsilon_{ij}(\mathbf{r}, t) - p(\mathbf{r}, t) \delta_{ij}, \quad (2.7)$$

$$\varepsilon_{ij}(\mathbf{r}, t) = \eta_n \left(\frac{\partial}{\partial r_i} u_j(\mathbf{r}, t) + \frac{\partial}{\partial r_j} u_i(\mathbf{r}, t) \right), \quad (2.8)$$

where η_n is the viscosity of the fluid.

Navier-Stokes has a third conservation law, one for energy. It describes the evolution of the local fluid temperature. For purposes of this thesis, we will assume isothermal fluids and negligible local heat production by the swimmers and by chemical reactions. Thus our flows are fully described by the first two Navier-Stokes equations.

2.1.2 Incompressible Navier-Stokes equations

The compressibility of most liquids is negligible, in contrast to gases, where compressibility may become relevant. This difference is characterized by the Mach number

$$\text{Ma} = \frac{u}{c_s},$$

where c_s is the speed of sound. Incompressibility may be assumed when $\text{Ma} \ll 1$. As a result, for the purposes of this thesis we may use

$$\rho(\mathbf{r}, t) \equiv \rho \quad (2.9)$$

and thus simplify equations 2.3 and 2.6 together with equation 2.7 to obtain

$$\nabla \cdot \mathbf{u}(\mathbf{r}, t) = 0, \quad (2.10)$$

$$\frac{\partial}{\partial t} \mathbf{u}(\mathbf{r}, t) + \mathbf{u}(\mathbf{r}, t) \nabla \cdot \mathbf{u}(\mathbf{r}, t) = -\nabla p(\mathbf{r}, t) + \eta_n \nabla^2 \mathbf{u}(\mathbf{r}, t) + \mathbf{F}^{\text{ext}}(\mathbf{r}, t), \quad (2.11)$$

where we have replaced \mathbf{F} with \mathbf{F}^{ext} to clarify that this is the applied force and does not contain the viscous forces internal to the fluid. These equations are the incompressible Navier-Stokes equations.

2.1.3 Stokes equations

We may further simplify the incompressible Navier-Stokes equations 2.10 and 2.11 by considering the characteristic time scale T , velocity scale U , and length scale L of the flow. These can be used to introduce rescaled quantities $\mathbf{r}^* = \mathbf{r}/L$, $\mathbf{u}^* = \mathbf{u}/U$, $t^* = t/T$, $p^* = Lp/(\eta_n U)$, and $\mathbf{F}^* = L^2 \mathbf{F}^{\text{ext}}/(\eta_n U)$. Note that we do not set T to L/U as it is not necessarily the time it takes to move by the characteristic length. Instead, T is the characteristic time on which the flow is driven, for example by an oscillation with a frequency

of T^{-1} [191]. Expressing equations 2.10 and 2.11 in terms of these new variables yields

$$\nabla_* \cdot \mathbf{u}^*(\mathbf{r}^*, t^*) = 0, \quad (2.12)$$

$$\begin{aligned} \text{Re} \left(\text{St} \frac{\partial}{\partial t^*} \mathbf{u}^*(\mathbf{r}^*, t^*) + \mathbf{u}^*(\mathbf{r}^*, t^*) \nabla_* \cdot \mathbf{u}^*(\mathbf{r}^*, t^*) \right) \\ = -\nabla_* p^*(\mathbf{r}^*, t^*) + \nabla_*^2 \mathbf{u}^*(\mathbf{r}^*, t^*) + \mathbf{F}^*(\mathbf{r}^*, t^*), \end{aligned} \quad (2.13)$$

where ∇_* differentiates with respect to \mathbf{r}^* and the Reynolds number

$$\text{Re} = \frac{\rho U L}{\eta_n}$$

and Strouhal number

$$\text{St} = \frac{L}{UT}$$

have been introduced. These will be discussed further in section 2.5. For now, it suffices to say that for microscale flows like in this thesis, $\text{Re} \ll 1$ may be assumed, but ReSt may still be on the order of unity. This yields the time-dependent or unsteady incompressible Stokes equation,

$$\frac{\partial}{\partial t} \mathbf{u}(\mathbf{r}, t) = -\nabla p(\mathbf{r}, t) + \eta_n \nabla^2 \mathbf{u}(\mathbf{r}, t) + \mathbf{F}^{\text{ext}}(\mathbf{r}, t). \quad (2.14)$$

Under the further assumption of $\text{St} \ll \text{Re}^{-1}$, we obtain the time-independent incompressible Stokes equation [192]

$$-\nabla p(\mathbf{r}, t) + \eta_n \nabla^2 \mathbf{u}(\mathbf{r}, t) + \mathbf{F}^{\text{ext}}(\mathbf{r}, t) = \mathbf{0}. \quad (2.15)$$

This form of the Stokes equation will be used throughout the thesis, and the assumption it is based on will be justified in section 2.5.

2.1.4 Generalized Stokes equations

The more general case of non-Newtonian fluids adds an extra stress $\boldsymbol{\tau}$ to equation 2.7. $\boldsymbol{\tau}$ evolves according to a constitutive equation. Its effect on the flow may be absorbed into equation 2.15's force via

$$\mathbf{F}^{\text{P}}(\mathbf{r}, t) = \sum_{j=1}^d \hat{\mathbf{e}}_j \sum_{i=1}^d \frac{\partial}{\partial r_i} \tau_{ij}(\mathbf{r}, t), \quad (2.16)$$

where $\hat{\mathbf{e}}_i$ is the i -th unit vector. The total force density $\mathbf{F}^{\text{ext}} = \mathbf{F} + \mathbf{F}^{\text{P}}$ is a sum of an applied force density and the force resulting from the added stress, which might stem from viscoelasticity, as discussed in the next section.

2.1.5 Viscoelastic fluids: Oldroyd-B

Theoretical descriptions of viscoelastic flows are commonly split into a Newtonian part and an additional constitutive equation (see section 2.1.4), which describes the stress evolution. There are many different constitutive equations that describe the wide range of complex fluids encountered in applications. These include Oldroyd-B [193], Jeffreys [194, 195], Giesekus [196], FENE-P [197], FENE-CR [198], or Phan-Thien-Tanner (PTT) [199]. Finitely extensible nonlinear elastic (FENE) refers to the interaction potential between monomers, which diverges logarithmically when the polymer is expanded or contracted from its equilibrium length [200]. Oldroyd-B, on the other hand, uses a harmonic potential. For simplicity's sake and because it is widely studied, we will focus on Oldroyd-B, though the methods discussed in this thesis can easily be extended to the more realistic models. Oldroyd-B's $\boldsymbol{\tau}$ corresponds to the conformation tensor of the constituent polymers, averaged over a small control volume [201]. It makes several strongly simplifying assumptions about the fluid, including that it is made up of dumbbell polymers with zero equilibrium length and that these are very dilute [202, 203], to arrive at the following constitutive equation:

$$\begin{aligned} \frac{\partial}{\partial t} \tau_{ij}(\mathbf{r}, t) = & - \sum_{k=1}^d u_k(\mathbf{r}, t) \frac{\partial}{\partial r_k} \tau_{ij}(\mathbf{r}, t) \\ & + \sum_{k=1}^d \tau_{ik}(\mathbf{r}, t) \frac{\partial}{\partial r_k} u_j(\mathbf{r}, t) + \sum_{k=1}^d \tau_{kj}(\mathbf{r}, t) \frac{\partial}{\partial r_k} u_i(\mathbf{r}, t) \\ & + \frac{\eta_p}{\lambda_p} \left(\frac{\partial}{\partial r_i} u_j(\mathbf{r}, t) + \frac{\partial}{\partial r_j} u_i(\mathbf{r}, t) \right) - \frac{1}{\lambda_p} \tau_{ij}(\mathbf{r}, t). \end{aligned} \quad (2.17)$$

Here, the first term corresponds to advection, the next two terms are due to the polymers being stretched by the velocity gradient, and the final two terms represent the polymer relaxation. λ_p is the relaxation time of the polymers, while η_p refers to the viscosity added to the fluid by their presence and is in first order proportional to the polymer concentration. For use with the finite volume (FV) scheme in section 4.2.3, flux and source terms are identified in order to re-cast equation 2.17 as a conservation law:

$$\frac{\partial}{\partial t} \tau_{ij}(\mathbf{r}, t) = - \frac{\partial}{\partial r_k} J_{ijk}(\mathbf{r}, t) + S_{ij}(\mathbf{r}, t) \quad (2.18)$$

$$J_{ijk}(\mathbf{r}, t) = u_k(\mathbf{r}, t) \tau_{ij}(\mathbf{r}, t) \quad (2.19)$$

$$\begin{aligned}
 S_{ij}(\mathbf{r}, t) &= \tau_{ij}(\mathbf{r}, t) \underbrace{\sum_{k=1}^d \frac{\partial}{\partial r_k} u_k(\mathbf{r}, t)}_{=0 \text{ per equation 2.10}} \\
 &+ \sum_{k=1}^d \tau_{ik}(\mathbf{r}, t) \frac{\partial}{\partial r_k} u_j(\mathbf{r}, t) + \sum_{k=1}^d \tau_{kj}(\mathbf{r}, t) \frac{\partial}{\partial r_k} u_i(\mathbf{r}, t) \\
 &+ \frac{\eta_p}{\lambda_p} \left(\frac{\partial}{\partial r_i} u_j(\mathbf{r}, t) + \frac{\partial}{\partial r_j} u_i(\mathbf{r}, t) \right) - \frac{1}{\lambda_p} \tau_{ij}(\mathbf{r}, t). \quad (2.20)
 \end{aligned}$$

2.2 Electrokinetic equations

The electrokinetic equations for bulk electrolytes describe the motion of a charged solute in a solvent fluid by a diffusion-advection process. They can be constructed by considering the conservation of mass and all the forces acting on the solute.

2.2.1 Diffusion-advection-migration processes

Let us take a similar approach as in section 2.1.1 and consider the solute in a small volume of fluid V_0 . The solute concentration is ρ_k , where the k runs over the different solute species. Any change of the amount of solute inside this small volume is due to a flux \mathbf{j}_k through ∂V_0 , the control volume's surface. This may be expressed as

$$\frac{\partial}{\partial t} \int_{V_0} \rho_k(\mathbf{r}, t) d^d r = - \int_{\partial V_0} \mathbf{j}_k(\mathbf{r}, t) \cdot \hat{\mathbf{n}} d^{d-1} r. \quad (2.21)$$

The surface integral may be transformed into a volume integral using Gauß's divergence theorem to obtain

$$\frac{\partial}{\partial t} \int_{V_0} \rho_k(\mathbf{r}, t) d^d r = - \int_{V_0} \nabla \cdot \mathbf{j}_k(\mathbf{r}, t) d^d r. \quad (2.22)$$

This expression holds for arbitrary V_0 , so the conservation law for the amount of solute may also be written in differential form,

$$\frac{\partial}{\partial t} \rho_k(\mathbf{r}, t) = -\nabla \cdot \mathbf{j}_k(\mathbf{r}, t). \quad (2.23)$$

This expression is often referred to as continuity equation for the solute.

To obtain the precise form of \mathbf{j}_k , we consider the effects that may move solute through the fluid. From Fick's law of diffusion [204], it is known

that thermal fluctuations even out any concentration differences in a fashion proportional to the concentration gradient. The proportionality constant for this is the diffusion coefficient D_k . Next, let us consider what happens when the solvent flows with a velocity of \mathbf{u} . The diffusion process happens in the reference frame co-moving with the fluid, so in the laboratory frame the solute moves with an additional velocity of \mathbf{u} . A Galilean transformation thus leads to the advective flux of $\rho_k \mathbf{u}$. Similarly, a force \mathbf{F} applied to the solute moves it with velocity $\mu_k \mathbf{F}$, where μ_k is the mobility. In an electric potential Φ , we have $\mathbf{F} = z_k e \nabla \Phi$ with z_k the ionic valency and e the unit charge. The mobility is given by the Einstein-Smoluchowski relation $D_k = \mu_k k_B T$ with k_B being Boltzmann's constant and T the absolute temperature [205, 206]. The complete expression for the flux thus is

$$\mathbf{j}_k(\mathbf{r}, t) = \underbrace{-D_k \nabla \rho_k(\mathbf{r}, t) - \frac{D_k}{k_B T} z_k e \rho_k(\mathbf{r}, t) \nabla \Phi(\mathbf{r}, t)}_{\mathbf{j}_k^{\text{diff}}} + \underbrace{\rho_k(\mathbf{r}, t) \mathbf{u}(\mathbf{r}, t)}_{\mathbf{j}_k^{\text{adv}}}. \quad (2.24)$$

$\mathbf{j}_k^{\text{diff}}$ is the Nernst-Planck equation, while in combination with equation 2.26 it is referred to as Poisson-Nernst-Planck.

The electrostatic potential Φ of the total charge

$$\rho_{\text{total}}(\mathbf{r}, t) = \sum_k z_k e \rho_k(\mathbf{r}, t) \quad (2.25)$$

is given by Poisson's equation

$$\nabla^2 \Phi(\mathbf{r}, t) = -\frac{1}{\varepsilon_0 \varepsilon_r} \rho_{\text{total}}(\mathbf{r}, t) = -\frac{4\pi \lambda_B k_B T}{e} \sum_k z_k \rho_k(\mathbf{r}, t), \quad (2.26)$$

with the Bjerrum length

$$\lambda_B = \frac{e^2}{4\pi \varepsilon_0 \varepsilon_r k_B T}. \quad (2.27)$$

A spatially homogeneous dielectric permittivity $\varepsilon_0 \varepsilon_r$ is assumed here. The Bjerrum length gives the distance at which the magnitude of the interaction between two unit charges equals thermal energy. For water at room temperature, $\lambda_B = 0.7$ nm.

Note that the construction of equation 2.24 contains several simplifying assumptions. The first one is that we require D_k to be a constant for each solute species. In reality however, its value depends on the surrounding fluid. For the purposes of this thesis, we may limit ourselves to water, but even there the diffusivity of one solute species may be affected by the presence

of other solute species. Formally, we have thus set the self-diffusivity to D_k and the cross-diffusivity to zero. The second assumption is that the electrostatic contribution to equation 2.24 decouples for the different k . As pointed out by Gupta et al. [207], this common simplification means that in the absence of an external field, each electrolyte needs to fulfill the local electroneutrality condition individually instead of collectively. Thus, if one of the ions has a much higher diffusivity than the others, the model will predict it to diffuse too slowly [207]. The final assumption lies in the construction of equation 2.10, which neglects the contribution of the solute to the total mass, but this is reasonable at solute concentrations up to several mol L^{-1} [208].

The force density couples the motion of the fluid to the dynamics of the solutes via the following equation [209]:

$$\mathbf{F}(\mathbf{r}, t) = k_B T \sum_k \frac{\mathbf{j}_k^{\text{diff}}(\mathbf{r}, t)}{D_k}. \quad (2.28)$$

This represents a frictional coupling proportional to the relative velocities of fluid and ions.

2.2.2 Poisson-Boltzmann theory

The electrokinetic equations of section 2.2.1 have a well-known solution: Poisson-Boltzmann (PB) theory. In equilibrium, there are no fluxes, $\mathbf{j}_k = \mathbf{0}$, and the net flow is zero, $\mathbf{u} = \mathbf{0}$. Under these conditions, the solution of equation 2.24 is a Boltzmann-distributed solute concentration:

$$\rho_k(\mathbf{r}, t) = \rho_k^0 \exp\left(-\frac{z_k e (\Phi(\mathbf{r}, t) - \Phi_0)}{k_B T}\right) \quad (2.29)$$

with ρ_k^0 and Φ_0 the concentration and potential at a reference location. Typically, the bulk concentration, i.e. at $r \rightarrow \infty$ or far away from any charged surfaces or objects, is used for ρ_k^0 , and the potential there is defined to be $\Phi_0 = 0$.

Inserting equation 2.29 into the Poisson equation 2.26 yields the PB equation [210, 211]:

$$\nabla^2 \Phi = - \sum_k \frac{\rho_k^0 z_k e}{\varepsilon_0 \varepsilon_r} \exp\left(-\frac{z_k e (\Phi(\mathbf{r}, t) - \Phi_0)}{k_B T}\right). \quad (2.30)$$

For the most common case of a monovalent salt solution, ($\rho_+^0 = \rho_-^0 = c_0$

and $z_+ = -z_- = 1$), this simplifies to

$$\nabla^2 \Phi = \frac{2c_0 e}{\varepsilon_0 \varepsilon_r} \sinh \left(\frac{e(\Phi(\mathbf{r}, t) - \Phi_0)}{k_B T} \right). \quad (2.31)$$

Expanding equation 2.30 in terms of Φ around the reference potential Φ_0 yields the Debye-Hückel approximation [212]:

$$\nabla^2 \Phi \approx - \sum_k \frac{\rho_k^0 z_k e}{\varepsilon_0 \varepsilon_r} + \sum_k \frac{\rho_k^0 z_k^2 e^2}{\varepsilon_0 \varepsilon_r k_B T} (\Phi(\mathbf{r}, t) - \Phi_0) \quad (2.32)$$

$$= \frac{\Phi(\mathbf{r}, t) - \Phi_0}{\lambda_D^2}. \quad (2.33)$$

The first term in equation 2.32 is zero due to electroneutrality, and the second term can be simplified by introducing the Debye length

$$\lambda_D = \frac{1}{\sqrt{\sum_k \frac{\rho_k^0 z_k^2 e^2}{\varepsilon_0 \varepsilon_r k_B T}}}, \quad (2.34)$$

which is the characteristic decay length of the electrostatic potential obtained as a solution to equation 2.32. It is also the characteristic length scale on which the charge distribution decays when moving away from a charged surface, as illustrated in figure 2.1. The layer of opposite-signed solute charge surrounding a charged object is called “diffuse layer”. It partially compensates, or screens, the object’s charge, which limits its electrostatic influence to within a few Debye lengths. This effective interaction range is between $3 \cdot 10^{-10}$ m and 10^{-8} m for concentrations in the most relevant range of 1 mol L^{-1} to $10^{-3} \text{ mol L}^{-1}$. The diffuse layer is one of the two parts of the electric double layer, the other one being the Stern layer, which consists of counterions loosely associated to the surface.

2.2.3 Diffusion-reaction processes

Chemical reactions taking place in the bulk fluid modify equation 2.23 by adding a source term that couples the different ρ_k to each other. This source term is

$$R_k(\mathbf{r}, t) = \gamma(\mathbf{r}, t) s_k, \quad (2.35)$$

with the reaction rate γ and the stoichiometric coefficients $\mathbf{s} = \{-a, -b, \dots, c, d, \dots\}$, which correspond to a chemical reaction $aA + bB + \dots \rightleftharpoons cC + dD +$

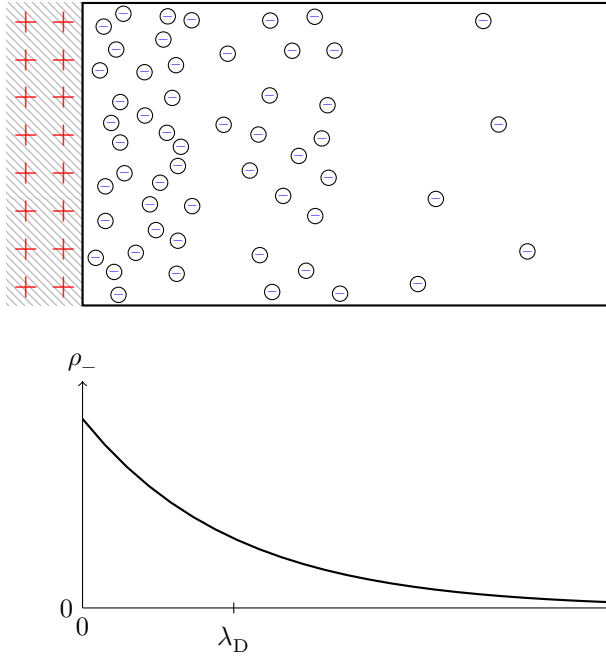


Figure 2.1: Illustration of the diffuse layer: at a charged surface (here indicated with +), the counterions (here -) assume an exponential distribution with a characteristic decay length corresponding to the Debye length λ_D .

... [213]. The reaction rate generally depends on the available concentrations of reactants via

$$\gamma(\mathbf{r}, t) = \Gamma \prod_{k \in \{a, b, \dots\}} (\rho_k(\mathbf{r}, t))^{o_k}, \quad (2.36)$$

where o_k is the reaction order and Γ the reaction rate constant. In most cases, $o_k = |s_k|$. Note that the units of Γ depend on the number of reactants involved and that the product only runs over the reactants.

2.3 Boundary conditions

To obtain unique solutions to the differential equations specified in the preceding sections, appropriate boundary conditions need to be specified.

2.3.1 Boundary conditions for fluid dynamics

For the Stokes equations 2.10 and 2.15, we will specify the flow velocity in the laboratory frame, e.g. the no-slip condition

$$\mathbf{u}(\mathbf{r}) \Big|_{\text{boundary}} \equiv \mathbf{0}, \quad (2.37)$$

on a wall or a specific surface velocity profile on a particle

$$\mathbf{u}(\mathbf{r}) \Big|_{\text{boundary}} \equiv \mathbf{u}(\mathbf{r}_b), \quad (2.38)$$

where \mathbf{r}_b lies on the boundary. The no-slip condition comes from the macroscopic observation that fluid sticks to surfaces. This is not necessarily true on the microscopic scale as the surface friction may be finite and vary, for example, with the surface's hydrophobicity [214–217]. In this case, a distance from the surface may be specified at which the flow velocity is zero, or equivalently an effective surface velocity at the surface. When no absolute but only relative velocities are given, such as when a swimmer propels itself through a fluid in the absence of walls, it is also necessary to specify that the overall fluid container is not moving, i.e.

$$\lim_{r \rightarrow \infty} \mathbf{u}(\mathbf{r}) \equiv \mathbf{0}. \quad (2.39)$$

It is not necessary to specify a separate boundary condition for the viscoelastic stress equation 2.17 as it is fully defined by the velocity boundary condition. The stress on the boundary is also generally not known a priori.

2.3.2 Boundary conditions for electrokinetics

For the Nernst-Planck equation 2.24, a flux needs to be specified at any surface. Usually this is a no-flux condition,

$$\mathbf{j}_k(\mathbf{r}) \Big|_{\text{boundary}} \equiv \mathbf{0}. \quad (2.40)$$

A reaction catalyzed by a surface may be specified as a virtual flux through the surface with normal $\hat{\mathbf{n}}$, which tends to be mathematically more convenient than expressing this reaction as a source term for equation 2.35 [213]:

$$\hat{\mathbf{n}} \cdot \mathbf{j}_k(\mathbf{r}) \Big|_{\text{boundary}} \equiv \rho_{\text{cat}}(\mathbf{r}_b, t) R_k(\mathbf{r}, t), \quad (2.41)$$

with ρ_{cat} the catalyst concentration on the boundary and R_k given by equation 2.35. Sometimes it is convenient to ignore these details of the reaction and instead model the reaction using an effective flux through the surface [35, 101, 213]:

$$\hat{\mathbf{n}} \cdot \mathbf{j}_k(\mathbf{r}) \Big|_{\text{boundary}} \equiv j_{k,b}(\hat{\mathbf{n}}). \quad (2.42)$$

The Poisson equation 2.26 does need a boundary condition in our case as we do not prescribe the potential on walls or swimmers, but instead explicitly consider them as part of the charge distribution equation 2.25. Uniqueness of the solution is guaranteed by the assumption that the system is charge-neutral,

$$\int_V \rho_{\text{total}}(\mathbf{r}, t) d^3r = 0, \quad (2.43)$$

where the integral goes over the entire simulation domain. In periodic boundary conditions, this condition is necessary as otherwise the electrostatic potential will become infinite [218].

2.4 Squirmers

Theoretical descriptions often use simple swimmer models that describe only the resulting hydrodynamic flow in a far-field approximation, which eliminates the complex details of a microswimmer's propulsion method. As self-propulsion is force-free [47, 219], the lowest nonzero term of its hydrodynamic multipole expansion is the dipole. It arises from the propulsion

force of the swimmer and the drag force exerted on it by the fluid, which are equal in magnitude but opposite in direction [220]. Only external fields like gravity would have a monopolar effect on the swimmer, so in experiments care must be taken to eliminate their influence. The force dipole decays with distance as r^{-2} , which justifies the often-applied truncation beyond this order. Point dipoles are, however, difficult to handle numerically, due to their inherent divergences [170, 221], while extended dipoles are inconvenient to analytic theory. The divergences can be mitigated by regularization [170, 222], but this is only possible for simple cases like Stokes flow (equations 2.10 and 2.15) and not for arbitrary fluids such as those that will be used in chapter 7.

A widely used model that can account for finite sizes of the swimmer is the squirmer model. Lighthill [20] originally introduced it to explain swimming by an oscillatory shape change. Blake [21] later used it to describe the microorganism *Paramecium*, which propels via a specific beat pattern of the cilia on its surface. Both authors expanded the flow at the swimmer's surface into spherical harmonics and discovered that the first two modes are sufficient to characterize the resulting flow. If the squirmer is rigid and impermeable, radial flow through the surface can further be ignored [148], so that the motion of cilia on the surface of a sphere of radius R_S can be described by the envelope [21]

$$\mathbf{u}(\mathbf{r}) \Big|_{|\mathbf{r}-\mathbf{r}_S|=R_S} = \left(B_1 + B_2 \frac{\hat{\mathbf{e}} \cdot (\mathbf{r} - \mathbf{r}_S)}{|\mathbf{r} - \mathbf{r}_S|} \right) \left(\frac{\hat{\mathbf{e}} \cdot (\mathbf{r} - \mathbf{r}_S)}{|\mathbf{r} - \mathbf{r}_S|} \frac{\mathbf{r} - \mathbf{r}_S}{|\mathbf{r} - \mathbf{r}_S|} - \hat{\mathbf{e}} \right), \quad (2.44)$$

which is used as the boundary condition equation 2.38. Here, the squirmer's center is at \mathbf{r}_S , B_1 and B_2 are constants, and $\hat{\mathbf{e}}$ is the unit orientation vector of the sphere.

The flow resulting from this boundary condition is governed by the Stokes equations 2.10 and 2.15. Under the condition of equation 2.44, these are solved by the flow field [21, 148]

$$\begin{aligned} \mathbf{u}_S(\mathbf{r}) = & B_1 \frac{R_S^3}{|\mathbf{r} - \mathbf{r}_S|^3} \left(\frac{\hat{\mathbf{e}} \cdot (\mathbf{r} - \mathbf{r}_S)}{|\mathbf{r} - \mathbf{r}_S|} \frac{\mathbf{r} - \mathbf{r}_S}{|\mathbf{r} - \mathbf{r}_S|} - \frac{1}{3} \hat{\mathbf{e}} \right) \\ & + B_2 \left(\frac{R_S^4}{|\mathbf{r} - \mathbf{r}_S|^4} - \frac{R_S^2}{|\mathbf{r} - \mathbf{r}_S|^2} \right) \left(\frac{3}{2} \left(\frac{\hat{\mathbf{e}} \cdot (\mathbf{r} - \mathbf{r}_S)}{|\mathbf{r} - \mathbf{r}_S|} \right)^2 - \frac{1}{2} \right) \frac{\mathbf{r} - \mathbf{r}_S}{|\mathbf{r} - \mathbf{r}_S|} \\ & + B_2 \frac{R_S^4}{|\mathbf{r} - \mathbf{r}_S|^4} \frac{\hat{\mathbf{e}} \cdot (\mathbf{r} - \mathbf{r}_S)}{|\mathbf{r} - \mathbf{r}_S|} \left(\frac{\hat{\mathbf{e}} \cdot (\mathbf{r} - \mathbf{r}_S)}{|\mathbf{r} - \mathbf{r}_S|} \frac{\mathbf{r} - \mathbf{r}_S}{|\mathbf{r} - \mathbf{r}_S|} - \hat{\mathbf{e}} \right) \end{aligned} \quad (2.45)$$

in the laboratory frame. This corresponds to the squirmer moving with a

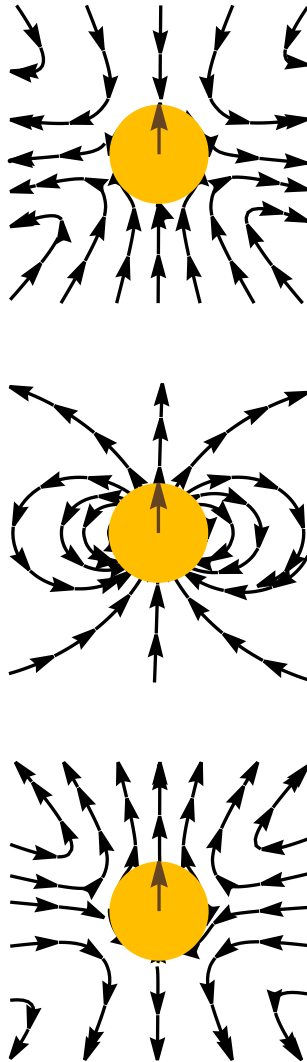


Figure 2.2: The three types of squirmers: pusher (top, $\beta < 0$), neutral (middle, $\beta = 0$), and puller (bottom, $\beta > 0$).

velocity [21, 148] of

$$\mathbf{v}_0 = \frac{2}{3}B_1\hat{\mathbf{e}}, \quad (2.46)$$

i.e., a velocity that depends only on the first mode and points in the direction of the squirmer's orientation vector $\hat{\mathbf{e}}$. Micrometer-sized swimmers in water exist in the low-Re limit according to equation 2.49, thus v_0 only sets the time scale without changing the physical behavior. This makes it convenient to scale out v_0 and introduce the dipolarity

$$\beta = \frac{B_2}{B_1} \quad (2.47)$$

as the ratio of the magnitudes of the second and first moment.

β classifies the shape of the flow field, with the sign distinguishing three different kinds of swimmers. A pusher with $\beta < 0$ pushes fluid away from its front and back (with $\hat{\mathbf{e}}$ pointing forward) and draws fluid in from its sides. A puller with $\beta > 0$ pulls fluid toward itself at front and back, pushing it away from its sides. At the transition point $\beta = 0$ lies the neutral squirmer, which moves fluid from front to back. Figure 2.2 illustrates these three types of squirmer. Biological examples of these three classes include *Escherichia coli* [49], *Chlamydomonas reinhardtii* [223], and *Paramecium* [224], respectively. The propulsion details of a chemical microswimmer can sometimes be mapped onto effective values of v_0 and β [154, 156].

2.5 Dimensionless numbers

It is common practice in fluid mechanics to introduce certain dimensionless numbers. Many phenomena do not depend on precise parameter values, but rather on the relative significance of individual physical effects. The purpose of the present section is to summarize those that are most relevant to this thesis.

Several of these numbers have already been given in section 2.1 and are reproduced here for convenience. The **Mach** number,

$$\text{Ma} = \frac{U}{c_s}, \quad (2.48)$$

gives the ratio between the maximal velocity U and the speed of sound c_s . When $\text{Ma} \ll 1$, incompressibility may be assumed as we have done in sections 2.1.2 and 2.1.3. This requirement is always fulfilled in soft matter physics. Certain simulation methods, like lattice Boltzmann (LB)

(section 4.1) or multi-particle collision dynamics (MPCD) [225, 226], introduce their own speed of sound, which is generally much lower than the physical one, so care must be taken to ensure that $\text{Ma} \ll 1$ is fulfilled even in simulation. The **Reynolds** number gives the ratio of inertial forces to viscous forces:

$$\text{Re} = \frac{\rho UL}{\eta}, \quad (2.49)$$

where L is a characteristic length scale of the flow and U a characteristic velocity. Re represents the relative importance of inertia. The Stokes equations of section 2.1.3 are only valid in the limit of $\text{Re} \ll 1$. For microscale flow, this is generally fulfilled as L is in the range of 10^{-9} m to 10^{-3} m, U is on the order of Ls^{-1} , ρ has a similar order of magnitude as that of water, and η is similar as or higher than for water. The **Strouhal** number,

$$\text{St} = \frac{L}{UT} = \frac{L\dot{\gamma}}{U}, \quad (2.50)$$

gives the ratio of the convective time scale to the characteristic time scale T of the flow. The product ReSt is also called **unsteady Reynolds** number [227], **oscillatory Reynolds** number [79, 228], or **Roshko** number [229] and describes the relative significance of transient effects. Typically, $\text{St} \ll \text{Re}^{-1}$, which permits the use of the time-independent Stokes equation 2.15. For flows periodically driven at a sufficiently high frequency $\dot{\gamma}$, it is possible to violate this requirement, in which case the unsteady Stokes equation 2.14 would need to be used [191]. This is not the case for the purposes of this thesis, but becomes relevant, for example, in the context of cilia and flagella [227] or flapping [79, 228].

Turning to viscoelastic fluids, the **Deborah** number is determined by the ratio of the elastic relaxation time to the characteristic time scale of the flow [230]:

$$\text{De} = \frac{\lambda_p U}{L}, \quad (2.51)$$

thus representing the degree of elasticity in response to a deformation. The **Weissenberg** number relates the elastic relaxation time to the characteristic rate at which the deformation is driven [230]:

$$\text{Wi} = \lambda_p \dot{\gamma}. \quad (2.52)$$

For an illustration of the difference between these two numbers in a simple cross-slot geometry, see figure 2.3. In many geometries, De and Wi are connected, sometimes even equal, and as a result they are commonly confused

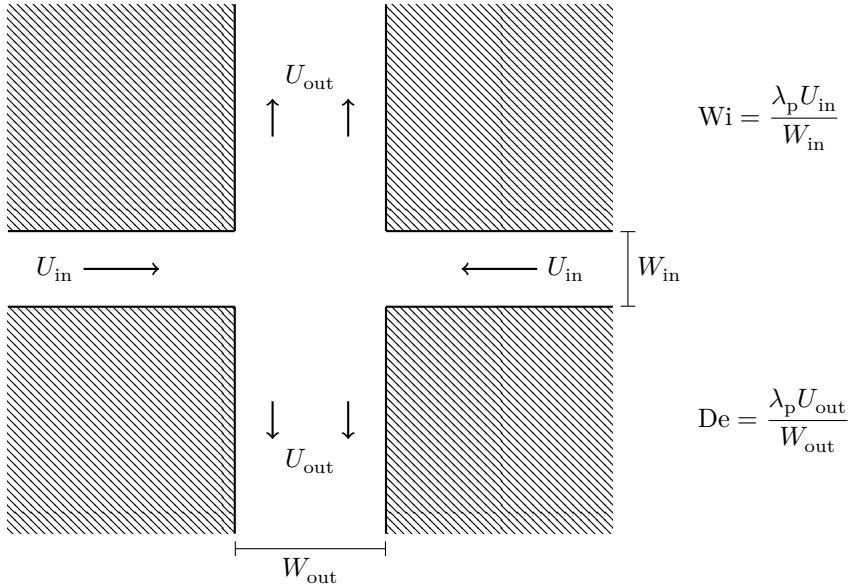


Figure 2.3: Schematic of the cross-slot geometry to illustrate Weissenberg and Deborah numbers. Wi is calculated based on the flow driven with velocity U_{in} into the inlet channel of width W_{in} . De is calculated based on the resulting flow with velocity U_{out} out of the outlet channel of width W_{out} . In this geometry, the two velocities are proportional due to mass conservation, $U_{out} = U_{in} W_{in} / W_{out}$, yielding a simple proportionality between De and Wi , but such a connection between the two dimensionless numbers does not exist in general.

2 Theoretical background

in literature [230]. It is convenient to introduce the polymer viscosity fraction

$$\xi = \frac{\eta_p}{\eta}, \quad (2.53)$$

which can easily be varied while keeping the total viscosity

$$\eta = \eta_n + \eta_p \quad (2.54)$$

constant.

Turning to electrokinetic phenomena, the **Péclet** number gives the ratio of advective to diffusive transport:

$$\text{Pe} = \frac{LU}{D} \quad (2.55)$$

with the diffusion coefficient D .

3 Semi-analytic methods

There are many different ways to solve the equations from chapter 2. Before moving on to a full numerical treatment in chapter 4, where generic and powerful computational methods will be introduced, let us discuss a simplified, semi-analytic approach. Here, it is necessary to identify only the most relevant physical aspects of a problem and absorb all the details into effective interactions.

This chapter introduces the Green's function for the Stokes equations 2.10 and 2.15 in section 3.1, which is the solution for a point-force applied to bulk fluid. The squirmer of section 2.4 is then decomposed into its hydrodynamic modes in section 3.2, which can be expressed as derivatives of the Green's function. The influence of a flat wall, spherical obstacle, or spherical cavity can be determined by the method of reflections as introduced in section 3.3. Faxén's laws in section 3.4 then gives us the effect that the resulting flow has on the squirmer, which can be used to construct its trajectory in section 3.5. Section 3.6 will conclude by drawing a comparison between the hydrodynamic modes and the more familiar electrostatic multipoles.

3.1 Oseen tensor

We first consider a Stokeslet [231, 232], the solution to equations 2.10 and 2.15 for a flow due to a force monopole \mathbf{F} applied at \mathbf{r}_S :

$$\mathbf{u}_{\text{FM}}(\mathbf{r}, \mathbf{r}_S, \mathbf{F}) = \frac{1}{8\pi\eta_h} \mathbf{M}(\mathbf{r}, \mathbf{r}_S) \mathbf{F} \quad (3.1)$$

with the Oseen tensor [233]

$$\mathbf{M}(\mathbf{r}, \mathbf{r}_S) = \frac{1}{|\mathbf{r} - \mathbf{r}_S|} \left(\mathbb{1} + \frac{(\mathbf{r} - \mathbf{r}_S) \otimes (\mathbf{r} - \mathbf{r}_S)}{|\mathbf{r} - \mathbf{r}_S|^2} \right). \quad (3.2)$$

As before, \otimes is the dyadic product. The Stokeslet is the Green's function to the Stokes equations. For different ways of deriving it, see reference 234; the most elegant one is based on fundamental properties of the Laplace and biharmonic functions [235].

3.2 Hydrodynamic mode decomposition

The flows of the higher hydrodynamic moments can be obtained from the Stokeslet equation 3.1 by differentiation [235–237]. For the force dipole, source dipole, and source quadrupole, this yields

$$\mathbf{u}_{\text{FD}}(\mathbf{r}, \mathbf{r}_S, \mathbf{F}, \mathbf{F}_{\text{FD}}) = -(\nabla_S \otimes \mathbf{u}_{\text{FM}}(\mathbf{r}, \mathbf{r}_S, \mathbf{F}))^\top \mathbf{F}_{\text{FD}}, \quad (3.3)$$

$$\mathbf{u}_{\text{SD}}(\mathbf{r}, \mathbf{r}_S, \mathbf{F}_{\text{SD}}) = -\frac{1}{2} \nabla_S^2 \mathbf{u}_{\text{FM}}(\mathbf{r}, \mathbf{r}_S, \mathbf{F}_{\text{SD}}), \quad (3.4)$$

$$\mathbf{u}_{\text{SQ}}(\mathbf{r}, \mathbf{r}_S, \mathbf{F}_{\text{SD}}, \mathbf{F}_{\text{SQ}}) = \frac{1}{3} (\nabla_S \otimes \mathbf{u}_{\text{SD}}(\mathbf{r}, \mathbf{r}_S, \mathbf{F}_{\text{SD}}))^\top \mathbf{F}_{\text{SQ}}, \quad (3.5)$$

respectively. Here, the subscript S on the differential operators refers to differentiation with respect to \mathbf{r}_S . \mathbf{F}_{FD} , \mathbf{F}_{SD} , and \mathbf{F}_{SQ} give the direction of infinitesimal displacement between two point forces, point sources, or source dipoles, respectively. For purposes of this thesis, these vectors will usually coincide, so we define

$$\mathbf{u}_{\text{FM}}(\mathbf{r}, \mathbf{r}_S) = \mathbf{u}_{\text{FM}}(\mathbf{r}, \mathbf{r}_S, \mathbf{F}), \quad (3.6)$$

$$\mathbf{u}_{\text{FD}}(\mathbf{r}, \mathbf{r}_S) = \mathbf{u}_{\text{FD}}(\mathbf{r}, \mathbf{r}_S, \mathbf{F}, \mathbf{F}), \quad (3.7)$$

$$\mathbf{u}_{\text{SD}}(\mathbf{r}, \mathbf{r}_S) = \mathbf{u}_{\text{SD}}(\mathbf{r}, \mathbf{r}_S, \mathbf{F}), \quad (3.8)$$

$$\mathbf{u}_{\text{SQ}}(\mathbf{r}, \mathbf{r}_S) = \mathbf{u}_{\text{SQ}}(\mathbf{r}, \mathbf{r}_S, \mathbf{F}, \mathbf{F}). \quad (3.9)$$

We can write the squirmer flow in terms of the multipole moments by identifying them in equation 2.45:

$$\begin{aligned} \mathbf{u}_S(\mathbf{r}) &= \frac{8\pi\eta_n}{3} B_1 R_S^3 \mathbf{u}_{\text{SD}}(\mathbf{r}, \mathbf{r}_S) + \frac{8\pi\eta_n}{2} B_2 R_S^2 \mathbf{u}_{\text{FD}}(\mathbf{r}, \mathbf{r}_S) \\ &\quad + \frac{8\pi\eta_n}{2} B_2 R_S^4 \mathbf{u}_{\text{SQ}}(\mathbf{r}, \mathbf{r}_S) \end{aligned} \quad (3.10)$$

with $\mathbf{F} = \hat{\mathbf{e}}$. This decomposition is illustrated by figure 3.1: a squirmer’s flow field is composed of a source dipole with r^{-3} decay and the prefactor B_1 , a force dipole with r^{-2} decay and a prefactor of B_2 , and a source quadrupole with r^{-4} decay and the same B_2 prefactor.

3.3 Method of reflections

The expressions of section 2.4 are valid in bulk only. The presence of a solid boundary can be incorporated via the method of reflections [238]. Here, a virtual flow originating from inside the obstacle is introduced. Its purpose

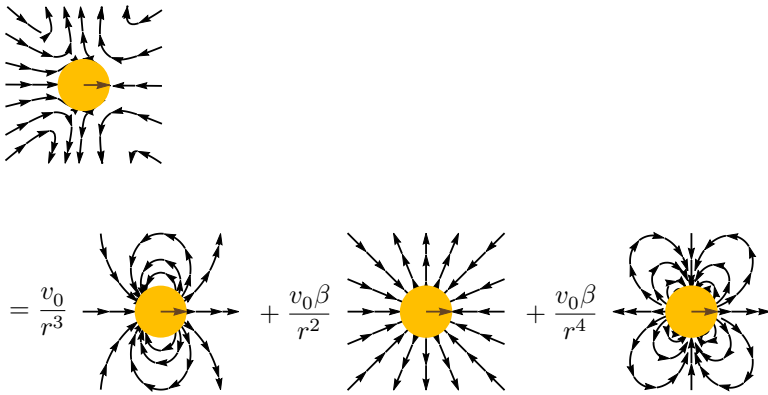


Figure 3.1: The squirmer's flow field is comprised of a source dipole, a force dipole, and a source quadrupole as per equation 3.10.

is to ensure fulfillment of the no-slip boundary condition equation 2.37 on the obstacle's surface. We can limit ourselves to obtaining the image of the Stokeslet $\mathbf{u}_{\text{FM}}(\mathbf{r}, \mathbf{r}_S)$ as section 3.2 permits to express any higher hydrodynamic modes in terms of a Stokeslet.

3.3.1 Reflection at a flat wall

For a flat wall, which without loss of generality we assume to be located at $z = 0$, this leads to the Blake tensor $\mathbf{B}(\mathbf{r}, \mathbf{r}_S)$. It is added to the Oseen tensor of equation 3.2 by the presence of a wall. It is a superposition of a force monopole, a source dipole, and two force dipoles [221, 239, 240],

$$\mathcal{R}_{\text{wall}}\mathbf{u}_{\text{FM}}(\mathbf{r}, \mathbf{r}_S) = \mathbf{B}(\mathbf{r}, \mathbf{r}_S)\mathbf{F} \quad (3.11)$$

$$\begin{aligned} &= -\mathbf{u}_{\text{FM}}(\mathbf{r}, \mathbf{r}_*, \mathbf{F}) + 2h^2\mathbf{u}_{\text{SD}}(\mathbf{r}, \mathbf{r}_*, 2F_z\hat{\mathbf{e}}_z - \mathbf{F}) \quad (3.12) \\ &\quad - 2h\mathbf{u}_{\text{FD}}(\mathbf{r}, \mathbf{r}_*, \hat{\mathbf{e}}_z, \mathbf{F} - F_z\hat{\mathbf{e}}_z) + 2h\mathbf{u}_{\text{FD}}(\mathbf{r}, \mathbf{r}_*, F_z\hat{\mathbf{e}}_z, \hat{\mathbf{e}}_z). \end{aligned}$$

These seemingly originate from a point \mathbf{r}_* on the other side of the wall and at the same distance $h = \frac{1}{2}|\mathbf{r}_* - \mathbf{r}|$ from the wall as the Stokeslet. This decomposition is illustrated in figure 3.2.

When \mathbf{F} is either parallel or perpendicular to the wall, one of the two force dipoles becomes zero, so it is often claimed [240–243] that the Blake tensor consists of a force monopole, only one force dipole, and a source dipole. A similar claim [244, 245] is sometimes made that the Blake tensor consists of a force monopole, a stresslet, and a source dipole, which is true when \mathbf{F} is parallel to the wall. The stresslet is a combination of a source monopole and two force dipoles [237, 246].

3.3.2 Reflection at a sphere

The image Stokeslet for a no-slip sphere is [163, 233, 247]

$$\mathcal{R}\mathbf{u}_{\text{FM}}(\mathbf{r}, \mathbf{r}_S) = \frac{1}{8\pi\eta_{\text{n}}}\mathcal{R}\mathbf{M}(\mathbf{r}, \mathbf{r}_S)\mathbf{F} \quad (3.13)$$

with the reflection operator \mathcal{R} given as

$$\begin{aligned} \mathcal{R}\mathbf{M}(\mathbf{r}, \mathbf{r}_S) &= -\frac{R}{r_S s_*} \mathbb{1} - \frac{R^3}{r_S^3 s_*^3} \mathbf{s}_* \otimes \mathbf{s}_* - \frac{(r^2 - R^2)(r_S^2 - R^2)}{2r_S^3} \Phi - \frac{r_S^2 - R^2}{r_S} \times \\ &\quad \left(\frac{1}{R^3 s_*} \mathbf{r}_* \otimes \mathbf{r}_* - \frac{R}{r_S^2 s_*^3} (\mathbf{r}_* \otimes \mathbf{s}_* + \mathbf{s}_* \otimes \mathbf{r}_*) + \frac{2\mathbf{r}_* \cdot \mathbf{s}_*}{R^3 s_*^3} \mathbf{r}_* \otimes \mathbf{r}_* \right). \end{aligned} \quad (3.14)$$

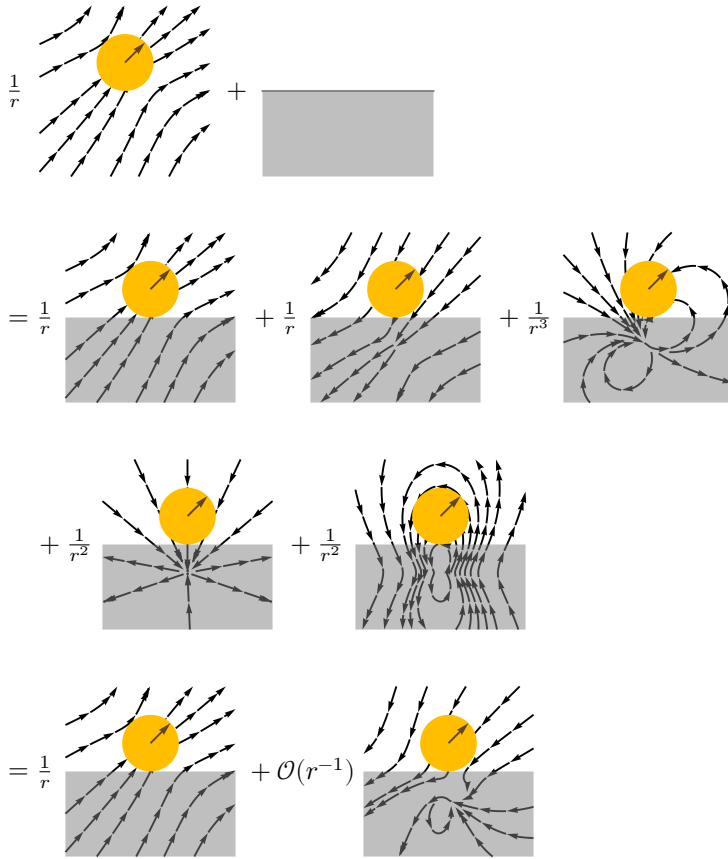


Figure 3.2: The Blake tensor, the image of the force monopole that obeys a no-slip condition on a wall, is comprised of a force monopole, a source dipole, and two force dipoles as per equation 3.12. The flow inside the shaded area, i.e. on the other side of the wall, has no physical reality, but is a mathematical tool to fulfill the boundary condition on the wall.

Here, for $r_S > R$:

$$\begin{aligned}
 \Phi = & -\frac{3}{Rs_*^3} \mathbf{s}_* \otimes \mathbf{r}_S + \frac{R}{s_*^3} \mathbb{1} - \frac{3R}{s_*^5} \mathbf{s}_* \otimes \mathbf{s}_* - \frac{2}{Rs_*^3} \mathbf{r}_* \otimes \mathbf{r}_S + \frac{6\mathbf{r}_* \cdot \mathbf{s}_*}{Rs_*^5} \mathbf{s}_* \otimes \mathbf{r}_S \\
 & + \frac{3R}{s_* r_* + \mathbf{r} \cdot \mathbf{r}_* - r_*^2} \left(\frac{1}{r_*^2 s_*} \mathbf{s}_* \otimes \mathbf{r}_* + \frac{1}{s_*^3} \mathbf{s}_* \otimes \mathbf{s}_* + \frac{s_* - r_*}{r_* s_*} \mathbb{1} \right) \\
 & - \frac{3R(r_* \mathbf{s}_* + s_* \mathbf{r}_*) \otimes (s_* \mathbf{r}_S - r_*^2 \mathbf{s}_* + s_* \mathbf{r}_* (\mathbf{r} - 2\mathbf{r}_*))}{r_*^2 s_*^2 (s_* r_* + \mathbf{r} \cdot \mathbf{r}_* - r_*^2)^2} \\
 & - \frac{3R(\mathbf{r} \otimes \mathbf{r}_* + r r_* \mathbb{1})}{r_*^2 r (r r_* + \mathbf{r} \cdot \mathbf{r}_*)} + \frac{3R(r_* \mathbf{r} + r r_*) \otimes (r_* \mathbf{r} + r r_*)}{r_*^2 r (r r_* + \mathbf{r} \cdot \mathbf{r}_*)^2}, \tag{3.15}
 \end{aligned}$$

and for $r_S < R$:

$$\begin{aligned}
 \Phi = & -\frac{6r_*^2}{Rs_*^5} \mathbf{s}_* \otimes \mathbf{r}_S + \frac{R}{s_*^3} \mathbb{1} + \frac{3R}{s_*^5} \mathbf{s}_* \otimes \mathbf{s}_* - \frac{2}{Rs_*^3} \mathbf{r}_* \otimes \mathbf{r}_S + \frac{6\mathbf{r} \cdot \mathbf{r}_*}{Rs_*^5} \mathbf{s}_* \otimes \mathbf{r}_S \\
 & - \frac{3((s_* r_S - R^2) \mathbf{r} \cdot \mathbf{r}_S + r^2 r_S^2)}{r_S^2 s_*^3 (r^2 r_*^2 - (\mathbf{r} \cdot \mathbf{r}_*)^2)} \mathbf{s}_* \otimes (R^2 \mathbf{r} - r_S \mathbf{r} \cdot \mathbf{r}_*) \\
 & + \left(\frac{\mathbf{s}_* \mathbf{r} \cdot \mathbf{r}_S}{s_* r_S} + \frac{(s_* r_S - R^2) \mathbf{r}_S}{r_S^2} + 2\mathbf{r} \right) \otimes \frac{3(R^2 \mathbf{r} - r_S \mathbf{r} \cdot \mathbf{r}_*)}{Rs_* (r^2 r_*^2 - (\mathbf{r} \cdot \mathbf{r}_*)^2)} \\
 & - \frac{3((s_* r_S - R^2) \mathbf{r} \cdot \mathbf{r}_S + r^2 r_S^2)}{R r_S^2 s_* (r^2 r_*^2 - (\mathbf{r} \cdot \mathbf{r}_*)^2)} (\mathbf{r}_* \otimes \mathbf{r}_S - R^2 \mathbb{1}) \\
 & - \frac{3((s_* r_S - R^2) \mathbf{r} \cdot \mathbf{r}_S + r^2 r_S^2)}{R r_S^2 s_* (r^2 r_*^2 - (\mathbf{r} \cdot \mathbf{r}_*)^2)^2} (2r_*^2 \mathbf{r} - 2\mathbf{r} \cdot \mathbf{r}_* \mathbf{r}_*) \otimes (R^2 \mathbf{r} - r_S \mathbf{r} \cdot \mathbf{r}_*), \tag{3.16}
 \end{aligned}$$

where the variables $\mathbf{r}_* = (R^2/r_S^2)\mathbf{r}_S$ and $\mathbf{s}_* = \mathbf{r} - \mathbf{r}_*$ have been introduced. For the limiting case of a flat wall ($R \rightarrow \infty$), the former has the geometric interpretation of the location of the image Stokeslet as in equation 3.12.

Similar expressions are also available for a source monopole near a flat wall [248] and near a sphere [249]. Equation 3.12 for the reflection by a flat wall is recovered from equation 3.13 by expanding around $R^{-1} = 0$. The expansion reveals that corrections are to leading order linear in the inverse radius.

We finally obtain the image squirmer,

$$\begin{aligned} \mathcal{R}\mathbf{u}_S(\mathbf{r}) &= \frac{8\pi\eta_n}{3}B_1R_S^3\mathcal{R}\mathbf{u}_{SD}(\mathbf{r},\mathbf{r}_S) + \frac{8\pi\eta_n}{2}B_2R_S^2\mathcal{R}\mathbf{u}_{FD}(\mathbf{r},\mathbf{r}_S) \\ &\quad + \frac{8\pi\eta_n}{2}B_2R_S^4\mathcal{R}\mathbf{u}_{SQ}(\mathbf{r},\mathbf{r}_S). \end{aligned} \quad (3.17)$$

One can exploit the linearity of the Stokes equation to change the order of operations. That is, we first apply the known reflection of equation 3.13 and then perform the differentiation of equations 3.3 to 3.5 [250]:

$$\begin{aligned} &= -\frac{8\pi\eta_n}{6}B_1R_S^3\nabla_S^2(\mathcal{R}\mathbf{u}_{FM}(\mathbf{r},\mathbf{r}_S)) \\ &\quad - \frac{8\pi\eta_n}{2}B_2R_S^2(\nabla_S \otimes (\mathcal{R}\mathbf{u}_{FM}(\mathbf{r},\mathbf{r}_S)))\mathbf{F} \\ &\quad - \pi\eta_n B_2R_S^4(\nabla_S \otimes \nabla_S^2(\mathcal{R}\mathbf{u}_{FM}(\mathbf{r},\mathbf{r}_S)))\mathbf{F}. \end{aligned} \quad (3.18)$$

The flow field

$$\mathbf{u}(\mathbf{r}) = \mathbf{u}_S(\mathbf{r}) + \mathcal{R}\mathbf{u}_S(\mathbf{r}) \quad (3.19)$$

fulfills the Stokes equations 2.10 and 2.15 and the no-slip boundary condition equation 2.37 on the obstacle. It does not, however, exactly fulfill the slip boundary condition equation 2.44 on the squirmer as this is not possible with a single reflection. An infinite series of reflections at the obstacle's and squirmer's surfaces would be required to respect both boundary conditions simultaneously, so the presented approach only provides a far-field approximation. It is also common practice to truncate equation 3.13 after $\mathcal{O}(r^4)$ to match the maximum order found in equation 2.45. In this case the slip boundary condition equation 2.44 is not exactly fulfilled, but the equations simplify considerably. For systems where equation 2.44 is only considered a leading-order approximation to the true nature of the swimmer, the truncation also serves to get a uniform error order.

3.4 Faxén's laws

Now that we have the flow field, we can calculate the squirmer's response to it via Faxén's laws [148, 251–254]. The first law states that a force-free sphere at position \mathbf{r} moves with velocity

$$\mathbf{v} = \left(1 + \frac{R_S^2}{6}\nabla^2\right)\mathbf{u}(\mathbf{r}). \quad (3.20)$$

The second law gives the angular velocity of the sphere as

$$\boldsymbol{\omega} = \frac{1}{2} \nabla \times \mathbf{u}(\mathbf{r}). \quad (3.21)$$

These laws are obtained from integrals over the surface of the sphere [255]. Conveniently, they give the full hydrodynamic effect on the sphere as a simple center-of-mass linear and angular velocity. Equations 3.20 and 3.21 can be used to calculate the response of the squirmer to the reflected flow $\mathcal{R}\mathbf{u}_S$. Its response to \mathbf{u}_S cannot be calculated this way as the flow diverges at \mathbf{r}_S ; however, we already know from equation 2.46 that \mathbf{u}_S makes the squirmer move with velocity $v_0 \hat{\mathbf{e}}$. While equations 3.20 and 3.21 are series expansions, all higher orders are zero for spheres in Stokes flow [252]. Faxén's third [253] and higher [256] laws are not needed as the squirmer is assumed to be rigid. Extensions to spheroidal [257, 258] and ellipsoidal [259] bodies are also available.

3.5 Integrating the squirmer's trajectory

In sections 3.1 to 3.4, we have only given the analytic expressions for the far-field hydrodynamics of a squirmer near a flat or curved wall. We now resort to a simple numerical method to solve the associated trajectory of the squirmer, as analytic solutions are not available. This requires choosing values for the free parameters, which are the starting position and orientation of the squirmer and the squirmer radius R_S and dipolarity β . Due to the symmetry of the problem, we can restrict ourselves to the $z = 0$ plane, while still considering the full three-dimensional problem. We can furthermore set $R_S = 1$ without loss of generality as there are no externally-defined length scales.

The flow field $\mathbf{u}(\mathbf{r}, t)$ due to the squirmer can be obtained from equation 3.19. All derivatives here are carried out analytically. The linear velocity $\mathbf{v}(t)$ and angular velocity $\boldsymbol{\omega}(t)$ of the squirmer is obtained from the flow via Faxén's equations 3.20 and 3.21. The derivatives in these are carried out numerically via two-sided central finite differences to avoid further increasing the number of terms in the expression, which is already approaching the limit of what can be computed efficiently. The analytic form of these derivatives is given in the following, though they were not obtained until after the simulations for swimming near a sphere were completed. The analytic form is required for the case of the cavity because singularities foil any attempt of evaluating the finite differences directly.

For $r_S > R$:

$$8\pi\eta_n \mathcal{R}u_{\text{FM}}(\mathbf{r}_S, \mathbf{r}_S) = -\frac{3R(3r_S^2 - R^2) \mathbf{F} \cdot \mathbf{r}_S}{4r_S^4 (r_S^2 - R^2)} \mathbf{r}_S - \frac{3R(r_S^2 + R^2)}{4r_S^2 (r_S^2 - R^2)} \mathbf{F} \quad (3.22)$$

$$8\pi\eta_n \mathcal{R}u_{\text{FD}}(\mathbf{r}_S, \mathbf{r}_S) = \frac{3R(F^2 r_S^6 - (-3R^2 r_S^2 + 3r_S^4 + R^4)(\mathbf{F} \cdot \mathbf{r}_S)^2)}{2r_S^6 (r_S^2 - R^2)^2} \mathbf{r}_S + \frac{3R^3(R^2 - 3r_S^2) \mathbf{F} \cdot \mathbf{r}_S}{2r_S^4 (r_S^2 - R^2)^2} \mathbf{F} \quad (3.23)$$

$$8\pi\eta_n \mathcal{R}u_{\text{SD}}(\mathbf{r}_S, \mathbf{r}_S) = \frac{3R(-4R^2 r_S^2 - 5r_S^4 + R^4) \mathbf{F} \cdot \mathbf{r}_S}{4r_S^4 (r_S^2 - R^2)^3} \mathbf{r}_S + \frac{R(-8R^2 r_S^4 - 3R^4 r_S^2 + 3r_S^6)}{4r_S^4 (r_S^2 - R^2)^3} \mathbf{F} \quad (3.24)$$

$$8\pi\eta_n \mathcal{R}u_{\text{SQ}}(\mathbf{r}_S, \mathbf{r}_S) = \frac{R(F^2 r_S^6 (-3r_S^2 - 7R^2) + (-5R^4 r_S^2 + 10R^2 r_S^4 + 12r_S^6 + R^6)(\mathbf{F} \cdot \mathbf{r}_S)^2)}{2r_S^6 (r_S^2 - R^2)^4} \mathbf{r}_S \\ - \frac{R(-5R^4 r_S^2 - 11R^2 r_S^4 + 3r_S^6 + R^6) \mathbf{F} \cdot \mathbf{r}_S}{2r_S^4 (r_S^2 - R^2)^4} \mathbf{F} \quad (3.25)$$

$$8\pi\eta_n \nabla^2 \mathcal{R}u_{\text{FM}}(\mathbf{r}, \mathbf{r}_S) \Big|_{\mathbf{r}=\mathbf{r}_S} = -\frac{3R(-4R^2 r_S^2 - 5r_S^4 + R^4) \mathbf{F} \cdot \mathbf{r}_S}{2r_S^4 (r_S^2 - R^2)^3} \mathbf{r}_S - \frac{R(-8R^2 r_S^4 - 3R^4 r_S^2 + 3r_S^6)}{2r_S^4 (r_S^2 - R^2)^3} \mathbf{F} \quad (3.26)$$

$$8\pi\eta_n \nabla^2 \mathcal{R}u_{\text{FD}}(\mathbf{r}, \mathbf{r}_S) \Big|_{\mathbf{r}=\mathbf{r}_S} = -\frac{3(F^2 R r_S^6 (r_S^2 + 5R^2) - R(-4R^4 r_S^2 + 6R^2 r_S^4 + 3r_S^6 + R^6)(\mathbf{F} \cdot \mathbf{r}_S)^2)}{r_S^6 (r_S^2 - R^2)^4} \mathbf{r}_S \\ - \frac{3R^3(-4R^2 r_S^2 - 9r_S^4 + R^4) \mathbf{F} \cdot \mathbf{r}_S}{r_S^4 (r_S^2 - R^2)^4} \mathbf{F} \quad (3.27)$$

$$8\pi\eta_n \nabla^2 \mathcal{R}u_{\text{SD}}(\mathbf{r}, \mathbf{r}_S) \Big|_{\mathbf{r}=\mathbf{r}_S} = \frac{3R(5R^4 r_S^2 + 25R^2 r_S^4 + 3r_S^6 - R^6) \mathbf{F} \cdot \mathbf{r}_S}{2r_S^4 (r_S^2 - R^2)^5} \mathbf{r}_S + \frac{3R(15R^4 r_S^2 + 15R^2 r_S^4 + r_S^6 + R^6)}{2r_S^2 (r_S^2 - R^2)^5} \mathbf{F} \quad (3.28)$$

$$\begin{aligned}
8\pi\eta_n \nabla^2 \mathcal{R}u_{\text{SQ}}(\mathbf{r}, \mathbf{r}_S)|_{\mathbf{r}=\mathbf{r}_S} &= \frac{RF^2 r_S^6 (42R^2 r_S^2 + 3r_S^4 + 35R^4)}{(r_S^3 - R^2 r_S)^6} \mathbf{r}_S \\
&\quad - \frac{(-6R^7 r_S^2 + 15R^5 r_S^4 + 64R^3 r_S^6 + 6Rr_S^8 + R^9) (\mathbf{F} \cdot \mathbf{r}_S)^2}{(r_S^3 - R^2 r_S)^6} \mathbf{r}_S \\
&\quad + \frac{Rr_S^2 (-6R^6 r_S^2 - 90R^4 r_S^4 - 62R^2 r_S^6 - 3r_S^8 + R^8) \mathbf{F} \cdot \mathbf{r}_S \mathbf{F}}{(r_S^3 - R^2 r_S)^6}
\end{aligned} \tag{3.29}$$

$$8\pi\eta_n \nabla \times \mathcal{R}u_{\text{FM}}(\mathbf{r}, \mathbf{r}_S)|_{\mathbf{r}=\mathbf{r}_S} = -\frac{3R}{2r_S^2 (r_S^2 - R^2)} \mathbf{F} \times \mathbf{r}_S \tag{3.30}$$

$$8\pi\eta_n \nabla \times \mathcal{R}u_{\text{FD}}(\mathbf{r}, \mathbf{r}_S)|_{\mathbf{r}=\mathbf{r}_S} = -\frac{3R^3 (R^2 - 3r_S^2) \mathbf{F} \cdot \mathbf{r}_S}{r_S^4 (r_S^2 - R^2)^3} \mathbf{F} \times \mathbf{r}_S \tag{3.31}$$

$$8\pi\eta_n \nabla \times \mathcal{R}u_{\text{SD}}(\mathbf{r}, \mathbf{r}_S)|_{\mathbf{r}=\mathbf{r}_S} = \frac{3R (6R^2 r_S^2 + r_S^4 + R^4)}{2r_S^2 (r_S^2 - R^2)^4} \mathbf{F} \times \mathbf{r}_S \tag{3.32}$$

$$8\pi\eta_n \nabla \times \mathcal{R}u_{\text{SQ}}(\mathbf{r}, \mathbf{r}_S)|_{\mathbf{r}=\mathbf{r}_S} = \frac{R (-5R^4 r_S^2 - 25R^2 r_S^4 - 3r_S^6 + R^6) \mathbf{F} \cdot \mathbf{r}_S}{r_S^4 (r_S^2 - R^2)^5} \mathbf{F} \times \mathbf{r}_S. \tag{3.33}$$

For $r_S < R$:

$$8\pi\eta_n \mathcal{K}u_{\text{FM}}(\mathbf{r}_S, \mathbf{r}_S) = -\frac{3(r_S^2 - 3R^2) \mathbf{F} \cdot \mathbf{r}_S}{4R^3 (r_S^2 - R^2)} \mathbf{r}_S + \frac{3(-3R^2 r_S^2 + r_S^4 + 4R^4)}{4R^3 (r_S^2 - R^2)} \mathbf{F} \quad (3.34)$$

$$8\pi\eta_n \mathcal{K}u_{\text{FD}}(\mathbf{r}_S, \mathbf{r}_S) = -\frac{3(F^2 R^2 - (\mathbf{F} \cdot \mathbf{r}_S)^2)}{2R (r_S^2 - R^2)^2} \mathbf{r}_S - \frac{3(r_S^2 - 3R^2) \mathbf{F} \cdot \mathbf{r}_S}{2R (r_S^2 - R^2)^2} \mathbf{F} \quad (3.35)$$

$$8\pi\eta_n \mathcal{K}u_{\text{SD}}(\mathbf{r}_S, \mathbf{r}_S) = -\frac{3(-4R^2 r_S^2 + r_S^4 + 11R^4) \mathbf{F} \cdot \mathbf{r}_S}{4(R^3 - Rr_S^2)^3} \mathbf{r}_S + \frac{(21R^4 r_S^2 - 12R^2 r_S^4 + 3r_S^6 - 20R^6)}{4(R^3 - Rr_S^2)^3} \mathbf{F} \quad (3.36)$$

$$\begin{aligned} 8\pi\eta_n \mathcal{K}u_{\text{SQ}}(\mathbf{r}_S, \mathbf{r}_S) &= \frac{(F^2 R^4 (3r_S^2 + 7R^2) - (-5R^2 r_S^2 + r_S^4 + 22R^4) (\mathbf{F} \cdot \mathbf{r}_S)^2)}{2R^3 (r_S^2 - R^2)^4} \mathbf{r}_S \\ &+ \frac{(13R^4 r_S^2 - 5R^2 r_S^4 + r_S^6 - 21R^6) \mathbf{F} \cdot \mathbf{r}_S}{2R^3 (r_S^2 - R^2)^4} \mathbf{F} \end{aligned} \quad (3.37)$$

$$8\pi\eta_n \nabla^2 \mathcal{K}u_{\text{FM}}(\mathbf{r}, \mathbf{r}_S) \Big|_{\mathbf{r}=\mathbf{r}_S} = \frac{3(-4R^2 r_S^2 + r_S^4 + 11R^4) \mathbf{F} \cdot \mathbf{r}_S}{2(R^3 - Rr_S^2)^3} \mathbf{r}_S + \frac{(-21R^4 r_S^2 + 12R^2 r_S^4 - 3r_S^6 + 20R^6)}{2(R^3 - Rr_S^2)^3} \mathbf{F} \quad (3.38)$$

$$\begin{aligned} 8\pi\eta_n \nabla^2 \mathcal{K}u_{\text{FD}}(\mathbf{r}, \mathbf{r}_S) \Big|_{\mathbf{r}=\mathbf{r}_S} &= \frac{3(F^2 R^2 (r_S^2 + 5R^2) + (r_S^2 - 7R^2) (\mathbf{F} \cdot \mathbf{r}_S)^2)}{R (r_S^2 - R^2)^4} \mathbf{r}_S \\ &- \frac{3(-4R^2 r_S^2 + r_S^4 + 15R^4) \mathbf{F} \cdot \mathbf{r}_S}{R (r_S^2 - R^2)^4} \mathbf{F} \end{aligned} \quad (3.39)$$

$$\begin{aligned}
8\pi\eta_n \nabla^2 \mathcal{R}\mathbf{u}_{\text{SD}}(\mathbf{r}, \mathbf{r}_S) \Big|_{\mathbf{r}=\mathbf{r}_S} &= \frac{3(7R^4 r_S^2 - 5R^2 r_S^4 + r_S^6 - 35R^6) \mathbf{F} \cdot \mathbf{r}_S}{2R^3 (r_S^2 - R^2)^5} \mathbf{r}_S \\
&\quad - \frac{3(5R^6 r_S^2 + 11R^4 r_S^4 - 5R^2 r_S^6 + r_S^8 + 20R^8)}{2R^3 (r_S^2 - R^2)^5} \mathbf{F}
\end{aligned} \tag{3.40}$$

$$\begin{aligned}
8\pi\eta_n \nabla^2 \mathcal{R}\mathbf{u}_{\text{SQ}}(\mathbf{r}, \mathbf{r}_S) \Big|_{\mathbf{r}=\mathbf{r}_S} &= \frac{(F^2 R^4 (-42R^2 r_S^2 - 3r_S^4 - 35R^4) - (9R^4 r_S^2 - 6R^2 r_S^4 + r_S^6 - 84R^6) (\mathbf{F} \cdot \mathbf{r}_S)^2)}{R^3 (r_S^2 - R^2)^6} \mathbf{r}_S \\
&\quad + \frac{(42R^6 r_S^2 + 18R^4 r_S^4 - 6R^2 r_S^6 + r_S^8 + 105R^8) \mathbf{F} \cdot \mathbf{r}_S}{R^3 (r_S^2 - R^2)^6} \mathbf{F}
\end{aligned} \tag{3.41}$$

$$8\pi\eta_n \nabla \times \mathcal{R}\mathbf{u}_{\text{FM}}(\mathbf{r}, \mathbf{r}_S) \Big|_{\mathbf{r}=\mathbf{r}_S} = \frac{3(r_S^2 - 2R^2)}{2R^3 (R^2 - r_S^2)} \mathbf{F} \times \mathbf{r}_S \tag{3.42}$$

$$8\pi\eta_n \nabla \times \mathcal{R}\mathbf{u}_{\text{FD}}(\mathbf{r}, \mathbf{r}_S) \Big|_{\mathbf{r}=\mathbf{r}_S} = -\frac{3(r_S^2 - 3R^2) \mathbf{F} \cdot \mathbf{r}_S}{R (R^2 - r_S^2)^3} \mathbf{F} \times \mathbf{r}_S \tag{3.43}$$

$$8\pi\eta_n \nabla \times \mathcal{R}\mathbf{u}_{\text{SD}}(\mathbf{r}, \mathbf{r}_S) \Big|_{\mathbf{r}=\mathbf{r}_S} = \frac{3(5R^4 r_S^2 - 4R^2 r_S^4 + r_S^6 - 10R^6)}{2R^3 (r_S^2 - R^2)^4} \mathbf{F} \times \mathbf{r}_S \tag{3.44}$$

$$8\pi\eta_n \nabla \times \mathcal{R}\mathbf{u}_{\text{SQ}}(\mathbf{r}, \mathbf{r}_S) \Big|_{\mathbf{r}=\mathbf{r}_S} = \frac{(7R^4 r_S^2 - 5R^2 r_S^4 + r_S^6 - 35R^6) \mathbf{F} \cdot \mathbf{r}_S}{R^3 (R^2 - r_S^2)^5} \mathbf{F} \times \mathbf{r}_S. \tag{3.45}$$

For $R \rightarrow \infty$, assuming, without loss of generality, a wall at $z = 0$ with $h = \mathbf{r}_S \cdot \hat{\mathbf{e}}_z > 0$:

$$8\pi\eta_n \mathcal{R}_{\text{wall}} \mathbf{u}_{\text{FD}}(\mathbf{r}_S, \mathbf{r}_S) = \frac{F^2 - 4hF_z - 3F_z^2}{8h^3} (F_x \hat{\mathbf{e}}_x + F_y \hat{\mathbf{e}}_y) + \frac{F^2(-8hF_z - 4h^2 - 3) + (-4h^2 - 3)F_z^2}{16h^4} \hat{\mathbf{e}}_z \quad (3.46)$$

$$8\pi\eta_n \mathcal{R}_{\text{wall}} \mathbf{u}_{\text{FM}}(\mathbf{r}_S, \mathbf{r}_S) = \frac{1}{8} \left(\frac{1}{h^3} - \frac{4}{h} \right) (F_x \hat{\mathbf{e}}_x + F_y \hat{\mathbf{e}}_y) - \frac{F^2(-h) + 4h^2F_z + 3hF_z^2 + F_z}{4h^3} \hat{\mathbf{e}}_z \quad (3.47)$$

$$8\pi\eta_n \mathcal{R}_{\text{wall}} \mathbf{u}_{\text{SD}}(\mathbf{r}_S, \mathbf{r}_S) = \frac{3F_z + h}{8h^4} (F_x \hat{\mathbf{e}}_x + F_y \hat{\mathbf{e}}_y) + \frac{3F^2 - 4hF_z - 9F_z^2}{16h^4} \hat{\mathbf{e}}_z \quad (3.48)$$

$$8\pi\eta_n \mathcal{R}_{\text{wall}} \mathbf{u}_{\text{SQ}}(\mathbf{r}_S, \mathbf{r}_S) = -\frac{3F^2 + F_z^2}{32h^5} (F_x \hat{\mathbf{e}}_x + F_y \hat{\mathbf{e}}_y) + \frac{(F^2 + F_z^2)(2F_z + h)}{16h^5} \hat{\mathbf{e}}_z \quad (3.49)$$

$$8\pi\eta_n \nabla^2 \mathcal{R}_{\text{wall}} \mathbf{u}_{\text{FM}}(\mathbf{r}, \mathbf{r}_S) \Big|_{\mathbf{r}=\mathbf{r}_S} = -\frac{3F_z + h}{4h^4} (F_x \hat{\mathbf{e}}_x + F_y \hat{\mathbf{e}}_y) + \frac{-3F^2 + 4hF_z + 9F_z^2}{8h^4} \hat{\mathbf{e}}_z \quad (3.50)$$

$$8\pi\eta_n \nabla^2 \mathcal{R}_{\text{wall}} \mathbf{u}_{\text{FD}}(\mathbf{r}, \mathbf{r}_S) \Big|_{\mathbf{r}=\mathbf{r}_S} = -\frac{3(3F^2 + F_z^2)}{16h^5} (F_x \hat{\mathbf{e}}_x + F_y \hat{\mathbf{e}}_y) + \frac{3(F^2 + F_z^2)(2F_z + h)}{8h^5} \hat{\mathbf{e}}_z \quad (3.51)$$

$$8\pi\eta_n \nabla^2 \mathcal{R}_{\text{wall}} \mathbf{u}_{\text{SD}}(\mathbf{r}, \mathbf{r}_S) \Big|_{\mathbf{r}=\mathbf{r}_S} = 0 \quad (3.52)$$

$$8\pi\eta_n \nabla^2 \mathcal{R}_{\text{wall}} \mathbf{u}_{\text{SQ}}(\mathbf{r}, \mathbf{r}_S) \Big|_{\mathbf{r}=\mathbf{r}_S} = 0 \quad (3.53)$$

$$8\pi\eta_n \nabla \times \mathcal{R}_{\text{wall}} \mathbf{u}_{\text{FM}}(\mathbf{r}, \mathbf{r}_S) \Big|_{\mathbf{r}=\mathbf{r}_S} = \frac{3F_z + 2h}{4h^3} (-F_y \hat{\mathbf{e}}_x + F_x \hat{\mathbf{e}}_y) \quad (3.54)$$

$$8\pi\eta_n \nabla \times \mathcal{R}_{\text{wall}} \mathbf{u}_{\text{FD}}(\mathbf{r}, \mathbf{r}_S) \Big|_{\mathbf{r}=\mathbf{r}_S} = \frac{3F^2 + 2hF_z + 3F_z^2}{8h^4} (-F_y \hat{\mathbf{e}}_x + F_x \hat{\mathbf{e}}_y) \quad (3.55)$$

$$8\pi\eta_n \nabla \times \mathcal{R}_{\text{wall}} \mathbf{u}_{\text{SD}}(\mathbf{r}, \mathbf{r}_S) \Big|_{\mathbf{r}=\mathbf{r}_S} = 0 \quad (3.56)$$

$$8\pi\eta_n \nabla \times \mathcal{R}_{\text{wall}} \mathbf{u}_{\text{SQ}}(\mathbf{r}, \mathbf{r}_S) \Big|_{\mathbf{r}=\mathbf{r}_S} = 0. \quad (3.57)$$

Here, \hat{e}_i is the unit vector in i -direction.

An Euler integrator,

$$\mathbf{r}(t) = \mathbf{r}(t - \Delta t) + \mathbf{v}(t)\Delta t, \quad (3.58)$$

then updates the position of the squirmer and the entire process is iterated to obtain the trajectory. The integrator's time step Δt is not relevant as low-Reynolds flow is time-independent; instead, the squirmer's v_0 determines the integrator's step size. In the calculations in chapter 6, we adaptively set

$$\Delta t = 0.01 \frac{1}{v_0} \max(h, R_S). \quad (3.59)$$

This allows for fast integration of the trajectory far away from the obstacle, where the squirmer moves in a (nearly) straight line, and a high resolution when the gap between the squirmer and the obstacle is small and the hydrodynamic interactions are strong. It is conceptually similar to adaptive step size control in numerical integration, reviewed e.g. in reference 260, though we use a static step size criterion instead of determining the ideal step size from an error estimator.

We include a hard-core repulsive potential that prevents the overlap of squirmer and obstacle by ensuring that $h \geq r_{\text{cut}}$. This modifies the integrator of equation 3.58 to become

$$\mathbf{r}(t) = \max(r_{\text{cut}} + R + R_S, r'(t)) \hat{\mathbf{r}}'(t) \quad (3.60)$$

with

$$\mathbf{r}'(t) = \mathbf{r}(t - \Delta t) + \mathbf{v}(t)\Delta t. \quad (3.61)$$

3.6 Electrostatic Green's function and multipoles

The Poisson equation 2.26,

$$\nabla^2 \Phi(\mathbf{r}, t) = -\frac{1}{\varepsilon_0 \varepsilon_r} \rho_{\text{total}}(\mathbf{r}, t),$$

has the well-known potential

$$\Phi_M(\mathbf{r}, t) = \frac{1}{4\pi\varepsilon_0\varepsilon_r} \frac{q_0}{|\mathbf{r} - \mathbf{r}_0(t)|} \quad (3.62)$$

for a point charge q_0 located at \mathbf{r}_0 . This is the Green's function of electrostatics, resembling what the Oseen tensor equation 3.2 is for a point force in

hydrodynamics, but with the difference that the former is for a scalar field and the latter for a vector field. The potential due to an arbitrary charge distribution ρ_{total} is thus given by

$$\Phi(\mathbf{r}, t) = \frac{1}{4\pi\epsilon_0\epsilon_r} \int_{\mathbb{R}^d} \frac{\rho_{\text{total}}(\mathbf{r}', t)}{|\mathbf{r} - \mathbf{r}'|} d^d r'. \quad (3.63)$$

A charge dipole $\mathbf{p}_0 = q_0 \mathbf{a}$ corresponds to two point charges $\pm q_0$ located at $\mathbf{r}_0 \pm \mathbf{a}/2$ in the limit of $a \rightarrow 0$. The corresponding fundamental solution is

$$\Phi_{\text{D}}(\mathbf{r}, t) = \frac{1}{4\pi\epsilon_0\epsilon_r} \frac{\mathbf{p}_0 \cdot (\mathbf{r} - \mathbf{r}_0(t))}{|\mathbf{r} - \mathbf{r}_0(t)|^3}. \quad (3.64)$$

Just like in the hydrodynamic case of equation 3.3, this expression can be obtained by differentiation of the Green's function:

$$\Phi_{\text{D}}(\mathbf{r}) = \frac{1}{q_0} \mathbf{p}_0 \cdot \nabla_0 \Phi_{\text{M}}(\mathbf{r}, t) = -\frac{1}{q_0} \mathbf{p}_0 \cdot \nabla \Phi_{\text{M}}(\mathbf{r}, t). \quad (3.65)$$

Here, the subscript $_0$ on the differential operator refers to differentiation with respect to \mathbf{r}_0 . Thanks to the linearity of Poisson's equation, the combined potential of a charge density ρ_{total} and dipole density $\mathbf{p}_{\text{total}}$ is obtained by superposition as

$$\Phi(\mathbf{r}, t) = \frac{1}{4\pi\epsilon_0\epsilon_r} \int_{\mathbb{R}^d} (\rho_{\text{total}}(\mathbf{r}', t) - \mathbf{p}_{\text{total}}(\mathbf{r}', t) \cdot \nabla) \frac{1}{|\mathbf{r} - \mathbf{r}'|} d^d r' \quad (3.66)$$

with the dipole density

$$\mathbf{p}_{\text{total}}(\mathbf{r}, t) = \int_{\mathbb{R}^d} \mathbf{r}' \rho_{\text{total}}(\mathbf{r}', t) d^d r'. \quad (3.67)$$

The force and torque exerted on a charge monopole q and charge dipole \mathbf{p} at \mathbf{r} by a potential Φ are given by

$$\mathbf{F}_{\text{M}}(t) = -q \nabla \Phi(\mathbf{r}, t), \quad (3.68)$$

$$\mathbf{M}_{\text{M}}(t) = 0, \quad (3.69)$$

$$\mathbf{F}_{\text{D}}(t) = -\nabla (\mathbf{p}_0 \cdot \nabla \Phi(\mathbf{r}, t)), \quad (3.70)$$

$$\mathbf{M}_{\text{D}}(t) = -\mathbf{p}_0 \times \nabla \Phi(\mathbf{r}, t). \quad (3.71)$$

The trajectories of point particles with monopoles and dipoles in an electric potential can be obtained from these expressions by (numerical) integration.

4 Computational methods

The equations introduced in chapter 2, particularly their coupled occurrence, are difficult to solve analytically. We therefore resort to approximations and numerical methods to understand the dynamics of these fluids and of (self-propelled) particles immersed therein. In chapter 3, we already made an attempt at an analytic method that delivers a far-field approximation to the Stokes equations 2.10 and 2.15 for certain simple geometries. In section 4.1, we show the lattice Boltzmann (LB) method that also includes near-field and can be coupled to the Poisson-Nernst-Planck equations 2.23, 2.24 and 2.26 and Oldroyd-B equation 2.17. These equations can be solved using the finite volume (FV) method of section 4.2. Section 4.3 introduces a simple electrostatics solver. Section 4.4 explains how moving boundary conditions can be incorporated into LB and FVs. Finally, section 4.5 references the software frameworks that were used to implement these methods and run the simulations.

4.1 Lattice Boltzmann

LB was originally derived from lattice gas automata in the 1980s [261–263]. The modern derivation directly from kinetic gas theory was introduced a decade later [264]. For the full details, please refer to the textbook by Krüger et al. [265] as this section will only give the resulting algorithm. Compared to other methods, its main advantage is that is fully local and even the necessary derivatives can be calculated from the populations in a single cell. The straightforward support of complex geometries, multiphase fluids, and thermal fluctuations make LB an attractive tool for many soft matter problems [266]. The main drawback of LB is its rather large memory footprint, which is generally the bottleneck of LB simulations.

LB constructs solutions to the Stokes equations 2.10 and 2.15 from the Boltzmann transport equation (BTE), which derives from the same conservation laws. The BTE describes the time evolution of $f(\mathbf{r}, \mathbf{v}, t)$, which is the probability distribution function of finding a single fluid molecule with velocity \mathbf{v} at position \mathbf{r} and time t . LB discretizes the BTE on a lattice, typically a square/cubic lattice in two/three dimensions, with grid spacing Δx and

discrete time steps Δt . Relaxation of f toward its Maxwellian equilibrium is linearized and only a finite set of velocities \mathbf{c}_i is permitted. The latter is usually chosen commensurate with the lattice, i.e. allowing probability to be exchanged solely between neighboring cells, to eliminate any need for interpolation [267, 268]. The probability distribution is thus replaced by the populations $f_i(\mathbf{r}, t) = f(\mathbf{r}, \mathbf{c}_i, t)$, with their equilibrium values $f_i^{\text{eq}}(\mathbf{r}, t)$.

We use the D3Q19 velocity set in three dimensions and D2Q9 for two-dimensional systems. In the general DdQq notation, d refers to the dimensionality and q to the number of velocity vectors pointing to neighbor cells — here these are the six face and twelve edge neighbors (or four edge and four corner neighbors in two dimensions). The employed two relaxation time (TRT) collision operator [269] relaxes symmetric (+) and antisymmetric (−) linear combinations of f_i separately, and only the symmetric relaxation time λ_+ affects the viscosity of the fluid. λ_- can be tuned to improve the accuracy of boundary conditions [270].

The full LB method is given by

$$f_i(\mathbf{r} + \mathbf{c}_i \Delta t, t + \Delta t) = f_i(\mathbf{r}, t) - \lambda_+ (f_i^+(\mathbf{r}, t) - f_i^{\text{eq}+}(\mathbf{r}, t)) - \lambda_- (f_i^-(\mathbf{r}, t) - f_i^{\text{eq}-}(\mathbf{r}, t)) + \Delta_i(\mathbf{r}, t) \quad (4.1)$$

with

$$f_i^\pm(\mathbf{r}, t) = \frac{1}{2} (f_i(\mathbf{r}, t) \pm f_{-i}(\mathbf{r}, t)), \quad (4.2)$$

$$f_i^{\text{eq}\pm}(\mathbf{r}, t) = \frac{1}{2} (f_i^{\text{eq}}(\mathbf{r}, t) \pm f_{-i}^{\text{eq}}(\mathbf{r}, t)), \quad (4.3)$$

$$f_i^{\text{eq}}(\mathbf{r}, t) = w_i \rho(\mathbf{r}, t) \left(1 + 3\mathbf{c}_i \cdot \mathbf{u}(\mathbf{r}, t) + \frac{1}{6} (\mathbf{c}_i \cdot \mathbf{u}(\mathbf{r}, t))^2 - \frac{1}{6} u(\mathbf{r}, t)^2 \right), \quad (4.4)$$

$$\eta_{\text{n}} = \rho(\mathbf{r}, t) \left(\frac{1}{3\lambda_+} - \frac{1}{6} \right), \quad (4.5)$$

$$\lambda_- = \frac{3}{16\lambda_+}, \quad (4.6)$$

where w_i is the lattice weight factor for \mathbf{c}_i and $-i$ is defined via $\mathbf{c}_{-i} = -\mathbf{c}_i$. The w_i are all positive, obey $\sum_{i=1}^q w_i = 1$, and are determined from an isotropy condition [271]. For D2Q9 and D3Q19, this yields $w_i = \frac{1}{9d-9}$ for $c_i = 1$ and $w_i = \frac{1}{36}$ for $c_i = \sqrt{2}$ [265]. Note that, by convention, \mathbf{c}_i has units of $\Delta x / \Delta t$.

The local fluid density $\rho(\mathbf{r}, t)$ appears explicitly because LB does not simulate a perfectly incompressible fluid. For consistency, one should always

verify in simulations that the fluid does not compress appreciably. LB does not simulate a perfectly Stokesian fluid either and deals with the full Navier-Stokes equation 2.6 instead; for microswimmer purposes this is actually an advantage because the choice between the steady Stokes equation 2.15 and the unsteady Stokes equation 2.14 does not need to be made explicitly. The populations f_i of the LB equation 4.1 and the macroscopic flow fields of the Stokes equations 2.10 and 2.15 are connected via

$$\rho(\mathbf{r}, t) = \sum_{i=1}^q f_i(\mathbf{r}, t), \quad (4.7)$$

$$\mathbf{u}(\mathbf{r}, t) = \frac{1}{\rho(\mathbf{r}, t)} \sum_{i=1}^q f_i(\mathbf{r}, t) \mathbf{c}_i + \frac{1}{2} \mathbf{F}^{\text{ext}}(\mathbf{r}, t) \frac{\Delta t}{\rho(\mathbf{r}, t) \Delta x^3}, \quad (4.8)$$

$$p(\mathbf{r}, t) = \frac{\Delta x^2}{3\Delta t^2} \rho(\mathbf{r}, t) \rho(\mathbf{r}, t). \quad (4.9)$$

Equation 4.1 is typically calculated in a two-step process as illustrated in figure 4.1: first, the right-hand side, the local collision operation, is applied, and then the streaming operation moves the resulting populations to the respective neighbor cells. This splitting is only an approximation; the exact variant would require application of a half collision, a streaming, and another half collision [272, 273]. The half steps can be fused together to eliminate the approximation, but this introduces the approximate half-time-step correction in equation 4.8 and complicates the physical interpretation of the first and last time step of a simulation.

$\Delta_i(\mathbf{r}, t)$ in equation 4.1 represents the force \mathbf{F}^{ext} applied to the fluid. One possible expression for it is given by Guo et al. [273–276]:

$$\begin{aligned} \Delta_i(\mathbf{r}, t) = \frac{3w_i\Delta t^3}{\Delta x^5} & \left(\left(1 - \frac{\lambda_+}{2} \right) \left(\frac{3\Delta t^2}{\Delta x^2} (\mathbf{F} \cdot \mathbf{c}_i) (\mathbf{u} \cdot \mathbf{c}_i) - \mathbf{F} \cdot \mathbf{u} \right) \right. \\ & \left. + \left(1 - \frac{\lambda_-}{2} \right) \mathbf{F} \cdot \mathbf{c}_i \right). \end{aligned} \quad (4.10)$$

Guo et al.'s model is constructed by requiring that its contribution to both stress and momentum is physically correct [277], while simpler force models only yield correct momentum.

Velocity boundary conditions can be imposed on the fluid by using [278]

$$f_i(\mathbf{r}_b + \mathbf{c}_i \Delta t, t + \Delta t) \equiv f_{-i}(\mathbf{r}_b, t) + \frac{6\rho w_i \Delta t^2}{\Delta x^2} \mathbf{c}_i \cdot \mathbf{u}_b, \quad (4.11)$$

where \mathbf{r}_b is a boundary node with velocity \mathbf{u}_b and $\mathbf{r}_b + \mathbf{c}_i \Delta t$ is a fluid node. For no-slip conditions $\mathbf{u}_b = \mathbf{0}$, this scheme corresponds to a bounce-back of the population as illustrated in figure 4.2.

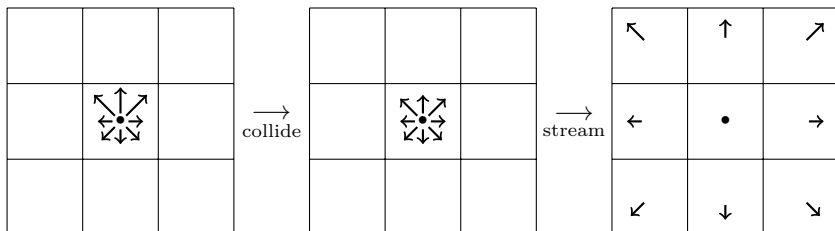


Figure 4.1: Illustration of the collision and streaming steps of LB. The former is a local operation that relaxes populations toward equilibrium, the latter moves the populations to the respective neighbor cells. Each arrow corresponds to one population belonging to its cell.

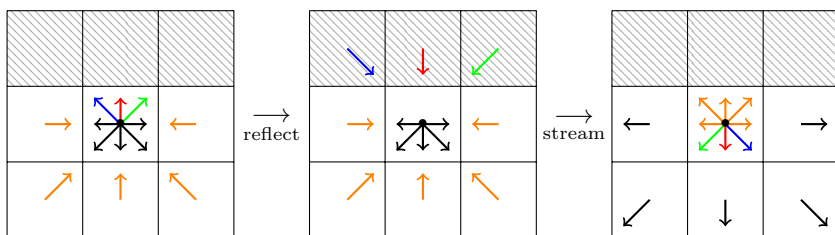


Figure 4.2: Illustration of the velocity bounce-back boundary condition for LB. To impose a no-slip boundary, populations pointing toward it are reflected before the streaming step is performed.

We do not consider thermal fluctuations of the solvent in this work. A consistent thermalization for the pure LB algorithm is available [279], and such fluctuations may be significant for nanoscale systems.

4.2 Finite volume method

The FV method [280] is generally suited for solving problems governed by conservation laws since it guarantees the conservation of, e.g., mass, momentum and energy to machine precision. This covers the Stokes equations 2.10 and 2.15, viscoelastic constitutive equations like equation 2.17, or the Nernst-Planck equations 2.23 and 2.24. For the Stokes equation, we prefer the LB method of the previous section for its more extensive particle coupling options, which will be discussed in section 4.4, but for use with the other equations, FVs are introduced in the following. We start out with

$$\frac{\partial Y_0}{\partial t}(\mathbf{r}, t) = -\nabla \cdot \mathbf{J}(\mathbf{r}, t) + S(\mathbf{r}, t) \quad (4.12)$$

as the most general continuity equation for a quantity Y_0 with an associated flux \mathbf{J} and a source term S . Both may be functions of Y_0 and other fields $\{Y_i\}_{i>0}$, as well as their spatial derivatives $\left\{ \frac{\partial^k}{\partial r_{j_1} \dots \partial r_{j_k}} Y_i \right\}_{i \geq 0, k \geq 1}$.

4.2.1 Discretization

Equation 4.12 is averaged over one cell's volume $V = \Delta x^d$ with surface unit normal $\hat{\mathbf{n}}$ to become

$$\frac{1}{V} \int_V \frac{\partial}{\partial t} Y_0(\mathbf{r}, t) = \frac{1}{V} \int_V (-\nabla \cdot \mathbf{J}(\mathbf{r}, t) + S(\mathbf{r}, t)) \quad (4.13)$$

$$\begin{aligned} &= \frac{\partial}{\partial t} \bar{Y}_0(\mathbf{r}, t) = -\frac{1}{V} \int_V \sum_{k=1}^d \frac{\partial}{\partial r_k} J_k(\mathbf{r}, t) d^d r + \bar{S}(\mathbf{r}, t) \\ &= -\frac{1}{V} \int_{\partial V} \sum_{k=1}^d J_k(\mathbf{r}, t) n_k d^{d-1} r + \bar{S}(\mathbf{r}, t), \end{aligned} \quad (4.14)$$

where Gauß's divergence theorem has been applied and the overbar indicates the volume average. By locating \bar{Y}_0 and \bar{S} at the cell center and \mathbf{J} between two cells as illustrated in figure 4.3, the discrete form of this equation is obtained as

$$\bar{Y}_0(\mathbf{r}, t + \Delta t) \approx -\frac{1}{V} \sum_{\ell=1}^q \sum_{k=1}^d J_k(\mathbf{r} + \frac{1}{2} \mathbf{c}_\ell \Delta t, t) c_{\ell k} + \bar{S}(\mathbf{r}, t) + \bar{Y}_0(\mathbf{r}, t), \quad (4.15)$$

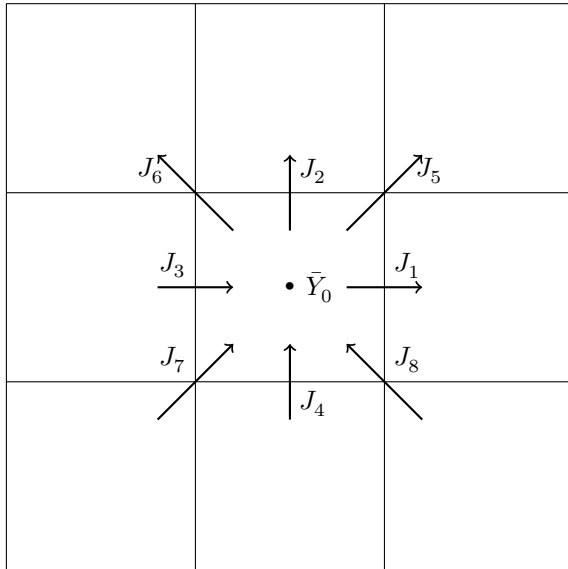


Figure 4.3: Illustration of the location of the variables in an FV scheme: a quantity \bar{Y}_0 is located at the cell centers, while its fluxes J_k exchange that quantity between neighboring cells.

where we have used the same grid spacing and time step as in section 4.1. The neighbor set $\{\mathbf{c}_i\}$ does not necessarily need to match the one used in section 4.1: for Oldroyd-B in section 4.2.3, we have found D3Q27/D2Q9 to deliver no appreciable advantage over D3Q7/D2Q5 [281] and have thus selected the latter for its lower computational cost, while for the electrokinetic equations in section 4.2.4, reference 282 recommends D3Q19.

Since \mathbf{J} , defined between cells, may depend on $\{Y_i\}$ and its derivatives, defined at cell centers, (a) numerical interpolation and (b) numerical differentiation is needed. For S , which is co-located with $\{Y_i\}$, only (c) numerical differentiation is needed. We restrict ourselves to the lowest-order variants of these numerical methods so that only quantities from immediate neighbor cells are needed. These are sufficient for most applications, but do not go beyond second derivatives. Section 4.2.2 references some higher-order versions that may provide better numerical stability or accuracy in certain situations.

For (a), we perform linear interpolation as

$$Y_i(\mathbf{r} + \frac{1}{2}\mathbf{c}_k\Delta t, t) \approx \frac{1}{2}(\bar{Y}_i(\mathbf{r}, t) + \bar{Y}_i(\mathbf{r} + \mathbf{c}_k\Delta t, t)). \quad (4.16)$$

For (b), we numerically differentiate:

$$\frac{\partial}{\partial r_k} Y_i(\mathbf{r} + \frac{1}{2}\mathbf{c}_k\Delta t, t) \approx \frac{1}{|c_k|}(\bar{Y}_i(\mathbf{r} + \mathbf{c}_k\Delta t, t) - \bar{Y}_i(\mathbf{r}, t)). \quad (4.17)$$

For (c), we numerically differentiate and average over the volume V of the cell whose midpoint is at \mathbf{r} :

$$\begin{aligned} \frac{1}{V} \int_V \frac{\partial}{\partial r'_i} Y_\ell(\mathbf{r}', t) d^d r' &= \frac{1}{V} \int_{-\Delta x/2}^{\Delta x/2} \dots \int_{-\Delta x/2}^{\Delta x/2} \left(Y_\ell(\mathbf{r} + \frac{\Delta x}{2} \hat{\mathbf{e}}_i, t) \right. \\ &\quad \left. - Y_\ell(\mathbf{r} - \frac{\Delta x}{2} \hat{\mathbf{e}}_i, t) \right) \frac{dr_1 \dots dr_d}{dr_i}, \end{aligned} \quad (4.18)$$

$$\begin{aligned} \frac{1}{V} \int_V \frac{\partial^2}{\partial r'^2_i} Y_\ell(\mathbf{r}', t) d^d r' &= \frac{1}{V} \int_{-\Delta x/2}^{\Delta x/2} \dots \int_{-\Delta x/2}^{\Delta x/2} \left(\frac{1}{4} Y_\ell(\mathbf{r} + \frac{\Delta x}{2} \hat{\mathbf{e}}_i, t) - \frac{1}{2} Y_\ell(\mathbf{r}, t) \right. \\ &\quad \left. + \frac{1}{4} Y_\ell(\mathbf{r} - \frac{\Delta x}{2} \hat{\mathbf{e}}_i, t) \right) \frac{dr_1 \dots dr_d}{dr_i}. \end{aligned} \quad (4.19)$$

Making the central-point approximation

$$\int_{-\Delta x/2}^{\Delta x/2} \cdots \int_{-\Delta x/2}^{\Delta x/2} Y_k(\mathbf{r} \pm \frac{\Delta x}{2} \hat{\mathbf{e}}_i, t) \frac{dr_1 \cdots dr_d}{dr_i} \approx \Delta x^{d-1} Y_k(\mathbf{r} \pm \frac{\Delta x}{2} \hat{\mathbf{e}}_i, t) \quad (4.20)$$

and inserting equation 4.16 yields the first-order FV discretization

$$\overline{\frac{\partial}{\partial r_i} Y_i(\mathbf{r}, t)} \approx \frac{1}{2\Delta x} (\bar{Y}_i(\mathbf{r} + \Delta x \hat{\mathbf{e}}_i, t) - \bar{Y}_i(\mathbf{r} - \Delta x \hat{\mathbf{e}}_i, t)), \quad (4.21)$$

which is identical to the corresponding finite difference (FD) scheme. Equation 4.20 may be replaced with an average over the velocity at the corners of the cell:

$$\begin{aligned} & \int_{-\Delta x/2}^{\Delta x/2} \cdots \int_{-\Delta x/2}^{\Delta x/2} Y_k(\mathbf{r} \pm \frac{\Delta x}{2} \hat{\mathbf{e}}_i, t) \frac{dr_1 \cdots dr_d}{dr_i} \\ & \approx \sum_{\ell=1}^d (1 - \delta_{i\ell}) \Delta x^{d-1} \left(Y_k(\mathbf{r} \pm \frac{\Delta x}{2} (\hat{\mathbf{e}}_i + \hat{\mathbf{e}}_\ell), t) + Y_k(\mathbf{r} \pm \frac{\Delta x}{2} (\hat{\mathbf{e}}_i - \hat{\mathbf{e}}_\ell), t) \right). \end{aligned} \quad (4.22)$$

This, however, does not produce a second-order FV scheme as the error order remains the same [283] and was thus not used.

4.2.2 Stability improvements

FV and FD schemes are known to exhibit numerical instabilities in certain situations, which result in spatial oscillations or ‘wiggles’ [281]. This is a particularly prominent problem in the context of Oldroyd-B as the model’s Péclet number [280], which relates advective transport to diffusive transport in the same way as equation 2.55 does for electrokinetic phenomena, is infinite due to the absence of a diffusive term in equation 2.17. We observed stress wiggles when performing the simulations of sections 7.2.4 and 7.2.5 with the scheme described in section 4.2.1. Another potential cause of the wiggles might be that the numerical scheme does not ensure positive semi-definiteness of $\boldsymbol{\tau}$, which is physically required but only guaranteed by some specialized numerical schemes [284].

Solutions proposed for Oldroyd-B include: using higher-order differentiation schemes [285], inserting an artificial diffusion term [286], or storing \mathbf{u} and $\boldsymbol{\tau}$ on two separate grids shifted relative to each other by half a cell

[287, 288]. These methods increase computational cost, modify the physics of the system, and make the implementation cumbersome, respectively, so we considered alternative techniques suggested in general FV literature. These include higher-order interpolation [280, 289] and differentiation [290] schemes, as well as upwind schemes [280, 282].

We resorted to the latter and chose an upwind variant called ‘‘corner-transport upwind scheme’’ suggested by references 282 and 291. Upwind schemes calculate advective fluxes like equation 4.24 or the last term of equation 4.33 not by interpolating quantities to the midpoint between two cells, but by using the quantity from either cell, depending on which way the flow points [280]. Reference 282’s method is geometrically motivated by virtually displacing the cell at \mathbf{r} in accordance with its velocity by $\mathbf{u}(\mathbf{r}, t)\Delta t$ and calculating the virtual cell’s overlap volume with all neighboring cells as illustrated in figure 4.4. This overlap corresponds to the fraction of $Y_0(\mathbf{r}, t)$ to be transferred to the respective neighboring cell:

$$J_i(\mathbf{r} + \frac{1}{2}\mathbf{c}_i\Delta t) = Y_0(\mathbf{r}, t) \frac{\Delta t}{\Delta x^{d-1}} \prod_{k=1}^d \int_{c_{ik}\Delta t}^{c_{ik}\Delta t + \Delta x} \theta(a - u_k(\mathbf{r}, t)\Delta t) \theta(u_k(\mathbf{r}, t)\Delta t + \Delta x - a) da \quad (4.23)$$

with the Heaviside step function θ . While this in principle results in fluxes in all D3Q27/D2Q9 directions, fluxes beyond the D3Q7/D2Q5 neighbor set are $\mathcal{O}(u^2)$, making them negligible here.

4.2.3 Finite volume Oldroyd-B

Our method is inspired by the LB-coupled FV solver for the electrokinetic equations discussed in section 4.2.4 [282] and has similarities to other FV Oldroyd-B solvers [287]. We found that the hybrid scheme of FDs and LB originally suggested by Su et al. [285] led to violation of energy conservation in the constitutive equation in the presence of boundaries, which translated into a violation of the conservation of momentum [292]. Moving boundary simulations as presented in section 7.2.5 were therefore impossible. This may seem surprising as FDs’ and FVs’ first-order schemes are identical, but the latter is only true in the absence of boundaries.

For equation 2.19, section 4.2.1 suggests

$$\mathbf{J}_i(\mathbf{r} + \frac{1}{2}\mathbf{c}_i\Delta t, t) = \frac{1}{|c_i|A_0} \boldsymbol{\tau}(\mathbf{r} + \frac{1}{2}\mathbf{c}_i\Delta t, t) \left(\mathbf{u}(\mathbf{r} + \frac{1}{2}\mathbf{c}_i\Delta t, t) \cdot \mathbf{c}_i \right), \quad (4.24)$$

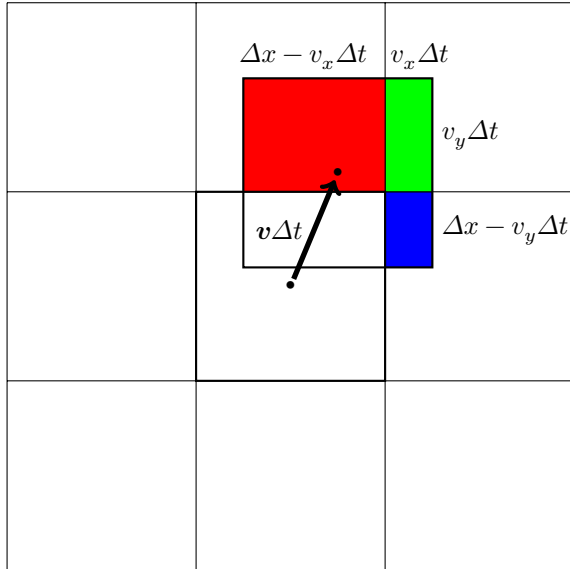


Figure 4.4: Illustration of the corner-transport upwind scheme, inspired by reference 282: a quantity \bar{Y}_0 is located in a cell and its advective fluxes J_k to the k -th neighboring cell are determined by calculating each neighbor cell's overlap with a cell virtually displaced by $\mathbf{v}\Delta t$.

where the projection onto \mathbf{c}_i and the prefactor

$$A_0 = \frac{1}{2d} \sum_{\ell=1}^q |c_\ell|. \quad (4.25)$$

account for the case of $q > 2d + 1$ [282]. However, we replace equation 4.24 with the corner-transport upwind scheme of equation 4.23 to improve numerical stability:

$$\begin{aligned} \mathbf{J}_i(\mathbf{r} + \frac{1}{2}\mathbf{c}_i\Delta t) = \\ \boldsymbol{\tau}(\mathbf{r}, t) \frac{\Delta t}{\Delta x^{d-1}} \prod_{k=1}^d \int_{c_{ik}\Delta t}^{c_{ik}\Delta t + \Delta x} \theta(a - u_k(\mathbf{r}, t)\Delta t) \theta(u_k(\mathbf{r}, t)\Delta t + \Delta x - a) da. \end{aligned} \quad (4.26)$$

For equation 2.20, section 4.2.1 yields

$$\begin{aligned} \bar{S}_{ij}(\mathbf{r}, t) = & \frac{1}{2\Delta x} \sum_{k=1}^d \tau_{ik}(\mathbf{r}, t) (u_j(\mathbf{r} + \Delta x \hat{\mathbf{e}}_k, t) - u_j(\mathbf{r} - \Delta x \hat{\mathbf{e}}_k, t)) \\ & + \frac{1}{2\Delta x} \sum_{k=1}^d \tau_{kj}(\mathbf{r}, t) (u_i(\mathbf{r} + \Delta x \hat{\mathbf{e}}_k, t) - u_i(\mathbf{r} - \Delta x \hat{\mathbf{e}}_k, t)) \\ & + \frac{\eta_p}{2\Delta x \lambda_p} (u_j(\mathbf{r} + \Delta x \hat{\mathbf{e}}_i, t) - u_j(\mathbf{r} - \Delta x \hat{\mathbf{e}}_i, t)) \\ & + \frac{\eta_p}{2\Delta x \lambda_p} (u_i(\mathbf{r} + \Delta x \hat{\mathbf{e}}_j, t) - u_i(\mathbf{r} - \Delta x \hat{\mathbf{e}}_j, t)) - \frac{1}{\lambda_p} \tau_{ij}(\mathbf{r}, t). \end{aligned} \quad (4.27)$$

The discrete form of the continuity equation 2.18 comes from equation 4.15 for each component of the stress tensor:

$$\begin{aligned} \bar{\tau}_{ij}(\mathbf{r}, t + \Delta t) \approx & -\frac{1}{\Delta x^3} \sum_{\ell=1}^q \sum_{k=1}^d J_{ijk}(\mathbf{r} + \frac{1}{2}\mathbf{c}_\ell\Delta t, t) c_{\ell k} \\ & + \bar{S}_{ij}(\mathbf{r}, t)\Delta t + \bar{\tau}_{ij}(\mathbf{r}, t). \end{aligned} \quad (4.28)$$

The force equation 2.16 is discretized in the fashion of section 4.2.1 by

averaging over the volume of a cell:

$$\begin{aligned}\bar{F}_j^{\text{P}}(\mathbf{r}, t) &= \frac{1}{V} \int_V \sum_{i=1}^d \frac{\partial}{\partial r_i} \tau_{ij}(\mathbf{r}, t) d^d r \\ &= \frac{1}{V} \int_{\partial V} \sum_{i=1}^d \tau_{ij}(\mathbf{r}, t) n_i d^{d-1} r\end{aligned}\quad (4.29)$$

$$\approx \frac{1}{A_0} \sum_{\ell=1}^q \frac{1}{|c_\ell|} \sum_{i=1}^d \tau_{ij}(\mathbf{r} + \frac{1}{2} \mathbf{c}_\ell \Delta t, t) c_{\ell i}, \quad (4.30)$$

where $\tau_{ij}(\mathbf{r} + \frac{1}{2} \mathbf{c}_i \Delta t)$ can be obtained via equation 4.16.

Boundaries across which no stress is transported can be imposed on the FV scheme by using

$$\mathbf{J}(\mathbf{r}_b + \frac{1}{2} \mathbf{c}_i \Delta t) \equiv 0, \quad (4.31)$$

where \mathbf{r}_b is a boundary node and $\mathbf{r}_b + \mathbf{c}_i \Delta t$ is a fluid node. $\boldsymbol{\tau}(\mathbf{r}_b)$ needs to be extrapolated so that the force can continue to be obtained via equation 4.30. We found constant extrapolation

$$\boldsymbol{\tau}(\mathbf{r}_b) \equiv \boldsymbol{\tau}(\mathbf{r}_b + \mathbf{c}_i \Delta t) \quad (4.32)$$

to be sufficient, but linear or quadratic extrapolation could be employed as needed.

As in our LB, thermal fluctuations are not included. The addition of noise to the stress fluxes — while obtaining the proper fluctuation-dissipation relation for the total fluid — is non-trivial and goes beyond the scope of this thesis. Thermalization of the FV Oldroyd-B solver based on existing numerical methods for fluctuating hydrodynamics [293] could be the subject of future study.

4.2.4 Lattice electrokinetics

The method proposed by Capuani et al. [282], which we call “lattice electrokinetics” (EK), discretizes equation 2.24 with the same stencil on the same lattice that LB is performed on. Rempfer et al. [209] have shown that the discretization originally proposed in reference 282 introduces errors scaling exponentially with $E/\Delta x$ where E is the applied electric field. We instead use a conventional FV discretization as introduced in section 4.2.1.

This results in

$$\begin{aligned}
& j_{ki}^{\text{diff}}(\mathbf{r} + \frac{1}{2}\mathbf{c}_i\Delta t, t) \\
&= \frac{D_k}{A_0 c_i \Delta t} (\rho_k(\mathbf{r}, t) - \rho_k(\mathbf{r} + \mathbf{c}_i \Delta t, t)) \\
&\quad - \frac{D_k z_k e}{k_B T A_0 c_i \Delta t} \frac{\rho_k(\mathbf{r}, t) + \rho_k(\mathbf{r} + \mathbf{c}_i \Delta t, t)}{2} (\Phi(\mathbf{r}, t) - \Phi(\mathbf{r} + \mathbf{c}_i \Delta t, t))
\end{aligned} \tag{4.33}$$

for the diffusive term, as in reference 209 and with A_0 from equation 4.25. For the advective term j_{ki}^{adv} , the upstream method of equation 4.23 is used [282] to obtain

$$\begin{aligned}
& j_{ki}^{\text{adv}}(\mathbf{r} + \frac{1}{2}\mathbf{c}_i\Delta t) = \\
& \rho_k(\mathbf{r}, t) \frac{\Delta t}{\Delta x^{d-1}} \prod_{\ell=1}^d \int_{c_{i\ell}\Delta t}^{c_{i\ell}\Delta t + \Delta x} \theta(a - u_\ell(\mathbf{r}, t)\Delta t) \theta(u_\ell(\mathbf{r}, t)\Delta t + \Delta x - a) da.
\end{aligned} \tag{4.34}$$

The index k runs over the N different solute species.

Once the fluxes have been calculated, they can be propagated using the discretization of the continuity equation 2.23 via equation 4.15,

$$\rho_k(\mathbf{r}, t + \Delta t) = \rho_k(\mathbf{r}, t) - \frac{\Delta t}{\Delta x^d} \sum_{i=1}^q (j_{ki}^{\text{diff}}(\mathbf{r}, t) + j_{ki}^{\text{adv}}(\mathbf{r}, t)). \tag{4.35}$$

The fluid coupling force is a direct discretization of equation 2.28 and is applied using equation 4.10:

$$\mathbf{F}_{\text{ext}}(\mathbf{r}, t) = \frac{k_B T \Delta x}{\Delta t} \sum_{k=1}^N \sum_{i=1}^q \frac{j_{ki}^{\text{diff}}(\mathbf{r}, t)}{D_k} \mathbf{c}_i. \tag{4.36}$$

Solving the electrostatics of equation 2.26 is discussed in section 4.3. Besides driving the migrative term of equation 4.33, electrostatics also results in a force acting on the colloidal particles, which is added to the hydrodynamic drag force of equations 4.47 and 4.48 before integrating the particle trajectory.

At this point, EK is only capable of handling stationary boundary conditions, such as walls and particles that are stationary with respect to the lattice. They are simply mapped into the LB fluid as a no-slip boundary in

all cells inside them and any EK solute fluxes into or out of these cells are set to zero:

$$j_{ki}(\mathbf{r}_b + \frac{1}{2}\mathbf{c}_i\Delta t) \equiv 0, \quad (4.37)$$

where \mathbf{r}_b is a boundary node and $\mathbf{r}_b + \mathbf{c}_i\Delta t$ is a fluid node. Prescribing normal fluxes other than zero via equation 2.41 would allow for the incorporation of chemical reactions occurring on the surface that lead to phenomena such as charge regulation and self-electrophoresis [35, 208]. Boundaries may be charged by considering their charge distribution $\rho_b(\mathbf{r}, t)$ as an additional summand when solving equation 2.26.

As in our LB, thermal fluctuations are not included. The addition of noise to the concentration fluxes — while obtaining the proper fluctuation-dissipation relation for the total fluid — is non-trivial and goes beyond the scope of this thesis. Thermalization of the EK algorithm based on existing numerical methods for fluctuating hydrodynamics of electrolytes [294, 295] has recently been considered in reference 6.

4.2.5 Chemical reactions

The chemical reactions of equation 2.35 become an additional source term on the right-hand side of equation 4.35 simply by integrating over the volume of a cell [213, 296]:

$$R_k(\mathbf{r}, t) = -\gamma s_k \rho_k(\mathbf{r}, t) + \gamma \sum_{i \neq k} s_i \rho_i(\mathbf{r}, t). \quad (4.38)$$

4.3 Fast Fourier electrostatics

The electrostatics of equation 2.26 is treated using any available lattice-based electrostatics solver. For this work, one based on fast Fourier transformations (FFTs) is used [297], but iterative solvers for linear equation systems, such as successive over-relaxation (SOR) or Krylov subspace methods, might also be applied [282, 298]. The non-FFT-based solvers are also capable of incorporating inhomogeneous dielectric coefficients ϵ_i ; the assumption of homogeneity has only entered into the specific form of Poisson's equation 2.26 used here. Even FFT-based solvers can approximate inhomogeneous dielectric coefficients by using the previous time step's electric potential to calculate the induced charges [299], which is valid in our limit where charges move much slower than $\Delta x/\Delta t$. Note that an Ewald-type splitting [300] is not needed as charges cannot be more narrowly localized than a single lattice cell; the short-range term of the Ewald summation would thus be

zero and the long-range term would be equivalent to what is introduced below. We may however have charge separation within a cell, so a dipolar electrostatics solver is also discussed below.

4.3.1 Charge monopoles

We start out by discretizing the Poisson equation 2.26,

$$\nabla^2 \Phi(\mathbf{r}, t) = -\frac{1}{\varepsilon_0 \varepsilon_r} \rho_{\text{total}}(\mathbf{r}, t),$$

with a $2d$ -point finite difference scheme to obtain

$$\frac{1}{\Delta x^2} \left(-(2d+1)\Phi(\mathbf{r}, t) + \sum_{k=1}^{2d+1} \Phi(\mathbf{r} + \mathbf{c}_i \Delta t, t) \right) = -\frac{1}{\varepsilon_0 \varepsilon_r} \rho_{\text{total}}(\mathbf{r}, t), \quad (4.39)$$

where the sum runs over the D3Q7/D2Q5 neighbor set. Any function $Y(\mathbf{r})$ on a regular grid with periodic boundary conditions can be expressed in terms of a discrete Fourier transformation:

$$\hat{Y}(\mathbf{k}) = \frac{1}{\sqrt{\prod_{j=1}^d N_j}} \sum_{r_1=0}^{N_1-1} \cdots \sum_{r_d=0}^{N_d-1} \exp\left(-2\pi i \sum_{j=1}^d \frac{k_j r_j}{N_j}\right) Y(\mathbf{r}) \quad (4.40)$$

$$Y(\mathbf{r}) = \frac{1}{\sqrt{\prod_{j=1}^d N_j}} \sum_{k_1=0}^{N_1-1} \cdots \sum_{k_d=0}^{N_d-1} \exp\left(2\pi i \sum_{j=1}^d \frac{k_j r_j}{N_j}\right) \hat{Y}(\mathbf{k}) \quad (4.41)$$

with the grid size $N_1 \times \cdots \times N_d$ matching the grid used for LB and EK. Inserting equation 4.41 into equation 4.39, one obtains

$$\begin{aligned} & -\frac{\Delta x^2}{\varepsilon_0 \varepsilon_r} \sum_{k_1=0}^{N_1-1} \cdots \sum_{k_d=0}^{N_d-1} \exp\left(2\pi i \sum_{j=1}^d \frac{k_j r_j}{N_j}\right) \hat{\rho}_{\text{total}}(\mathbf{k}, t) \\ & = 2 \sum_{k_1=0}^{N_1-1} \cdots \sum_{k_d=0}^{N_d-1} \exp\left(2\pi i \sum_{j=1}^d \frac{k_j r_j}{N_j}\right) \left(\sum_{j=1}^d 2 \cos\left(\frac{\pi k_j}{N_j}\right) - d \right) \hat{\Phi}(\mathbf{k}, t). \end{aligned} \quad (4.42)$$

The fact that the discrete Fourier transformation is an orthonormal basis means that this equality is fulfilled for each summand individually [297], so

$$\hat{\Phi}(\mathbf{k}, t) = -\frac{\Delta x^2}{2\varepsilon_0 \varepsilon_r \left(\sum_{j=1}^d \cos\left(\frac{2\pi k_j}{N_j}\right) - d \right)} \hat{\rho}_{\text{total}}(\mathbf{k}, t). \quad (4.43)$$

The backward discrete Fourier transformed of equation 4.43's proportionality factor is the discrete form of the Green's function of electrostatics in equation 3.63 [297]. Since it does not depend on time, it can be pre-computed for all \mathbf{k} at the beginning of the simulation. Going from equation 4.42 to equation 4.43, a division has been performed which is undefined for $k = 0$ unless $\hat{\rho}(\mathbf{0}, t) = 0$. This yields the requirement that the system must be charge-neutral [297],

$$Q_{\text{total}} = \sum_{r_1=0}^{N_1-1} \cdots \sum_{r_d=0}^{N_d-1} \rho_{\text{total}}((r_1, \dots, r_d)^\top, t) = 0. \quad (4.44)$$

The convolution of the charge with the Green's function can efficiently be performed using FFTs, which are an efficient way of evaluating equations 4.40 and 4.41. ρ_{total} is FFTed into $\hat{\rho}_{\text{total}}$ via equation 4.40, multiplied according to equation 4.43 to obtain $\hat{\Phi}$, and then inverse-FFTed into Φ via equation 4.41.

4.3.2 Charge dipoles

The same method may also be used to compute the potential due to a charge dipole density $\mathbf{p}_{\text{total}}$ by applying concepts from section 3.6. We know from equation 3.65 that the transition from monopole to dipole corresponds to the application of the operator $-\mathbf{p}_{\text{total}} \cdot \nabla$. In Fourier space, this becomes a multiplication with $-i\mathbf{k} \cdot \mathbf{p}_{\text{total}}$. The dipolar equivalent to equation 4.43 is thus [301]

$$\hat{\Phi}_{\text{D}}(\mathbf{k}, t) = i \frac{\Delta x^2}{2\epsilon_0\epsilon_r \left(\sum_{j=1}^d \cos\left(\frac{2\pi k_j}{N_j}\right) - d \right)} \mathbf{k} \cdot \hat{\mathbf{p}}_{\text{total}}(\mathbf{k}, t), \quad (4.45)$$

and the potential due to a combined distribution of charge monopoles and dipoles can be obtained by adding equations 4.43 and 4.45, exactly as was done in equation 3.65. The backward discrete Fourier transformed of equation 4.45's proportionality factor is the discrete form of the fundamental solution for dipoles in equation 3.65.

4.4 Moving boundaries

There is a variety of methods that incorporate particles into an LB fluid [266], ranging from point-particle descriptions [302, 303] to particles that are resolved on the grid [304, 305]. In this work, we are interested in the latter, since for the study of phoretic interactions of self-propelled particles,

one typically needs to resolve the particle surface where the propulsion is taking place as discussed in section 1.2.2. Thus the moving boundary method introduced by Ladd [304] and later improved upon by Aidun et al. [305] is the obvious choice to achieve coupling. The method is applicable for particles much larger than the size of a grid cell and considers the cells inside the particle as no-slip conditions in the particle-co-moving frame.

4.4.1 Moving-boundary lattice Boltzmann

A colloidal particle with its geometric center at \mathbf{r} moving with velocity \mathbf{v} and angular velocity $\boldsymbol{\omega}$ corresponds to a velocity boundary condition of

$$\mathbf{u}_b(\mathbf{r}_b, t) = \mathbf{v}(t) + \boldsymbol{\omega}(t) \times (\mathbf{r}_b - \mathbf{r}(t)), \quad (4.46)$$

which can be applied via equation 4.11. The velocity bounce-back operation between the boundary cell \mathbf{r}_b and the fluid cell $\mathbf{r}_b + \mathbf{c}_i \Delta t$ transfers linear and angular momentum to the particle, corresponding to a force and torque

$$\mathbf{F}(t) = \Delta x^3 \sum_{i=1}^q \mathbf{c}_i (f_i(\mathbf{r}_b, t) + f_{-i}(\mathbf{r}_b + \mathbf{c}_i \Delta t, t)), \quad (4.47)$$

$$\mathbf{M}(t) = \Delta x^3 \sum_{i=1}^q (\mathbf{r}_b - \mathbf{r}) \times \mathbf{c}_i (f_i(\mathbf{r}_b, t) + f_{-i}(\mathbf{r}_b + \mathbf{c}_i \Delta t, t)) \quad (4.48)$$

acting on the particle. Unlike Ladd's original algorithm [304], we do not average $\mathbf{F}(t)$ and $\mathbf{M}(t)$ over two time steps. This is generally only necessary if oscillations in these quantities are observed between consecutive time steps [306]. Note that the net force and torque of the system is still zero for a microswimmer [19]: the above force and torque just account for momentum transferred between fluid and particle. The particle trajectory is obtained by summing these forces and torques, along with any externally applied ones, and integrating numerically with a symplectic Euler integrator. The symplecticity makes the simulation stable for longer times as it significantly improves the conservation of energy and momentum.

As a particle moves across the lattice, the set of cells overlapped by the particle changes. The original method by Ladd [304] has some shortcomings, due to the presence of fluid inside the particle. These shortcomings include forces exerted on the particle by the internal fluid [307] and the requirement that the particle's density is the same or larger than that of the fluid. The modification by Aidun et al. [305] removes this unphysical fluid. This allows the particle's density to be less than that of the fluid, but significant density differences lead to oscillations unless means are taken to improve numerical

stability [308]. However, one now needs to destroy fluid in cells that are newly overlapped by a particle and create fluid in cells that are vacated. The former is straightforward to do, while the latter requires choosing a value for each of the f_i in the cell where new fluid is to be created. This initialization of the new fluid cell is problematic, as LB has q microscopic degrees of freedom, more than the $d + 1$ specified by the hydrodynamic boundary condition. Thus, new fluid populations are created at their equilibrium value, $f_i(\mathbf{r}_{\text{new}}, t) = f_i^{\text{eq}}(\mathbf{r}_{\text{new}}, t)$ from equation 4.4, whose velocity $\mathbf{u}_b(\mathbf{r}_{\text{new}}, t)$ is given by equation 4.46. This creation and destruction of populations violates instantaneous mass conservation, but is unproblematic as average mass is conserved. In fact, fluid mass cannot be conserved in this scheme as conserving it would violate the incompressibility of the fluid. This is not strictly a problem since LB itself is not perfectly incompressible as discussed in section 4.1, but is in conflict with the Stokes equation 2.10 we are trying to model using it. However, the time-averaged fluid mass fluctuates around the correct value while the particle traverses the grid. Momentum conservation during creation and destruction of populations is ensured by applying a force to the particle that balances any momentum destroyed or created:

$$\mathbf{F}(t) = \pm \frac{\Delta x^d}{\Delta t} \rho(\mathbf{r}_f, t) \mathbf{u}(\mathbf{r}_f, t). \quad (4.49)$$

Further enhancements of the moving-boundary LB method are reviewed in reference 309.

4.4.2 Moving-boundary electrokinetics

In section 4.4.1, the well-known moving boundary method for LB was introduced. It is not mass-conserving, so a straightforward adaptation to EK would cause the amount of solute to vary over time and thus violate charge conservation. Furthermore, as the solute charge is typically far less homogeneously distributed than the fluid mass, one can expect that charge would not even be conserved on average over long time scales. A simulation undergoing such a net charge drift will typically not be able to produce physically correct results.

4.4.2.1 Simple charge conservation scheme

To avoid a net charge drift, any solute from a cell \mathbf{r}_{old} newly claimed by a particle needs to be expelled and redistributed into the $N_f \leq q - 1$

surrounding non-boundary cells:

$$\rho_k^*(\mathbf{r}_{\text{old}} + \mathbf{c}_i \Delta t, t) = \rho_k(\mathbf{r}_{\text{old}} + \mathbf{c}_i \Delta t, t) + \frac{1}{N_f} \rho_k(\mathbf{r}_{\text{old}}, t). \quad (4.50)$$

The \mathbf{c}_i point to the respective neighboring cells.

Cells vacated behind the particle are refilled by taking the sum of the solute concentration of the surrounding non-boundary cells and dividing it by $N_f + 1$ to account for the fact that this amount of solute will now be shared with one additional cell. This means that the solute concentration

$$\rho_k^*(\mathbf{r}_{\text{new}}, t) = \frac{1}{N_f + 1} \sum_{i=1}^{N_f} \rho_k(\mathbf{r}_{\text{new}} + \mathbf{c}_i \Delta t, t) \quad (4.51)$$

is put into the vacated cell at \mathbf{r}_{new} . To conserve total solute mass, that amount is then removed from the surrounding non-fluid cells in amounts proportional to their current solute concentration:

$$\rho_k^*(\mathbf{r}_{\text{new}} + \mathbf{c}_i \Delta t, t) = \rho_k(\mathbf{r}_{\text{new}} + \mathbf{c}_i \Delta t, t) - \frac{1}{N_f} \rho_k^*(\mathbf{r}_{\text{new}}, t). \quad (4.52)$$

It should be noted that expulsion and vacation do not necessarily happen at the same time in the front and back of a moving particle, and thus the total number of boundary cells oscillates over time. The whole scheme is illustrated in figure 4.5.

4.4.2.2 Enhanced partial volume scheme

The scheme introduced in section 4.4.2.1 has the disadvantage that it moves large amounts of solute at few points in time, specifically entire cells' worth of solute in single simulation time steps. Therefore, as we will see in section 8.2, the particle's velocity can vary quite strongly during the time steps after a cell has been claimed or vacated. To reduce these effects, we propose a partial volume scheme which is illustrated in figure 4.6.

In the following, $\Psi(\mathbf{r}, t)$ is a field describing the volume fraction of the cell at \mathbf{r} that is overlapped by a particle, with $\Psi = 1$ meaning that the cell is completely inside the particle and $\Psi = 0$ completely outside. In the calculation of the diffusive fluxes from equation 4.33, the concentrations are replaced with ones that take into account that all solute resides in the non-overlapped part of the cells:

$$\rho_k(\mathbf{r}, t) \rightarrow \frac{\rho_k(\mathbf{r}, t)}{1 - \Psi(\mathbf{r}, t)}. \quad (4.53)$$

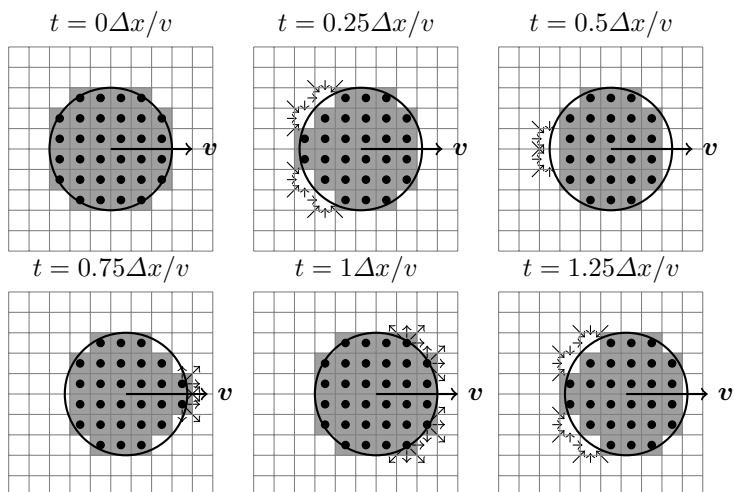


Figure 4.5: Illustration of the mass conservation modification to the Ladd boundary scheme to make it usable for EK. Cells whose center is inside the particle are considered to be boundary nodes. The arrows indicate how solute is drawn into vacated cells (panes 2, 3, and 6) and expelled from newly-overlapped cells (panes 4 and 5).

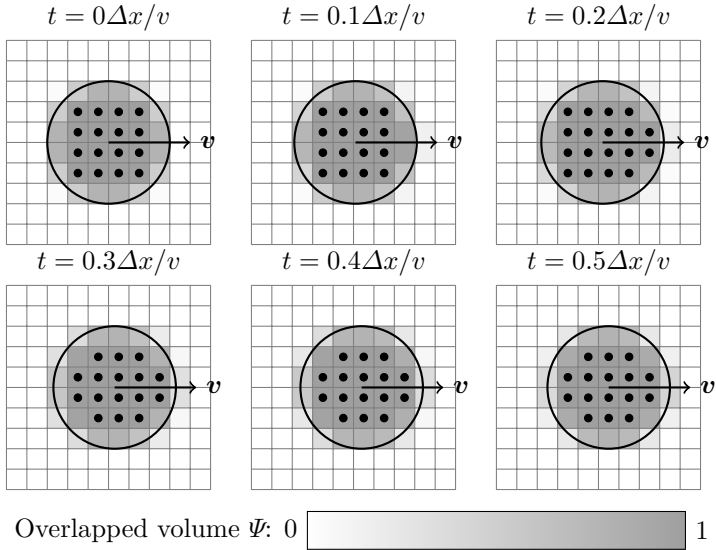


Figure 4.6: Illustration of the partial volume scheme for moving boundaries in EK. The shading of the cells inside the particle corresponds to the overlapped volume Ψ to indicate how the particle's charge is distributed across the cell layer at its surface. In the calculation of the diffusive flux, the concentrations are scaled with $1 - \Psi$ to determine the effective concentrations.

To prevent the resulting diffusive fluxes from diverging as $\Psi \rightarrow 1$, we renormalize them by scaling them with the volume:

$$\begin{aligned}
 & j_{ki}^{\text{diff}}(\mathbf{r} + \frac{1}{2}\mathbf{c}_i\Delta t, t) \\
 & \rightarrow j_{ki}^{\text{diff}}(\mathbf{r} + \frac{1}{2}\mathbf{c}_i\Delta t, t)(1 - \Psi(\mathbf{r}, t))(1 - \Psi(\mathbf{r} + \mathbf{c}_i\Delta t, t)).
 \end{aligned} \tag{4.54}$$

This leads to the following modified expression for the flux:

$$\begin{aligned}
 & j_{ki}^{\text{diff}}(\mathbf{r} + \frac{1}{2}\mathbf{c}_i\Delta t, t) \\
 & = \left(\frac{D_k}{A_0 c_i \Delta t} \left(\frac{\rho_k(\mathbf{r}, t)}{1 - \Psi(\mathbf{r}, t)} - \frac{\rho_k(\mathbf{r} + \mathbf{c}_i\Delta t, t)}{1 - \Psi(\mathbf{r} + \mathbf{c}_i\Delta t, t)} \right) \right. \\
 & \quad - \frac{D_k z_k e}{2k_B T A_0 c_i \Delta t} \left(\frac{\rho_k(\mathbf{r}, t)}{1 - \Psi(\mathbf{r}, t)} + \frac{\rho_k(\mathbf{r} + \mathbf{c}_i\Delta t, t)}{1 - \Psi(\mathbf{r} + \mathbf{c}_i\Delta t, t)} \right) \\
 & \quad \left. \cdot (\Phi(\mathbf{r}, t) - \Phi(\mathbf{r} + \mathbf{c}_i\Delta t, t)) \right) (1 - \Psi(\mathbf{r}, t))(1 - \Psi(\mathbf{r} + \mathbf{c}_i\Delta t, t)).
 \end{aligned} \tag{4.55}$$

With this change, refilling vacated cells as per equations 4.51 and 4.52 is no longer necessary. They can be set to zero concentration and will be filled up by the diffusive flux again as Ψ increases. The renormalization also needs to be taken into account when considering surface reactions via equation 2.41, where the reaction now operates not only on the cell at $\mathbf{r}_b + \mathbf{c}_i\Delta t$, but also on $\mathbf{r}_b + 2\mathbf{c}_i\Delta t$ in shares of $1 - \Psi(\mathbf{r}_b + \mathbf{c}_i\Delta t, t)$ and $\Psi(\mathbf{r}_b + \mathbf{c}_i\Delta t, t)$, respectively.

We approximate Ψ numerically by subdividing each cell into 2^d equally-sized sub-cells and determining how many of these are completely inside and completely outside the particle. For those cells that are neither, the subdivision is recursively repeated up to a maximum depth of $n_{\text{max}} = 4$. This can be formally expressed as

$$\Psi(\mathbf{r}, t) \approx \Psi_0(\mathbf{r}, \Delta x, \mathcal{P}(t)) \tag{4.56}$$

with

$$\Psi_n(\mathbf{r}, \Delta x, \mathcal{P}(t)) = \begin{cases} 1 & K(\mathbf{r}, \Delta x, \mathcal{P}(t)) = 2^d \\ 0 & K(\mathbf{r}, \Delta x, \mathcal{P}(t)) = 0 \\ \frac{1}{2^d} K(\mathbf{r}, \Delta x, \mathcal{P}(t)) & n = n_{\text{max}} \\ \frac{1}{2^d} \sum_{i=1}^{2^d} \Psi_{n+1}(\mathbf{r} + \mathbf{c}_i \frac{\Delta x}{4}, \frac{\Delta x}{2}, \mathcal{P}(t)) & \text{else} \end{cases} \tag{4.57}$$

where the sum runs over the 2^d neighbor vectors $\mathbf{c}_i = (\pm 1, \dots, \pm 1)^\top$ pointing through the cell corners. The function K counts how many corners of the axis-aligned cube with edge length Δx centered at \mathbf{r} are inside the particle. Assuming a spherical particle of radius R centered at \mathbf{r}_0 , it becomes

$$K(\mathbf{r}, \Delta x, \mathcal{P}(t)) = K(\mathbf{r}, \Delta x, \mathbf{r}_0(t), R) = \sum_{i=1}^{2^d} \theta \left(R - \left| \mathbf{r} + \mathbf{c}_i \frac{\Delta x}{2} - \mathbf{r}_0(t) \right| \right). \quad (4.58)$$

Expelling solute from a cell that is claimed by a particle via equation 4.50 is, however, still necessary — even with the modified expression for the flux — as the cell is not necessarily completely empty by the time it is claimed, due to the discretized motion of the colloid. The expelled amount of solute with equation 4.55 is much smaller than with equation 4.33 and thus the effect of this sudden change on the simulation is reduced to acceptable levels.

One further source of sudden variations in solute fluxes is the change in electrostatic potential when the volume across which a particle's charge is distributed varies due to the fluctuation in the number of boundary cells. Therefore, when calculating the electrostatic potential, each particle's total charge Q is distributed among all cells that are at least partially overlapped by that particle:

$$\rho_b(\mathbf{r}, t) = Q \frac{\Psi(\mathbf{r}, t)}{V_p}, \quad (4.59)$$

with V_p the particle's (non-discrete) volume. Inhomogeneous charge distributions are also possible as long as the charge in a cell varies smoothly while the cell is slowly claimed or vacated by the colloidal particle.

Formally, every partially-filled cell at \mathbf{r}_s on the surface of the particle now contains a charge dipole $\mathbf{p}(\mathbf{r}_s)$: the part of the cell that lies inside the particle contains the charge $\rho_b(\mathbf{r}_s, t)$, while the rest of the cell contains mostly charge of the opposite sign from the electric double layer. These dipoles have been neglected for purposes of this thesis, but the method sketched out in the rest of this paragraph could be used to calculate electrostatic interactions more completely. The dipole density of equation 3.67 might be obtained by a modified version of the subdivision scheme of equation 4.56. The potential due to these dipoles could be calculated using the method of section 4.3.2. The force exerted by the dipoles on the monopoles in the fluid and in the particle would be calculated from the potential as before, in a fashion resembling equation 3.68. The force and torque exerted on the dipoles would need to be calculated by discretizing equations 3.70 and 3.71

as in section 4.2 and applying the result to the particle centered at \mathbf{r} :

$$\begin{aligned}
 \mathbf{F}(t) &= -\nabla(\mathbf{p}(\mathbf{r}_s, t) \cdot \nabla\Phi(\mathbf{r}, t)) \\
 &= -(\mathbf{p}(\mathbf{r}_s, t) \cdot \nabla)(\nabla\Phi(\mathbf{r}, t)) - \mathbf{p}(\mathbf{r}_s, t) \times \underbrace{(\nabla \times (\nabla\Phi(\mathbf{r}, t)))}_{=\mathbf{0}} \\
 &\approx \sum_{i=1}^d \sum_{j=1}^d p_i(\mathbf{r}_s, t) \Xi_{ij}(\mathbf{r}_s, t) \hat{\mathbf{e}}_j,
 \end{aligned} \tag{4.60}$$

$$\begin{aligned}
 \mathbf{M}(t) &= -\mathbf{p}(\mathbf{r}_s, t) \times \nabla\Phi(\mathbf{r}, t) + (\mathbf{r}_s - \mathbf{r}) \times \mathbf{F}(t). \\
 &\approx \mathbf{p}(\mathbf{r}_s, t) \times \sum_{i=1}^d \frac{1}{2\Delta x} (\Phi(\mathbf{r} - \Delta x \hat{\mathbf{e}}_i, t) - \Phi(\mathbf{r} + \Delta x \hat{\mathbf{e}}_i, t)) \hat{\mathbf{e}}_i \\
 &\quad + (\mathbf{r}_s - \mathbf{r}) \times \mathbf{F}(t),
 \end{aligned} \tag{4.61}$$

with

$$\begin{aligned}
 \Xi_{ii}(\mathbf{r}, t) &= \frac{1}{2\Delta x} (-\Phi(\mathbf{r} + \Delta x \hat{\mathbf{e}}_i, t) + 2\Phi(\mathbf{r}, t) - \Phi(\mathbf{r} - \Delta x \hat{\mathbf{e}}_i, t)), \\
 \Xi_{ij}(\mathbf{r}, t) &= \frac{1}{4\Delta x^2} (-\Phi(\mathbf{r} + \Delta x \hat{\mathbf{e}}_i + \Delta x \hat{\mathbf{e}}_j, t) + \Phi(\mathbf{r} + \Delta x \hat{\mathbf{e}}_i - \Delta x \hat{\mathbf{e}}_j, t) \\
 &\quad + \Phi(\mathbf{r} - \Delta x \hat{\mathbf{e}}_i + \Delta x \hat{\mathbf{e}}_j, t) - \Phi(\mathbf{r} - \Delta x \hat{\mathbf{e}}_i - \Delta x \hat{\mathbf{e}}_j, t)).
 \end{aligned}$$

4.4.3 Moving-boundary Oldroyd-B

The moving boundary method has been extended to FV schemes in section 4.4.2 for application in chapter 8 and reference 299, but only in the context of ion concentrations propagating according to the electrokinetic equations. Now, we take a similar path to apply it to the $\boldsymbol{\tau}$ of a viscoelastic medium. Section 4.4.2 takes precautions to ensure that charge is conserved. We do the same here to ensure that stress — whose diagonal elements correspond to stored energy — is not created or destroyed while cells are converted between fluid and solid. Section 4.4.2.2 further calculates the fraction of a cell that is overlapped by the particle and uses that information to smooth out the conversion process, which chapter 8 finds to significantly decrease oscillations in the particle's speed. For the simulations in section 7.2.5, we find such smoothing to be unnecessary, and thus adapt the simpler scheme of section 4.4.2.1 in the following:

A fluid cell at \mathbf{r}_{old} that is destroyed in front of the particle has its stress distributed among the surrounding fluid cells as

$$\boldsymbol{\tau}^*(\mathbf{r}_{\text{old}} + \mathbf{c}_i \Delta t, t) = \boldsymbol{\tau}(\mathbf{r}_{\text{old}} + \mathbf{c}_i \Delta t, t) + \frac{1}{N_f} \boldsymbol{\tau}(\mathbf{r}_{\text{old}}, t). \tag{4.62}$$

A cell behind the particle that is created with new fluid receives

$$\boldsymbol{\tau}^*(\mathbf{r}_{\text{new}}, t) = \frac{1}{N_f + 1} \sum_{i=1}^{N_f} \boldsymbol{\tau}(\mathbf{r}_{\text{new}} + \mathbf{c}_i \Delta t, t), \quad (4.63)$$

and the corresponding amount is removed from the neighboring cells:

$$\boldsymbol{\tau}^*(\mathbf{r}_{\text{new}} + \mathbf{c}_i \Delta t, t) = \boldsymbol{\tau}(\mathbf{r}_{\text{new}} + \mathbf{c}_i \Delta t, t) - \frac{1}{N_f} \boldsymbol{\tau}(\mathbf{r}_{\text{new}}, t + \Delta t). \quad (4.64)$$

4.5 Implementation

Most of the methods described in this chapter have been implemented in the context of the `waLBerla` framework. `waLBerla` is written in modern C++ and started out as a high-performance framework for LB algorithms [310], but over time evolved into a framework for grid-based algorithms in general [9]. It provides fields and other basic data structures, as well as the domain decomposition necessary to store pieces of these fields in blocks of equal numbers of cells, allowing them to be distributed across multiple nodes of a compute cluster. Exchange of data between neighboring blocks, e.g. via ghost layers or reductions, is possible using a communication module based on the Message Passing Interface (MPI) [311]. Fields can be exported to files for use with visualization software such as ParaView [312], or for checkpointing and resuming simulations [313].

`waLBerla` contains a number of hand-written lattice algorithms, called “sweeps” or “kernels”, including one for the LB variant described in section 4.1. Maintaining a large number of implementations of LB and other algorithms is unsustainable, especially since each of them had to be manually optimized for efficiency on current and future compute clusters. Therefore, recent work has focused on automatically generating and optimizing them. The `pystencils` project [314] is able to automatically generate optimal kernels for mathematical expressions of the form

$$Y_0(\mathbf{r}, t + \Delta t) = f(\{Y_i(\mathbf{r} + \mathbf{c}_j \Delta t, t + \Delta t)\}_{i,j}). \quad (4.65)$$

Any local lattice algorithm can be expressed in this way, so `pystencils` is predestined for use with a companion project: `lbmpy` [315] can generate such expressions for LBs with any combination of neighbor set, force model, relaxation model, thermalized or athermal, etc., again including the one described in section 4.1. `pystencils` is also capable of automatically performing FV discretizations, so it can generate code for the viscoelastic and electrokinetic methods of section 4.2.

waLBerla also contains one non-local lattice algorithm, namely the FFT. Its purpose is the electrostatics solver of section 4.3, and it is implemented using the PFFT library [316]. A multigrid solver is also available for the same purpose [317], but the FFT solver is generally expected to be more efficient except for very large problem sizes, strong parallelization, or with varying dielectric coefficients. Complementing the lattice methods, waLBerla includes a rigid-body dynamics module which can be used for the simulation of particles [318, 319]. Particles can be coupled to LB with the method described in section 4.4 [309, 320].

Locally-refined grids are also supported by the lattice algorithms [321] and the rigid-body dynamics module [308] to focus computational accuracy on regions of interest, e.g. the vicinity of a particle or surface. Unfortunately, the resolution is constant over an entire block, and neighboring blocks can only have resolution ratios of 2 : 1. This means that only gradual resolution changes are possible, rendering this approach effective mainly for the problem of taking the bulk limit. Similarly, systems with strong gradients like the ones discussed in sections 7.2.3 and 7.2.4 would lend themselves well to refinement. On the other hand, systems where the resolution changes frequently, such as required for a moderately dense suspension of particles, thus only have a minor benefit while at the same time introducing computational overhead and considerable additional complexity to the simulation.

waLBerla¹, pystencils², and lbmpy³ are available as open-source code on their respective web sites. The far-field method of chapter 3 was obviously not implemented into waLBerla, but its code is published too⁴.

¹<https://www.walberla.net/>

²<https://pypi.org/project/pystencils/>

³<https://pypi.org/project/lbmpy/>

⁴<https://doi.org/10.24416/uu01-bmgd4e>

5 A lattice Boltzmann model for squirmers

Directed motion, or motility, is of paramount importance to biology [322]. For example, it allows bacteria to move toward a food source [323] and fish to swim in formations that protect them from predators [45]. Such systems are inherently out of equilibrium. In the presence of other bacteria, motility can lead to collective effects [324–326] bearing resemblance of the schooling of fish or the swarming of birds, suggesting that the specifics of the propulsion, or even the length scale on which it occurs, have little effect on the overall behavior. Yet we know that these two situations are drastically different from the perspective of interactions via the medium, which are tied to the way the organisms achieve propulsion [45].

To experimentally better understand how the propulsion method affects the motion of an individual biological swimmer and how the motion affects the collective behavior of many biological swimmers together, artificial analogues have been developed. Realizations include catalytic [26, 105] and self-thermophoretic [40, 110] propulsion methods. These models have a well-defined geometrical shape and characterizable chemical properties, thus eliminating biological complications like shape changes or the beating of cilia. Yet, despite their simplicity, they show the same kinds of collective effects as their biological counterparts [119, 122].

Theoretical description of motility and the associated out-of-equilibrium phenomena is possible using models such as the one by Vicsek [52] or the active Brownian particle (ABP) model [172–174]. These approaches have been quite successful in qualitatively capturing the behaviors observed in nature. However both neglect the hydrodynamic interactions mediated by the surrounding fluid, which can be important for microorganisms and their artificial counterparts [45]. One way to overcome this limitation is the squirmer model [20, 21]: here, the microswimmer is described as a spherical object with a simple inhomogeneous surface slip velocity, typically suspended in a Newtonian fluid. The squirmer model’s long-ranged hydrodynamic interactions lead to reorientation like in the Vicsek model, and, when complemented with a near-field repulsion, it accounts for the collisions that are captured by the ABP model. The squirmer model has proven to be an

effective tool to model the effect of hydrodynamics in suspensions of both bacteria and man-made swimmers [75, 157, 158]. Further advantages of computer simulations include providing additional insight by giving direct access to quantities that are difficult or impossible to measure in experiment and by allowing for easy modification of parameters.

In this chapter, we implement the squirmer model numerically using the lattice Boltzmann (LB) method [261], making use of the Ladd moving boundary conditions [304, 305]. LB is in general a Navier-Stokes solver, but it can serve as a Stokes solver at the Reynolds numbers relevant to the systems considered in this thesis. The main advantages of LB over competing methods are momentum and mass conservation to machine precision, very low compressibility and good obedience of the Stokes regime, as well as facile coupling to suspended particles. Furthermore, the algorithm scales to parallelize across large supercomputers [9, 310] and is fully deterministic. One shortcoming compared to methods [327, 328] based on the Lorentz reciprocal theorem [329] is that LB does not permit Reynolds numbers that are exactly zero; the achieved Reynolds numbers are usually orders of magnitude closer to unity than the actual physical Reynolds number of the swimmer. To eliminate inertial effects, one thus needs to scale simulation parameters until the point is found where a further decrease of the Reynolds number does not change the result.

Previous simulational studies of squirmers have used methods such as multi-particle collision dynamics (MPCD) [65, 129, 149], the smooth profile method (SP) [330], the finite element method (FEM) [331–333], the boundary element method (BEM) [148, 152, 153, 334], and Stokesian dynamics (SD) [161, 162, 164, 335], but also LB [151, 157, 336, 337]. We verify our implementation against well-known results from the literature [148, 153] and show that even for these basic cases several new things may be learned. Specifically, we study squirmers in bulk both individually and scattering off each other, as well as a squirmer oscillating between the two walls of a channel. In chapter 6, we will follow up by considering the interaction between a squirmer and an immobile spherical obstacle. We find that LB is well-capable of reproducing results obtained from other methods [148, 153], but requires a higher resolution to reproduce accurate results than is known from experience with passive particles in LB. This insight will enable us to accurately simulate dense suspensions of squirmers in the future and to study phenomena such as motility-induced phase separation (MIPS) [55, 65, 75, 158].

The remainder of this chapter is laid out as follows: In section 5.1, we summarize the relevant aspects of the LB method. In section 5.2, we apply this numerical method to squirmers in bulk and interacting with boundaries

and other squirmers. There, we also discuss implementation problems that arise and how our simulations compare to previous implementations, before we conclude in section 5.3.

5.1 Model and methods

In this chapter, we consider squirmers in Stokes flow and various geometries. The Stokes equations of section 2.1.3 are solved using the LB method of section 4.1. The squirmer, introduced in section 2.4, is incorporated through the moving boundary scheme of section 4.4.1. The squirmer's surface velocity, equation 2.44, is added to the moving boundary's surface velocity, equation 4.46. A short-range Weeks-Chandler-Andersen (WCA) repulsion per equation 5.1 between pairs of swimmers, as well as between swimmer-obstacle pairs, is included in addition to the hydrodynamic forces of equations 4.47 and 4.49. Based on the sum of the forces of equations 4.47 to 4.49 and 5.1, the swimmer's trajectory can be integrated using a standard symplectic Euler scheme. We employ the `waLBerla` simulation framework as summarized in section 4.5. The same method has been implemented in previous works by other authors [157, 336–339].

We should point out the following concerning our LB calculations here: The minimal gap between squirmer and obstacle that LB can accurately resolve is limited to sizes around the lattice constant Δx , due to our LB's lack of lubrication corrections [162, 254, 340]. Note that such corrections exist for driven spheres and some other shapes, but a specific implementation for a squirmer has not yet been formulated, due to the complexity of the boundary problem. We therefore impose a short-ranged WCA potential [341] between the obstacle and squirmer. This is a smooth approximation to a hard-core repulsion and is given by

$$U(\mathbf{r}_S) = 4\epsilon \left(\frac{\sigma}{|\mathbf{r} - \mathbf{r}_S|} \right)^{12} - 4\epsilon \left(\frac{\sigma}{|\mathbf{r} - \mathbf{r}_S|} \right)^6 + \epsilon, \quad (5.1)$$

for $0 < |\mathbf{r} - \mathbf{r}_S| < 2^{1/6}\sigma$ and set to 0 for $|\mathbf{r} - \mathbf{r}_S| \geq 2^{1/6}\sigma$. The force $\mathbf{F}(\mathbf{r}_S) = -\nabla_S U(\mathbf{r}_S)$ ensures that the squirmer at \mathbf{r}_S and obstacle at \mathbf{r} remain sufficiently separated. A minimal distance of one LB cell is achieved with $\epsilon = 1\rho\Delta x^5/\Delta t^2$ and $\sigma = 1.34\Delta x$. ∇_S differentiates with respect to \mathbf{r}_S . We do not resort to actual hard-core repulsions, as a discontinuous potential leads to issues with the underlying algorithm for the positional update of our squirmer in `waLBerla` [9, 309, 310].

5.2 Validation

In this section, we describe the simple validation tests for our numerical implementation. We start with the far field, where we simulate the bulk flow field and interactions between two squirmers. After that, we investigate a system where the near field plays a dominant role, namely a squirmer confined in a narrow cylindrical tube. We refer to section 6.4.5 for the scattering of a squirmer off a spherical obstacle, where near and far field are both important.

5.2.1 Squirmers in bulk

In figure 5.1, we show the flow fields of the three types of squirmer in bulk fluid. As LB is typically used with periodic boundary conditions, a direct comparison to equation 2.45 would require either an extremely large simulation domain in LB or incorporating the effect of the periodic images into the analytic solution [342, 343]. The latter would require an Ewald summation approach [162, 344], but can be approximated by summing over a spherical shell of periodic images [170, 342]. The largest differences between this approximate periodic analytic solution and the LB solution are found at $\pm 45^\circ$ from \hat{e} , where the flow magnitude is small. Ignoring these regions, the mean error is around 8% at a resolution of $R = 8\Delta x$. Both of these deviations can be attributed to discretization errors. As we will discuss below, R (in units of the lattice spacing) needs to have a certain minimal value to avoid more severe discretization artifacts.

5.2.2 Impact of resolution

Figure 5.1 was obtained at a resolution of 8 cells per squirmer radius, i.e. $R = 8\Delta x$. In moving-boundary simulations of passive spheres, one typically aims for a resolution of $R \approx 4\Delta x$ which provides sufficient accuracy while minimizing computational effort [340]. In literature, resolutions around $R = 8\Delta x$ are often used for squirmers [336, 338, 339], but usually not explicitly justified. Some authors [157, 337, 345] do use smaller resolutions around $R = 3\Delta x$, which for squirmers appears to only give usable results in the authors' specific case without preferred direction. Problems at low resolutions were first mentioned in reference 346. We find that resolutions below a value of $R \approx 6\Delta x$ lead to strong oscillations in the flow field, causing an alternating velocity pattern along the direction in which the squirmer moves, see figure 5.2.

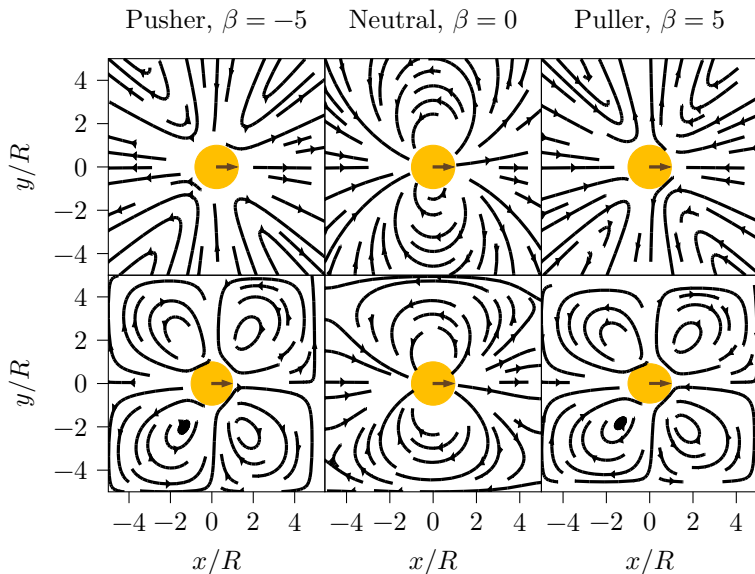


Figure 5.1: Top: the analytic flow fields of squirmers with $\beta \in \{-5, 0, 5\}$ in an unbounded domain ($L = \infty$), as in figure 2.2. The red arrows indicate that the squirmer is oriented such that it moves to the right. Bottom: the flow fields of the same squirmers at a resolution of $R = 8\Delta x$ as obtained via LB in a cubic box of length $L = 10R$ with periodic boundary conditions. As one can see, the flow field is heavily influenced by the periodicity. The analytic solution can also be determined for periodic boundary conditions and is indistinguishable from the corresponding flow fields obtained by LB.

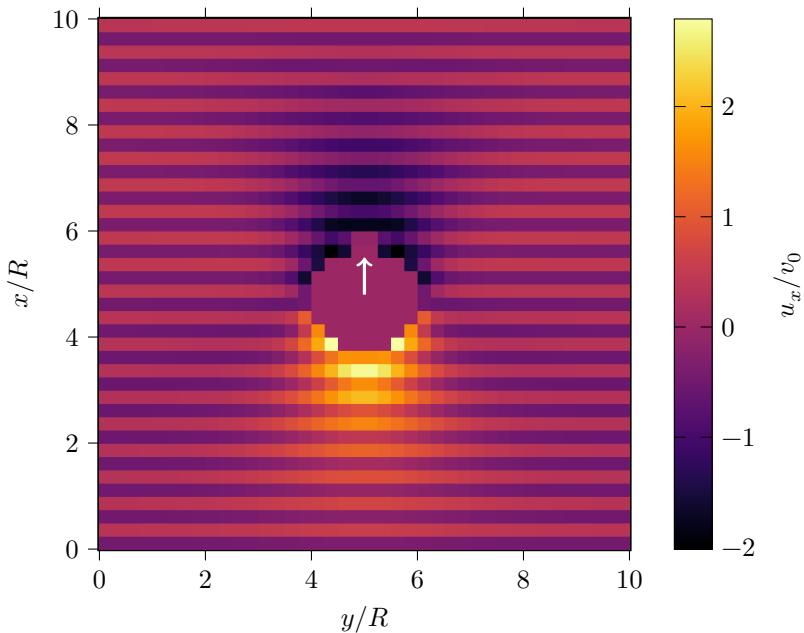


Figure 5.2: Visualization of the deteriorated flow field after simulating a squirmer of radius $R = 4\Delta x$ in a box of length $L = 10\Delta x$ for $T = 1.5 \cdot 10^5 \Delta t$. u_x , the x -component of the fluid velocity, is shown in the xy -plane and normalized by the squirmer speed v_0 . The arrow shown in gray indicates the squirmer's orientation.

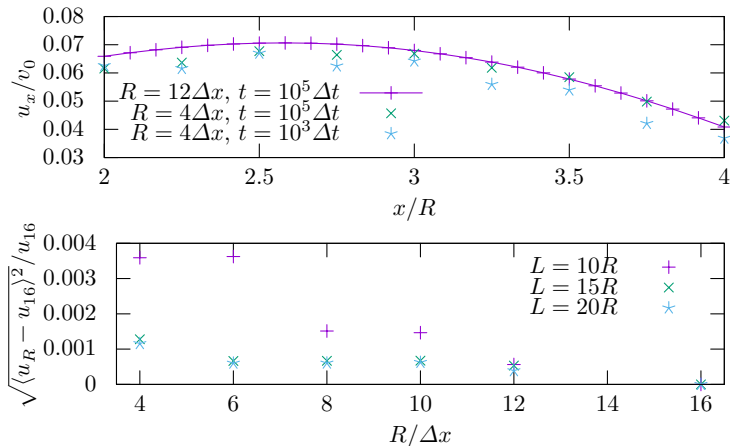


Figure 5.3: Top: flow velocity u_x , normalized by the squirmer speed v_0 , along the x -axis for $L = 10R$. For high resolutions ($R = 12\Delta x$), the curve is smooth, while for low resolutions ($R = 4\Delta x$) an alternating pattern of faster and slower cells is visible that grows more distinct over time, matching the stripes in figure 5.2. Bottom: Standard deviation of the velocity error obtained by comparing the flow field u_R at a radius R to that of a high-resolution simulation ($R = 16\Delta x$) for the entire simulation domain. Larger values correspond to more inhomogeneous errors, i.e., the development of the alternating pattern described in the main text. Time $t = 1000\Delta t$ and different box sizes $L \in \{10R, 15R, 20R\}$ are shown. The difference between $L = 15R$ and $L = 20R$ can be attributed to our error fitting procedure.

As seen in figure 5.3, the magnitude of the oscillation increases over time, suggesting a self-reinforcing numerical artifact. While at short times, the true flow can still be obtained by averaging over the oscillation, after several million time steps, they become so strong that the true flow is almost completely obscured. Eventually the simulation becomes unstable because LB does not accurately handle strong velocity gradients like those in figure 5.2 well. This phenomenon is most often seen in systems with a preferred direction. Alarcón et al. [157, 337], for example, do not see this effect because they have dense suspensions of squirmers that continuously change their orientations. For comparison, in MPCD, squirmer radii of three collision cells, each of which contain an average of 80 MPCD particles, are reported to have been used [65]. MPCD does not use a fixed grid, so it is less prone to discretization artifacts like the one discussed here. Since the computational effort for an LB cell and for an MPCD particle are on the same order of magnitude, the resolution requirement can be considered to be similar for LB and MPCD.

In figure 5.4, we show how the squirmer’s speed v depends on the resolution as given by the squirmer’s radius R and on the box length L . In analytic theory and in LB in the infinite-resolution limit, this speed equals the squirmer parameter v_0 from equation 2.46. In figure 5.4 we observe that we approach v_0 from below as resolution increases. At $R = 6\Delta x$, we are already within 0.5% of the correct value (0.2% at $R = 12\Delta x$) for the largest box size. For the smaller box sizes, the interaction of the squirmer with its periodic images decreases the velocity slightly. For comparison, the same data is also plotted for a passive sphere being dragged through a resting fluid at otherwise identical parameters. The periodicity effect is much weaker for the squirmer than for the passive sphere since the latter’s flow is monopolar to leading order and thus decays more slowly than the squirmer’s. Despite the seemingly good agreement of the observed squirmer velocity with the prescribed squirmer velocity even for small resolutions, the stripe pattern discussed in the previous paragraph massively modifies the flow field, to the extent that simulations at small resolutions simply give no meaningful results.

While the squirmer moves across the lattice, some variation in its speed is expected due to the sphere being composed of varying numbers of discrete cubes. As expected, figure 5.4 shows that the variation decreases with resolution, however the variation is much larger than for the equally-resolved passive sphere dragged through the fluid. The latter can be attributed to the cause of the motion — the squirmer is dragged along by the flow its own surface causes — and to the fact that this surface is significantly affected by the slight changes in the number of cells occupied by a sphere as it moves.

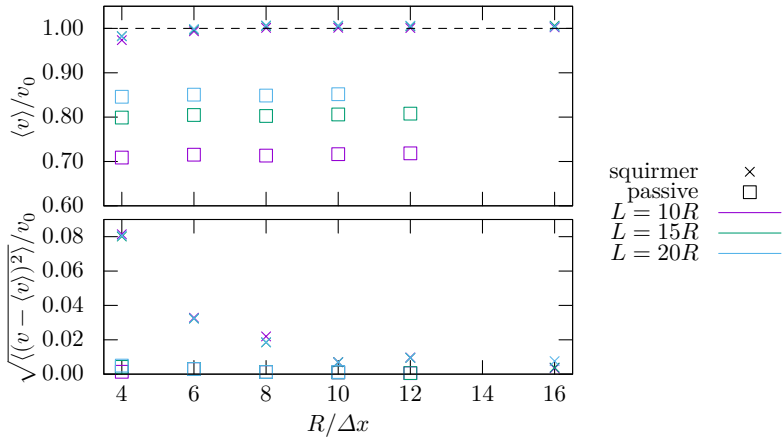


Figure 5.4: Top: A squirmer’s (orange) and a passive sphere’s (blue) mean velocity $\langle v \rangle$, normalized by the expected bulk speed v_0 , as a function of the resolution of the squirmer/passive sphere. Bottom: Normalized variance of the respective bodies’ velocities indicating the spread around the mean velocity. The resolution is given by the radius R in lattice units. We show results for three box sizes as given by the edge length L , also in lattice units.

For a graphical explanation of this problem, see section 4.4, which discusses a solution to a related problem for the electrophoretically-driven particle of chapter 8. For the squirmer, an approach based on the method of Noble and Torczynski [347] might prove useful.

5.2.3 Interaction between two squirmers

Now that we have confirmed that our LB implementation is capable of producing the correct flow around a squirmer, we check that a squirmer correctly reacts to the flow produced by another squirmer. This geometry is illustrated in figure 5.5. The results in this section are reproduced from reference 348. Here, we approximated the situation first considered by Ishikawa et al. [148], who positioned two squirmers facing opposite each other, separated by a distance of $12R$ and spaced apart laterally by varying distances d . They solved for the trajectories using BEM, which assumes an infinite fluid domain size and discretizes the squirmers' surfaces. In our LB calculations, we used a squirmer radius of $R = 9\Delta x$ and a cubic, periodic simulation domain with edge length $L = 250\Delta x$ to approximate the bulk calculation of reference 148.

Figure 5.6 shows the resulting trajectories and those of reference 148. There is good agreement and our trajectories are considerably smoother than those given by Ishikawa et al. [148]. Part of the deviations can be attributed to the use of periodic boundary conditions in our simulation [170], while Ishikawa et al. were able to perform their calculations in bulk. The interactions with the periodic images in this case cause the squirmers to move slightly closer than they would in bulk. The increased smoothness is mostly related to the advancement in computational performance since 2006 and not an intrinsic issue with BEM. It is worth noting that we have used a far coarser resolution for our squirmers than used by Ishikawa et al. because we also need to discretize the entire fluid volume, while BEM only discretizes the surface. The good match between the much finer BEM resolution and our LB results is promising for simulations at much higher squirmer volume fractions, where we can reasonably expect to be able to maintain our current resolution and thus keep roughly the same simulation speed.

5.2.4 Squirmer in a cylindrical channel

Now that we have determined the resolution required for an accurate simulation and checked that two squirmers interact with each other correctly, we can investigate systems where the near field plays a dominant role. LB does not make use of the method of reflections to capture the effect of solid/no-slip

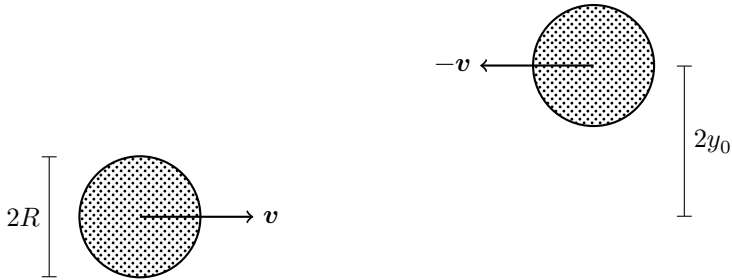


Figure 5.5: Geometry of the two passing squirmers of radius R with lateral separation $2y_0$ and initial propulsion direction \mathbf{v} .

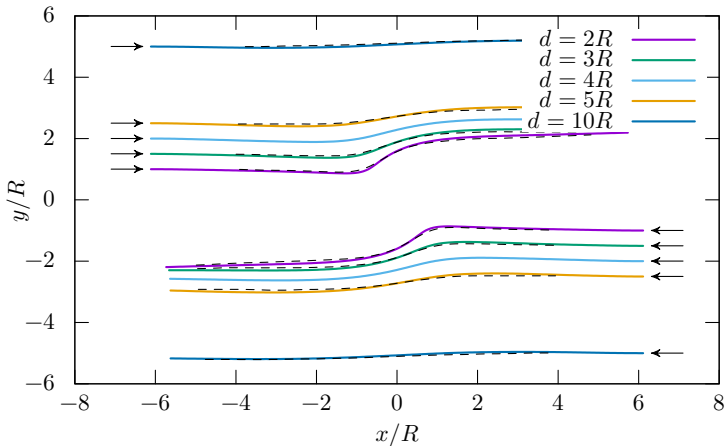


Figure 5.6: Trajectories of two squirmers with $\beta = 5$ passing each other. The initial configuration is specified by the initial lateral separation $d = 2y_0$ and the separation in the direction of their original orientation. The results of reference 148 are shown as dashed lines. Our LB simulations are performed for squirmers with $R = 9\Delta x$ in a periodic box of length $L = 250\Delta x$.

boundaries like in section 3.3 and therefore can accurately reproduce the near-field flow when squirmers approach obstacles closer than their diameter. Recall from section 5.1 that we do not include lubrication corrections, which would be necessary to accurately capture the flow between two objects that are spaced less than Δx apart. Keeping this in mind, we can now perform simulations where the near-field flow plays a role. Zhu et al. [153] study a neutral ($\beta = 0$) squirmer oscillating in a tube with circular diameter $D = 20R/3$ and length $L = 3\pi R$ with a periodic boundary condition only along its length, starting from different distances y_0 to the boundary and an initial orientation parallel to the symmetry axis. This geometry is illustrated in figure 5.7. The results in this section are reproduced from reference 348.

The trajectories we obtain are compared to the results from reference 153 in figure 5.8. Both the oscillation amplitude and the period match to within 3% of the literature value. The reorientation of the squirmer when it is near the wall is a near-field effect, so the agreement confirms that our LB method sufficiently captures it. Since Zhu et al. [153] use BEM with local mesh refinement [148, 224] when squirmer and wall are near contact, they capture near-field effects more accurately than LB does at the resolution we used. This explains the slight deviations in the trajectories of figure 5.8, but the good agreement confirms that the system is rather robust to these differences. To obtain equally good results in LB at manageable computational effort, one would need to resort to an adaptive grid resolution [321].

5.3 Summary

We have described in detail our implementation of a hydrodynamic squirmer model in an LB fluid dynamics solver, where we build upon a large body of literature on this topic [261, 304, 305]. We have confirmed in four scenarios that our LB squirmer implementation can accurately reproduce signature features of the squirmer model, including: (i) The analytic flow field around the squirmer, accounting for periodicity effects. (ii) The interaction between two squirmers, as originally obtained by Ishikawa et al. [148] using the BEM. (iii) The oscillation of a squirmer in a cylindrical tube as studied originally using BEM by Zhu et al. [153]. (iv) Section 6.4.5 will successfully make use of the same method to study the scattering and orbiting of a squirmer around a spherical obstacle.

Through our study we have also demonstrated that the LB squirmer implementation is sensitive to discretization artifacts, more so than has been reported for passive particles. Throughout the literature various values of the resolution of the squirmer are used. Here, we show that a refinement

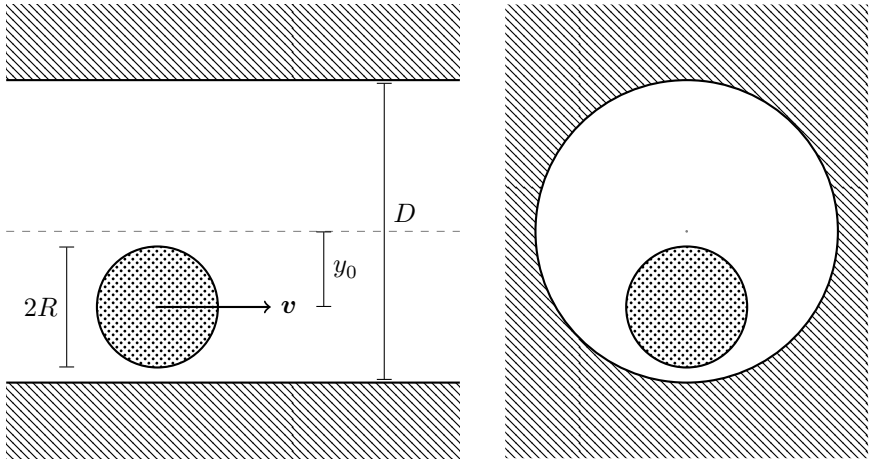


Figure 5.7: Geometry of the squirmer of radius R in the cylindrical channel of diameter D , viewed in cross-section (left) and along the channel (right). The squirmer's initial propulsion direction is \mathbf{v} and it starts off-centered by y_0 .

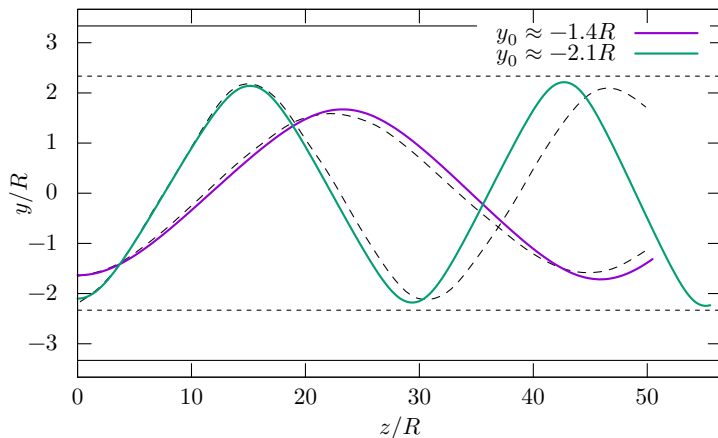


Figure 5.8: Trajectories of squirmers ($R = 9\Delta x$) with different initial displacements y_0 inside a tube of length $L = 3\pi R$ and circular diameter $D = 20R/3$, compared to the results of reference 153, which simulates the equivalent system using BEM. These are shown using black dashes. The dotted lines indicate the point of closest approach before the squirmer touches the boundary, which itself is marked using the lines at the top and bottom of the plot.

of at least 8 lattice cells for the radius of the squirmer is necessary to avoid numerical artifacts in the flow field. These artifacts are particularly pronounced in situations where there is persistent motion and may lead to severe numerical instabilities.

We have confirmed that LB is capable of accurately reproducing results obtained with other methods. Since LB offers several advantages over competing methods — such as particle coupling without re-meshing (unlike FEM and BEM), incompressibility (unlike MPCD), and correct near-field hydrodynamics (unlike SD) — it provides a useful tool for the hydrodynamic study of microswimmers.

We have made our LB squirmer implementation available within the open-source software `waLBerla` [9, 310], which will make it possible for anyone to simulate large-scale systems containing many squirmers and complex boundary conditions. In LB the computational effort depends only on the number of cells; the number of squirmers contributes very little to the overall simulation time. It should be noted that we have not incorporated lubrication corrections [162, 340] here, which will be a topic for further method development.

The only other freely-available implementation of squirmers in LB that we are aware of is in Ludwig [157, 337, 349]; however the one in `waLBerla` may be easier to extend for advanced problems such as chemical squirmers [154], uses one of the most efficient LB implementations [9, 310], and can make use of adaptive grid refinement [321] to reduce computational effort in systems with inhomogeneous particle concentrations.

6 Hydrodynamic mobility reversal of squirmers near flat and curved surfaces

An increasing body of experimental and theoretical work demonstrates that the proximity of surfaces has an important effect on the behavior of self-propelled particles. In biology, spermatozoa [90, 350, 351] and bacteria [70] can circle near a flat wall, which has been attributed to hydrodynamic interactions and the specifics of flagellar beating [32, 47, 352–357]. Artificial self-propelled particles, which can move through the catalytic decomposition of hydrogen peroxide [25, 26], i.e., chemical swimmers, also respond to the presence of a surface [111, 358–361]. In this case, there can be both a hydrodynamic [151, 163, 237, 238, 352, 362] and a chemical coupling to the surface [359, 361, 363–366], which themselves are intimately linked through the way they lead to self-propulsion [25, 26, 34, 35, 106, 107, 132, 367–371].

Experimentally, chemical swimmers are well known to be orientationally locked near a flat surface [359, 361]. This locking has been linked to specifics of the reaction mechanism and the local hydrodynamic interactions that it induces [359, 364]. Chemical swimmers may also follow the surface topology. For example, they interact with small variations of the substrate’s height [111, 361], as has been qualitatively described using simple theoretical model swimmers [361]. In addition, chemical patterning of the surface has been shown to significantly modify the mobility of a chemical swimmer [372–376]. These man-made swimmers can also follow strongly curved surfaces, even leading them to orbit around spherical obstacles [358, 360, 377].

The orbiting of swimmers has been studied extensively using hydrodynamic descriptions [163, 164, 378]. In the far field, the associated hydrodynamic problem is typically solved using the method-of-reflections approximation [238] and Faxén’s law [251, 252]. Spagnolie et al. [163] account for the leading-order hydrodynamic force-dipole moment in their analysis and find that there is a critical radius for orbiting. Only pusher swimmers — ones that have an extensile flow field — enter such a trajectory [163]; pullers on the other hand are trapped in a hovering state, wherein they point straight

into the surface. A similar far-field approach has been taken by Kurzthaler and Stone [362] to study the interaction of a squirmer with a corrugated planar surface. Method-of-reflections approximations have also been applied to chemical interactions to study the problem of a chemically-propelled swimmer at an obstacle [366, 379].

The methods of reflections is known to break down for small swimmer-obstacle separations [237]. In the lubrication regime, which captures the behavior for vanishing gap sizes, a swimmer's ability to follow a path along a planar wall has been examined [336, 339]. Specifically, Lintuvuori et al. [336] studied a squirmer, which is a simple model swimmer that accounts for finite-size contributions to the flow field. The results for a squirmer near a flat wall may be readily transferred to orbiting around objects with low curvature. Unfortunately, lubrication theory does not provide substantial insight other than for the hovering state, wherein the swimmer's direction of motion points into the obstacle and no tangential displacement occurs.

A combination of lubrication theory (zero separation, $d \ll R$) and far-field results (infinite separation, $d \gg R$) is often used in an attempt to bridge the gap between these two regimes without having to calculate the exact near-field hydrodynamics [164, 336, 339]. This approximation gives rise to steady orbiting pullers and oscillatory orbits for pushers [336], the latter of which are a result of a competition between the two regimes. The critical radius for orbiting will also be reduced by this interplay [164].

In the case of a flat wall, the intermediate regime has been resolved using the boundary element method (BEM) [152], as well as the lattice Boltzmann (LB) method [167, 336, 339], and multi-particle collision dynamics (MPCD) [380]. Ishimoto and Gaffney [152] observe that a puller squirmer moves stably along the wall, pointing slightly toward it. Lintuvuori et al. [336] reproduce the behaviors found in their analytic predictions, which combine the far field and lubrication regimes. However, this level of analysis has not yet been performed for orbiting.

In this chapter, we examine in-depth the effect of the surface curvature on the hydrodynamic orbiting of a squirmer and take the limit to the behavior near a flat surface. To efficiently explore parameter space, we employ far-field approximations, as well as the LB method [261, 262, 265, 304] that accurately resolves the near-field flows. Using this approach we reproduce the three behaviors reported in literature: orbiting around the sphere/sliding along the wall, scattering, and hovering [152, 163, 164, 336]. Surprisingly, we find a second type of orbiting in both our hydrodynamic approaches where the swimmer effectively moves in the direction opposite to its bulk motion. Backward orbiting appears for strong pusher squirmers and supersedes the forward orbiting predicted for a point-like dipole swimmer using identical

hydrodynamic parameters [163]. This behavior can be shown to result from fluid recirculation in the gap between the squirmer and the surface leading to strong forces opposing forward motion. In the limit of a flat wall, we similarly find backward sliding.

The behavior of a squirmer near an obstacle is controlled by the strength and sign of its dipole moment and is also sensitive to the curvature of the obstacle. Scattering takes place for sufficiently neutral squirmers, which only have a source dipole flow field in bulk, while hovering and orbiting require the presence of a force-dipole contribution to the flow field. We find that the minimal force-dipole moment that leads to orbiting scales quadratically with the curvature for puller squirmers. Backward orbiting/sliding and hovering can be suppressed by introducing short-ranged repulsions between the squirmer and the surface. However, backward motion supplants forward motion even for imposed gap sizes of one tenth of the squirmer radius.

We will focus on hydrodynamic interactions here, but our results are also of interest to the ongoing study of motion of chemical swimmers near surfaces. We will show that it is possible to reverse the mobility of a swimmer by modifying its hydrodynamic force-dipole moment without changing the bulk swim velocity. This strong response to the presence of a surface underpins the need for more experiments performed in bulk in order to isolate the effect of environmental changes on swimmer mobility. Our predictions provide a stepping stone toward understanding the richer behaviors encountered when introducing coupling between solute gradients and hydrodynamic flow fields [154–156].

Before proceeding further, we should note that after the work presented in this chapter was completed, Chaithanya and Thampi [167] have also applied LB to obtain the trajectory of squirmers at a spherical obstacles and inside spherical cavities. They find the same classes of trajectories and further quantify them in terms of retention time, average separation between squirmer and obstacle/cavity, tangential velocity, and scattering angle.

The remainder of this chapter is laid out as follows: Section 6.1 summarizes the squirmer model and describes the problem considered. We also explain how the hydrodynamics are solved to obtain trajectories of the squirmers. In section 6.2, we give a characterization of these trajectories, before using lubrication theory in section 6.3 to further rationalize the observations. Our main results are presented in section 6.4, wherein we discuss the influence of obstacle size, short-range repulsion, and higher-order hydrodynamic moments. We conclude and present an outlook in section 6.5.

6.1 Model and methods

In this chapter, we study the interaction of a squirmer of radius R_S with a spherical obstacle of radius R (or a flat wall, corresponding to $R \rightarrow \infty$) as illustrated in figure 6.1. The squirmer is free to move and its position is $\mathbf{r}_S = (x, y)^\top$ with the superscript denoting transposition, while the obstacle is fixed at the origin. Figure 6.2 introduces the angles and distances used to describe the squirmer's position and orientation: φ is the angle between the squirmer's orientation $\hat{\mathbf{e}}$ and the tangent plane at the closest point on the obstacle's surface; α is the angle between the direction of the squirmer's velocity \mathbf{v} and the tangent plane; and h is the size of the gap between the squirmer's and the obstacle's surfaces. Initially, the squirmer is located far away from the obstacle — we effectively take the limit to infinity — at different distances y_0 from the x -axis. $\hat{\mathbf{e}}$ points along the x -axis, corresponding to $\varphi_0 = \arcsin(y_0/R_S) - 90^\circ$. For the case of the flat wall, the squirmer starts at a large distance above the wall and oriented at different φ_0 against it. Subscript zeros ($_0$) here refer to the respective variable at time $t = 0$.

In chapter 3, we described the pieces needed for a simple far-field method that can be used to determine how the model's parameters — like dipolarity β , angle of incidence φ_0 , and size ratio R/R_S — affect the squirmer's ability to enter into an orbit around or be scattered at the obstacle. In the present chapter, we take the squirmer model (section 2.4), perform a hydrodynamic multipole decomposition (section 3.2), introduce the method of reflections to account for the obstacle's presence (section 3.3), use Faxén's law to calculate the response of the squirmer to fluid flow (section 3.4), and numerically integrate the trajectory (section 3.5).

Neither the far-field calculations of sections 3.1 to 3.5 nor the lubrication considerations of section 6.3 are able to accurately capture the intermediate near-field regime. The squirmer enters this regime when it comes close to the obstacle, and we therefore resort to the LB method [261, 262] to test our far-field predictions. As a Navier-Stokes solver, LB excels at coupled fluid-particle simulations and flows in complex geometries [304]. MPCD [149, 381] would have been similarly suitable. We use the same LB method and implementation as in chapter 5 to determine the influence of near-field effects, the details of which are given in section 5.1. While LB correctly incorporates near-field hydrodynamic effects, it is computationally much more expensive than the far-field-only model. The trade-off of using a far-field method for a problem that is potentially near-field-dependent will be justified by section 6.4.3, where we compare some results to ones obtained with the near-field-capable method.

The LB calculations in section 6.4.5 use a resolution of eight lattice cells

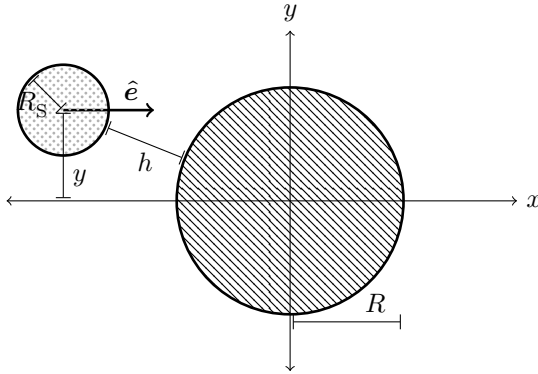


Figure 6.1: The geometry of the system investigated: The obstacle of radius R is located at the origin, while the squirmer of radius R_S and orientation \hat{e} is at $(x, y)^\top$. The size of the gap between the two objects is h . For the case of the flat wall ($R \rightarrow \infty$), y loses its meaning, but the other quantities remain well-defined.

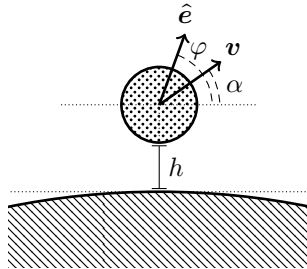


Figure 6.2: The angles φ and α are between the tangent plane at the closest point on the obstacle's surface and the squirmer's orientation \hat{e} and direction of motion \mathbf{v} , respectively. The length h is the size of the gap between squirmer and obstacle.

per squirmer radius ($R_S = 8\Delta x$) as per the resolution requirement identified in section 5.2.2. This allows for accurate capturing of flow fields down to gaps of $h \gtrsim R_S/8$. The calculations further employ a periodic calculation domain of size $L \times L \times H$ with $L = \max(5.5R, 160\Delta x)$ and $H = \max(2.6R, 80\Delta x)$. The viscosity is set to $\eta = 0.8\rho\Delta x^2/\Delta t$. The squirmer is initially located at $(\max(0.3R, 9\Delta x), y_0, H/2)^\top$, while the obstacle is at $(L/2, L/2, H/2)^\top$.

6.2 Characterization

We start our analysis of the behavior of a squirmer near a spherical obstacle using the far-field hydrodynamic theory of sections 3.3 to 3.5. To determine the different behaviors, we vary the three free parameters in the model: the relative obstacle size R/R_S , the squirmer dipolarity β , and the initial off-axis position y_0 (or equivalently, the initial incidence angle φ_0). We pick $R/R_S \in \{1, 2, 5, 10, 20, 50, 100, 200, 500\}$ and $y_0 \in [0, 10R]$ spaced roughly exponentially, $\beta \in [-30, 30]$ spaced linearly, and $r_{\text{cut}}/R_S \in \{0, 0.01, 0.1, 0.2\}$.

6.2.1 Trajectories

Inspecting the resulting trajectories reveals four general classes of behavior, examples of which are shown in figure 6.3a-d. (a) corresponds to a forward orbit; (b) is a scattering trajectory; in (c) the squirmer hovers above obstacle's surface; (d) is a backward orbit. Figure 6.3e shows the size of the gap between the squirmer and the obstacle over time. Here, one can see that a decaying oscillation is modulated onto the forward orbit, while the oscillation of the backward orbit is quite stable. These oscillations are reminiscent of those observed in references 152 and 336. Figure 6.3fg shows the direction of the squirmer's orientation vector $\hat{\mathbf{e}}$ and velocity vector \mathbf{v} , respectively.

To identify the origin of the three different kinds of bound trajectories more clearly, these angles are illustrated in figure 6.4: In a forward orbit, $\hat{\mathbf{e}}$ and \mathbf{v} are roughly parallel ($\hat{\mathbf{e}} \cdot \mathbf{v} > 0$), while in a backward orbit they are antiparallel ($\hat{\mathbf{e}} \cdot \mathbf{v} < 0$). Hovering is a case where \mathbf{v} points almost straight into the obstacle, so the squirmer is stuck in place. A squirmer is considered hovering when it moves at a speed of $v < v_0/100$ or has $|\alpha - \varphi| < 3^\circ$. The precise choice of these limits may appear arbitrary, but we found that most orbiting trajectories exhibit angles that either much larger or much smaller. If the trajectory is oscillatory, we average the angle over at least one orbit.

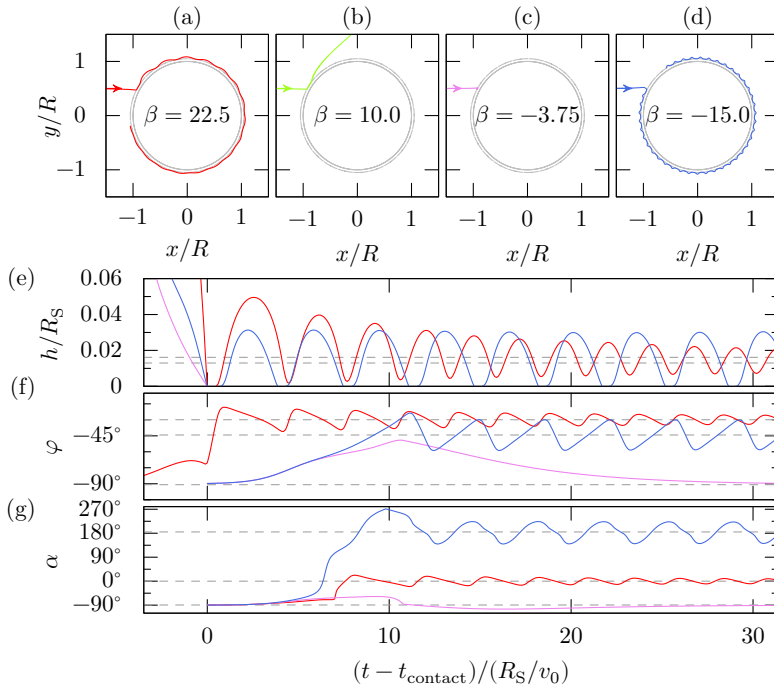


Figure 6.3: (a-d) Trajectories for different β , leading to a forward orbit (red, $\beta = 22.5$), scattering (green, $\beta = 10$), a hovering state (violet, $\beta = -3.75$) and a backward orbit (blue, $\beta = -15$). The solid gray circle indicates the position of the obstacle, while the dashed gray circle indicates the closest possible approach. (e) The surface-to-surface gap size h/R_S between squirmer and obstacle over time. The dashed gray lines indicate the long-time mean gap size. (f) The angle φ between the obstacle's surface and the squirmer's orientation vector over time. (g) The angle α between the obstacle's surface and the squirmer's direction of motion over time. The dashed gray lines indicate the long-time mean angles. All calculations used $R = 20R_S$, $y_0 = 0.5R$, $r_{\text{cut}} = 0$. Time t_{contact} is the time at which the squirmer first made contact ($h = r_{\text{cut}}$) with the obstacle.

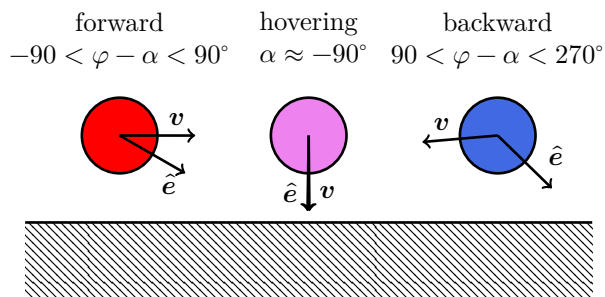


Figure 6.4: The bound states correspond to characteristic values of the angles introduced in figure 6.2. Forward orbiting/sliding corresponds to \mathbf{v} and $\hat{\mathbf{e}}$ approximately parallel, backward orbiting/sliding to \mathbf{v} and $\hat{\mathbf{e}}$ approximately antiparallel, and hovering is \mathbf{v} pointing approximately perpendicularly into the obstacle. The angles illustrated here correspond to the dashed lines in figure 6.3fg.

Lastly, we should note that all of the above classes of trajectories are also obtained in our LB calculations per chapter 5. However, the specific parameters for which these behaviors are observed are different. We will come back to this in section 6.4.5.

6.2.2 Interpreting the bound states

We examine the flow fields in figure 6.5a-c to identify the hydrodynamic reason behind the observed bound states. Our far-field analysis relies on Faxén’s laws, equations 3.20 and 3.21, to implicitly carry out the surface integrals that specify the forces and torques that move and reorient the squirmer in proximity to the boundary. However, we will argue here that applying the intuitive arguments encountered in lubrication theory, see section 6.3, gives insight into the origin of the various bound states. Lubrication theory states that the dynamics of the squirmer is governed by the viscous dissipation taking place at the point of closest approach [336]. In the far field, one can expect a dominant contribution to the surface integral to also come from this point, especially for small separation.

Let us now consider the flow generated by the squirmer at the location of the boundary, without accounting for the boundary’s presence. Thus, we are considering the ‘unmodified’ (bulk) flow field of the squirmer, evaluated at the point of closest approach. The ‘unmodified’ fluid velocity at this point is provided in figure 6.6, which decomposes it into components parallel and perpendicular to the boundary. This figure also shows the separate contributions of the various hydrodynamic modes to the ‘unmodified’ flow field around the squirmer. Clearly, the source quadrupole moment gives rise to the strongest parallel flow in this scenario. The perpendicular components of the force dipole and source quadrupole essentially balance, such that ‘unmodified’ flow ‘into’ the wall is dominated by the source dipole.

The perpendicular component is associated with motion toward/away from the boundary and is thus not of interest here. Focusing on the boundary-parallel contribution and dominant flow of the source quadrupole, we obtain ‘unmodified’ flow fields due to this term as depicted in figure 6.5d-f. Zoom-ins on the region of smallest separation are provided in figure 6.5g-i, where we should again stress that we only indicate the position of the boundary, but do not account for it in drawing the flow lines. Clearly, the zero-velocity boundary condition is not satisfied. To achieve this condition at the point of closest approach, we can assign a velocity to the swimmer that is equal in magnitude, but oppositely directed. Hence, a forward-moving (figure 6.5adg), hovering (figure 6.5beh), and backward-moving (figure 6.5cfi) state are expected.

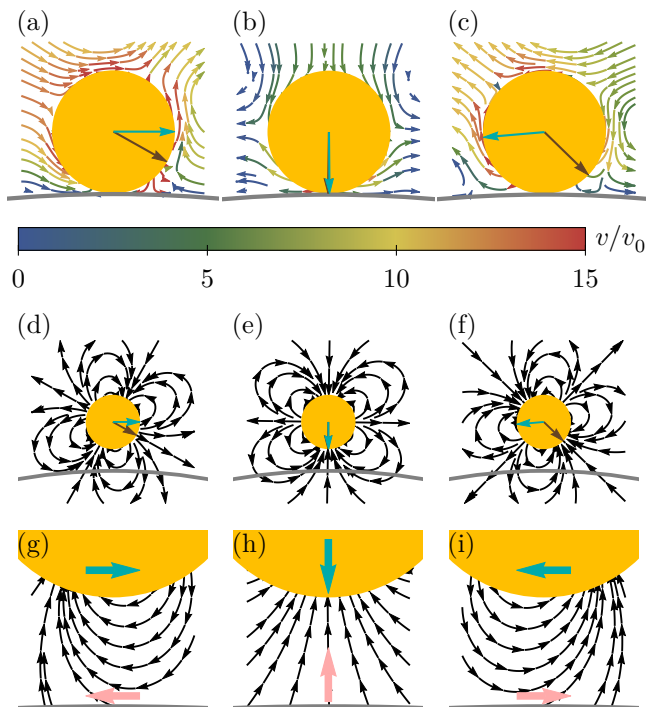


Figure 6.5: The flow around the squirmer in the (a) forward (puller), (b) hovering (pusher), and (c) backward (pusher) configurations of figure 6.4. The cyan arrow indicates \mathbf{v} , while the brown one marks $\hat{\mathbf{e}}$. The gray line indicates the position of the no-slip wall. (d-f) The same configurations, but showing the bulk flow due to the source quadrupole moment only, where we have not accounted for the boundary condition. (g-i) Zoom-ins on the gap in (d-f), showing that the source quadrupole leads to a flow at the surface (closest point) corresponding to the pink arrow. The closest point dominates the dynamics, and to satisfy the boundary condition, the swimmer effectively moves with \mathbf{v} as indicated by the cyan arrow.

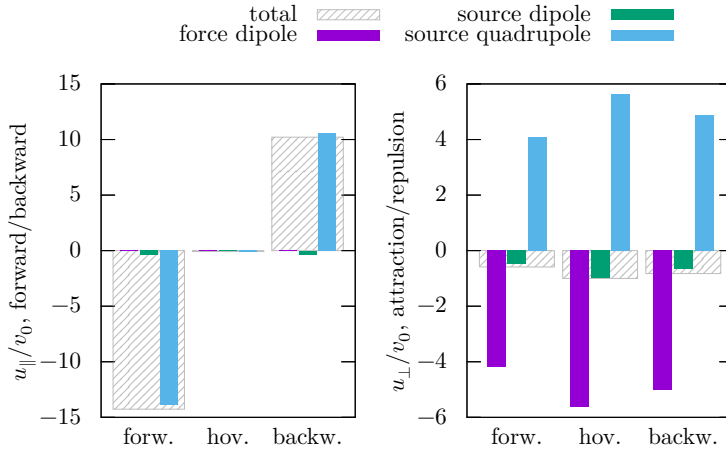


Figure 6.6: Bar graph showing the relative contributions of the hydrodynamic modes to the motion of the squirmer, as measured by the bulk flow generated at the point closest to the obstacle (not accounting for this boundary, as per the limitations discussed in section 3.3.2). The parallel \mathbf{u}_{\parallel} and perpendicular \mathbf{u}_{\perp} components of this flow velocity — corresponding to the configurations given in figure 6.3 — are provided in the left- and right-hand panels, respectively. The colored bars indicate the contributions of the three hydrodynamic modes, while the net effect is provided by the shaded area.

The above argument relies on the strong reduction that the dynamics of the squirmer is sufficiently dominated by the point of closest approach, which is only true in the lubrication limit. In addition, we estimate the contribution there through the flow field around a squirmer in bulk fluid. The above explanation should thus be seen as a means to develop some intuition for the behavior of the squirmer, but not as a full proof. Section 6.4.3 will show that this intuition is, however, accurate, as removal of the source quadrupole term strongly alters the dynamics. Similarly, increasing the separation between the squirmer and boundary sufficiently for longer-ranged hydrodynamic modes to dominate also eliminates the backward-orbiting state. This will be done in section 6.4.2 by varying the short-range interaction potential.

6.3 Stability analysis using lubrication theory

The flow in a small gap between two objects is formally the regime of lubrication theory [148, 382, 383]. It assumes that the flow is dominated by the interaction between those points where the surfaces are closest. For a squirmer near a flat wall, Lintuvuori et al. [336] give

$$\frac{d\varphi}{dt} = \omega = \frac{3v_0}{2R_S} \cos \varphi (1 - \beta \sin \varphi) \hat{e}_\varphi + \mathcal{O}\left(\frac{1}{\log \frac{h}{R_S}}\right) \quad (6.1)$$

$$v = 0 + \mathcal{O}\left(\frac{1}{\log \frac{h}{R_S}}\right) \quad (6.2)$$

where \hat{e}_φ is the angular unit vector in our angle convention. This means that lateral translation vanishes but rotation remains possible.

Solving the above equation for the stationary state $\omega = 0$ yields one stable solution, $\varphi = -90^\circ$ at $\beta < -1$. This corresponds to the hovering state of a pusher. However, the interplay between the lubrication regime and far-field reorientation can lead to orbiting states of both the puller and pusher [336].

Note that lubrication theory is an extreme limit where far-field hydrodynamics become irrelevant and only one term at infinitely close separation remains of the near-field flow. The typical gap sizes h we find in this chapter fall in between those where far-field hydrodynamics is applicable ($h \gtrsim R_S$) and those where lubrication theory is valid ($\log(h/R_S) \ll -1$). This necessitates verification of such predictions using methods that deal with the intermediate regime, the near field.

6.4 Results

We are now able to use the observations of section 6.2 to classify trajectories into distinct categories corresponding to the four archetypal trajectories of figure 6.3. This allows us to construct state diagrams in parameter space using the efficient far-field method of sections 3.3 to 3.5. To produce two-dimensional β - y_0 diagrams, r_{cut} and R/R_S are chosen to be constant values. From the data set discussed in the previous section, one can already obtain coarse state diagrams by performing a Voronoi construction [384] to identify polygonal regions in the two-dimensional parameter space. Each of these regions is associated with a (y_0, β) data point and contains all points that are closer to this data point than to any other data point. The entire region is then filled with the color assigned to the behavior observed for the respective data point. We now refine the coarse diagram: One can identify polygon vertices that connect polygons of different color (i.e., that lie on the edge of a state's region). A new calculation is then started at each of the identified vertices. This procedure is repeated until a sufficiently smooth diagram is obtained.

The topology of these state diagrams is roughly as follows. At $y_0 = 0$, only hovering states can be found because the symmetry remains unbroken. For nonzero y_0 , the strongest pushers follow oscillating backward orbits. Decreasing the squirmer strength successively leads to hovering, a forward orbit with decaying oscillation, and another hovering state, before transitioning to scattering near $\beta = 0$. Pullers of sufficient strength again enter into forward orbits with decaying oscillation. Another region of forward orbits is found for strong pushers near $y_0 = R_S$, but with a persistent oscillation. In the rest of this section, we will discuss various influences on the state diagram: (1) the obstacle size, (2) the short-range repulsion, (3) the different hydrodynamic moments, (4) the sign of the curvature, and (5) near-field flow.

6.4.1 Effects of obstacle size

State diagrams for a representative selection of obstacle sizes R and constant $r_{\text{cut}} = 0$ are shown in figure 6.7. At the smallest obstacle, $R = R_S$, one observes that strong pushers ($\beta < 0$) enter into forward orbits. The critical value of β below which the squirmer is captured is constant below $y_0 \approx 1.5R$ and decreases beyond this point. Between the orbiting and the scattering states lies a hovering state that also extends to $y_0 \approx 1.5R$.

As R increases, one first observes that the y_0 required to capture the squirmer decreases. Simultaneously, the forward orbits are mostly replaced

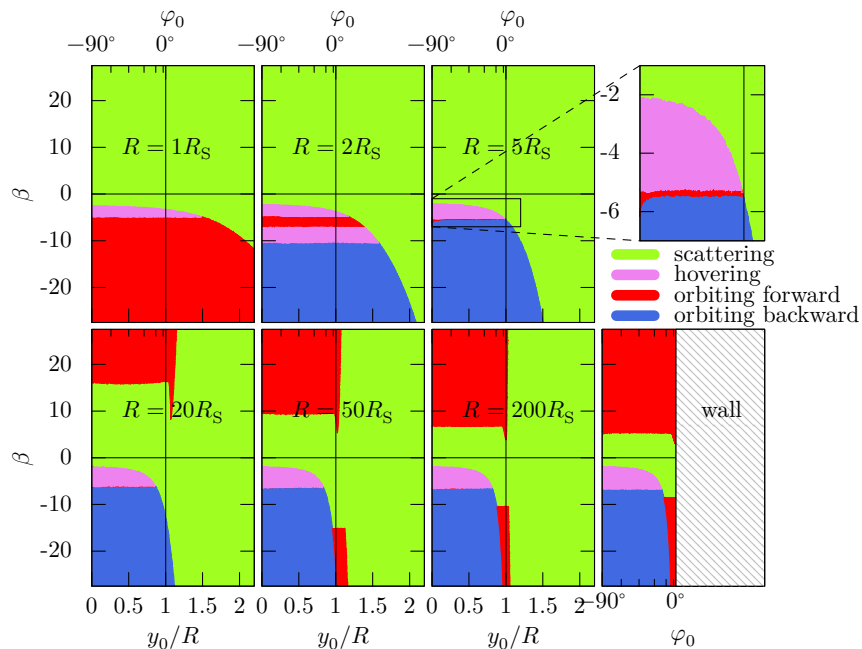


Figure 6.7: The influence of obstacle-squirmer size ratio: State diagrams indicating the way the squirmer behavior depends on dipolarity β and initial position y_0 (or equivalently, initial orientation φ_0) with different R and constant $r_{\text{cut}} = 0$. Forward orbits are red, backward orbits blue, hovering is violet and scattering is green, as indicated in the legend and used throughout. The former three (bound) states correspond to specific relative angles of the squirmer's orientation and motion, which are illustrated in figure 6.4.

with backward orbits, though a small region of forward orbiting remains, and for $R \approx 2R_S$ a second hovering region appears, between the backward orbits and the hovering states (see inset in figure 6.7). This region of forward orbits quickly shrinks as R increases and corresponds to a set of edge-case trajectories, e.g., ones where the squirmer moves just slightly faster than the criterion we picked to delimit orbiting from hovering.

Further increase of R introduces a forward orbiting state for strong pullers ($\beta > 0$); the critical β that separates these forward orbits from scattering is independent of y_0 for $y_0 < R$ and decreases as R increases. Furthermore, at $y_0 \approx R$, the forward orbiting state extends significantly into the scattering state's region. This peninsula of red in figure 6.7 appears because the squirmer approaches the obstacle in such a way that no hydrodynamic reorientation is required to swing into orbit.

Finally, one observes a second forward orbiting state that develops for strong pushers. This one is near $y_0 \approx R$, unlike the other states, which can be entered at $y_0 \approx 0$. At $R = 200$, the state diagram is already almost indistinguishable from the case for a flat wall ($R \rightarrow \infty$). In the latter case, y_0 becomes meaningless and is replaced by φ_0 , which is a well-defined quantity even for finite radii, but cannot describe $y_0 > R$.

In figure 6.8, we have extracted the position of the critical values of β for the transitions observed in figure 6.7. The transitions from scattering to hovering and from hovering to backward orbiting are nearly independent of β . The transition between scattering and forward orbiting happens at $\beta \propto R^{-2}$ for pullers at $y_0 \approx 0$ and at $\beta \propto -R^{-1}$ for pushers at $y_0 \approx R$. This scaling disagrees with Spagnolie et al.'s prediction [163] for the pusher, $\beta \propto -R^{-1/2}$, but as discussed in section 6.4.3, the deviation is fully explained by a modeling difference.

Figure 6.11ab shows the swimmer's speed $\mathbf{v} \cdot \hat{\mathbf{e}}_\varphi$ tangential to the obstacle's surface for the different size ratios and dipolarities. Forward orbits correspond to $\mathbf{v} \cdot \hat{\mathbf{e}}_\varphi > 0$ and backwards orbits to $\mathbf{v} \cdot \hat{\mathbf{e}}_\varphi < 0$. The squirmer increases its speed with increasing $|\beta|$ at constant R_S and speeds up slightly with increasing R_S at constant β . The critical dipolarity corresponding to a specific size ratio as displayed in Figure 6.7 is also shown, with the velocity of an unbound trajectory drawn as $v = v_0$ and the velocity of a hovering state $v \approx 0$. Here it is evident that the speed of the squirmer does not change when making a state transition, e.g. by varying β from slightly above to slightly below its critical value. This is in line with the experimental findings of reference 127, where a catalytic swimmer orbits a cylindrical post at almost the same speed as it swims in bulk.

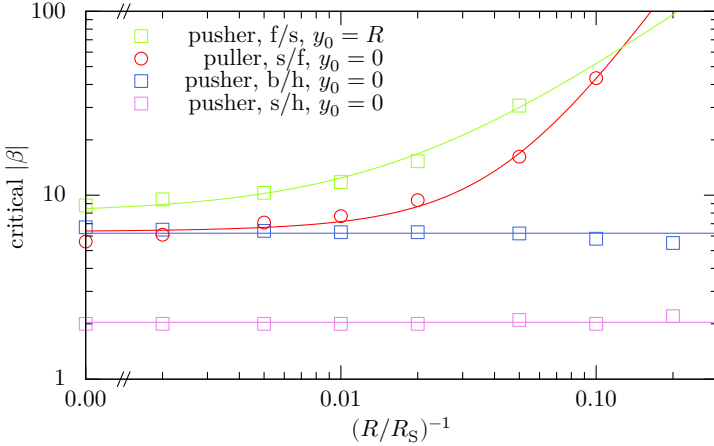


Figure 6.8: From figure 6.7 we can extract critical values of β that mark the transition from one state to another. Blue is the transition between backward orbiting (b) and hovering (h), violet is the transition between hovering and scattering (s), and red is the transition between hovering and forward orbiting (f), all near $y_0 = 0$. Green is the transition from forward orbiting to scattering near $y_0 = R$. The error bars are comparable to the symbol size and result from the finite size of the regions produced by the Voronoi construction and also from the slightly diffuse transition regions (see the inset of figure 6.7).

6.4.2 Effects of short-range repulsion

Thus far, we have assumed $r_{\text{cut}} = 0$, letting the squirmer and obstacle touch. However, realistic swimmers typically repel each other and from obstacles at short distances [336], e.g., due to electrostatics [237], phoretic interactions [156], or near-field hydrodynamics [237]. To study this effect, we pick $R = 20R_S$, where the state diagram contains all the features seen at other obstacle radii. We then construct iteratively refined Voronoi diagrams for $r_{\text{cut}}/R_S \in \{0, 0.01, 0.1, 0.2\}$ in figure 6.9.

Making the step from $r_{\text{cut}} = 0$ to $r_{\text{cut}} = 0.01R_S$ introduces an additional length scale into the problem. Despite the small absolute magnitude of this r_{cut} , this leads to the appearance of the transition from scattering to a forward orbit for pushers near $y_0 = R$. While one cannot see this forward orbiting state in the diagram for $r_{\text{cut}} = 0$, it is expected there at $\beta \approx -40$ per figure 6.8 and visible in figure 6.7 for larger R . Increasing r_{cut} further moves both transitions between scattering and forward orbits to smaller $|\beta|$. At $r_{\text{cut}} = 0.1R_S$, the hovering state has vanished completely. At $r_{\text{cut}} = 0.2R_S$, the backward orbiting state has vanished too and is replaced by forward orbits, which have now extended to smaller y_0 .

The disappearance of the hovering state at relatively moderate short-range repulsion is again in line with our attribution of the observations to the quadrupole term, which at small β can only dominate for the smallest gap sizes. Even $r_{\text{cut}} = 0.2R_S$ is sometimes a realistic model for short-range repulsion, for example for chemical nanoswimmers with extended electric double layers [34, 385]. This could explain why backward orbits are not encountered more commonly in experiment and theory.

6.4.3 Effects of higher-order hydrodynamic modes

In the previous section, we have already observed that backward orbits and hovering are very much dependent on near-field interactions. This even goes to the extent that backward orbits are completely suppressed if squirmer and obstacle are kept sufficiently far apart. The results suggest that one of the higher hydrodynamic modes in equation 2.45 causes this behavior, since they dominate the flow only on short distances. We perform two additional far-field calculations to quantify this effect: (i) one that drops the source quadrupole from equations 3.10, 3.17 and 3.18 but is otherwise identical to the method used for section 6.4.1, and (ii) one that furthermore drops the squirmer's source dipole, leaving only the force dipole flow and moving the squirmer directly via v_0 .

Again, we pick $R = 20R_S$ and $r_{\text{cut}} = 0$ and obtain the state diagram in

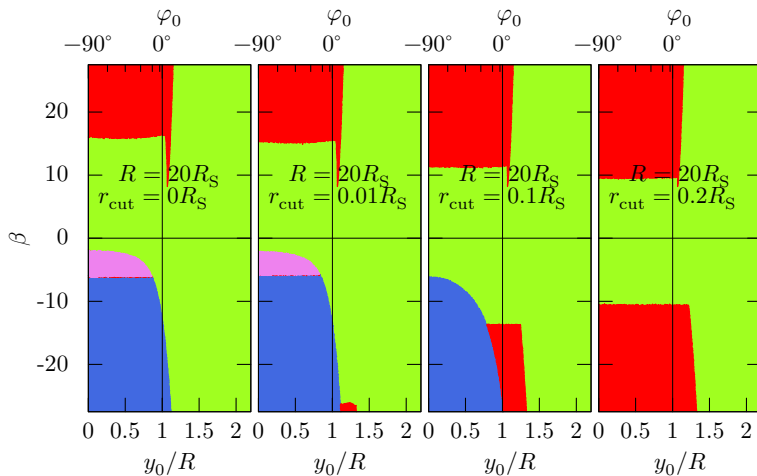


Figure 6.9: The influence of non-hydrodynamic interactions: State diagrams of the squirmer-obstacle interaction with color coding as in figure 6.7. The dipolarity β and initial position y_0 (or equivalently, initial orientation φ_0) are varied at constant $R = 20R_S$. From left to right we increase the short-range repulsion, $r_{\text{cut}}/R_S = 0, 0.01, 0.1,$ and 0.2 .

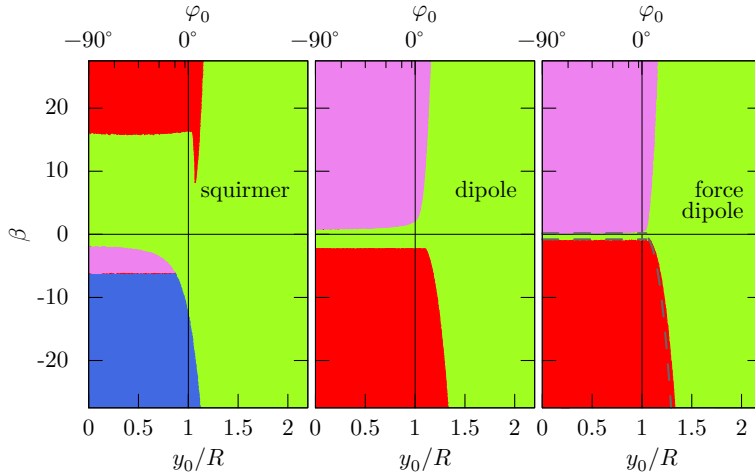


Figure 6.10: The influence of higher-order hydrodynamic moments: State diagrams of the squirmer-obstacle interaction with color coding as in figure 6.7. The obstacle radius is maintained at $R = 20R_S$, while the dipolarity β and initial position y_0 (or equivalently, initial orientation φ_0) are varied. From left to right, different hydrodynamic models are considered: squirmer, force and source dipole, and force dipole. The gray dashed lines in the right panel indicate the position of the transition as predicted by reference 163.

figure 6.10. One can see that the lack of a quadrupole term replaces the backward orbits and hovering states with forward orbits. It also converts the forward orbits into a hovering state down to much smaller β . Further dropping the source dipole allows for direct comparison with Spagnolie et al. [163], who predict the position of the transition: They suggest that pushers orbit for $\beta < -\sqrt{1024R_S/81R}$ as long as $y_0 < 0.86\beta^{2/5}(R/R_S)^{1/5} + R/R_S$, while they see pullers hovering for $\beta > 32R_S/9R$. We reproduce these predictions quite well as seen in figure 6.10. The remaining deviation is consistent with reference 163, where the critical $|\beta|$ is found to be slightly larger than predicted. Furthermore there is a slight difference in modeling, namely that Spagnolie et al. do not include the swimmer's finite R_S in equation 3.20. We do not show a separate state diagram for a swimmer with only a source dipole since this case simply corresponds to $\beta = 0$ for a squirmer or a dipole swimmer, where only scattering is observed.

Figure 6.11c-f shows the tangential speed of the two types of dipole swimmers. The effects of dipolarity and size ratio are less pronounced than for the squirmer: the pullers' only bound states are hovering, where $v \approx 0$ is observed, and the pushers' only bound states are forward orbits. The dipole swimmer speeds up slightly with increasing $|\beta|$ at constant R_S and slows down with increasing R_S at constant β . The latter is the opposite of the behavior seen for the squirmer. The force dipole swimmer slows down with increasing β , which is in opposition to both the squirmer and the dipole, but happens to an even lesser extent than for the dipole. Reference 127 observes a spherical, pusher-type, catalytic swimmer at a cylindrical post in experiment and finds the velocity independent of post diameter. This is consistent with figure 6.11 under the assumption that there is no quadrupolar contribution to the catalytic swimmer. The tangential speeds also align with the relative contributions of the hydrodynamic multipoles in figure 6.6: the force dipole is the weakest propellant at the obstacle, followed by the source dipole, and the source quadrupole. The source quadrupole's contribution is the only one that switches sign, so only the squirmer can exhibit backward motion.

6.4.4 Swimming inside a cavity

We can shed further light on the role of curvature by flipping its sign. Section 6.4.1's study of a squirmer near a spherical obstacle corresponds to swimming at a positively-curved surface, whereas swimming inside a spherical cavity corresponds to a swimming at a negatively-curved surface. State diagrams for a representative selection of cavity sizes R and constant $r_{\text{cut}} = 0$ are shown in figure 6.12. Note that forward orbits can no longer be

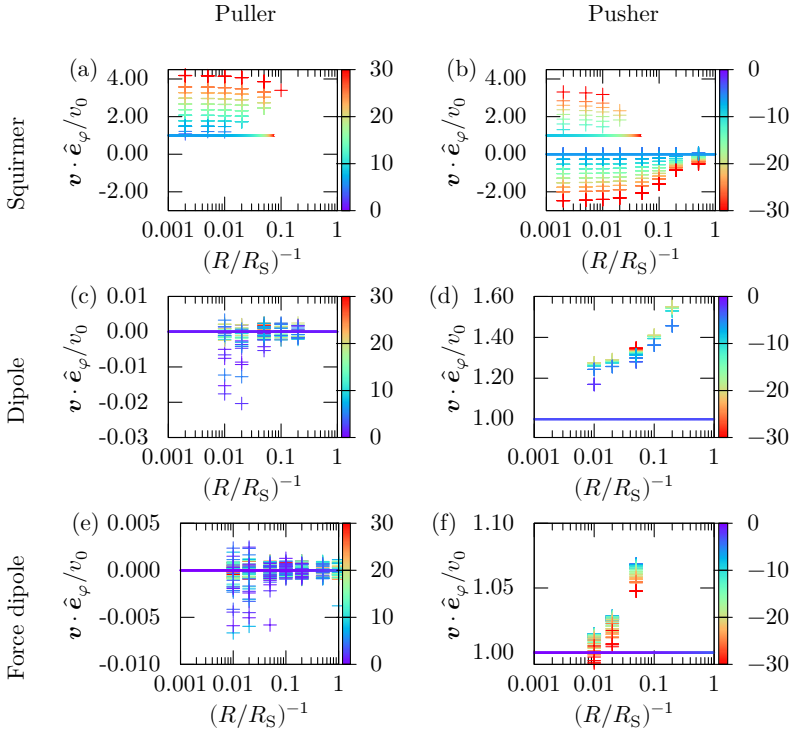


Figure 6.11: The influence of obstacle size and dipolarity on the velocity of the (ab) squirmer, (cd) force and source dipole, and (ef) force dipole: the average speed tangential to the obstacle’s surface for bound states is shown, where the colors correspond to the dipolarity β . The forward orbits have $\mathbf{v} \cdot \hat{\mathbf{e}}_\varphi > 0$, backward orbits < 0 , and hovering ≈ 0 . The horizontal lines indicate the critical values for state transitions from figure 6.8 for the squirmer and the corresponding quantities for the other swimmers.

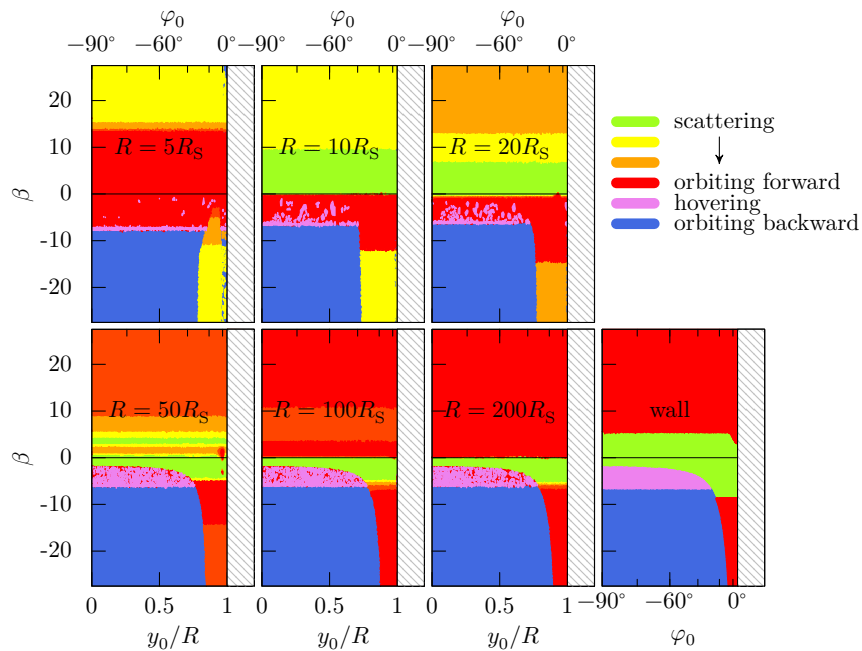


Figure 6.12: The influence of obstacle-squirmers size ratio on swimming inside a spherical cavity: State diagrams with β , y_0 (or φ_0), and R varied in the same way as in figure 6.7. The spectrum of states from scattering to forward orbits is represented by the colors green, yellow, orange, and red (with an increasing gap size oscillation amplitude in this order), while backward orbits are blue and hovering is violet.

fully distinguished from scattering events: a squirmer that leaves its bound state will move in a straight line only until it reaches the cavity surface again, where it has another chance to enter a bound state. To classify this spectrum of states, we consider the amplitude of the relative gap size h/R over time. $h/R \approx 0$ is expected to correspond to the forward orbits, and we introduce additional colors in the state diagram that each correspond to $0.1h/R$ increments.

At the greatest cavity size, the result for the flat wall from figure 6.7 is largely reproduced: Sufficiently strong pushers enter into backward orbits unless they approach nearly parallel to the surface, in which case they enter into a forward orbit. With decreasing strength, the transition region of hovering and a scattering region is recovered. Orbits are found for a wider range of parameters for the cavity than for the obstacle due to a self-stabilization effect discussed in the next paragraph. For pullers, forward orbiting is found unconditionally, while in the case of the flat wall $\beta \gtrsim 6$ was required to enter into an orbit. The transition region of increasing gap size oscillations is small enough to be barely visible in the state diagram. As R is decreased, the critical β for pushers to enter into forward orbits near $y_0 \approx R$ increases (even crossing the $\beta = 0$ line for the smallest cavity) and, once it has surpassed the critical β between hovering and backward orbiting near $y_0 \approx 0$, it becomes independent of y_0 . Eventually, a lower critical β develops for the pusher below which the orbits become increasingly oscillatory. Simultaneously, the hovering state becomes increasingly diffuse and indistinguishable from slow forward orbits. A critical β below which pullers cannot orbit forward appears for $R \lesssim 50R_S$ and increases with increasing curvature. At the same time, the transition region of oscillatory forward orbits (between the forward orbiting state and the scattering state) becomes more prominent.

The expansion of the regions where forward orbits are found inside the spherical cavity (figure 6.12) compared to outside the spherical obstacle (figure 6.7) can be explained by a self-stabilization effect: At the obstacle, any perturbation that takes the swimmer off its bound trajectory will cause the swimmer to move away. Inside the cavity, however, the swimmer will eventually encounter the surface again after swimming in a straight line. In this sense, the flat wall behaves similar to the obstacle and not the cavity as there is no chance for another encounter with the wall after a sufficiently strong perturbation. The self-stabilization effect corresponds to only a slight increase in gap size oscillation amplitude, so it is not visible in the color scheme of figure 6.12.

The dependency on higher-order hydrodynamic moments that we investigated for a spherical obstacle in section 6.4.3 can also be studied inside

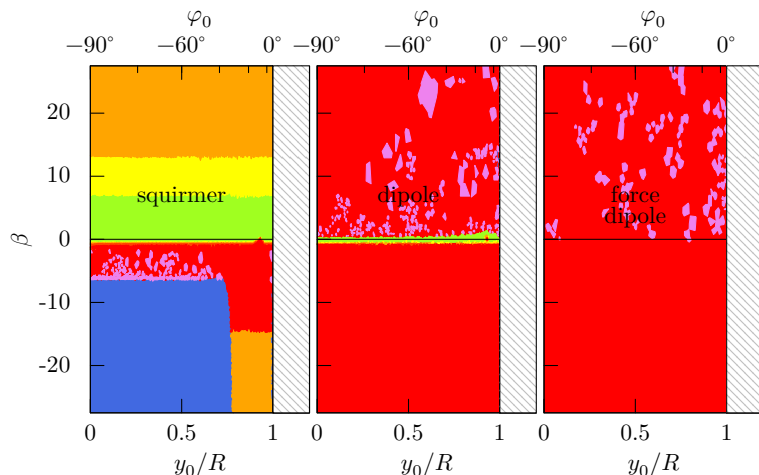


Figure 6.13: The influence of higher-order hydrodynamic moments on swimming inside a spherical cavity: State diagrams of the squirmer-obstacle interaction with color coding as in figure 6.12. The obstacle radius is maintained at $R = 20R_S$, while the dipolarity β and initial position y_0 (or equivalently, initial orientation φ_0) are varied. From left to right, different hydrodynamic models are considered: squirmer, force and source dipole, and force dipole.

the spherical cavity. The resulting figure 6.13 however leads to the same conclusion as before: the richness of the observed behavior is due to the quadrupole term, with dipole pushers orbiting and pullers hovering and only a small region near $\beta = 0$ exhibiting scattering trajectories. For the force-dipole swimmers, no scattering is observed. In both cases, the hovering region is rather diffuse and indistinguishable from a slow forward orbit.

6.4.5 Accounting for the near field

Finally, we come to the results obtained using our LB calculations, with the same method as in chapter 5. These are computationally much more involved, and we were therefore only able to sample a few points to verify the general trends of our far-field prediction. Initial simulations for this were performed in reference 346. We restrict ourselves to $R/R_S \in \{2, 5, 20\}$ and a few values of β and y_0 . The state diagram in figure 6.14 shows that scattering is generally more prevalent than in the previous far-field-only calculations. Backward orbits are still observed, but their critical dipolarity increases more rapidly with decreasing curvature. Forward orbits, which in the far field are primarily predicted for pullers, are now found in the case of sufficiently strong pushers when the obstacle size is large enough. Hovering states are possible for both pushers and pullers of sufficient strength, whenever the curvature is low.

These observations confirm that all four states found in the far-field model are indeed allowed by the near-field flow. Most notably, backward orbits of strong pushers appear in both far-field and LB models. However, agreement with the far-field model and with lubrication theory is only obtained to a certain degree. This is expected due to the difference in hydrodynamic modeling, but the choice of Weeks-Chandler-Andersen (WCA) as in equation 5.1 as opposed to hard-core repulsion might play an additional role. Literature also uses a variety of repulsion potentials, including ones softer than WCA [164], and hard-core repulsion [163]. The observed rapid decrease of β with R for backward orbiting places the backward sliding state ($R \rightarrow \infty$) outside the capabilities of our LB calculations.

6.5 Summary

We have employed three hydrodynamic methods to investigate the behavior of a squirmer near a spherical obstacle or a flat wall or inside a spherical cavity. Our primary results are derived using a simple far-field approximation, which lends itself to an efficient exploration of parameter space. Depending on

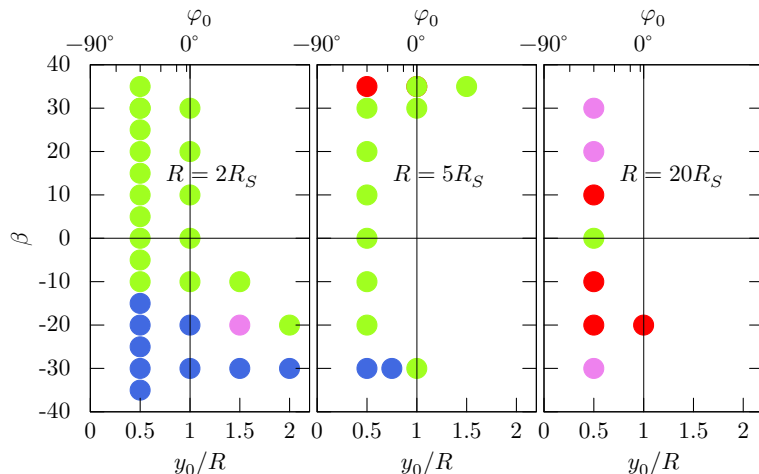


Figure 6.14: The influence of near-field hydrodynamics: State diagrams obtained via the LB method indicate the interaction between the squirmer and obstacle as a function of dipolarity β and initial position y_0 (or equivalently, initial orientation φ_0); the color coding is as in figure 6.7. From left to right three values of $R = 2, 5,$ and $20R_S$ are considered. Compare to figure 6.7 to see the differences caused by the near field.

the squirmer dipolarity, incidence angle, obstacle curvature, and short-range repulsion, this revealed four classes of trajectories: scattering, forward orbits, backward orbits, and hovering. Three of these trajectory classes have been previously reported, but the backward orbits constitute a new class that appears only for strong pushers.

Using the far-field approximation allowed us to construct state diagrams that cover the entire parameter space. We obtained all four classes for reasonable dipolarity parameters whenever the squirmer size is less than roughly half the size of the obstacle. Comparison to calculations that exclude the squirmer's quadrupole term reconcile our results with those of Spagnolie et al. [163]. This clearly attributes hovering and backward orbiting to the quadrupole. Thus, accounting for the finite size of the swimmer in the hydrodynamic multipole expansion introduces a richer behavior. Inside a cavity, orbits are found for a wider range of parameters due to self-stabilization effects not present at the obstacle or wall.

We also computed trajectories for several parameter sets using the LB method to investigate whether the reported far-field behaviors persist even when taking into account near-field details. While the exact positions of the transition between classes are altered, the qualitative behavior stays the same. Most importantly, we reproduce the predicted backward orbiting for the strong pushers in these calculations, showing that this effect is not an artifact of our approximation.

Our results indicate a mechanism of mobility reversal with respect to the bulk that is exclusively due to the hydrodynamic interaction of a swimmer with a surface. However, biological or artificial swimmers may additionally interact chemically or electrostatically with surfaces. Simple mappings of chemical swimmers onto a squirmer [154–156] are known not to qualitatively capture their behavior at small separation [155, 156]. Thus, such effects need to be accounted for in unison with the hydrodynamics [366, 379, 386]. The present theory and LB calculations provide a stepping stone toward analysis of (electro)chemical contributions to the orbiting of artificial swimmers.

7 An extensible lattice Boltzmann method for viscoelastic flows

Recent years have seen a surge of interest in the study of viscoelastic fluids, due to increased experimental understanding and several intriguing results that were obtained in these media. In particular, microswimmers in viscoelastic fluids show a richer set of behaviors than possible in simple (Newtonian) fluids, which include: the self-propulsion of a microswimmer through time-reversible actuation [77, 78, 387, 388], which is forbidden in a Newtonian fluid at low Reynolds number by Purcell’s scallop theorem [19] as described in section 1.1.2; the self-propulsion of a spatially symmetric microswimmer through spontaneous symmetry breaking [39]; enhanced rotational diffusion of thermophoretic Janus swimmers, due to time-delayed translation-rotation coupling in polymer suspensions [389]; a peak in the motility of *Escherichia coli* bacteria as a function of the polymer concentration and thus complexity of the fluid [130]; and a fundamental change in the way a microorganism propels in response to the rheology of the medium [390]. With the majority of industrially and biologically relevant fluids being complex fluids with internal structure and a non-Newtonian rheology [391, 392], many more such surprises lie ahead of us.

This has motivated the development of a wide range of theoretical and numerical methods. However, solving the associated hydrodynamic problem remains an open challenge, both in terms of efficiency and in defining the relevant constitutive equations. Much of the numerical work has focused on well-established, albeit basic, models of complex media, such as polymeric fluids described by Oldroyd-B [193] and FENE-P [197, 393]. Examples of such solvers applied to microfluidic problems include the finite volume (FV) method [394, 395], the finite element method (FEM) [331, 396], multi-particle collision dynamics (MPCD) [397, 398], dissipative particle dynamics (DPD) [399], the immersed boundary method (IBM) [390], smoothed-particle hydrodynamics (SPH) [400, 401], as well as explicit-polymer models based on Stokesian dynamics (SD) [402], lattice Boltzmann (LB) [203], and MPCD [169]. The open problem is how to simulate a fluid with a well-defined rheological response, while also allowing for the incorporation of colloidal particles. LB methods [261, 262, 265] hold particular promise to achieve this

goal due to their computational efficiency [9] and facile boundary [278] and particle coupling [266, 302–305], as has been demonstrated in Newtonian media. A wide variety of viscoelastic LB schemes have been conceived over the years [285, 286, 403–414]. However, despite this long history, which we will summarize in section 7.1.1, there remain multiple unresolved issues, especially with regard to boundary conditions.

In this chapter, we address the issues of simulating a viscoelastic fluid using LB with arbitrarily-shaped, moving boundaries. Our method is inspired by the Su et al. [285] algorithm for an Oldroyd-B fluid, which we re-derive as an FV scheme similar to that of Oliveira et al. [287]. This ensures momentum conservation and allows us to introduce a boundary coupling that makes no assumptions on the stress at the boundary [292]. Compared to the LB schemes described in the literature, further advantages include low memory usage and the absence of unphysical diffusion terms. After referring to sections 2.1.3, 2.1.5 and 2.5 for the relevant theory and laying out our numerical method in section 7.1, we benchmark our algorithm using several standard rheological tests: time-dependence of the planar Poiseuille flow in section 7.2.1, steady shear flow in section 7.2.2, the instabilities in lid-driven-cavity flow in section 7.2.3, and extensional flow in the four-roll mill in section 7.2.4. Next, we examine the effect of the coupling of translation and rotation on the sedimentation of a sphere in section 7.2.5, showing that we reproduce the shear-induced speed-up. We do the same for two connected spheres in section 7.2.6 and a squirmer in section 7.2.7. We discuss our findings and conclude with an outlook on future applications in section 7.3.

7.1 Model and methods

This chapter considers Oldroyd-B flow in various geometries with different boundary conditions, as well as rigid bodies in such a fluid. Just as the equations in sections 2.1.3 and 2.1.5 are split into a Newtonian part and a viscoelastic constitutive equation, here in the form of Oldroyd-B, we employ two separate numerical methods. The former is solved via LB (section 4.1), while the latter uses the FV method (section 4.2.3). Section 7.1.1 gives a brief overview of two decades’ worth of viscoelastic LB literature to justify this specific combination of methods. Section 7.1.2 explains how code generation techniques can be used to create a method and implementation that are independent of the specific choice of constitutive equation. The moving boundary scheme for LB and FVs is given in sections 4.4.1 and 4.4.3, respectively. It is also combined with the squirmer model of section 2.4 as described in section 5.1.

7.1.1 Background on viscoelastic lattice Boltzmann

As early as 1997, Giraud et al. [403, 404] used LB to compute the response of the Jeffreys fluid. This was followed up by Ispolatov and Grant [405], who employed LB to solve a linear Maxwell model, by implementing the elastic-stress contribution as a body force onto their fluid. Similar approaches were followed by Li and Fang [406] and Frantziskonis [407]. Later, Frank and Li [408, 409] went beyond the body-force coupling and introduced the effect of elastic stress directly into the second moment of the equilibrium distribution, an approach which has recently been revisited by Dellar [410]. Other coupling forms were considered by Onishi et al. [411] and Osmanlic and Körner [412], who employ a Fokker-Planck-like evolution of microscopic dumbbell-shaped polymers in a viscous fluid. This type of system is theoretically known to result in a viscoelastic response that resembles Oldroyd-B [415]. More direct approaches to reproducing Oldroyd-B were followed by Su et al. [285] and Karra [413], who solved the stress evolution equation for the corresponding constitutive relation directly using the LB fluid velocity as input to a finite difference scheme. Malaspinas et al. [286] and Su et al. [414] similarly used an LB scheme as a generic differential equation solver and treated the viscoelastic stress tensor component-wise, for both the Oldroyd-B and FENE-P constitutive relations.

Phillips and Roberts [416] provide a more in-depth review of the cited methods for viscoelastic fluids, as well as LB methods for generalized Newtonian fluids without viscoelastic memory. The latter include shear-thinning and shear-thickening fluids using a variety of shear-dependent viscosity models such as power-law [417–423], Cross [424], Carreau [422], or Bingham [425]; as well as specialized models for blood such as Casson [426, 427], Carreau-Yasuda [427, 428], or K-L [427]. For a discussion of LB methods that deal with viscoelastic behavior of active fluids [186, 188], see the review by Carenza et al. [429].

The viscoelastic LB schemes listed above are not applied to problems with boundaries [403, 408], do not require explicit treatment of the stress [405–407, 409], or use bounce-back rules to impose specific boundary conditions on the stress [404, 410]. Some extrapolate stress onto boundaries to allow for cases where no analytic expression exists [286, 414], while others can only be applied to systems for which the stress at the boundary is known beforehand [285]. As suggested by the large number of ways to treat stress at boundaries, and in spite of the significant development of LB-based viscoelastic solvers over the past two decades, incorporation of moving objects and handling of complex boundary geometries remains problematic. In the following, we build upon this body of knowledge and introduce a general method capable

of handling complex and moving boundaries. By doing so, we overcome the limitations of previous viscoelastic LB algorithms.

7.1.2 Implementation

The Python module `pystencils` [314] can be used to automatically generate code for grid-based algorithms, either for use in Python or for `waLBerla`, see section 4.5. We have extended it with a generator for FV discretizations that automatically derives the expressions in section 4.2.3 when provided with the Oldroyd-B equations 2.18 to 2.20. By instead supplying, for example, the FENE-P constitutive equation [197], it would be possible to simulate that model without writing any additional code.

There are several other fluid dynamics software packages that allow the user to provide such equations and automatically derive discretizations for them, e.g. `Dedalus` [430] or `OpenFOAM` [431]. The combination of `pystencils` and `waLBerla`, however, is unique in that it allows for arbitrarily-shaped boundary conditions that change over time, which can be put to use for the moving boundaries of section 4.4. We forgo `waLBerla` for the two-dimensional simulations, since they do not require rigid-body dynamics or parallelization, and run these simulations completely from Python. In this case, LB is provided by the `lbmpy` module [315], also described in section 4.5.

7.2 Validation and results

In this section, we solve multiple rheological benchmark systems to verify the correctness of our algorithm and implementation by comparing against results from literature. We then simulate systems involving moving boundary conditions and translation-rotation coupling in order to demonstrate the strength of the method.

7.2.1 Time-dependent Poiseuille flow

The planar Poiseuille geometry consists of an infinitely long channel of width L , through which flow is driven by a homogeneous force along the channel, $\mathbf{F} = F_x \hat{\mathbf{e}}_x$. The channel walls impose a no-slip condition $\mathbf{u}((x, 0)^\top, t) = \mathbf{u}((x, L)^\top, t) = \mathbf{0}$, while the infinite length can be achieved via periodic boundary conditions in y -direction. This setup is illustrated in figure 7.1 and results in a parabolic steady-state flow profile. Starting this flow in a resting Newtonian fluid causes the steady-state flow to be approached in a monotonous fashion. In a viscoelastic medium, however, the flow velocity

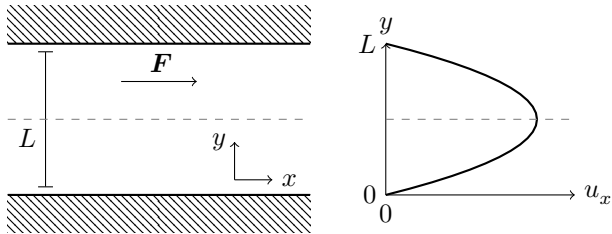


Figure 7.1: Geometry of the planar Poiseuille flow system. A force \mathbf{F} is applied to a fluid in a periodic channel of width L , which leads to a parabolic profile across the channel for the flow velocity u_x along the channel. The dashed line indicates where the flow velocity is measured for further analysis.

can overshoot its steady-state value and then decay to it on a time scale of λ_p . This is due to the storage of energy in the elastic medium, which is released back into the fluid on the time scale λ_p . Reference 432 provides an analytic expression for the time-dependent flow profile in a liquid B' model:

$$u_x((x, y)^\top, t) \propto \frac{y}{h} - \frac{y^2}{h^2} - 8 \sum_{n=1}^{\infty} \frac{\sin(\frac{n\pi}{h}(2n-1))}{(2n-1)^3 \pi^3} \exp\left(-\frac{\alpha_n t}{2\lambda_p}\right) G_n\left(\frac{t}{\lambda_p}\right) \quad (7.1)$$

with

$$G_n(T) = \begin{cases} \cosh\left(\frac{\beta_n T}{2}\right) + \frac{\gamma_n}{\beta_n} \sinh\left(\frac{\beta_n T}{2}\right) & \alpha_n^2 - 4\frac{\text{Wi}}{\text{Re}}(2n-1)^2 \pi^2 \geq 0 \\ \cos\left(\frac{\beta_n T}{2}\right) + \frac{\gamma_n}{\beta_n} \sin\left(\frac{\beta_n T}{2}\right) & \alpha_n^2 - 4\frac{\text{Wi}}{\text{Re}}(2n-1)^2 \pi^2 < 0 \end{cases},$$

$$\alpha_n = 1 + (1 - \xi) \frac{\text{Wi}}{\text{Re}} (2n-1)^2 \pi^2,$$

$$\beta_n = \sqrt{\left| \alpha_n^2 - 4\frac{\text{Wi}}{\text{Re}} (2n-1)^2 \pi^2 \right|},$$

$$\gamma_n = 1 - (1 + \xi) \frac{\text{Wi}}{\text{Re}} (2n-1)^2 \pi^2.$$

The liquid B' model model has been shown to be equivalent to Oldroyd-B [433, 434].

We choose the channel width $L = 28\Delta x$, applied force $F_x = 10^{-5} \rho \Delta x^4 / \Delta t^2$, Newtonian viscosity $\eta_n = \rho \Delta x^2 / \Delta t - \eta_p$, polymer viscosity ratios $\xi \in \{0.1, 0.3, 0.5, 0.7, 0.9\}$, and polymer relaxation times $\lambda_p / \Delta t \in \{1000, 3000, 5000, 7000, 9000\}$ for our test simulations. This corresponds to a Reynolds number of

$$\text{Re} = \frac{\rho u_x((x, L/2)^\top, \infty) L}{\eta} = \frac{\rho F_x L^3}{8\eta^2} = 0.03, \quad (7.2)$$

which is well within the low-Reynolds regime we are interested in. The Weissenberg number is

$$\text{Wi} = \frac{u_x((x, L/2)^\top, \infty) \lambda_p}{L} = \frac{F_x L \lambda_p}{8\eta} \in [0.04, 0.32]. \quad (7.3)$$

Figure 7.2 shows the flow velocity $u_x((x, L/2)^\top, t)$ over time for various polymer viscosity ratios ξ at constant polymer relaxation time $\lambda_p = 3000\Delta t$. One can see that the magnitude of the overshoot increases with ξ . For the largest values of ξ , the flow can even decay to its final speed in an oscillatory

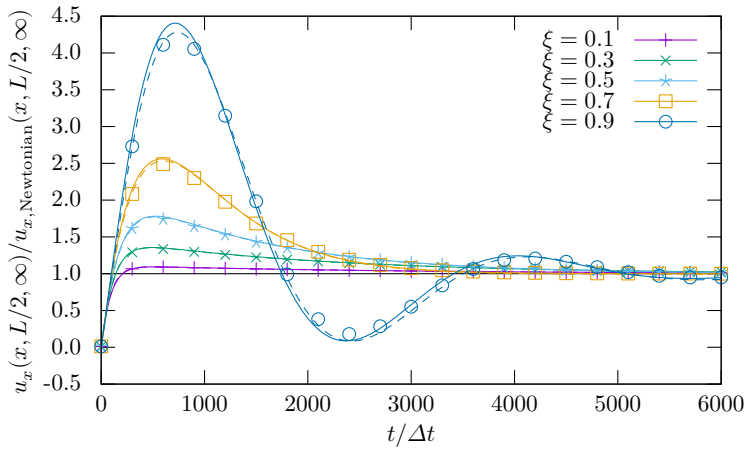


Figure 7.2: Velocity at the center of a planar Poiseuille channel over time for varying viscosity ratios ξ and polymer relaxation time $\lambda_p = 3000\Delta t$. Symbols are numerical calculations, and lines show the analytic prediction by reference 432. The solid lines use L from the input parameters, whereas the dashed lines allow it to be a free fit parameter.

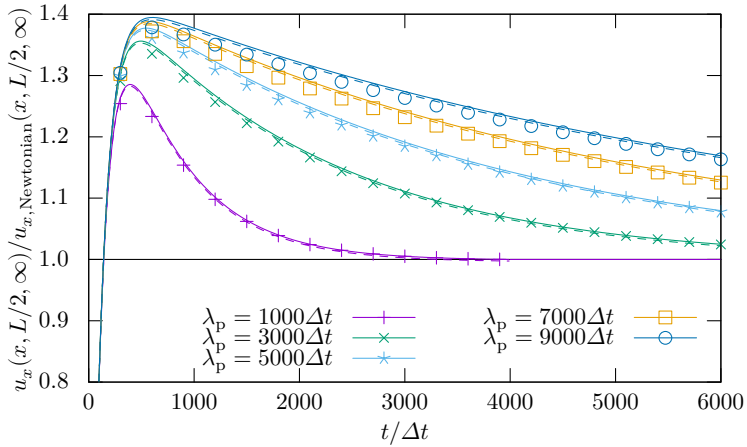


Figure 7.3: Velocity at the center of a planar Poiseuille channel over time for viscosity ratio $\xi = 0.3$ and varying polymer relaxation times λ_p . Symbols are numerical calculations, and lines show the analytic prediction by reference 432. The solid lines use L from the input parameters, whereas the dashed lines allow it to be a free fit parameter.

fashion. Figure 7.3 keeps $\xi = 0.3$ constant and varies λ_p . Here it is clear that the magnitude of the overshoot increases with λ_p , which is also the characteristic decay time of the overshoot.

Figures 7.2 and 7.3 additionally show the analytic expression, equation 7.1, for comparison. The agreement with the analytics can be improved to around 1% in all cases if L is used as a fit parameter. This is justified by the fact that the boundary position in LB is not guaranteed to be exactly at the edge of the cell [435] and that the extrapolation of equation 4.32 introduces an error for the FV method. The resulting L differs from the input parameter by ± 0.6 cells, or ± 0.3 per boundary, well within the range expected for regular LB.

7.2.2 Steady shear flow

The planar Couette geometry is similar to that of section 7.2.1, but replaces the applied force with a velocity boundary condition of $\mathbf{u}((x, L)^\top, t) = u_0 \hat{\mathbf{e}}_x$ on one of the planes, as illustrated in figure 7.4. This relative motion leads to a linear steady-state velocity profile across the channel. The first normal stress difference,

$$N_1 = \tau_{xx} - \tau_{yy} = 2\eta_p \lambda_p \frac{u_0^2}{L^2}, \quad (7.4)$$

is expected to be constant over the entire channel, as obtained by solving equation 2.17 with the given velocity profile. We choose the channel width $L = 28\Delta x$, the applied velocity $u_0 = 10^{-3}\Delta x/\Delta t$, Newtonian viscosity $\eta_n = \rho\Delta x^2/\Delta t - \eta_p$, polymer viscosity ratios $\xi \in \{0.2, 0.4, 0.6, 0.8\}$, and polymer relaxation times $\lambda_p/\Delta t \in [1000, 20000]$ for our test simulations. They are run until sufficiently converged, which we find to be the case at $t = 10\lambda_p$. We find that N_1 agrees with the prediction to within 0.2% across all parameters. Appreciable deviations ($\sim 5\%$) are only seen in the cells directly at the boundaries, where this is expected due to the stress extrapolation by equation 4.32.

7.2.3 Lid-driven cavity

The lid-driven cavity consists of a square flow cell of edge length L , with no-slip boundaries on three sides and a constant velocity boundary condition of $\mathbf{u}((x, L)^\top, t) = u_0 \hat{\mathbf{e}}_x$ on the top side. This is depicted in figure 7.5, which also illustrates the shape of the resulting flow: a primary vortex develops near the top center of the flow cell and secondary vortices arise in the lower corners. The exact position of the center of the primary vortex, as well as the position y of the minimum of $u_x((L/2, y)^\top, \infty)$ and the positions x of the

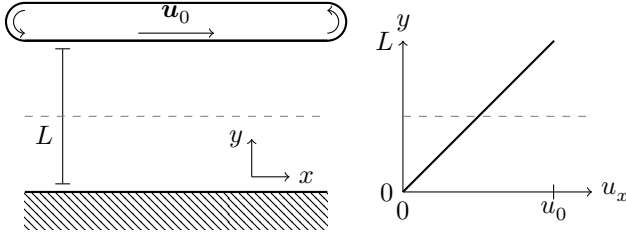


Figure 7.4: Geometry of the planar Couette flow system. A velocity boundary condition of u_0 is applied to one side of a fluid in a periodic channel of width L , which leads to a linear profile across the channel for the flow velocity u_x along the channel.

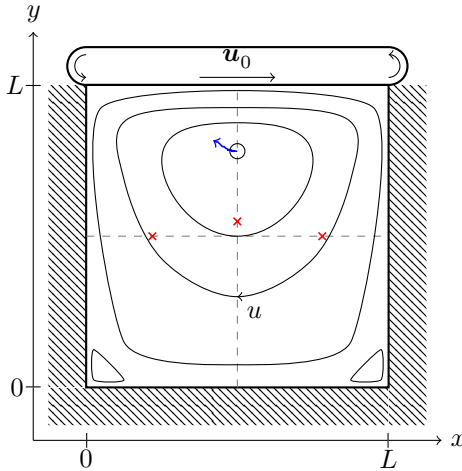


Figure 7.5: Geometry of the lid-driven cavity system. A square flow cell of size L has no-slip boundaries on three sides and a constant-velocity boundary condition of u_0 along the fourth. The resulting flow develops a primary vortex near the top middle of the cell. Along the dashed lines, flow velocity minima and maxima are found at the red crosses. The blue arrow indicates how the vortex center moves as Wi is increased from 0 to 1.

minimum and maximum of $u_y((x, L/2)^\top, \infty)$ vary with the flow parameters and have been extensively studied in literature [436–440], making them well-suited for comparison in the following.

We choose width and height $L = 194\Delta x$ for the flow cell, Newtonian viscosity $\eta_n = \rho\Delta x^2/\Delta t - \eta_p$, applied velocity $u_0 = 10^{-4}\Delta x/\Delta t$, polymer viscosity ratio $\xi = 0.5$, and polymer relaxation times λ_p such that Weissenberg numbers $Wi \in [0, 1]$ are obtained. For $Wi = 0$, $\xi \rightarrow 0$ is also used. The Weissenberg and Deborah numbers are [437]

$$Wi = De = \frac{\lambda_p u_0}{L}, \quad (7.5)$$

coinciding due to the unit aspect ratio of the cell. The Reynolds number is given by

$$Re = \frac{\rho u_0 L}{\eta} = 0.02, \quad (7.6)$$

again placing us in the low-Reynolds regime.

For numerical reasons, the velocity boundary condition is not applied as given above. Instead, a regularization is used to remove the infinite flow divergence in the top corners. A common choice is

$$\mathbf{u}((x, L)^\top, t) = 16u_0 \left(\frac{x}{L}\right)^2 \left(1 - \frac{x}{L}\right)^2 \hat{\mathbf{e}}_x. \quad (7.7)$$

This regularization leaves the qualitative flow features untouched, but thwarts quantitative comparison with the unregularized simulations of reference 436. The same regularization is employed by references 437–440 and shall be used in the comparison below.

Figure 7.6 shows the positions of the primary vortex and the flow velocity extrema in our simulations. Error bars correspond to the size of a cell plus the potential deviation of the true boundary position from the prescribed boundary position. One can see that the general trend from references 437–440 is recovered semi-quantitatively, with the exception of the nonlinear deviation of the x -component of the vortex center. Results vary significantly between these references, so that a quantitative comparison is not drawn. However, in view of this, the result in figure 7.6 gives confidence in our method’s accuracy. The speed with which our results were obtained, as well as the ability to refine these significantly, provide opportunities for future benchmarking.

The flow velocity at the points of interest is shown in figure 7.7. Values differ between references 437–440 by factors of up to 2, so we only plot the comparison to reference 440. This reference has matching flow velocities at

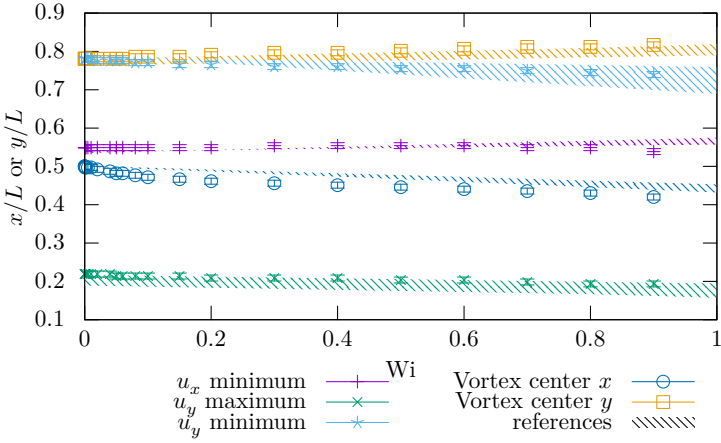


Figure 7.6: Positions of the primary vortex and flow extrema in the lid-driven cavity. Colors refer to the different points. Symbols are our results, while the hatched areas indicates the range covered by the numerical results from references 437–440.

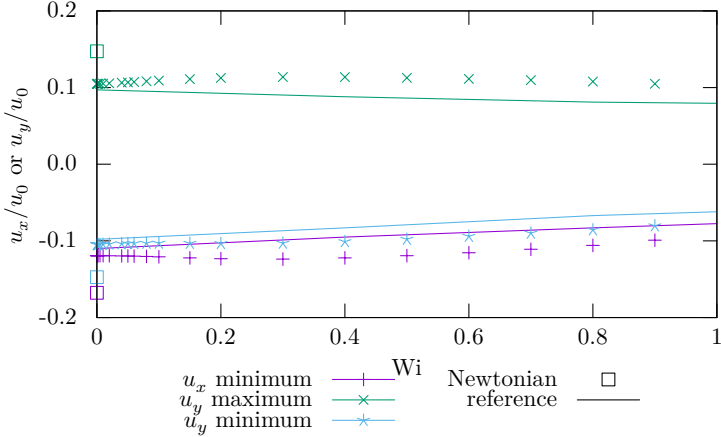


Figure 7.7: Velocity of the flow extrema in the lid-driven cavity. Colors refer to the different points. Symbols are our results, while the line refers to numerical results from reference 440. The square symbols indicate Newtonian simulations ($\xi \rightarrow 0$) and match results from reference 437, while the others are viscoelastic ($\xi = 0.5$).

$Wi \rightarrow 0$ and exhibits the same trend of decreasing velocity magnitudes as our results. The vortex is observed to move toward the top left as Wi is increased. The minimum of u_x moves down slightly, while both the minimum and the maximum of u_y move toward the left. The deviations from the results in literature are expected as the system is very sensitive to resolution, especially at larger Wi . Our resolution was chosen such that the results had sufficiently converged.

We also performed one simulation at $\xi \rightarrow 0$, the Newtonian case, and observe that this yields a different velocity than $Wi \rightarrow 0$ at constant $\xi = 0.5$. The velocity obtained in the former way agrees with that reported by reference 437 to within 1%. The latter way corresponds to the case of instantaneous polymer relaxation, but not vanishing viscoelasticity.

7.2.4 Four-roll mill

The four-roll mill consists of a square cell with length L and periodic boundary conditions. A force field of

$$\mathbf{F}(\mathbf{r}, t) = \frac{8\pi^2\eta_n u_0}{L^2} \begin{pmatrix} \sin(\frac{2\pi}{L}x) \cos(\frac{2\pi}{L}y) \\ \cos(\frac{2\pi}{L}x) \sin(\frac{2\pi}{L}y) \end{pmatrix} \quad (7.8)$$

is applied to it, resulting in four counter-rotating rolls as illustrated in figure 7.8. Reference 441 provides an analytic prediction for the steady-state stress in the vicinity of the central point, where the flow is purely extensional, i.e., $\mathbf{u}((L/2, L/2)^\top, t) = \alpha(\hat{\mathbf{e}}_x - \hat{\mathbf{e}}_y)$.

We choose cell size $L = 214\sqrt{2}\Delta x$, Newtonian viscosity $\eta_n = 1.5\rho\Delta x^2/\Delta t$, polymer viscosity ratio $\xi = \frac{1}{3}$, maximum velocity $u_0 = 10^{-3}\Delta x/\Delta t$, and polymer relaxation times $\lambda_p/\Delta t \in [1000, 24000]$. The simulation is run until sufficiently converged, which we find to be the case at $t = 20\lambda_p$. The Weissenberg number is given by [441, 442]

$$Wi = \frac{4\pi\lambda_p u_0}{L}, \quad (7.9)$$

and the Reynolds number is low at

$$Re = \frac{\rho u_0 L}{\eta} = 0.1. \quad (7.10)$$

We found that our simulations lead to a decoupling of the stress at the center point from the rest of the domain due to the upwind scheme from section 4.2.2. To avoid this, we rotated the lattice by 45° relative

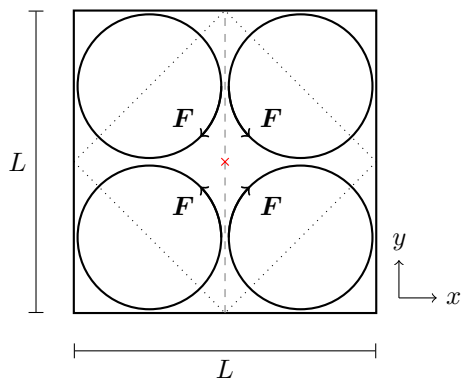


Figure 7.8: Geometry of the four-roll mill. Four counter-rotating forces F are applied to a periodic square flow cell of size L . This leads to a pure extensional flow at the center of the cell. Velocity and stress will be measured along the dashed line. The dotted square indicates the actual simulation domain used, which still obeys the periodic boundary conditions.

to the system as indicated in figure 7.8, while ensuring that the periodic continuation of the system remains intact. We would like to stress that this is a rather unusual situation, which only appears here due to the high level of symmetry and the divergence at the central point. Such behavior will not commonly appear in soft matter systems, but when it does, it is easily identified in the stress profiles.

Figure 7.9a-d shows the stress component τ_{xx} along a vertical line going through the center of the cell, which is marked with a red cross in figure 7.8. A comparison with reference 441 is drawn by fitting with its local solution, also found in reference 443,

$$\tau_{xx}((L/2, y)^\top, \infty) = \frac{2\eta_p \text{Wi}_{\text{eff}}}{\lambda_p(1 - 2\text{Wi}_{\text{eff}})} + C \left| \frac{y}{L} - \frac{1}{2} \right|^{(1-2\text{Wi}_{\text{eff}})/\text{Wi}_{\text{eff}}}. \quad (7.11)$$

We fit via C while keeping $\text{Wi}_{\text{eff}} = \lambda_p \alpha$ constant, as well as via both C and Wi_{eff} . We find that Wi_{eff} only differs by less than 1% between the two fits, yet the latter fit is significantly better. This is because fitting an exponent is very sensitive to small deviations. For $\text{Wi}_{\text{eff}} < 1/4$, the structure of the stress profile is not captured well by the fit. This is due to the lack of a singularity, as equation 7.11 was constructed with a singularity in mind [441]. Beyond this value, three regimes of solutions are recovered: continuous and differentiable at the center ($\text{Wi}_{\text{eff}} < 1/3$), continuous but not differentiable at the center ($1/3 \leq \text{Wi}_{\text{eff}} < 1/2$), and diverging at the center ($\text{Wi}_{\text{eff}} \geq 1/2$). We reproduce the expected regimes, albeit with the caveat that divergences in our scheme are not present, due to the smoothing of solutions that its discretization imposes. Figure 7.9e plots Wi_{eff} that we obtained from the fits via Wi . Comparison with the corresponding plot from reference 441 is excellent up to $\text{Wi}_{\text{eff}} \approx 0.4$ (corresponding to $\text{Wi} \approx 0.75$), as expected due to implicit smoothing of the divergences.

7.2.5 Sedimenting sphere

So far, all systems investigated were two-dimensional and had constant boundary conditions. To demonstrate our algorithm's capabilities beyond this, we simulate the sedimentation of a rotating sphere. A sphere of radius R is placed in a cubic box of size L^3 with periodic boundary conditions. A constant force $\mathbf{F} = F_z \hat{\mathbf{e}}_z$ is applied to the sphere and the counterforce $-\mathbf{F}$ is distributed evenly among all fluid cells so that the net momentum of the system remains zero. Furthermore, a constant torque $\mathbf{M} = M_z \hat{\mathbf{e}}_z$ is applied to the sphere to rotate it around the z -axis; a counter-torque on the fluid is not needed [444]. The geometry is illustrated in figure 7.10.

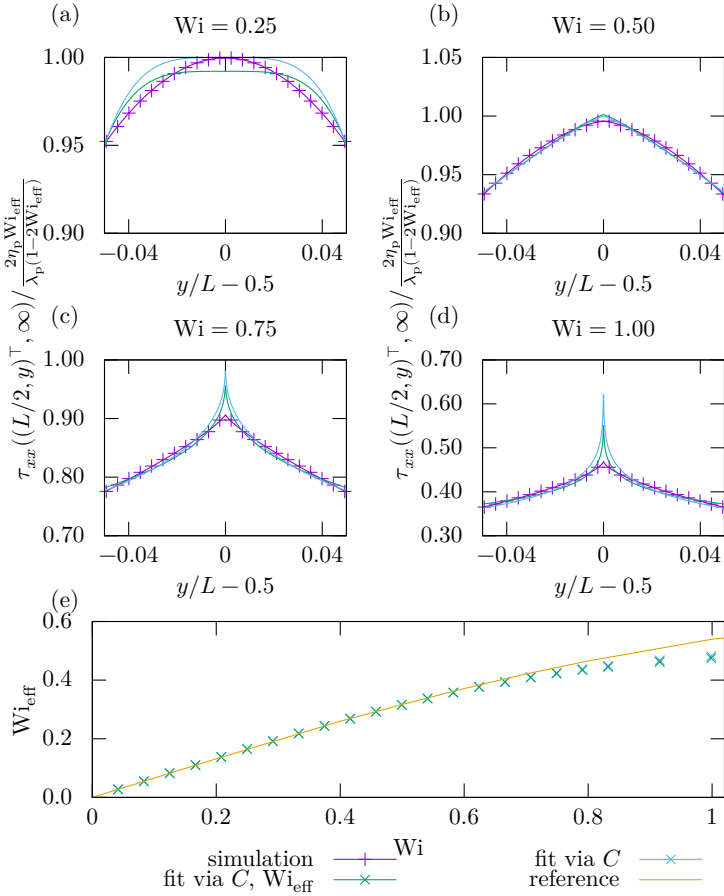


Figure 7.9: (a-d) Stress $\tau_{xx}((L/2, y)^\top, \infty)$ near the center of the four-roll mill for different polymer relaxation times λ_p . Symbols are our results, with their connecting line coming from fitting equation 7.11 with an added offset. The other lines are fits with equation 7.11 via one or two parameters. (e) Wi_{eff} plotted over the Weissenberg number Wi . Symbols are our results, while the line comes from reference 441.

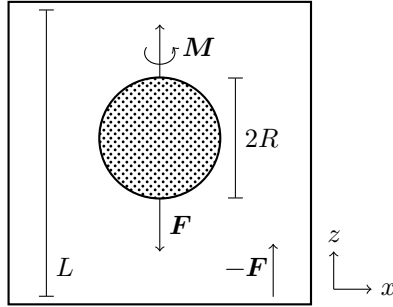


Figure 7.10: Geometry of the sedimenting sphere system. A sphere of radius R sediments under velocity \mathbf{v} due to an applied force \mathbf{F} in a periodic cubic box of length L . A torque \mathbf{M} is applied to the sphere to rotate it with velocity $\boldsymbol{\omega}$.

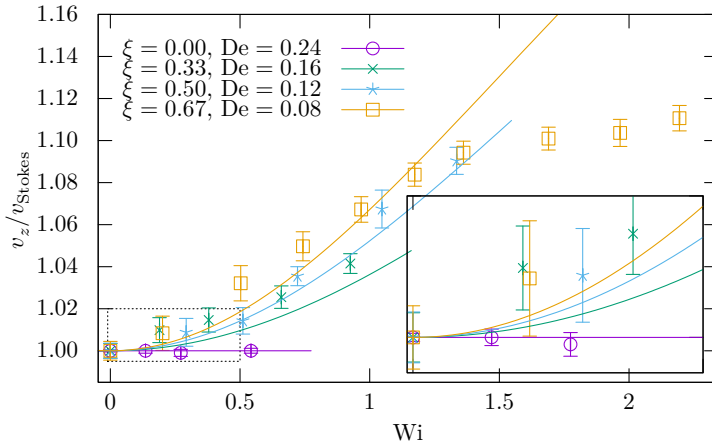


Figure 7.11: Sedimentation velocity of a rotating sphere in an Oldroyd-B fluid. Symbols with error bars are our results, while the lines are theoretical predictions from reference 445 for the same parameters (ending at Wi_{\max} as per equation 7.17). The inset displays an enlargement of the lower left region of the large graph indicated by the dotted box.

We choose our parameters as $R = 8\Delta x$, $L/R \in [7.5, 30]$, $F_z = 0.008\rho\Delta x^4/\Delta t^2$, $\eta_n = \frac{1}{6}\rho\Delta x^2/\Delta t$, $\eta_p/\eta_n \in \{0, \frac{1}{2}, 1, 2\}$ and $\lambda_p = 6000\Delta t$. The simulation is run until the velocity \mathbf{v} of the sphere has converged, for which $t = 10\lambda_p$ tends to suffice. We can assume $M_z = 0$ since it does not change the order of magnitude of the sedimentation velocity \mathbf{v} [445] and employ Stokes' law,

$$v_{\text{Stokes}} = \frac{F}{6\pi\eta R}, \quad (7.12)$$

in order to estimate the Reynolds number for our parameter range as

$$\text{Re} = \frac{2\rho v_{\text{Stokes}} R}{\eta} = \frac{\rho F}{3\pi\eta^2} \in [0.003, 0.03], \quad (7.13)$$

which lies well in the low-Reynolds regime. The Weissenberg and Deborah numbers of the system are given by [445]

$$\text{Wi} = \lambda_p \omega_z \quad (7.14)$$

$$\text{De} = \frac{\lambda_p v_0}{R}, \quad (7.15)$$

where $\boldsymbol{\omega} = \omega_z \hat{\mathbf{e}}_z$ is the measured angular velocity of the sphere. v_0 is the sedimentation velocity measured for $\omega_z = 0$, with all other parameters kept equal. ω_z can be varied by changing the applied torque M_z . M_z is chosen such that we cover a range of Weissenberg numbers while staying below a certain value of the tangential velocity $v_t = \omega_z R$ in order to not jeopardize the LB's stability. To achieve this, we define a maximum surface Reynolds number

$$\text{Re}_{t,\text{max}} = \frac{2\rho v_{t,\text{max}} R}{\eta} \equiv 0.1, \quad (7.16)$$

which can be used to obtain a maximum allowed Weissenberg number as

$$\text{Wi}_{\text{max}} = \lambda_p \omega_{\text{max}} = \frac{\lambda_p \text{Re}_{t,\text{max}} \eta}{2\rho R^2}. \quad (7.17)$$

The parameters provided above correspond to four sets of simulations with different polymer viscosity fractions ξ . Within each set, the variation of ω_z or M_z corresponds to a change in Wi , which makes the horizontal axis of figure 7.11. To obtain the value on the vertical axis, first an exponential decay is fitted to $\mathbf{v}(t)$ to extrapolate to $t \rightarrow \infty$, and then simulations at different L are used to extrapolate it to $L \rightarrow \infty$ (under the assumption that

the periodic interactions scale like a force monopole, i.e. L^{-1}). The fit error of these two processes is used to obtain the plot error bars. In figure 7.11, we also compare to an analytic solution by Housiadas [445], who expanded v in terms of De for arbitrary ξ and $\chi = Wi/De$ to obtain

$$\frac{v}{v_{\text{Stokes}}} = 1 + \xi De^2 C_2 - \xi De^4 C_4 \quad (7.18)$$

with

$$\begin{aligned} C_2 &= -0.01031 - 0.0057143\xi - (0.12208 - 0.0095238\xi)\chi^2 \\ C_4 &= C_{40} + \chi^2 C_{42} + \chi^4 C_{44} \\ C_{40} &= 0.013945 + 0.00017174\xi - 0.0024713\xi^2 + 0.00050884\xi^3 \\ C_{42} &= 0.060266 + 0.0067056\xi - 0.013849\xi^2 + 0.0058942\xi^3 \\ C_{44} &= 0.04645\xi - 0.011483\xi^2 - 0.00039651\xi^3. \end{aligned}$$

They then perform a Padé transformation [446] to improve convergence, resulting in

$$\frac{v}{v_{\text{Stokes}}} = 1 + \xi \frac{De^2 C_2^2}{C_2 - De^2 C_4}. \quad (7.19)$$

Agreement is mostly within error bars up to $Wi \approx 1$. Deviations beyond that are comparable to those found by reference 445's own comparison to numerical results from reference 447 for similar parameters. This shows that our method reproduces the analytic solution in its range of validity, while behaving similar to other methods beyond that realm. In the absence of rotation ($Wi = 0$), viscoelastic effects become negligible ($v \approx v_{\text{Stokes}}$) for an Oldroyd-B fluid, but they may be observed with other constitutive relations like Giesekus even for purely linear motion [448].

7.2.6 Two-sphere snowman

The next system to be considered is one whose behavior differs drastically between the Newtonian and the viscoelastic case. It consists of a snowman-shaped object rotated by an applied torque $\mathbf{M} = M_z \hat{\mathbf{e}}_z$. In a Newtonian fluid, it does not move, while a viscoelastic fluid allows it to move in the direction of the smaller sphere [449]. When the two spheres are made to counter-rotate, it was found that motion happens in the opposite direction [450]. The former behavior has been experimentally demonstrated [451, 452], where the rotation is induced by a magnetic field. The snowman is composed of two spheres of radii R_1 and R_2 with a center-to-center distance of h and rigidly connected by a cylinder that does not interact hydrodynamically.

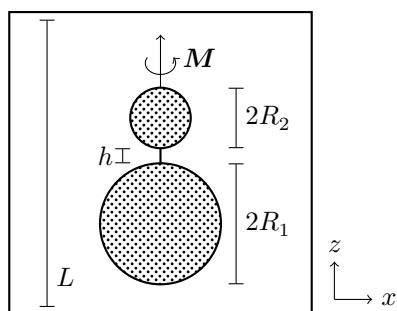


Figure 7.12: Geometry of the two-sphere snowman. Two spheres of radii R_1 and R_2 , connected by a hydrodynamically invisible rod, are placed in a periodic cubic box of length L . A torque \mathbf{M} is applied to the snowman to rotate it with velocity $\boldsymbol{\omega}$, which causes it to move at velocity \mathbf{v} .

Without loss of generality, we assume $R_1 \geq R_2$. The geometry is illustrated in figure 7.12.

We choose our parameters as $R_1 = 16\Delta x$, $R_2 = 0.5R_1$, $L/R_1 \in [12, 24]$, $h/R_1 \in [2, 5]$, $\eta_n = \frac{1}{6}\rho\Delta x^2/\Delta t$, $\eta_p = \eta_n$ and $\lambda_p = 6000\Delta t$. M_z is picked such that $Wi = 0.1$ is obtained. The Weissenberg number is given by [449]

$$Wi = \lambda_p \omega_z. \quad (7.20)$$

The Reynolds number is estimated as

$$Re = \frac{2\rho v_z R_1}{\eta} \approx 10^{-2}. \quad (7.21)$$

As in section 7.2.5, time and box size are extrapolated to infinity, though this time under the assumption that the periodic interactions scale like L^{-2} since the leading-order mode is a force dipole. The extrapolation error is combined with the error due to the grid resolution and the slight deviation of the measured Wi from its intended value to obtain error bounds. Our results displayed in figure 7.13 agree with the calculations of reference 449 within the error bars except for our smallest values of h . We also tried simulations for the smallest geometrically permissible $h = R_1 + R_2$, but find that these simulations become unstable, starting from the cells around the point where the two spheres touch. This is expected as standard LB cannot handle fluid in confinement regions on the length scale of Δx ; this problem cannot be circumvented by increasing the grid resolution. As we increase h , the simulation becomes stable for $h \gtrsim R_1 + R_2 + 4\Delta x$, yet the velocity of the snowman does not converge until $h \gtrsim R_1 + 2R_2$. This problem does not appear to be explicable by the small gap size, but might have other causes, such as the rigid coupling between the two spheres being incompatible with their hydrodynamic interaction. Note that this is not a limitation of our algorithm, but rather of LB itself. It is unclear whether this issue is in any way related to the one observed in section 5.2.2.

7.2.7 Squirmer

As the final system, we consider a microswimmer. One of the simplest hydrodynamic models for one is the squirmer [20, 21], which was introduced in section 2.4. It was inspired by the microorganism *Paramecium*, whose cilia perform a certain beat pattern that can be described by the boundary condition of equation 2.44. For details on how this can be incorporated into an LB simulation via moving boundaries, see chapter 5. Unlike the snowman of section 7.2.6, the squirmer propels without external actuation.

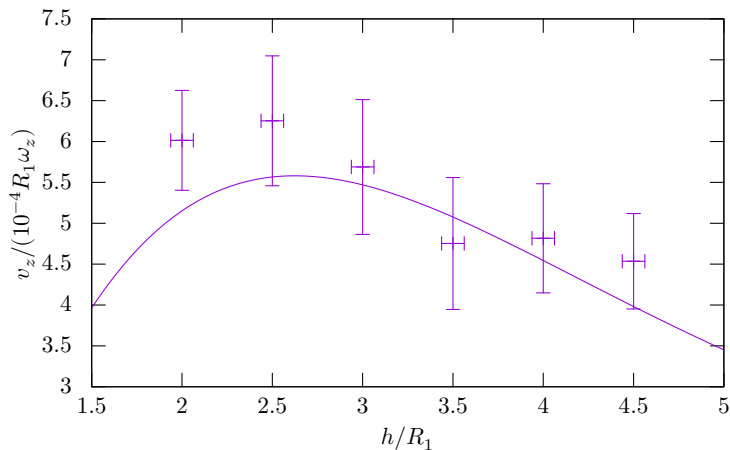


Figure 7.13: Translational velocity of a rotating two-sphere snowman in an Oldroyd-B fluid. Symbols with error bars are our results, while the lines are calculations from reference 449 for the same parameters. $\xi = 0.5$, $Wi = 0.1$ and $R_2/R_1 = 0.5$ were used.

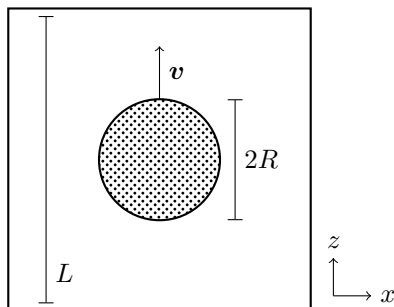


Figure 7.14: Geometry of the squirmer system. A squirmer of radius R moves at velocity \mathbf{v} in a periodic cubic box of length L .

In a Newtonian fluid in the absence of boundaries, it moves at a constant speed of $\mathbf{v}_0 = \frac{2}{3}B_1\hat{e}$. In a viscoelastic fluid, its velocity depends on the Weissenberg number [453].

We choose our parameters as $R = 8\Delta x$, $L/R \in [10, 30]$, $\eta_n = \frac{1}{6}\rho\Delta x^2/\Delta t$, $\eta_p = \eta_n$, and $\beta \in \{-1, 0, -1\}$. We vary $v_0 \in \{10^{-4}, 10^{-3}\}$ and $\lambda_p/\Delta t \in [600, 6000]$ to obtain different Weissenberg numbers. The Weissenberg number is given by [453]

$$\text{Wi} = \frac{\lambda_p B_1}{R}. \quad (7.22)$$

Since the viscoelastic effects do not change the order of magnitude of the propulsion velocity, we can again estimate the Reynolds number by its Newtonian value,

$$\text{Re} = \frac{2\rho v_0 R}{\eta} \in [0.005, 0.05], \quad (7.23)$$

which is again sufficiently small.

Time and box size are again extrapolated to infinity as described in section 7.2.5. The extrapolation error is combined with the error due to the grid resolution to obtain error bounds. Figure 7.15 shows our results and compares them with the prediction by Binagia et al. [453] and Housiadas et al. [454], who expanded v_z in terms of Wi for arbitrary ξ to obtain

$$\frac{v_z}{v_0} = 1 + \xi(\text{Wi}U_1 + \text{Wi}^2U_2 + \text{Wi}^3U_3 + \text{Wi}^4U_4) \quad (7.24)$$

with

$$\begin{aligned} U_1 &= -0.2\beta \\ U_2 &= -0.53986 - 0.62118\beta^2 - 0.063736\xi\beta^2 \\ U_3 &= \beta(2.0038 - 0.20025\xi - 0.21489\xi^2 \\ &\quad + 0.65822\beta^2 + 0.20304\xi\beta^2 - 0.16241\xi^2\beta^2) \\ U_4 &= -0.48158 + 1.7141\xi - 0.66789\xi^2 - 1.4845\beta^2 \\ &\quad + 6.467\xi\beta^2 - 1.4402\xi^2\beta^2 - 0.54389\xi^3\beta^2 - 0.20571\beta^4 \\ &\quad + 2.181\xi\beta^4 - 0.46279\xi^2\beta^4 - 0.19509\xi^3\beta^4. \end{aligned}$$

This is again Padé-transformed [446] to result in

$$\frac{v}{v_{\text{Stokes}}} = 1 + \xi \frac{\text{Wi}(U_1^2U_3 - U_1U_2^2) - \text{Wi}^2(U_2^3 - 2U_1U_2U_3 + U_1^2U_4)}{(\text{Wi}U_3 - U_2^2) + \text{Wi}(U_2U_3 - U_1U_4) + \text{Wi}^2(U_2U_4 - U_3^2)}. \quad (7.25)$$

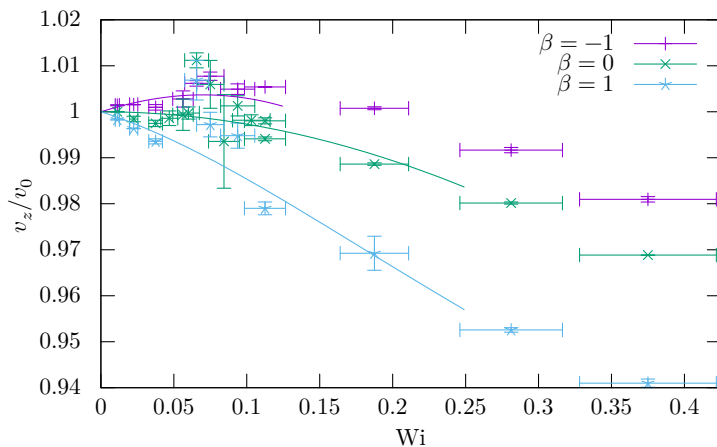


Figure 7.15: Propulsion velocity of puller, neutral and pusher squirmers in an Oldroyd-B fluid with $\xi = 0.5$. Symbols with error bars are our results, while the lines are theoretical predictions from references 453 and 454 for the same parameters.

This expression is valid for $Wi \leq (4 - 4\beta)^{-1}$ with $\beta \leq \frac{1}{3}$ or $Wi \leq (2 + 2\beta)^{-1}$ with $\beta > \frac{1}{3}$ [454]. Beyond this Weissenberg number, the Oldroyd-B model becomes singular at the poles of the squirmer, however this is not observable in our simulations due to the implicit regularization induced by the lattice. Most other viscoelastic constitutive equations would not be constrained to the low- Wi regime like this [454–456]. Recent work by Housiadas et al. [454] revealed that the cause of the viscoelastic influence on the propulsion differs between the different constitutive equations: in Oldroyd-B and FENE-P it is attributed to a pressure difference between front and back, while in Giesekus elastic stresses at the poles are found to be dominant.

We find agreement between our results and the prediction mostly within error bars. A significant unexplained deviation is observed around $Wi \approx 0.07$, where velocity increases by several percent compared to the expected value. The position of this peak is independent of parameters like β or R . Orienting the squirmer such that it swims in $(1, 1, 1)^\top$ direction instead of $(0, 0, 1)^\top$ as before, however, moves the peak to $Wi \approx 0.1$, or $\sqrt{3}$ times its previous value. This suggests that not all periodicity artifacts have been accounted for. Even though the results have been extrapolated to infinite box size, weak interactions with periodic images of the squirmer with a different scaling behavior may still be present.

7.3 Summary

We have introduced a method to simulate Oldroyd-B fluids with LB. It uses moving boundaries to allow for the simulation of suspended colloids. We validated our method against several rheological benchmark problems and determined it to correspond well with literature for Weissenberg and Deborah numbers and viscosity fractions between zero and one, a regime relevant for many colloidal systems. We also validated our method for specific colloidal problems, spheres sedimenting under an applied torque and squirmers swimming, where analytic and numerical predictions are recovered in their regime of validity. Computational effort scales linearly with the number of fluid cells, while the computational cost of adding particles is negligible compared to that of simulating the fluid. Published data on the benchmarks we considered for this work covered only a small parameter space, i.e. the few most relevant points, therefore we make our full data set available to serve as a reliable reference for future investigations¹. The simulation code is also provided to enable others to study similar systems

¹<https://doi.org/10.24416/UU01-2AFZSW>

at parameters and resolutions of their choosing. Finally, thanks to the use of automatic code generation, our model and implementation are easily extensible to other viscoelastic models. Incorporating thermal fluctuations [293] is also conceivable.

Our viscoelastic, moving-boundary LB facilitates future study of dense colloidal suspensions in viscoelastic fluids. This might include the collective sedimentation of colloids [457], which goes beyond the single-body effects discussed in section 7.2.5. The field of self-propelled colloids is of particular interest to us. Previous reports of viscoelastic enhancement of rotational diffusivity [389], for example, have spurred interest in the community. Simulation studies [169] however could not discern whether this was an effect of viscoelasticity or merely of an inhomogeneous polymer concentration. Our method does away with the explicit consideration of polymers and might settle such questions. Besides effective propulsion models [169, 453], fully-resolved propulsion models as in chapter 8 might also be used, which would permit investigating complex phenomena arising from the interplay of hydrodynamics, viscoelasticity, electrostatics and phoretic interactions, such as those experimentally studied in reference 458. Our new and extensively validated method provides a first stepping stone toward such future physical modeling.

8 Moving charged particles in lattice Boltzmann-based electrokinetics

The dynamics of electrolytic solutions is essential to the description of most processes in (bio)chemistry and soft matter physics. This includes electrostatic screening via the formation of double layers, electro-osmotic flow [132, 459–461], electrophoresis [462–465], and self-electrophoresis [25, 33–35, 139, 369, 466]. Industrial applications range from DNA sequencing [467, 468] and oil recovery [469] to the detection [470], separation [471], and characterization [472] of analyte molecules. The coupled occurrence of diffusion, hydrodynamics, and electrostatics, often referred to as electrokinetics or electrohydrodynamics, gives rise to complex physical behavior. Electrokinetic processes involve dynamics on vastly different length scales with double layers typically having a nanometer scale in aqueous solution and system geometries often ranging from several micrometers to millimeters. The small length scales make it difficult to access the nanoscopic details in experiment, while the large discrepancy in length scales poses a challenge to simulation methods.

Existing methods that solve the electrokinetic equations numerically are based on a variety of algorithms for hydrodynamics, generally falling into two classes. Firstly, particle-based algorithms, which include dissipative particle dynamics (DPD) [473, 474] and multi-particle collision dynamics (MPCD) [475, 476]. Secondly, continuum (grid-based) algorithms, which encompass methods like the finite element method (FEM) [35, 139, 369, 477], the boundary element method (BEM) [478–480], the boundary integral method (BIM) [138], finite differences (FDs) [481], finite volumes (FVs) [482], lattice electrokinetics (EK) based on lattice Boltzmann (LB) [282, 483], and the smooth profile method (SP) [484]. For additional details, we refer to the overviews given in references 469 and 485.

The particle-based methods solve the full time-dependent problem and are intrinsically able to include mobile charged colloids and macromolecules. The downside of these methods is that solute ions, water, and macromolecules

are resolved on the same scale. This sets a low limit for the maximum size of the simulation domain, given current computational abilities.

Continuum solvers allow for the study of systems with much larger length scales because the ions are not resolved. In general, introducing moving boundaries into numerical solvers for the continuum electrokinetic equations poses a more challenging problem than for their particle-based counterparts. Tackling this issue, however, is well worth the effort, as it grants access to the wide variety of physical problems beyond those that can be studied via Galilean transformation to the rest frame of the charged object, an approach that is not possible in general. Moving particles will permit the study of interactions of multiple (self-)electrophoretically driven colloids, as well as their interactions with any stationary boundaries in the system.

When it comes to resolving large system sizes, the FEM has proven itself to be a very efficient solver for the stationary electrokinetic equations. FEM has been successfully applied in arbitrary geometries and for a diverse range of physical systems, including: nanopores [486–488], self-electrophoresing colloids [35, 139, 140, 369, 489–491], and electro-osmotic pumping [492, 493]. The strength of the FEM lies in its ability to adaptively increase the resolution in regions with high gradients, i.e., the electric double layers. The downside is that the treatment of time-dependent boundary positions is computationally exceedingly expensive, due to the constant need for re-meshing. Nevertheless, there are examples of its application to phoretic problems with moving boundaries [494].

An alternative to FEM was proposed by Capuani et al. [282]. Their EK method uses FVs to solve the diffusion-advection of solute and FDs to solve the electrostatics problem. For hydrodynamics, they exploit the computational efficiency of the LB method [261, 266]. Unlike earlier methods that aimed to achieve a similar level of description [483], EK propagates the solute by considering solute fluxes between neighboring lattice cells instead of concentrations in lattice cells, thus ensuring local mass conservation and reducing discretization artifacts [282]. Unlike the FEM and the grid-based method of reference 481, this can be used to solve the full time-dependent electrokinetic equations in a fixed geometry. Furthermore, EK, like LB, is a local algorithm, with the exception of the electrostatics solver, making it generally more efficient than FEM and other solvers, which are fully non-local.

Of specific interest is EK's ability to resolve the particles' surfaces as boundary conditions on the grid. This allows for the study of extended objects and straightforward incorporation of local variation of the surface properties, which is, e.g., useful in studying self-propelled particles [134] as discussed in section 1.2.2. Extending this method further with dynamically-

adaptive grid refinement, a common practice in LB [321], will constitute an algorithm fully capable of directly modeling microfluidic systems.

The EK method has previously been used to study problems such as electrophoresis [495] and sedimentation [282] of single charged spherical colloids. Other applications include charge transport in porous media [496, 497] and the translocation of DNA molecules through nanopores [498], where this method can tremendously reduce computational effort when compared to particle-based methods, and thus enable one to reach experimentally relevant length and time scales.

Direct solutions of the electrokinetic equations, a highly coupled system of equations, are available through the Poisson-Boltzmann (PB) theory of section 2.2.2, but are limited to equilibrium systems and rarely analytically possible, even less so in arbitrary geometries. Therefore, we resort to numerical methods to solve them. While approaches like linearizing the problem and solving it using perturbation theory [462] are available, we solve the full nonlinear equations by discretizing them on a lattice.

In this chapter, we present an extension of the EK method proposed by Capuani et al. [282] to include moving boundaries. For the underlying LB method, a moving boundary scheme [304, 305] is already widely employed for moving particles. To adapt the EK method for moving boundaries, we first introduce solute mass and charge conservation by displacing solute from cells that are claimed by a moving particle. We subsequently add a partial volume smoothing to reduce the effect of a cell being claimed in a single time step. We do so by incorporating a term in the solute flux calculation that depends on the amount of volume in a cell that is overlapped by a particle. This allows for a gradual expulsion of solute from a cell as it is increasingly overlapped.

We validate our method by considering the problem of electrophoresis of spherical colloids in an external field. We observe that the moving boundary method is capable of reproducing results using the Capuani method with fixed boundaries (in the co-moving frame). Moreover, we observe that the smoothing term is necessary to prevent strong variations in the particle velocity due to the grid discretization — it reduces the oscillations by more than a factor of 10. The added computational cost due to the moving boundaries amounts to approximately a 10% increase per time step, compared to the stationary boundary algorithm of Capuani et al. [282]. The method we describe retains the flexibility and efficiency of the LB and EK methods, while granting the EK method access to an entire class of problems where the relative motion of multiple particles is of relevance.

The remainder of this chapter is laid out as follows: In section 8.1, we summarize the governing equations and the numerical methods, including

a novel method for coupling moving particles with EK. In section 8.2, we validate the new method by comparing equivalent electrophoretic and electro-osmotic systems. We conclude in section 8.3.

8.1 Model and methods

In this chapter, we consider colloidal particles suspended in an electrolyte solution. The latter is described by the Stokes equations (section 2.1.3) and the electrokinetic equations (section 2.2). They are solved by the LB method (section 4.1) and the EK method (section 4.2.4), respectively. For the electrostatics, the solver of section 4.3 is used. Section 4.4.1 describes the moving boundary method for coupling particles into LB, while section 4.4.2 describes our new method for combining moving boundaries with EK.

The `walBerla` framework is detailed in section 4.5. At the time this chapter's simulations were performed, `pystencils` had not been developed yet and the rigid body dynamics module was not fully integrated into `walBerla`, so `walBerla` modules originally developed for use in reference 213 were employed. Nowadays, the same method can be constructed from components that are available in `walBerla` itself.

8.2 Validation

In this section, we perform several simulations with known results to confirm that the accuracy of the newly-devised method. The first one involving only a single colloid undergoing electrophoresis can be performed without moving boundaries by means of a Galilean transformation, so it lends itself to comparison with the well-established EK method with fixed boundaries. The second one involves a suspension of electrophoresing colloids; since they can move freely relative to each other and relative to the lattice, the use of moving boundaries is mandatory.

8.2.1 Electrophoresis of a single colloid

To validate the moving boundary EK method described in section 4.4.2, we choose a simple system consisting of an electrophoresing sphere. Specifically, we simulate a single, homogeneously charged, spherical colloid in a cubic box with periodic boundary conditions undergoing electrophoresis in a uniform external electric field, as illustrated in figure 8.1. This system has already been studied extensively using the EK method without moving boundaries by considering the equivalent problem of electro-osmotic flow [495].

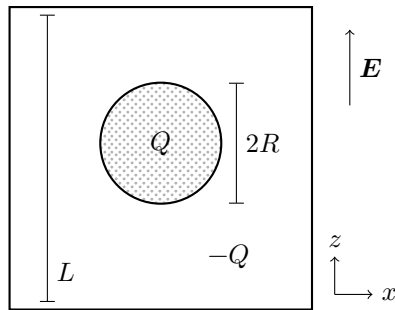


Figure 8.1: Geometry of the electrophoresing colloid. A spherical particle with radius R and charge Q is dragged through an electrolyte solution by an electric field \mathbf{E} in a periodic cubic box of length L . Counterions to the sphere are present in the fluid, so the overall system is charge-neutral.

The parameters used are given in table 8.1. They were chosen to match one of the data points of reference 495. A salt concentration of $c = 10^{-3} \text{ mol L}^{-1}$ is experimentally relevant [499–502] and the (effective) colloid charge of $Q = 30e$ is realistic for a particle of radius $R = 4 \cdot 10^{-9} \text{ m}$. The Debye length resulting from equation 2.34, $\lambda_D = 10 \text{ nm}$ for that concentration, is neither in the thin ($\lambda_D \ll R$) nor thick ($\lambda_D \gg R$) double layer limit and should thus demonstrate the capability of the method to deal with these intermediate regimes. The charge of $Q = 30e$ was chosen such that the Debye-Hückel theory of equation 2.32 is not applicable — the requirement being $e\zeta < k_B T$ with $\zeta = Qk_B T \lambda_B / e(R + R^2/\lambda_D)$ — while for $Q = 3e$, it is. The salt concentration c and the grid spacing Δx need to be chosen such that one Debye length is resolved by a minimum of approximately 4 cells, as we will see during validation. This precludes us from using a salt concentration of much higher than $c = 10^{-3} \text{ mol L}^{-1}$ without increasing the grid resolution. However, sufficiently resolving the double layer is a general requirement of the EK method [282], as well as for FEM and other algorithms, and not specific to the use of moving boundaries. We will compare the results of the different simulation methods via a single number, the reduced electrophoretic mobility [503]:

$$\tilde{\mu} = \frac{6\pi\eta\lambda_B}{e} \frac{v}{E}, \quad (8.1)$$

where v is the speed of the particle’s motion relative to the bulk fluid and E is the applied electric field.

Figure 8.2 compares results obtained for the same parameter set (particle radius $R \approx 4 \cdot 10^{-9} \text{ m}$, particle charge $Q = 30e$, and salt concentration $c = 10^{-3} \text{ mol L}^{-1}$) for a simulation with a fixed particle, a moving particle without, and a moving particle with the partial volume scheme, respectively. The effective particle radius in the moving scheme is obtained by counting the number of cells that are completely inside the particle, averaging that number over the simulation time, and setting it equal to the sphere volume $(4/3)\pi R^3$. This allows us to choose R such that the moving and stationary simulations study the same physical system. One can see that both moving particle methods on average agree with the fixed boundary simulation’s stationary mobility value to within 1.4% and 2.4%, respectively. Agreement of the full time evolution is not expected as the electro-osmotic (fixed boundary) and electrophoretic (moving boundary) problems are, in fact, only equivalent in the stationary state. The method without partial volumes results in a mobility oscillating with an amplitude of 20.3% around the mean and a period corresponding to the time it takes the particle to move forward by one grid cell. On the other hand, the partial volume scheme of

Temperature	$T = 298.15 \text{ K}$
Relative permittivity	$\epsilon_r = 78.54$
Fluid density	$\rho = 997.04 \text{ kg m}^{-3}$
Viscosity	$\eta = 0.8937 \cdot 10^{-3} \text{ Pa s}$
Salt concentration	$c = 10^{-3} \text{ mol L}^{-1}$ $c = 10^{-4} \text{ mol L}^{-1}$
Salt valency	$z_{\pm} = \pm 1$
Diffusion coefficient	$\bar{D} = 2 \cdot 10^{-9} \text{ m}^2 \text{ s}^{-1}$
External field	$E = 256.9 \cdot 10^3 \text{ V m}^{-1}$
Sphere radius	$R \approx 3 \cdot 10^{-9} \text{ m to } 8 \cdot 10^{-9} \text{ m}$
Sphere charge	$Q = 3 e = 0.4807 \cdot 10^{-18} \text{ C}$ $Q = 30 e = 4.807 \cdot 10^{-18} \text{ C}$
Density of particle	$\rho_p = 2\rho$
Box length	$L = 64 \cdot 10^{-9} \text{ m}$
Length unit	$\Delta x = 10^{-9} \text{ m}$
Mass unit	$\Delta m = \rho \Delta x^3 = 9.97 \cdot 10^{-25} \text{ kg}$
Energy unit	$\Delta E = k_B T = 4.12 \cdot 10^{-21} \text{ J}$
Time unit	$\Delta t = \sqrt{\Delta m \Delta x^2 / \Delta E}$ $= 1.56 \cdot 10^{-11} \text{ s}$
LB grid spacing	Δx
LB time step	$0.2 \Delta t$

Table 8.1: Parameters used in the simulation and their conversion to simulation units. Note that our choice of $\rho_p = 2\rho$ is arbitrary and irrelevant to the working of our algorithm, as verified for a single system where we used $\rho_p = \rho$.

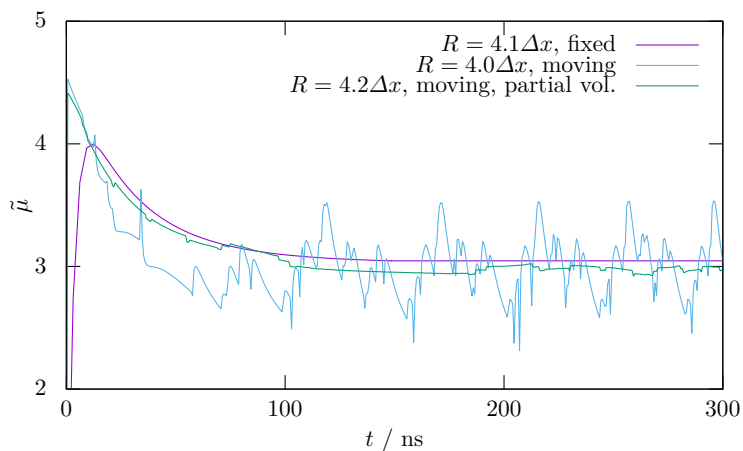


Figure 8.2: Comparison of the transient behavior (t denotes time) of the reduced electrophoretic mobility $\tilde{\mu}$ for the fixed particle (purple curve), the particle moving via the simple moving boundary scheme (blue curve), and the particle moving via the partial volume scheme (green curve). Here, $R = 4 \cdot 10^{-9}$ m, $Q = 30e$, and $c = 10^{-3}$ mol L $^{-1}$ were used.

section 4.4.2.2 reduces the mobility oscillations to 1.7%, which is generally small enough to consider any instantaneous value to be a good estimate for the true value. The period remains bound to the time it takes for the particle to move forward by one cell.

To ensure that the method does not adversely affect the shape of the electric double layer around the colloid, we examine the charge distribution around the colloid in figure 8.3. We see there is a small deviation close to the colloid's surface, but we can attribute this to the slight difference in particle size, as discussed above.

We further validated the partial volume method by running additional simulations with various salt concentrations c , particle charges Q , and particle radii R . The results are presented in figure 8.4 and are compared with reference results obtained by solving the electrokinetic equations with the FEM solver COMSOL. Note that we use a finite but large simulation domain in the FEM model, while the EK model handles periodic boundary conditions naturally; this may lead to slight differences in the results obtained with both methods. We observe an excellent agreement between fixed and moving boundary simulations, as well as the FEM reference results. The agreement improves as the particle size is increased, and thus the quality of the staircase approximation to its spherical shape. For example, for $R \approx 7 \cdot 10^{-9}$ m, $Q = 30e$, and $c = 10^{-3}$ mol L⁻¹, the oscillation amplitude drops to 1.3%. The remaining difference in the mobility is easily explained by a slight mismatch in volume (and thus effective radius) between the fixed and the moving particle.

Finally, we examined the speed of our simulation compared to the method of Capuani et al. [282] for the geometries that we considered. The moving boundary algorithm adds only 2% to the simulation time per time step, when compared to the equivalent fixed boundary simulation. Our smoothing results in a further increase of less than 10% in time, when compared to the non-smoothed moving boundaries. Together, this shows that our method does not incur an unreasonable computational cost and can therefore be straightforwardly applied to domain sizes that are currently accessible to the Capuani et al. method [282, 495].

8.2.2 Electrophoresis of a colloidal suspension

In this section, we consider the electrophoresis of a system comprised of several spheres. This allows us to verify our moving boundary method in a more physically complex system with interactions that the original Capuani et al. method could not access. We pick one parameter set ($R \approx 4 \cdot 10^{-9}$ m, $Q = 30e$, and $c = 10^{-3}$ mol L⁻¹) and repeat the simulation from

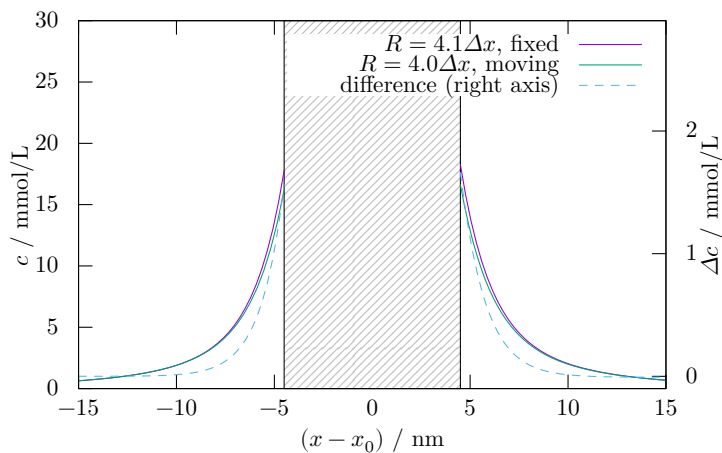


Figure 8.3: Comparison of the shape of the double layer around the colloid for the fixed and moving particles. Here, $R \approx 4 \cdot 10^{-9}$ m, $Q = 30e$, and $c = 10^{-3}$ molL $^{-1}$ were used. The shaded area refers to the space taken up by the colloid. The dashed line shows the absolute difference between the two charge distributions.

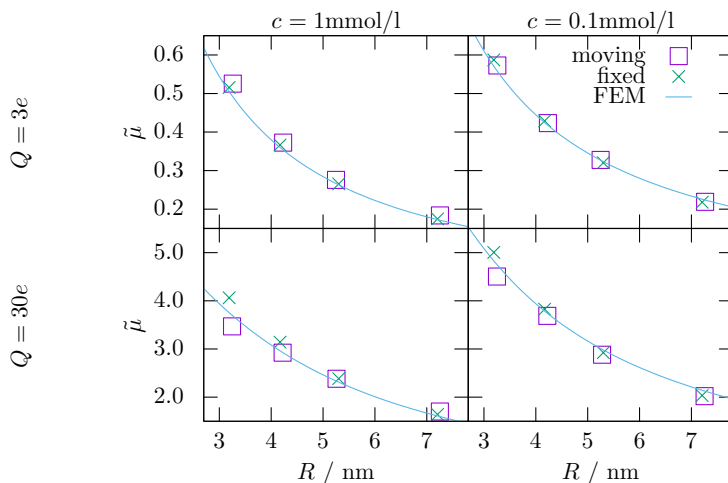


Figure 8.4: Comparison of the steady-state value of the electrophoretic mobility for different values of R , c , and Q .

the previous section. At these parameters, the volume fraction is about 0.1% and the double layers do not overlap noticeably, therefore only long-ranged hydrodynamic interactions are expected to mediate interactions between the colloids. Instead of having one spherical colloid interact with only its periodic images, we now enlarge the simulation box and add additional identical spheres while keeping the colloidal volume fraction constant. The colloids are either positioned randomly in a cubic box or in a regular lattice in a cuboidal box. This kind of simulation is typically performed to ensure the results do not suffer from artifacts of the periodic boundary conditions [499]. As opposed to the single colloid and its periodic images, which always maintain their relative positions, the colloids in this simulation are free to move relative to each other.

Figure 8.5 shows that the electrophoretic mobility is indeed mostly independent of the number of colloids, varying 0.9% from the average and 1.8% from the value for one colloid in periodic boundary conditions. This matches the findings of Lobaskin et al. [499] using colloids modeled with the Ahlrichs-Dünweg coupling [302, 444, 504], where agreement to within a few percent was found. The results of the previous section are therefore not artifacts of the periodicity of the simulation domain. For the case of a cubic simulation domain, we furthermore observe that the alignment of the colloids on a regular body-centered cubic lattice is a stable configuration.

8.3 Summary

Summarizing, we have introduced a method to simulate electrokinetic phenomena in colloidal suspensions. Our scheme builds upon the EK algorithm, which itself is capable of simulating moving colloids only by considering them as stationary boundary conditions in the Galilean-transformed (co-moving) frame. Motion of the colloids relative to the lattice can be incorporated by employing a method similar to the moving boundary method for LB. A key modification is required, however: We introduce mass conservation for the solute species in order to conserve charge. This is accomplished by redistributing solute from and to cells neighboring the ones that were recently vacated and claimed by the particle, respectively.

The above procedure is, in principle, sufficient to enable the simulation of, for example, colloidal electrophoresis. However, in practice, further improvements are desirable to allow for the simulation of colloids with as few LB cells as possible. To reduce the effects of sudden and strong solute fluxes, when a cell is claimed or vacated by a particle, a smoothing scheme by partial volumes is introduced. That is, the electrokinetic equations are

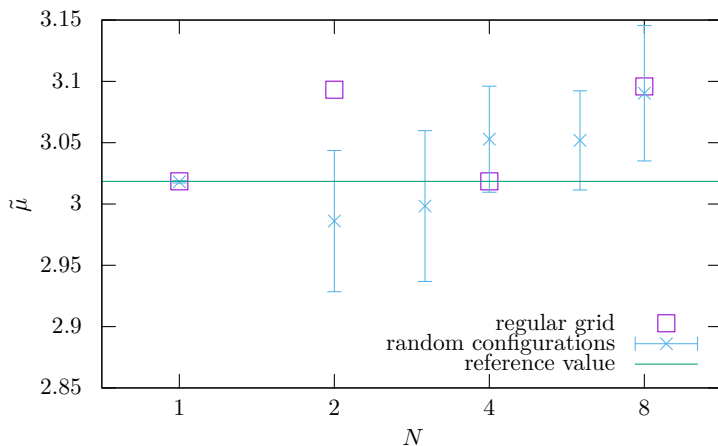


Figure 8.5: Comparison of the steady-state value of the electrophoretic mobility for different numbers of colloids at constant volume fraction. Here, $R \approx 4 \cdot 10^{-9}$ m, $Q = 30e$, and $c = 10^{-3}$ mol L $^{-1}$ were used. The error bars show the spread of values for different initial random placements of colloids in cubic boxes, while the squares show the value obtained for initial placement on a regular lattice.

solved for an effective concentration that incorporates what fraction of a cell is actually accessible to the solute, i.e., not overlapped by a colloid. This form of smoothing reduces the lattice artifacts by more than an order of magnitude in our test simulations. We also showed that having smoothing and moving boundaries only slows down the simulation by 10% and 2% respectively, compared to the original EK algorithm.

We validated our method for the electrophoresis of spherical colloids. For a single sphere, we find excellent agreement of the reduced steady-state electrophoretic mobility $\tilde{\mu}$ with the one obtained for the equivalent problem of electro-osmotic flow around a fixed sphere (co-moving frame). One can also obtain a reliable estimate for the mobility without the smoothing via partial volumes, but in this case it is necessary to average $\tilde{\mu}$ over one period of its oscillations. While this is a feasible solution for the system under consideration here, systems where the transient behavior of multiple particles is of interest would require averaging over many periods, thus requiring much longer overall simulation times. Alternatively, the oscillations could be reduced by increasing the grid resolution. This is again not desirable, as it comes with a steep increase in required computation time — performing the same simulation at twice the grid resolution takes eight times as much computing time. It is therefore clear that our smoothing is a prerequisite for the efficient study of electrokinetic moving boundary problems.

Our moving boundary EK method was further verified for the electrophoresis of multiple spheres that were free to move and interact. We find the electrophoretic mobility of the spheres to be almost independent of their initial arrangement. Such a simulation can only be performed with moving boundaries and thus demonstrates the power of the method presented.

Note that our moving boundary EK method imposes no limitations on simulation parameters beyond those already present in the original non-moving algorithm. These requirements include sufficient discretization of the double layer and limitations on the choice of time step, diffusivity, and grid discretization [282]. Furthermore, it leaves the EK and LB algorithms almost unmodified, which makes it easy to incorporate into existing LB or EK simulation codes. Finally, it also does not influence the scaling behavior of these algorithms as the work required to map a particle onto the lattice is linear in the number of lattice cells and particles.

In this investigation, we have primarily studied the case of external electrophoresis of a single colloid. As we have shown, however, our method can also be employed to investigate cases where Galilean transformation to a co-moving frame for the study of an equivalent electro-osmotic is not possible. These types of systems will be the subject of future work and could include a diverse range of systems. For example, our method is readily applicable

to study the translocation, characterization, concentration, separation, and transport of DNA, proteins, and other biochemical analytes; interactions between oppositely charged nanoparticles in an oscillatory electric field; collective dynamics of self-electrophoresing colloids (see sections 1.1.4, 1.2.2 and 2.2.3), and many others. Our work thus opens the door for the study of a wide range of physical systems that were previously inaccessible to continuum lattice-based methods.

9 Summary and outlook

We have discussed a number of simulation techniques for microswimmers in this thesis, with particular focus on those that resolve the region around a swimmer's surface. The latter is a prerequisite to accurately modeling hydrodynamic interactions and to accounting for effects that depend on the details of the propulsion mechanism. We did so by building upon existing methods, either significantly expanding the capabilities of the method or identifying and resolving its weaknesses. This made these methods better suited to the specific conditions and environments encountered by artificial and biological microswimmers, such as electrolyte solutions, viscoelastic fluids, and the proximity of surfaces and other swimmers. The use of lattice methods combined a high degree of numerical accuracy with computational efficiency. We extensively validated our methods and determined their domain of applicability. Theoretical explanations for hydrodynamic mobility reversal were found that had not previously been reported. An important feature of my work is that I developed models that are broadly applicable. For example, the lattice Boltzmann (LB) method for viscoelastic media allows for facile switching between constitutive relations. The rest of the present chapter will summarize my achievements under these aspects and provide an outlook on future extensions and applications worthwhile of further research.

Chapter 1 started with a general overview of the field of active matter, pointing out the various means of propulsion that have been considered experimentally and which physical aspects need to be accounted for to accurately capture them in simple models. The most common modeling approaches were introduced and grouped by their level of detail. This led us to the LB method, which is well established in fluid dynamics and soft matter physics. It has previously been extended to allow for particle coupling and the modeling of various kinds of complex fluids and is thus well-suited for the intents of this thesis. In chapter 2, the theoretical background to the problems studied was laid out. This included the transport of mass and momentum in a fluid, as described by the Stokes equations. We considered a simple linear constitutive relation to describe Newtonian fluids like water, as well as a nonlinear one, specifically the Oldroyd-B model for viscoelastic fluids. Next, the transport dynamics of solute ions by Poisson-Nernst-Planck

processes were presented. Together with chemical reactions, they can serve as the basis for propulsion by self-electrophoresis or self-diffusiophoresis. The squirmer was also introduced as a simplified, purely hydrodynamic propulsion model. It is well-suited for validation purposes due to its widespread use in literature. At the same time, it offers sufficient complexity that unexpected results on its behavior in non-Newtonian fluids and at surfaces can still be found today. In chapter 3, we discussed analytic far-field methods relevant to the study of the squirmer model. Chapter 4 moved on to models that allow for near-field resolution. In it, we introduced computational methods based on LB, finite volumes (FVs), and fast Fourier transformation (FFT). The development of these methods went hand-in-hand with the results presented in chapters 5 to 8, which we lay out next:

Chapter 5, previously published in reference 2, validated an LB model for squirmers. The squirmer equation served as a boundary condition on particles' surfaces, which were incorporated using the moving boundary method. While such models have been used before, no systematic information on resolution requirements was available. We found that the model can become numerically unstable at low resolutions for which passive particles behave well and achieve accuracies that are widely accepted in the field. Resolution effects were particularly pronounced when there was a preferred direction in the system. We also noticed that strong pusher squirmers are able to swim backwards along surfaces, an observation that inspired the following chapter.

Chapter 6, building upon reference 3, studied a squirmer at flat, convex, and concave walls using a far-field model. The simplicity of the model and the low dimensionality of the parameter space enabled us to fully determine the conditions under which the squirmer swims forward or backward along the wall, scatters off it, or hovers in front of it. The backward motion could be attributed to the source quadrupole component of the squirmer flow. Mobility reversal had previously been attributed to phoretic or electrostatic interactions, but our result demonstrated that hydrodynamics alone are sufficient. Recently, Chaithanya and Thampi [167] explored this direction further: They quantified the trajectories in terms of properties like scattering angles or average distance and performed further LB comparison, finding their results consistent with ours. Open questions remain, however, about the influence of higher-order multipoles — like the force quadrupole or the octupoles — which are not present in the simplest squirmer, but appear in natural and artificial microswimmers. Artificial swimmers involve chemical fields in addition to the hydrodynamics, an aspect whose far-field description has recently received attention [366, 379, 386]. That work could serve as a starting point to determine whether the propulsion details of an artificial

swimmer suppress or enhance mobility reversal.

In chapter 7, part of which has been published in reference 4, we constructed and validated a lattice model for viscoelastic fluids. An FV scheme was coupled to LB, ensuring momentum conservation while enabling particle coupling via an extension of the moving boundary scheme. It should be noted that implementation using the code-generation capabilities of the `walBerla` and `pystencils` frameworks allows for the effortless extension of our code to arbitrary constitutive relations. We validated our method for Oldroyd-B as it is the simplest constitutive relation, but the step to more realistic viscoelastic models can be made by simply replacing an equation. As part of the validation, a lid-driven cavity was simulated, where we substantially improved upon the available literature results. We published our high-resolution data set to serve as a future reference. Viscoelastic translation-rotation coupling was confirmed by the simulation of two rigidly-coupled spheres spinning due to an applied torque; motion along the rotation axis is only observed in viscoelastic fluids. The step from external actuation to the autonomous propulsion of microswimmers was made by again simulating a squirmer, for which analytic reference solutions are available in literature for various constitutive equations. Simulating a squirmer may, however, be problematic due to flow singularities at its poles as discussed in recent literature [454, 455]. Similarly, the singularity at the center of the four-roll mill required special attention. More complex viscoelastic models like FENE-P or Giesekus should be used in future work to avoid these. Such models also resemble biological fluids more accurately and are thus better suited to the study of bacteria or medical microrobots. Thermal fluctuations are relevant for some applications [169, 389] and their incorporation into continuum models like ours has become conceivable based on recent work [293].

Chapter 8, based on reference 1, extended an existing LB-FV model for electrolyte solutions by the addition of moving boundaries. Validation was performed by considering colloidal electrophoresis in the co-moving and laboratory frames, i.e. with moving and with stationary boundaries. It is worth noting that a partial-volume smoothing scheme was needed to mitigate adverse effects that occur when lattice cells are converted between fluid and solid. This smoothing derives from the idea that all solute is in that part of a cell that is not occupied by the particle; an appropriately renormalized Nernst-Planck equation could thus provide sub-grid resolution. This method was intended to provide the basis for simulations of self-electrophoretic colloids by adding chemical reactions as described in section 4.2.5 [35, 213]. Interactions between the smoothing scheme and the reactions unfortunately made this much more difficult than anticipated, hence the actual application

of this method to microswimmers is left to future research. Caveats to our implementation were provided in section 4.4.2.2, and we proposed a solution to the identified issues in section 4.3.2.

The combined methods of chapters 7 and 8, along with this future extension to self-electrophoresis, will provide a valuable tool for the study of chemical microswimmers in almost arbitrary fluid environments. The analytic expressions for the flow fields caused by the different hydrodynamic modes near a boundary provided in section 3.5 will prove useful to the future study of microswimming in confinement. The implementation and reference data on the lid-driven cavity in section 7.2.3 will serve as a useful benchmark for future development of numerical methods for viscoelasticity.

Bibliography

- [1] M. Kuron, G. Rempfer, F. Schornbaum, M. Bauer, C. Godenschwager, C. Holm, and J. de Graaf, “Moving charged particles in lattice Boltzmann-based electrokinetics”, *Journal of Chemical Physics* **145**, 214102 (2016).
- [2] M. Kuron, P. Stärk, C. Burkard, J. de Graaf, and C. Holm, “A lattice Boltzmann model for squirmers”, *Journal of Chemical Physics* **150**, 144110 (2019).
- [3] M. Kuron, P. Stärk, C. Holm, and J. de Graaf, “Hydrodynamic mobility reversal of squirmers near flat and curved surfaces”, *Soft Matter* **15**, 5908 (2019).
- [4] M. Kuron, C. Stewart, J. de Graaf, and C. Holm, “An extensible lattice Boltzmann method for viscoelastic flows: complex and moving boundaries in Oldroyd-B fluids”, *European Physical Journal E* **44**, 1 (2021).
- [5] M. Kuron, P. Kreissl, and C. Holm, “Toward Understanding of Self-Electrophoretic Propulsion under Realistic Conditions: From Bulk Reactions to Confinement Effects”, *Accounts of Chemical Research* **51**, 2998 (2018).
- [6] I. Tischler, F. Weik, R. Kaufmann, M. Kuron, R. Weeber, and C. Holm, “A thermalized electrokinetics model including stochastic reactions suitable for multiscale simulations of reaction-advection-diffusion systems”, *ChemRxiv preprint*, [10.33774/chemrxiv-2021-39nhv](https://doi.org/10.33774/chemrxiv-2021-39nhv) (2021).
- [7] M. Kuron and A. Arnold, “Role of geometrical shape in like-charge attraction of DNA”, *European Physical Journal E* **38**, 20 (2015).
- [8] F. Weik, R. Weeber, K. Szuttor, K. Breitsprecher, J. de Graaf, M. Kuron, J. Landsgesell, H. Menke, D. Sean, and C. Holm, “ESPReso 4.0 – an extensible software package for simulating soft matter systems”, *European Physical Journal Special Topics* **227**, 1789 (2019).

- [9] M. Bauer, S. Eibl, C. Godenschwager, N. Kohl, M. Kuron, C. Rettinger, F. Schornbaum, C. Schwarzmeier, D. Thönnnes, H. Köstler, and U. Rüde, “waLBerla: A block-structured high-performance framework for multiphysics simulations”, *Computers & Mathematics with Applications* **81**, 478 (2021).
- [10] J. R. Porter, “Antony van Leeuwenhoek: tercentenary of his discovery of bacteria.”, *Bacteriological Reviews* **40**, 260 (1976).
- [11] N. Lane, “The unseen world: reflections on Leeuwenhoek (1677) ‘Concerning little animals’”, *Philosophical Transactions of the Royal Society of London, Series B: Biological Sciences* **370**, 20140344 (2015).
- [12] H. C. Berg, “Bacterial behaviour”, *Nature* **254**, 389 (1975).
- [13] H. C. Berg, “Chemotaxis in bacteria”, *Annual Review of Biophysics and Bioengineering* **4**, 119 (1975).
- [14] G. K. Batchelor, “Developments in microhydrodynamics”, in *Proceedings of the 14th IUTAM Congress of Theoretical and Applied Mechanics, Delft, 1976* (1977), pages 33–55, ISBN: 978-0-7204-0549-1.
- [15] G. I. Taylor, “Analysis of the swimming of microscopic organisms”, *Proceedings of the Royal Society of London, Series A: Mathematical and Physical Sciences* **209**, 447 (1951).
- [16] G. I. Taylor, “The action of waving cylindrical tails in propelling microscopic organisms”, *Proceedings of the Royal Society of London, Series A: Mathematical and Physical Sciences* **211**, 225 (1952).
- [17] G. I. Taylor, *Low Reynolds Number Flow*, edited by A. H. Shapiro, video at <http://techtv.mit.edu/collections/ifluids/videos/32604-low-reynolds-number-flow>, transcript at <http://web.mit.edu/hml/ncfmf/07LRNF.pdf>, National Committee for Fluid Mechanics Films, 1966.
- [18] H. C. Berg and R. A. Anderson, “Bacteria swim by rotating their flagellar filaments”, *Nature* **245**, 380 (1973).
- [19] E. M. Purcell, “Life at low Reynolds number”, *American Journal of Physics* **45**, 3 (1977).
- [20] M. J. Lighthill, “On the squirming motion of nearly spherical deformable bodies through liquids at very small Reynolds numbers”, *Communications on Pure and Applied Mathematics* **5**, 109 (1952).
- [21] J. R. Blake, “A spherical envelope approach to ciliary propulsion”, *Journal of Fluid Mechanics* **46**, 199 (1971).

- [22] R. P. Feynman, “There’s plenty of room at the bottom”, *Engineering and Science* **23**, 22 (1960).
- [23] G. A. Ozin, I. Manners, S. Fournier-Bidoz, and A. Arsenault, “Dream nanomachines”, *Advanced Materials* **17**, 3011 (2005).
- [24] M. Sitti, “Voyage of the microrobots”, *Nature* **458**, 1121 (2009).
- [25] W. F. Paxton, K. C. Kistler, C. C. Olmeda, A. Sen, S. K. St. Angelo, Y. Cao, T. E. Mallouk, P. E. Lammert, and V. H. Crespi, “Catalytic nanomotors: autonomous movement of striped nanorods”, *Journal of the American Chemical Society* **126**, 13424 (2004).
- [26] J. R. Howse, R. A. L. Jones, A. J. Ryan, T. Gough, R. Vafabakhsh, and R. Golestanian, “Self-motile colloidal particles: from directed propulsion to random walk”, *Physical Review Letters* **99**, 048102 (2007).
- [27] S. J. Ebbens and J. R. Howse, “In pursuit of propulsion at the nanoscale”, *Soft Matter* **6**, 726 (2010).
- [28] S. Sengupta, M. E. Ibele, and A. Sen, “Fantastic voyage: designing self-powered nanorobots”, *Angewandte Chemie International Edition* **51**, 8434 (2012).
- [29] J. Elgeti, R. G. Winkler, and G. Gompper, “Physics of microswimmers — single particle motion and collective behavior: a review”, *Reports on Progress in Physics* **78**, 056601 (2015).
- [30] C. Dombrowski, L. Cisneros, S. Chatkaew, R. E. Goldstein, and J. O. Kessler, “Self-Concentration and Large-Scale Coherence in Bacterial Dynamics”, *Physical Review Letters* **93**, 098103 (2004).
- [31] J. Dunkel, S. Heidenreich, K. Drescher, H. H. Wensink, M. Bär, and R. E. Goldstein, “Fluid dynamics of bacterial turbulence”, *Physical Review Letters* **110**, 228102 (2013).
- [32] C. Bechinger, R. D. Leonardo, H. Löwen, C. Reichhardt, G. Volpe, and G. Volpe, “Active particles in complex and crowded environments”, *Reviews of Modern Physics* **88**, 045006 (2016).
- [33] S. Ebbens, D. A. Gregory, G. Dunderdale, J. R. Howse, Y. Ibrahim, T. B. Liverpool, and R. Golestanian, “Electrokinetic effects in catalytic platinum-insulator Janus swimmers”, *Europhysics Letters* **106**, 58003 (2014).
- [34] A. T. Brown and W. C. K. Poon, “Ionic effects in self-propelled Pt-coated Janus swimmers”, *Soft Matter* **10**, 4016 (2014).

- [35] A. T. Brown, W. C. K. Poon, C. Holm, and J. de Graaf, “Ionic screening and dissociation are crucial for understanding chemical self-propulsion in polar solvents”, *Soft Matter* **13**, 1200 (2017).
- [36] Y. Ibrahim, R. Golestanian, and T. B. Liverpool, “Multiple phoretic mechanisms in the self-propulsion of a Pt-insulator Janus swimmer”, *Journal of Fluid Mechanics* **828**, 318 (2017).
- [37] J. Schwarz-Linek, J. Arlt, A. Jepson, A. Dawson, T. Vissers, D. Mioli, T. Pilizota, V. A. Martinez, and W. C. K. Poon, “*Escherichia coli* as a model active colloid: a practical introduction”, *Colloids and Surfaces B: Biointerfaces* **137**, 2 (2016).
- [38] Z. Izri, M. N. Van Der Linden, S. Michelin, and O. Dauchot, “Self-propulsion of pure water droplets by spontaneous Marangoni-stress-driven motion”, *Physical Review Letters* **113**, 248302 (2014).
- [39] L. W. Rogowski, J. Ali, X. Zhang, J. N. Wilking, H. C. Fu, and M. J. Kim, “Symmetry breaking propulsion of magnetic microspheres in nonlinearly viscoelastic fluids”, *Nature Communications* **12**, 1 (2021).
- [40] I. Buttinoni, G. Volpe, F. Kümmel, G. Volpe, and C. Bechinger, “Active Brownian motion tunable by light”, *Journal of Physics: Condensed Matter* **24**, 284129 (2012).
- [41] R. Wittkowski, A. Tiribocchi, J. Stenhammar, R. J. Allen, D. Marenduzzo, and M. E. Cates, “Scalar φ^4 field theory for active-particle phase separation”, *Nature Communications* **5**, 4351 (2014).
- [42] A. P. Solon, J. Stenhammar, M. E. Cates, Y. Kafri, and J. Tailleur, “Generalized thermodynamics of phase equilibria in scalar active matter”, *Physical Review E* **97**, 020602 (2018).
- [43] U. Seifert, “Stochastic thermodynamics, fluctuation theorems and molecular machines”, *Reports on Progress in Physics* **75**, 126001 (2012).
- [44] S. C. Takatori and J. F. Brady, “Towards a thermodynamics of active matter”, *Physical Review E* **91**, 032117 (2015).
- [45] M. C. Marchetti, J.-F. Joanny, S. Ramaswamy, T. B. Liverpool, J. Prost, M. Rao, and R. A. Simha, “Hydrodynamics of soft active matter”, *Reviews of Modern Physics* **85**, 1143 (2013).
- [46] S. Ramaswamy, R. A. Simha, and J. Toner, “Active nematics on a substrate: Giant number fluctuations and long-time tails”, *Europhysics Letters* **62**, 196 (2003).

- [47] E. Lauga and T. R. Powers, “The hydrodynamics of swimming microorganisms”, *Reports on Progress in Physics* **72**, 096601 (2009).
- [48] J. M. Yeomans, D. O. Pushkin, and H. Shum, “An introduction to the hydrodynamics of swimming microorganisms”, *European Physical Journal Special Topics* **223**, 1771 (2014).
- [49] K. Drescher, J. Dunkel, L. H. Cisneros, S. Ganguly, and R. E. Goldstein, “Fluid dynamics and noise in bacterial cell–cell and cell–surface scattering”, *Proceedings of the National Academy of Sciences* **108**, 10940 (2011).
- [50] R. Matas-Navarro, R. Golestanian, T. B. Liverpool, and S. M. Fielding, “Hydrodynamic suppression of phase separation in active suspensions”, *Physical Review E* **90**, 032304 (2014).
- [51] J. Toner and Y. Tu, “Flocks, herds, and schools: A quantitative theory of flocking”, *Physical Review E* **58**, 4828 (1998).
- [52] T. Vicsek, A. Czirók, E. Ben-Jacob, I. Cohen, and O. Shochet, “Novel type of phase transition in a system of self-driven particles”, *Physical Review Letters* **75**, 1226 (1995).
- [53] J. Tailleur and M. E. Cates, “Statistical mechanics of interacting run-and-tumble bacteria”, *Physical Review Letters* **100**, 218103 (2008).
- [54] M. E. Cates, D. Marenduzzo, I. Pagonabarraga, and J. Tailleur, “Arrested phase separation in reproducing bacteria creates a generic route to pattern formation”, *Proceedings of the National Academy of Sciences* **107**, 11715 (2010).
- [55] M. E. Cates and J. Tailleur, “Motility-induced phase separation”, *Annual Review of Condensed Matter Physics* **6**, 219 (2015).
- [56] A. P. Solon, J. Stenhammar, M. E. Cates, Y. Kafri, and J. Tailleur, “Generalized thermodynamics of motility-induced phase separation: phase equilibria, Laplace pressure, and change of ensembles”, *New Journal of Physics* **20**, 075001 (2018).
- [57] B. Partridge and C. F. Lee, “Critical motility-induced phase separation belongs to the Ising universality class”, *Physical Review Letters* **123**, 068002 (2019).
- [58] K. Kruse, J.-F. Joanny, F. Jülicher, J. Prost, and K. Sekimoto, “Asters, vortices, and rotating spirals in active gels of polar filaments”, *Physical Review Letters* **92**, 078101 (2004).
- [59] F. Jülicher, K. Kruse, J. Prost, and J.-F. Joanny, “Active behavior of the cytoskeleton”, *Physics Reports* **449**, 3 (2007).

- [60] L. Giomi, M. J. Bowick, P. Mishra, R. Sknepnek, and M. C. Marchetti, “Defect dynamics in active nematics”, *Philosophical Transactions of the Royal Society of London, Series A: Mathematical, Physical and Engineering Sciences* **372**, 20130365 (2014).
- [61] A. Doostmohammadi, J. Ignés-Mullol, J. M. Yeomans, and F. Sagués, “Active nematics”, *Nature Communications* **9**, 1 (2018).
- [62] F. Kogler and S. H. L. Klapp, “Lane formation in a system of dipolar microswimmers”, *Europhysics Letters* **110**, 10004 (2015).
- [63] J. Yan, M. Han, J. Zhang, C. Xu, E. Luijten, and S. Granick, “Reconfiguring active particles by electrostatic imbalance”, *Nature Materials* **15**, 1095 (2016).
- [64] A. Sokolov, S. Zhou, O. D. Lavrentovich, and I. S. Aranson, “Individual behavior and pairwise interactions between microswimmers in anisotropic liquid”, *Physical Review E* **91**, 013009 (2015).
- [65] M. Theers, E. Westphal, K. Qi, R. G. Winkler, and G. Gompper, “Clustering of microswimmers: interplay of shape and hydrodynamics”, *Soft Matter* **14**, 8590 (2018).
- [66] F. J. Schwarzendahl and M. G. Mazza, “Hydrodynamic interactions dominate the structure of active swimmers’ pair distribution functions”, *Journal of Chemical Physics* **150**, 184902 (2019).
- [67] J. Elgeti and G. Gompper, “Microswimmers near surfaces”, *European Physical Journal Special Topics* **225**, 2333 (2016).
- [68] H. Moore, K. Dvorakova, N. Jenkins, and W. Breed, “Exceptional sperm cooperation in the wood mouse”, *Nature* **418**, 174 (2002).
- [69] Rothschild, “Non-random distribution of bull spermatozoa in a drop of sperm suspension”, *Nature* **198**, 1221 (1963).
- [70] H. C. Berg and L. Turner, “Chemotaxis of bacteria in glass capillary arrays. *Escherichia coli*, motility, microchannel plate, and light scattering”, *Biophysical Journal* **58**, 919 (1990).
- [71] M. J. Kim and K. S. Breuer, “Enhanced diffusion due to motile bacteria”, *Physics of Fluids* **16**, L78 (2004).
- [72] A. Sokolov, R. E. Goldstein, F. I. Feldchtein, and I. S. Aranson, “Enhanced mixing and spatial instability in concentrated bacterial suspensions”, *Physical Review E* **80**, 031903 (2009).
- [73] J. Stenhammar, C. Nardini, R. W. Nash, D. Marenduzzo, and A. Morozov, “Role of correlations in the collective behavior of microswimmer suspensions”, *Physical Review Letters* **119**, 028005 (2017).

- [74] V. Škultéty, C. Nardini, J. Stenhammar, D. Marenduzzo, and A. Morozov, “Swimming suppresses correlations in dilute suspensions of pusher microorganisms”, *Physical Review X* **10**, 031059 (2020).
- [75] A. Zöttl and H. Stark, “Hydrodynamics determines collective motion and phase behavior of active colloids in quasi-two-dimensional confinement”, *Physical Review Letters* **112**, 118101 (2014).
- [76] E. Lauga, “Life around the scallop theorem”, *Soft Matter* **7**, 3060 (2011).
- [77] T. Qiu, T.-C. Lee, A. G. Mark, K. I. Morozov, R. Münster, O. Mierka, S. Turek, A. M. Leshansky, and P. Fischer, “Swimming by reciprocal motion at low Reynolds number”, *Nature Communications* **5**, 5119 (2014).
- [78] T. Normand and E. Lauga, “Flapping motion and force generation in a viscoelastic fluid”, *Physical Review E* **78**, 061907 (2008).
- [79] E. Lauga, “Continuous breakdown of Purcell’s scallop theorem with inertia”, *Physics of Fluids* **19**, 061703 (2007).
- [80] D. Gonzalez-Rodriguez and E. Lauga, “Reciprocal locomotion of dense swimmers in Stokes flow”, *Journal of Physics: Condensed Matter* **21**, 204103 (2009).
- [81] M. Hubert, O. Trosman, Y. Collard, A. Sukhov, J. Harting, N. Vandewalle, and A.-S. Smith, “Scallop Theorem and Swimming at the Mesoscale”, *Physical Review Letters* **126**, 224501 (2021).
- [82] E. Lauga and D. Bartolo, “No many-scallop theorem: Collective locomotion of reciprocal swimmers”, *Physical Review E* **78**, 030901 (2008).
- [83] R. Trouilloud, S. Y. Tony, A. E. Hosoi, and E. Lauga, “Soft swimming: Exploiting deformable interfaces for low Reynolds number locomotion”, *Physical Review Letters* **101**, 048102 (2008).
- [84] C. Brennen and H. Winet, “Fluid mechanics of propulsion by cilia and flagella”, *Annual Review of Fluid Mechanics* **9**, 339 (1977).
- [85] H. C. Berg, “The rotary motor of bacterial flagella”, *Annual Review of Biochemistry* **72**, 19 (2003).
- [86] R. G. Winkler and G. Gompper, “Hydrodynamics in motile active matter”, in *Handbook of Materials Modeling: Methods: Theory and Modeling*, edited by W. Andreoni and S. Yip (Springer, 2020), pages 1471–1491, ISBN: 978-3-319-44676-9.

- [87] C. A. Solari, K. Drescher, and R. E. Goldstein, “The flagellar photoreponse in *Volvox* species (Volvocaceae, Chlorophyceae)”, *Journal of Phycology* **47**, 580 (2011).
- [88] S. Sengupta, K. K. Dey, H. S. Muddana, T. Tabouillot, M. E. Ibele, P. J. Butler, and A. Sen, “Enzyme molecules as nanomotors”, *Journal of the American Chemical Society* **135**, 1406 (2013).
- [89] X. Ma, A. C. Hortelão, T. Patiño, and S. Sánchez, “Enzyme Catalysis To Power Micro/Nanomachines”, *ACS Nano* **10**, 9111 (2016).
- [90] B. M. Friedrich, I. H. Riedel-Kruse, J. Howard, and F. Jülicher, “High-precision tracking of sperm swimming fine structure provides strong test of resistive force theory”, *Journal of Experimental Biology* **213**, 1226 (2010).
- [91] S. S. Suarez, “Mammalian sperm interactions with the female reproductive tract”, *Cell and Tissue Research* **363**, 185 (2016).
- [92] J. P. Celli, B. S. Turner, N. H. Afdhal, S. Keates, I. Ghiran, C. P. Kelly, R. H. Ewoldt, G. H. McKinley, P. So, S. Erramilli, et al., “*Helicobacter pylori* moves through mucus by reducing mucin viscoelasticity”, *Proceedings of the National Academy of Sciences* **106**, 14321 (2009).
- [93] P. C. Y. Lau, J. R. Dutcher, T. J. Beveridge, and J. S. Lam, “Absolute quantitation of bacterial biofilm adhesion and viscoelasticity by microbead force spectroscopy”, *Biophysical Journal* **96**, 2935 (2009).
- [94] N. Heddergott, T. Krüger, S. B. Babu, A. Wei, E. Stellamanns, S. Uppaluri, T. Pfohl, H. Stark, and M. Engstler, “Trypanosome motion represents an adaptation to the crowded environment of the vertebrate bloodstream”, *PLoS Pathogens* **8**, e1003023 (2012).
- [95] R. Dreyfus, J. Baudry, M. L. Roper, M. Fermigier, H. A. Stone, and J. Bibette, “Microscopic artificial swimmers”, *Nature* **437**, 862 (2005).
- [96] T. Sanchez, D. Welch, D. Nicastro, and Z. Dogic, “Cilia-like beating of active microtubule bundles”, *Science* **333**, 456 (2011).
- [97] Y. Hong, N. M. K. Blackman, N. D. Kopp, A. Sen, and D. Velegol, “Chemotaxis of nonbiological colloidal rods”, *Physical Review Letters* **99**, 178103 (2007).
- [98] A. Sen, M. Ibele, Y. Hong, and D. Velegol, “Chemo and phototactic nano/microbots”, *Faraday Discussions* **143**, 15 (2009).
- [99] J. Adler, “Chemoreceptors in bacteria”, *Science* **166**, 1588 (1969).

- [100] S. Fournier-Bidoz, A. C. Arsenault, I. Manners, and G. A. Ozin, “Synthetic self-propelled nanorotors”, *Chemical Communications*, 441 (2005).
- [101] J. L. Moran, P. M. Wheat, and J. D. Posner, “Locomotion of electrocatalytic nanomotors due to reaction induced charge autoelectrophoresis”, *Physical Review E* **81**, 065302 (2010).
- [102] W. F. Paxton, A. Sen, and T. E. Mallouk, “Motility of catalytic nanoparticles through self-generated forces”, *Chemistry: A European Journal* **11**, 6462 (2005).
- [103] P. Mitchell, “Self-electrophoretic locomotion in microorganisms: Bacterial flagella as giant ionophores”, *FEBS Letters* **28**, 1 (1972).
- [104] M. de Corato, X. Arqu e, T. Pati no, M. Arroyo, S. S nchez, and I. Pagonabarraga, “Self-propulsion of active colloids via ion Release: theory and experiments”, *Physical Review Letters* **124**, 108001 (2020).
- [105] A. Erbe, M. Zientara, L. Baraban, C. Kreidler, and P. Leiderer, “Various driving mechanisms for generating motion of colloidal particles”, *Journal of Physics: Condensed Matter* **20**, 404215 (2008).
- [106] R. Golestanian, T. B. Liverpool, and A. Ajdari, “Propulsion of a molecular machine by asymmetric distribution of reaction products”, *Physical Review Letters* **94**, 220801 (2005).
- [107] R. Golestanian, T. B. Liverpool, and A. Ajdari, “Designing phoretic micro- and nano-swimmers”, *New Journal of Physics* **9**, 126 (2007).
- [108] B. Sabass and U. Seifert, “Dynamics and efficiency of a self-propelled, diffusiphoretic swimmer”, *Journal of Chemical Physics* **136**, 064508 (2012).
- [109] A. M. Brooks, M. Tasinkevych, S. Sabrina, D. Velegol, A. Sen, and K. J. M. Bishop, “Shape-directed rotation of homogeneous micromotors via catalytic self-electrophoresis”, *Nature Communications* **10**, 1 (2019).
- [110] H.-R. Jiang, N. Yoshinaga, and M. Sano, “Active motion of a Janus particle by self-thermophoresis in a defocused laser beam”, *Physical Review Letters* **105**, 268302 (2010).
- [111] G. Volpe, I. Buttinoni, D. Vogt, H.-J. K ummerer, and C. Bechinger, “Microswimmers in patterned environments”, *Soft Matter* **7**, 8810 (2011).
- [112] S. S nchez, A. A. Solovev, S. M. Harazim, C. Deneke, Y. Feng Mei, and O. G. Schmidt, “The smallest man-made jet engine”, *Chemical Record* **11**, 367 (2011).

- [113] Y.-J. Chen, Y. Nagamine, and K. Yoshikawa, “Self-propelled motion of a droplet induced by Marangoni-driven spreading”, *Physical Review E* **80**, 016303 (2009).
- [114] C. Jin, C. Krüger, and C. C. Maass, “Chemotaxis and autochemotaxis of self-propelling droplet swimmers”, *Proceedings of the National Academy of Sciences* **114**, 5089 (2017).
- [115] A. Bricard, J.-B. Caussin, N. Desreumaux, O. Dauchot, and D. Bartolo, “Emergence of macroscopic directed motion in populations of motile colloids”, *Nature* **503**, 95 (2013).
- [116] E. Han, L. Zhu, J. W. Shaevitz, and H. A. Stone, “Low-Reynolds-number, biflagellated Quincke swimmers with multiple forms of motion”, *Proceedings of the National Academy of Sciences* **118**, e2022000118 (2021).
- [117] B.-W. Park, J. Zhuang, O. Yasa, and M. Sitti, “Multifunctional bacteria-driven microswimmers for targeted active drug delivery”, *ACS Nano* **11**, 8910 (2017).
- [118] D. O. Pushkin and J. M. Yeomans, “Fluid mixing by curved trajectories of microswimmers”, *Physical Review Letters* **111**, 188101 (2013).
- [119] M. Ibele, T. E. Mallouk, and A. Sen, “Schooling behavior of light-powered autonomous micromotors in water”, *Angewandte Chemie International Edition* **48**, 3308 (2009).
- [120] I. Theurkauff, C. Cottin-Bizonne, J. Palacci, C. Ybert, and L. Bocquet, “Dynamic clustering in active colloidal suspensions with chemical signaling”, *Physical Review Letters* **108**, 268303 (2012).
- [121] I. Buttinoni, J. Bialké, F. Kümmel, H. Löwen, C. Bechinger, and T. Speck, “Dynamical clustering and phase separation in suspensions of self-propelled colloidal particles”, *Physical Review Letters* **110**, 238301 (2013).
- [122] J. Palacci, S. Sacanna, A. P. Steinberg, D. J. Pine, and P. M. Chaikin, “Living crystals of light-activated colloidal surfers”, *Science* **339**, 936 (2013).
- [123] A. Wysocki, R. G. Winkler, and G. Gompper, “Cooperative motion of active Brownian spheres in three-dimensional dense suspensions”, *Europhysics Letters* **105**, 48004 (2014).
- [124] E. Lushi, H. Wioland, and R. E. Goldstein, “Fluid flows created by swimming bacteria drive self-organization in confined suspensions”, *Proceedings of the National Academy of Sciences* **111**, 9733 (2014).

- [125] A. Reinmüller, H. J. Schöpe, and T. Palberg, “Self-Organized Cooperative Swimming at Low Reynolds Numbers”, *Langmuir* **29**, 1738 (2013).
- [126] T. Bäuerle, A. Fischer, T. Speck, and C. Bechinger, “Self-organization of active particles by quorum sensing rules”, *Nature Communications* **9**, 1 (2018).
- [127] S. Ketzetzi, M. Rinaldin, P. Dröge, J. de Graaf, and D. J. Kraft, “Activity-induced microswimmer interactions and cooperation in one-dimensional environments”, arXiv preprint [arXiv:2103.07335](https://arxiv.org/abs/2103.07335) (2021).
- [128] C. A. Solari, J. O. Kessler, and R. E. Goldstein, “Motility, mixing, and multicellularity”, *Genetic Programming and Evolvable Machines* **8**, 115 (2007).
- [129] M. Theers, E. Westphal, G. Gompper, and R. G. Winkler, “Modeling a spheroidal microswimmer and cooperative swimming in a narrow slit”, *Soft Matter* **12**, 7372 (2016).
- [130] V. A. Martinez, J. Schwarz-Linek, M. Reufer, L. G. Wilson, A. N. Morozov, and W. C. K. Poon, “Flagellated bacterial motility in polymer solutions”, *Proceedings of the National Academy of Sciences* **111**, 17771 (2014).
- [131] T. Y. Molotilin, V. Lobaskin, and O. I. Vinogradova, “Electrophoresis of Janus particles: A molecular dynamics simulation study”, *Journal of Chemical Physics* **145**, 244704 (2016).
- [132] J. L. Anderson, “Colloid transport by interfacial forces”, *Annual Review of Fluid Mechanics* **21**, 61 (1989).
- [133] M. N. Popescu, W. E. Uspal, and S. Dietrich, “Self-diffusiophoresis of chemically active colloids”, *European Physical Journal Special Topics* **225**, 2189 (2016).
- [134] A. Scagliarini and I. Pagonabarraga, “Unravelling the role of phoretic and hydrodynamic interactions in active colloidal suspensions”, *Soft Matter* **16**, 8893 (2020).
- [135] M. N. Popescu, W. E. Uspal, and S. Dietrich, “Chemically active colloids near osmotic-responsive walls with surface-chemistry gradients”, *Journal of Physics: Condensed Matter* **29**, 134001 (2017).
- [136] R. Niu, P. Kreissl, A. T. Brown, G. Rempfer, D. Botin, C. Holm, T. Palberg, and J. de Graaf, “Microfluidic pumping by micromolar salt concentrations”, *Soft Matter* **13**, 1505 (2017).

- [137] E. Kanso and S. Michelin, “Phoretic and hydrodynamic interactions of weakly confined autophoretic particles”, *Journal of Chemical Physics* **150**, 044902 (2019).
- [138] R. Kohl, E. Corona, V. Cheruvu, and S. Veerapaneni, “Fast and accurate solvers for simulating Janus particle suspensions in Stokes flow”, arXiv preprint [arXiv:2104.14068](https://arxiv.org/abs/2104.14068) (2021).
- [139] J. L. Moran and J. D. Posner, “Role of solution conductivity in reaction induced charge auto-electrophoresis”, *Physics of Fluids* **26**, 042001 (2014).
- [140] P. Kreissl, C. Holm, and J. de Graaf, “The efficiency of self-phoretic propulsion mechanisms with surface reaction heterogeneity”, *Journal of Chemical Physics* **144**, 204902 (2016).
- [141] Y. Daghighi, Y. Gao, and D. Li, “3D numerical study of induced-charge electrokinetic motion of heterogeneous particle in a microchannel”, *Electrochimica acta* **56**, 4254 (2011).
- [142] C. M. Pooley and J. M. Yeomans, “Lattice Boltzmann simulation techniques for simulating microscopic swimmers”, *Computer Physics Communications* **179**, 159 (2008).
- [143] T.-H. Wu, R.-S. Guo, G.-W. He, Y.-M. Liu, and D. Qi, “Simulation of swimming of a flexible filament using the generalized lattice-spring lattice-Boltzmann method”, *Journal of Theoretical Biology* **349**, 1 (2014).
- [144] Y. Yang, V. Marceau, and G. Gompper, “Swarm behavior of self-propelled rods and swimming flagella”, *Physical Review E* **82**, 031904 (2010).
- [145] S. B. Babu and H. Stark, “Modeling the locomotion of the African trypanosome using multi-particle collision dynamics”, *New Journal of Physics* **14**, 085012 (2012).
- [146] F. Lugli, E. Brini, and F. Zerbetto, “Shape governs the motion of chemically propelled janus swimmers”, *Journal of Physical Chemistry C* **116**, 592 (2011).
- [147] D. A. Fedosov, A. Sengupta, and G. Gompper, “Effect of fluid–colloid interactions on the mobility of a thermophoretic microswimmer in non-ideal fluids”, *Soft Matter* **11**, 6703 (2015).
- [148] T. Ishikawa, M. P. Simmonds, and T. J. Pedley, “Hydrodynamic interaction of two swimming model micro-organisms”, *Journal of Fluid Mechanics* **568**, 119 (2006).

- [149] M. T. Downton and H. Stark, “Simulation of a model microswimmer”, *Journal of Physics: Condensed Matter* **21**, 204101 (2009).
- [150] I. O. Götze and G. Gompper, “Mesoscale simulations of hydrodynamic squirmer interactions”, *Physical Review E* **82**, 041921 (2010).
- [151] I. Llopis and I. Pagonabarraga, “Hydrodynamic interactions in squirmer motion: Swimming with a neighbour and close to a wall”, *Journal of Non-Newtonian Fluid Mechanics* **165**, 946 (2010).
- [152] K. Ishimoto and E. A. Gaffney, “Squirmer dynamics near a boundary”, *Physical Review E* **88**, 062702 (2013).
- [153] L. Zhu, E. Lauga, and L. Brandt, “Low-Reynolds-number swimming in a capillary tube”, *Journal of Fluid Mechanics* **726**, 285 (2013).
- [154] S. Michelin and E. Lauga, “Phoretic self-propulsion at finite Péclet numbers”, *Journal of Fluid Mechanics* **747**, 572 (2014).
- [155] Y. Ibrahim and T. B. Liverpool, “How walls affect the dynamics of self-phoretic microswimmers”, *European Physical Journal Special Topics* **225**, 1843 (2016).
- [156] M. N. Popescu, W. E. Uspal, Z. Eskandari, M. Tasinkevych, and S. Dietrich, “Effective squirmer models for self-phoretic chemically active spherical colloids”, *European Physical Journal E* **41**, 145 (2018).
- [157] F. Alarcón and I. Pagonabarraga, “Spontaneous aggregation and global polar ordering in squirmer suspensions”, *Journal of Molecular Liquids* **185**, 56 (2013).
- [158] G. Gonnella, D. Marenduzzo, A. Suma, and A. Tiribocchi, “Motility-induced phase separation and coarsening in active matter”, *Comptes Rendus Physique* **16**, 316 (2015).
- [159] J. Blaschke, M. Maurer, K. Menon, A. Zöttl, and H. Stark, “Phase separation and coexistence of hydrodynamically interacting microswimmers”, *Soft Matter* **12**, 9821 (2016).
- [160] A. Zöttl and H. Stark, “Emergent behavior in active colloids”, *Journal of Physics: Condensed Matter* **28**, 253001 (2016).
- [161] T. Ishikawa and T. J. Pedley, “Coherent structures in monolayers of swimming particles”, *Physical Review Letters* **100**, 088103 (2008).
- [162] T. Ishikawa, J. T. Locsei, and T. J. Pedley, “Development of coherent structures in concentrated suspensions of swimming model microorganisms”, *Journal of Fluid Mechanics* **615**, 401 (2008).

- [163] S. E. Spagnolie, G. R. Moreno-Flores, D. Bartolo, and E. Lauga, “Geometric capture and escape of a microswimmer colliding with an obstacle”, *Soft Matter* **11**, 3396 (2015).
- [164] A. Chamolly, T. Ishikawa, and E. Lauga, “Active particles in periodic lattices”, *New Journal of Physics* **19**, 115001 (2017).
- [165] D. Papavassiliou and G. P. Alexander, “The many-body reciprocal theorem and swimmer hydrodynamics”, *Europhysics Letters* **110**, 44001 (2015).
- [166] A. R. Sprenger, V. A. Shaik, A. M. Ardekani, M. Lisicki, A. J. T. M. Mathijssen, F. Guzmán-Lastra, H. Löwen, A. M. Menzel, and A. Daddi-Moussa-Ider, “Towards an analytical description of active microswimmers in clean and in surfactant-covered drops”, *European Physical Journal E* **43**, 1 (2020).
- [167] K. V. S. Chaithanya and S. P. Thampi, “Wall-curvature driven dynamics of a microswimmer”, *Physical Review Fluids* **6**, 083101 (2021).
- [168] A. Zöttl and J. M. Yeomans, “Enhanced bacterial swimming speeds in macromolecular polymer solutions”, *Nature Physics* **15**, 554 (2019).
- [169] K. Qi, E. Westphal, G. Gompper, and R. G. Winkler, “Enhanced rotational motion of spherical squirmer in polymer solutions”, *Physical Review Letters* **124**, 068001 (2020).
- [170] J. de Graaf and J. Stenhammar, “Lattice-Boltzmann simulations of microswimmer-tracer interactions”, *Physical Review E* **95**, 023302 (2017).
- [171] D. Bárdfalvy, H. Nordanger, C. Nardini, A. Morozov, and J. Stenhammar, “Particle-resolved lattice Boltzmann simulations of 3-dimensional active turbulence”, *Soft Matter* **15**, 7747 (2019).
- [172] F. Schweitzer, W. Ebeling, and B. Tilch, “Complex motion of Brownian particles with energy depots”, *Physical Review Letters* **80**, 5044 (1998).
- [173] W. Ebeling, F. Schweitzer, and B. Tilch, “Active Brownian particles with energy depots modeling animal mobility”, *BioSystems* **49**, 17 (1999).
- [174] P. Romanczuk, M. Bär, W. Ebeling, B. Lindner, and L. Schimansky-Geier, “Active Brownian particles”, *European Physical Journal Special Topics* **202**, 1 (2012).

- [175] J. Stenhammar, D. Marenduzzo, R. J. Allen, and M. E. Cates, “Phase behaviour of active Brownian particles: the role of dimensionality”, *Soft Matter* **10**, 1489 (2014).
- [176] A. P. Solon, M. E. Cates, and J. Tailleur, “Active brownian particles and run-and-tumble particles: A comparative study”, *European Physical Journal Special Topics* **224**, 1231 (2015).
- [177] Y. Hatwalne, S. Ramaswamy, M. Rao, and R. A. Simha, “Rheology of active-particle suspensions”, *Physical Review Letters* **92**, 118101 (2004).
- [178] T. B. Liverpool and M. C. Marchetti, “Bridging the microscopic and the hydrodynamic in active filament solutions”, *Europhysics Letters* **69**, 846 (2005).
- [179] D. Saintillan and M. J. Shelley, “Active suspensions and their nonlinear models”, *Comptes Rendus Physique* **14**, 497 (2013).
- [180] S. Heidenreich, J. Dunkel, S. H. L. Klapp, and M. Bär, “Hydrodynamic length-scale selection in microswimmer suspensions”, *Physical Review E* **94**, 020601 (2016).
- [181] H. Reinken, S. H. L. Klapp, M. Bär, and S. Heidenreich, “Derivation of a hydrodynamic theory for mesoscale dynamics in microswimmer suspensions”, *Physical Review E* **97**, 022613 (2018).
- [182] B. Liebchen, D. Marenduzzo, I. Pagonabarraga, and M. E. Cates, “Clustering and pattern formation in chemorepulsive active colloids”, *Physical Review Letters* **115**, 258301 (2015).
- [183] S. Paliwal, J. Rodenburg, R. van Roij, and M. Dijkstra, “Chemical potential in active systems: predicting phase equilibrium from bulk equations of state?”, *New Journal of Physics* **20**, 015003 (2018).
- [184] D. Nesbitt, G. Pruessner, and C. F. Lee, “Uncovering novel phase transitions in dense dry polar active fluids using a lattice Boltzmann method”, *New Journal of Physics* **23**, 043047 (2021).
- [185] H. Chen and J.-L. Thiffeault, “Shape matters: a Brownian microswimmer in a channel”, *Journal of Fluid Mechanics* **916**, A15 (2021).
- [186] D. Marenduzzo, E. Orlandini, M. E. Cates, and J. M. Yeomans, “Steady-state hydrodynamic instabilities of active liquid crystals: Hybrid lattice Boltzmann simulations”, *Physical Review E* **76**, 031921 (2007).

- [187] E. Orlandini, M. E. Cates, D. Marenduzzo, L. Tubiana, and J. M. Yeomans, “Hydrodynamic of Active Liquid Crystals: A Hybrid Lattice Boltzmann Approach”, *Molecular Crystals and Liquid Crystals* **494**, 293 (2008).
- [188] M. E. Cates, O. Henrich, D. Marenduzzo, and K. Stratford, “Lattice Boltzmann simulations of liquid crystalline fluids: active gels and blue phases”, *Soft Matter* **5**, 3791 (2009).
- [189] T. Kozhukhov and T. N. Shendruk, *Active Multi-Particle Collision Dynamics: Collision Operators for Coarse Grained Simulation of Active Nematic Liquid Crystals*, APS March Meeting, 2021.
- [190] J. Stenhammar, A. Tiribocchi, R. J. Allen, D. Marenduzzo, and M. E. Cates, “Continuum theory of phase separation kinetics for active Brownian particles”, *Physical Review Letters* **111**, 145702 (2013).
- [191] A. Morozov and S. E. Spagnolie, “Introduction to Complex Fluids”, in *Complex Fluids in Biological Systems: Experiment, Theory, and Computation*, edited by S. E. Spagnolie (Springer Science+Business Media, New York, 2015), pages 3–52, ISBN: 978-1-4939-2065-5.
- [192] G. G. Stokes, “On the effect of the internal friction of fluids on the motion of pendulums”, *Transactions of the Cambridge Philosophical Society* **9**, 8 (1851).
- [193] J. G. Oldroyd, “On the formulation of rheological equations of state”, *Proceedings of the Royal Society of London, Series A: Mathematical and Physical Sciences* **200**, 523 (1950).
- [194] H. Jeffreys, *The Earth: Its Origin, History and Physical Constitution* (Cambridge University Press, Cambridge, 1976), ISBN: 978-0-521-20648-8.
- [195] R. B. Bird, R. C. Armstrong, and O. Hassager, *Dynamics of Polymeric Liquids, Volume 1: Fluid Mechanics* (Wiley-Interscience, New York, 1987), ISBN: 978-0-471-80245-7.
- [196] H. Giesekus, “A simple constitutive equation for polymer fluids based on the concept of deformation-dependent tensorial mobility”, *Journal of Non-Newtonian Fluid Mechanics* **11**, 69 (1982).
- [197] A. Peterlin, “Hydrodynamics of macromolecules in a velocity field with longitudinal gradient”, *Journal of Polymer Science Part B: Polymer Letters* **4**, 287 (1966).
- [198] M. D. Chilcott and J. M. Rallison, “Creeping flow of dilute polymer solutions past cylinders and spheres”, *Journal of Non-Newtonian Fluid Mechanics* **29**, 381 (1988).

- [199] N. Phan-Thien and R. I. Tanner, “A new constitutive equation derived from network theory”, *Journal of Non-Newtonian Fluid Mechanics* **2**, 353 (1977).
- [200] K. Kremer and G. S. Grest, “Dynamics of entangled linear polymer melts: A molecular-dynamics simulation”, *Journal of Chemical Physics* **92**, 5057 (1990).
- [201] M. Deville and T. B. Gatski, *Mathematical Modeling for Complex Fluids and Flows* (Springer Science+Business Media, Berlin, 2012), ISBN: 978-3-642-43560-7.
- [202] R. B. Bird, C. F. Curtiss, R. C. Armstrong, and O. Hassager, *Dynamics of Polymeric Liquids, Volume 2: Kinetic Theory* (Wiley-Interscience, New York, 1987), ISBN: 978-0-471-80244-0.
- [203] A. Jayaram, “Explicit Modelling of Viscoelastic Media Based on the Lattice-Boltzmann Method”, Master’s thesis (University of Stuttgart, 2018).
- [204] A. Fick, “Ueber Diffusion”, *Annalen der Physik* **170**, 59 (1855).
- [205] A. Einstein, “Über die von der molekularkinetischen Theorie der Wärme geforderte Bewegung von in ruhenden Flüssigkeiten suspendierten Teilchen”, *Annalen der Physik* **322**, 549 (1905).
- [206] M. von Smoluchowski, “Zur Kinetischen Theorie der Brownschen Molekularbewegung und der Suspensionen”, *Annalen der Physik* **326**, 756 (1906).
- [207] A. Gupta, S. Shim, L. Issah, C. McKenzie, and H. A. Stone, “Diffusion of multiple electrolytes cannot be treated independently: model predictions with experimental validation”, *Soft Matter* **15**, 9965 (2019).
- [208] J. de Graaf, G. Rempfer, and C. Holm, “Diffusiophoretic Self-Propulsion for Partially Catalytic Spherical Colloids”, *IEEE Transactions on NanoBioscience* **14**, 272 (2015).
- [209] G. Rempfer, G. B. Davies, C. Holm, and J. de Graaf, “Reducing spurious flow in simulations of electrokinetic phenomena”, *Journal of Chemical Physics* **145**, 044901 (2016).
- [210] M. Gouy, “Sur la constitution de la charge électrique à la surface d’un électrolyte”, *Journal de Physique Théorique et Appliquée* **9**, 457 (1910).
- [211] D. L. Chapman, “A contribution to the theory of electrocapillarity”, *Philosophical Magazine* **25**, 475 (1913).

- [212] P. Debye and E. Hückel, “Zur Theorie der Elektrolyte. I. Gefrierpunktserniedrigung und verwandte Erscheinungen”, *Physikalische Zeitschrift* **24**, 185 (1923).
- [213] M. Kuron, “Efficient Lattice Boltzmann Algorithms for Colloids Undergoing Electrophoresis”, Master’s thesis (University of Stuttgart, 2015).
- [214] A. Ajdari and L. Bocquet, “Giant amplification of interfacially driven transport by hydrodynamic slip: Diffusio-osmosis and beyond”, *Physical Review Letters* **96**, 186102 (2006).
- [215] L. Bocquet and J.-L. Barrat, “Flow boundary conditions from nano- to micro-scales”, *Soft Matter* **3**, 685 (2007).
- [216] D. M. Huang, C. Sendner, D. Horinek, R. R. Netz, and L. Bocquet, “Water Slippage versus Contact Angle: A Quasiuniversal Relationship”, *Physical Review Letters* **101**, 226101 (2008).
- [217] S. Ketzetzi, J. de Graaf, R. P. Doherty, and D. J. Kraft, “Slip length dependent propulsion speed of catalytic colloidal swimmers near walls”, *Physical Review Letters* **124**, 048002 (2020).
- [218] A. Arnold and C. Holm, “Efficient methods to compute long range interactions for soft matter systems”, in *Advanced Computer Simulation Approaches for Soft Matter Sciences II*, edited by C. Holm and K. Kremer, *Advances in Polymer Science* 185 (Springer, Berlin, 2005), pages 59–109, ISBN: 978-3-540-26091-2.
- [219] T. Ishikawa, “Suspension biomechanics of swimming microbes”, *Journal of The Royal Society Interface* **6**, 815 (2009).
- [220] A. J. T. M. Mathijssen, A. Doostmohammadi, J. M. Yeomans, and T. N. Shendruk, “Hydrodynamics of micro-swimmers in films”, *Journal of Fluid Mechanics* **806**, 35 (2016).
- [221] A. J. T. M. Mathijssen, D. O. Pushkin, and J. M. Yeomans, “Tracer trajectories and displacement due to a micro-swimmer near a surface”, *Journal of Fluid Mechanics* **773**, 498 (2015).
- [222] R. Cortez, L. Fauci, and A. Medovikov, “The method of regularized Stokeslets in three dimensions: analysis, validation, and application to helical swimming”, *Physics of Fluids* **17**, 031504 (2005).
- [223] K. Drescher, R. E. Goldstein, N. Michel, M. Polin, and I. Tuval, “Direct measurement of the flow field around swimming microorganisms”, *Physical Review Letters* **105**, 168101 (2010).

- [224] T. Ishikawa and M. Hota, “Interaction of two swimming *Paramecia*”, *Journal of Experimental Biology* **209**, 4452 (2006).
- [225] G. Gompper, T. Ihle, D. M. Kroll, and R. G. Winkler, “Multi-particle collision dynamics: A particle-based mesoscale simulation approach to the hydrodynamics of complex fluids”, in *Advanced Computer Simulation Approaches for Soft Matter Sciences III*, edited by C. Holm and K. Kremer, *Advances in Polymer Science* 221 (Springer, Berlin, 2009), pages 1–87, ISBN: 978-3-540-87705-9.
- [226] C.-C. Huang, G. Gompper, and R. G. Winkler, “Hydrodynamic correlations in multiparticle collision dynamics fluids”, *Physical Review E* **86**, 056711 (2012).
- [227] D. Wei, P. G. Dehnavi, M.-E. Aubin-Tam, and D. Tam, “Measurements of the unsteady flow field around beating cilia”, *Journal of Fluid Mechanics* **915**, A70 (2021).
- [228] K. Ishimoto, “A spherical squirming swimmer in unsteady Stokes flow”, *Journal of Fluid Mechanics* **723**, 163 (2013).
- [229] I. Fouxon and Y. Or, “Inertial self-propulsion of spherical microswimmers by rotation-translation coupling”, *Physical Review Fluids* **4**, 023101 (2019).
- [230] J. M. Dealy, “Weissenberg and Deborah numbers—their definition and use”, *Rheology Bulletin* **79** (2), 14 (2010).
- [231] H. A. Lorentz, “Eene algemeene stelling omtrent de beweging eener vloeistof met wrijving en eenige daaruit afgeleide gevolgen”, *Verslagen der Afdeeling Natuurkunde van de Koninklijke Akademie van Wetenschappen* **5**, 168 (1896).
- [232] G. J. Hancock, “The self-propulsion of microscopic organisms through liquids”, *Proceedings of the Royal Society of London, Series A: Mathematical and Physical Sciences* **217**, 96 (1953).
- [233] C. W. Oseen, *Neuere Methoden und Ergebnisse in der Hydrodynamik*, edited by E. Hilb (Akademische Verlagsgesellschaft, Leipzig, 1927).
- [234] M. Lisicki, “Four approaches to hydrodynamic Green’s functions—the Oseen tensors”, arXiv preprint [arXiv:1312.6231](https://arxiv.org/abs/1312.6231) (2013).
- [235] C. Pozrikidis, *Boundary integral and singularity methods for linearized viscous flow* (Cambridge University Press, Cambridge, 1992), ISBN: 978-0-511-62412-4.
- [236] A. T. Chwang and T. Y.-T. Wu, “Hydromechanics of low-Reynolds-number flow. Part 2. Singularity method for Stokes flows”, *Journal of Fluid Mechanics* **67**, 787 (1975).

- [237] S. E. Spagnolie and E. Lauga, “Hydrodynamics of self-propulsion near a boundary: predictions and accuracy of far-field approximations”, *Journal of Fluid Mechanics* **700**, 105 (2012).
- [238] B. U. Felderhof, “Hydrodynamic interaction between two spheres”, *Physica A: Statistical Mechanics and its Applications* **89**, 373 (1977).
- [239] J. R. Blake, “A note on the image system for a stokeslet in a no-slip boundary”, *Mathematical Proceedings of The Cambridge Philosophical Society* **70**, 303 (1971).
- [240] Y. von Hansen, M. Hinczewski, and R. R. Netz, “Hydrodynamic screening near planar boundaries: Effects on semiflexible polymer dynamics”, *Journal of Chemical Physics* **134**, 235102 (2011).
- [241] N. Uchida and R. Golestanian, “Hydrodynamic synchronization between objects with cyclic rigid trajectories”, *European Physical Journal E* **35**, 1 (2012).
- [242] M. Lisicki, B. Cichocki, and E. Wajnryb, “Near-wall diffusion tensor of an axisymmetric colloidal particle”, *Journal of Chemical Physics* **145**, 034904 (2016).
- [243] A. Daddi-Moussa-Ider and S. Gekle, “Brownian motion near an elastic cell membrane: A theoretical study”, *European Physical Journal E* **41**, 1 (2018).
- [244] E. M. Gauger, M. T. Downton, and H. Stark, “Fluid transport at low Reynolds number with magnetically actuated artificial cilia”, *European Physical Journal E* **28**, 231 (2009).
- [245] F. Meng, D. Matsunaga, J. M. Yeomans, and R. Golestanian, “Magnetically-actuated artificial cilium: a simple theoretical model”, *Soft Matter* **15**, 3864 (2019).
- [246] G. K. Batchelor, “The stress system in a suspension of force-free particles”, *Journal of Fluid Mechanics* **41**, 545 (1970).
- [247] C. Aponte-Rivera and R. N. Zia, “Simulation of hydrodynamically interacting particles confined by a spherical cavity”, *Physical Review Fluids* **1**, 023301 (2016).
- [248] J. R. Blake and A. T. Chwang, “Fundamental singularities of viscous flow”, *Journal of Engineering Mathematics* **8**, 23 (1974).
- [249] A. Chamolly and E. Lauga, “Stokes flow due to point torques and sources in a spherical geometry”, *Physical Review Fluids* **5**, 074202 (2020).

- [250] D. Lopez and E. Lauga, “Dynamics of swimming bacteria at complex interfaces”, *Physics of Fluids* **26**, 400 (2014).
- [251] H. Faxén, “Die Bewegung einer starren Kugel längs der Achse eines mit zäher Flüssigkeit gefüllten Rohres”, *Arkiv för matematik, astronomi och fysik* **17**, 1 (1922).
- [252] H. Brenner, “The Stokes resistance of an arbitrary particle IV — arbitrary fields of flow”, *Chemical Engineering Science* **19**, 703 (1964).
- [253] G. K. Batchelor and J. T. Green, “The hydrodynamic interaction of two small freely-moving spheres in a linear flow field”, *Journal of Fluid Mechanics* **56**, 375 (1972).
- [254] L. Durlofsky, J. F. Brady, and G. Bossis, “Dynamic simulation of hydrodynamically interacting particles”, *Journal of Fluid Mechanics* **180**, 21 (1987).
- [255] B. P. Bet, “Getting in Shape. Swimming with Stokes and Surfing with Brinkman”, PhD thesis (Utrecht University, 2018), ISBN: 978-94-028-0906-0.
- [256] M. Puljiz and A. M. Menzel, “Displacement field around a rigid sphere in a compressible elastic environment, corresponding higher-order Faxén relations, as well as higher-order displaceability and rotatability matrices”, *Physical Review E* **99**, 053002 (2019).
- [257] H. Hasimoto, “An Extension of Faxen’s Law to the Ellipsoid of Revolution”, *Journal of the Physical Society of Japan* **52**, 3294 (1983).
- [258] S. Kim, “A note on Faxen laws for nonspherical particles”, *International Journal of Multiphase Flow* **11**, 713 (1985).
- [259] S. Kim, “Singularity solutions for ellipsoids in low-Reynolds-number flows: with applications to the calculation of hydrodynamic interactions in suspensions of ellipsoids”, *International Journal of Multiphase Flow* **12**, 469 (1986).
- [260] G. Söderlind, “Automatic control and adaptive time-stepping”, *Numerical Algorithms* **31**, 281 (2002).
- [261] G. R. McNamara and G. Zanetti, “Use of the Boltzmann-equation to simulate lattice-gas automata”, *Physical Review Letters* **61**, 2332 (1988).
- [262] F. J. Higuera, S. Succi, and R. Benzi, “Lattice gas dynamics with enhanced collisions”, *Europhysics Letters* **9**, 345 (1989).

- [263] F. J. Higuera and J. Jiménez, “Boltzmann approach to lattice gas simulations”, *Europhysics Letters* **9**, 663 (1989).
- [264] X. He and L.-S. Luo, “Theory of the lattice Boltzmann method: From the Boltzmann equation to the lattice Boltzmann equation”, *Physical Review E* **56**, 6811 (1997).
- [265] T. Krüger, H. Kusumaatmaja, A. Kuzmin, O. Shardt, G. Silva, and E. M. Viggen, *The Lattice Boltzmann Method: Principles and Practice* (Springer International Publishing, Cham, 2017), ISBN: 978-3-319-44647-9.
- [266] B. Dünweg and A. J. C. Ladd, “Lattice Boltzmann Simulations of Soft Matter Systems”, in *Advanced Computer Simulation Approaches for Soft Matter Sciences III*, edited by C. Holm and K. Kremer, *Advances in Polymer Science* 221 (Springer, Berlin, 2009), pages 89–166, ISBN: 978-3-540-87705-9.
- [267] P. Brookes, “Lattice Boltzmann in the Finite Knudsen Number Flow Regime”, Master’s thesis (University of Melbourne, 2009).
- [268] J. Meng and Y. Zhang, “Accuracy analysis of high-order lattice Boltzmann models for rarefied gas flows”, *Journal of Computational Physics* **230**, 835 (2011).
- [269] I. Ginzburg, F. Verhaeghe, and D. d’Humières, “Two-relaxation-time lattice Boltzmann scheme: About parametrization, velocity, pressure and mixed boundary conditions”, *Communications in Computational Physics* **3**, 427 (2008).
- [270] I. Ginzburg, F. Verhaeghe, and D. d’Humières, “Study of simple hydrodynamic solutions with the two-relaxation-times lattice Boltzmann scheme”, *Communications in Computational Physics* **3**, 519 (2008).
- [271] G. Silva and V. Semiao, “Truncation errors and the rotational invariance of three-dimensional lattice models in the lattice Boltzmann method”, *Journal of Computational Physics* **269**, 259 (2014).
- [272] P. J. Dellar, “An interpretation and derivation of the lattice Boltzmann method using Strang splitting”, *Computers & Mathematics with Applications* **65**, 129 (2013).
- [273] U. D. Schiller, “A unified operator splitting approach for multi-scale fluid–particle coupling in the lattice Boltzmann method”, *Computer Physics Communications* **185**, 2586 (2014).

- [274] Z. Guo, C. Zheng, and B. Shi, “Discrete lattice effects on the forcing term in the lattice Boltzmann method”, *Physical Review E* **65**, 046308 (2002).
- [275] U. D. Schiller, “Thermal fluctuations and boundary conditions in the lattice Boltzmann method”, PhD thesis (Johannes Gutenberg-Universität Mainz, 2008).
- [276] B. Postma and G. Silva, “Force methods for the two-relaxation-times lattice Boltzmann”, *Physical Review E* **102**, 063307 (2020).
- [277] A. J. C. Ladd and R. Verberg, “Lattice-Boltzmann simulations of particle-fluid suspensions”, *Journal of Statistical Physics* **104**, 1191 (2001).
- [278] Q. Zou and X. He, “On pressure and velocity boundary conditions for the lattice Boltzmann BGK model”, *Physics of Fluids* **9**, 1591 (1997).
- [279] B. Dünweg, U. D. Schiller, and A. J. C. Ladd, “Statistical mechanics of the fluctuating Lattice-Boltzmann equation”, *Physical Review E* **76**, 36704 (2007).
- [280] H. K. Versteeg and W. Malalasekera, *An Introduction to Computational Fluid Dynamics: The Finite Volume Method* (Pearson Education, Essex, 2007), ISBN: 978-0-13-127498-3.
- [281] S. Mazumder, *Numerical Methods for Partial Differential Equations: Finite Difference and Finite Volume Methods* (Academic Press, London, 2015), ISBN: 978-0-12-849894-1.
- [282] F. Capuani, I. Pagonabarraga, and D. Frenkel, “Discrete solution of the electrokinetic equations”, *Journal of Chemical Physics* **121**, 973 (2004).
- [283] M. Abramowitz and I. Stegun, *Handbook of Mathematical functions* (Dover Publications, New York, 1970), ISBN: 978-0-486-61272-0.
- [284] R. Fattal and R. Kupferman, “Constitutive laws for the matrix-logarithm of the conformation tensor”, *Journal of Non-Newtonian Fluid Mechanics* **123**, 281 (2004).
- [285] J. Su, J. Ouyang, X. Wang, and B. Yang, “Lattice Boltzmann method coupled with the Oldroyd-B constitutive model for a viscoelastic fluid”, *Physical Review E* **88**, 053304 (2013).
- [286] O. Malaspinas, N. Fiétier, and M. Deville, “Lattice Boltzmann method for the simulation of viscoelastic fluid flows”, *Journal of Non-Newtonian Fluid Mechanics* **165**, 1637 (2010).

- [287] P. J. Oliveira, F. T. Pinho, and G. A. Pinto, “Numerical simulation of non-linear elastic flows with a general collocated finite-volume method”, *Journal of Non-Newtonian Fluid Mechanics* **79**, 1 (1998).
- [288] M. A. Alves, F. T. Pinho, and P. J. Oliveira, “The flow of viscoelastic fluids past a cylinder: finite-volume high-resolution methods”, *Journal of Non-Newtonian Fluid Mechanics* **97**, 207 (2001).
- [289] C. M. Rhie and W. L. Chow, “Numerical study of the turbulent flow past an airfoil with trailing edge separation”, *AIAA Journal* **21**, 1525 (1983).
- [290] Ž. Lilek and M. Perić, “A fourth-order finite volume method with colocated variable arrangement”, *Computers & Fluids* **24**, 239 (1995).
- [291] P. Colella, “Multidimensional upwind methods for hyperbolic conservation laws”, *Journal of Computational Physics* **87**, 171 (1990).
- [292] C. Stewart, “Development of a Lattice-Boltzmann Based Oldroyd-B Model for Simulating Viscoelastic Fluids”, Master’s thesis (University of Stuttgart, 2018).
- [293] M. Hütter, P. D. Olmsted, and D. J. Read, “Fluctuating viscoelasticity based on a finite number of dumbbells”, *European Physical Journal E* **43**, 1 (2020).
- [294] A. Donev, A. Nonaka, Y. Sun, T. Fai, A. Garcia, and J. Bell, “Low Mach number fluctuating hydrodynamics of diffusively mixing fluids”, *Communications in Applied Mathematics and Computational Science* **9**, 47 (2014).
- [295] J.-P. Péraud, A. Nonaka, A. Chaudhri, J. B. Bell, A. Donev, and A. L. Garcia, “Low Mach number fluctuating hydrodynamics for electrolytes”, *Physical Review Fluids* **1**, 074103 (2016).
- [296] J. H. M. ten Thije Boonkamp and M. J. H. Anthonissen, “The finite volume-complete flux scheme for advection-diffusion-reaction equations”, *Journal of Scientific Computing* **46**, 47 (2011).
- [297] G. Rempfer, “A Lattice based Model for Electrokinetics”, Master’s thesis (University of Stuttgart, 2013).
- [298] A. Meister, *Numerik linearer Gleichungssysteme: Eine Einführung in moderne Verfahren*, 3rd edition (Vieweg Verlag, Wiesbaden, 2008), ISBN: 978-3-8348-9446-5.
- [299] N. Rivas, S. Frijters, I. Pagonabarraga, and J. Harting, “Mesoscopic electrohydrodynamic simulations of binary colloidal suspensions”, *Journal of Chemical Physics* **148**, 144101 (2018).

- [300] P. P. Ewald, “Die Berechnung optischer und elektrostatischer Gitterpotentiale”, *Annalen der Physik* **369**, 253 (1921).
- [301] C. Sagui, L. G. Pedersen, and T. A. Darden, “Towards an accurate representation of electrostatics in classical force fields: Efficient implementation of multipolar interactions in biomolecular simulations”, *Journal of Chemical Physics* **120**, 15 (2004).
- [302] P. Ahlrichs and B. Dünweg, “Lattice-Boltzmann simulation of polymer-solvent systems”, *International Journal of Modern Physics C* **9**, 1429 (1998).
- [303] R. W. Nash, R. Adhikari, and M. E. Cates, “Singular forces and pointlike colloids in lattice Boltzmann hydrodynamics”, *Physical Review E* **77**, 026709 (2008).
- [304] A. J. C. Ladd, “Numerical simulations of particulate suspensions via a discretized Boltzmann equation. Part 1. Theoretical foundation”, *Journal of Fluid Mechanics* **271**, 285 (1994).
- [305] C. K. Aidun, Y. Lu, and E.-J. Ding, “Direct analysis of particulate suspensions with inertia using the discrete Boltzmann equation”, *Journal of Fluid Mechanics* **373**, 287 (1998).
- [306] C. Rettinger, “Fully Resolved Simulation of Particulate Flows with a Parallel Coupled Lattice Boltzmann and Discrete Element Method”, PhD thesis (Friedrich-Alexander-Universität Erlangen-Nürnberg, 2021), in preparation.
- [307] C. P. Lowe, D. Frenkel, and A. J. Masters, “Long-time tails in angular momentum correlations”, *Journal of Chemical Physics* **103**, 1582 (1995).
- [308] L. Werner, C. Rettinger, and U. Rüde, “Coupling fully resolved light particles with the Lattice Boltzmann method on adaptively refined grids”, *International Journal for Numerical Methods in Fluids* **93**, 3280 (2021).
- [309] C. Rettinger and U. Rüde, “A comparative study of fluid-particle coupling methods for fully resolved lattice Boltzmann simulations”, *Computers & Fluids* **154**, 74 (2017).
- [310] C. Godenschwager, F. Schornbaum, M. Bauer, H. Köstler, and U. Rüde, “A framework for hybrid parallel flow simulations with a trillion cells in complex geometries”, in *Proceedings of the International Conference on High Performance Computing, Networking, Storage and Analysis* (2013), ISBN: 978-1-4503-2378-9.

- [311] *The Message Passing Interface (MPI) Standard*, MPI Consortium, 2004.
- [312] U. Ayachit, *The ParaView Guide: A Parallel Visualization Application* (Kitware, Inc., USA, 2015), ISBN: 978-1-930934-30-6.
- [313] N. Kohl, J. Hötzer, F. Schornbaum, M. Bauer, C. Godenschwager, H. Köstler, B. Nestler, and U. Rüde, “A scalable and extensible check-pointing scheme for massively parallel simulations”, *International Journal of High Performance Computing Applications* **33**, 571 (2019).
- [314] M. Bauer, J. Hötzer, D. Ernst, J. Hammer, M. Seiz, H. Hierl, J. Hönig, H. Köstler, G. Wellein, B. Nestler, and U. Rüde, “Code generation for massively parallel phase-field simulations”, in *Proceedings of the International Conference for High Performance Computing, Networking, Storage and Analysis* (2019), ISBN: 978-1-4503-6229-0.
- [315] M. Bauer, H. Köstler, and U. Rüde, “lbmpy: Automatic code generation for efficient parallel lattice Boltzmann methods”, *Journal of Computational Science* **49**, 101269 (2021).
- [316] M. Pippig, “PFFT: An extension of FFTW to massively parallel architectures”, *SIAM Journal on Scientific Computing* **35**, C213 (2013).
- [317] D. Bartuschat and U. Rüde, “Parallel multiphysics simulations of charged particles in microfluidic flows”, *Journal of Computational Science* **8**, 1 (2015).
- [318] K. Iglberger and U. Rüde, “Massively parallel rigid body dynamics simulations”, *Computer Science – Research and Development* **23**, 159 (2009).
- [319] S. Eibl and U. Rüde, “A modular and extensible software architecture for particle dynamics”, in *Proceedings of the 8th International Conference on Discrete Element Method* (2019).
- [320] J. Götz, K. Iglberger, C. Feichtinger, S. Donath, and U. Rüde, “Coupling multibody dynamics and computational fluid dynamics on 8192 processor cores”, *Parallel Computing* **36**, 142 (2010).
- [321] F. Schornbaum and U. Rüde, “Massively Parallel Algorithms for the Lattice Boltzmann Method on Non-uniform Grids”, *SIAM Journal on Scientific Computing* **38**, C96 (2016).
- [322] M. E. Cates, “Diffusive transport without detailed balance in motile bacteria: does microbiology need statistical physics?”, *Reports on Progress in Physics* **75**, 042601 (2012).

- [323] C. Hoell and H. Löwen, “Theory of microbe motion in a poisoned environment”, *Physical Review E* **84**, 042903 (2011).
- [324] D. B. Kearns, “A field guide to bacterial swarming motility”, *Nature Reviews Microbiology* **8**, 634 (2010).
- [325] H. H. Wensink, J. Dunkel, S. Heidenreich, K. Drescher, R. E. Goldstein, H. Löwen, and J. M. Yeomans, “Meso-scale turbulence in living fluids”, *Proceedings of the National Academy of Sciences* **109**, 14308 (2012).
- [326] J. Gachelin, A. Rousselet, A. Lindner, and E. Clement, “Collective motion in an active suspension of *Escherichia coli* bacteria”, *New Journal of Physics* **16**, 025003 (2014).
- [327] H. A. Stone and A. D. T. Samuel, “Propulsion of microorganisms by surface distortions”, *Physical Review Letters* **77**, 4102 (1996).
- [328] R. Pöhl, M. N. Popescu, and W. E. Uspal, “Axisymmetric spheroidal squirmers and self-diffusiophoretic particles”, *Journal of Physics: Condensed Matter* **32**, 164001 (2020).
- [329] J. Happel and H. Brenner, *Low Reynolds Number Hydrodynamics: With Special Applications to Particulate Media*, 2nd edition, Mechanics of fluids and transport processes (Martinus Nijhoff Publishers, The Hague, 1983), ISBN: 978-90-247-2877-0.
- [330] J. J. Molina, Y. Nakayama, and R. Yamamoto, “Hydrodynamic interactions of self-propelled swimmers”, *Soft Matter* **9**, 4923 (2013).
- [331] L. Zhu, E. Lauga, and L. Brandt, “Self-propulsion in viscoelastic fluids: Pushers vs. pullers”, *Physics of Fluids* **24**, 051902 (2012).
- [332] N. Aguillon, A. Decoene, B. Fabrèges, B. Maury, and B. Semin, “Modelling and simulation of 2D stokesian Squirmers”, *ESAIM: Proceedings* **38**, 36 (2012).
- [333] M. de Corato and G. D’Avino, “Dynamics of a microorganism in a sheared viscoelastic liquid”, *Soft Matter* **13**, 196 (2017).
- [334] W. E. Uspal, M. N. Popescu, S. Dietrich, and M. Tasinkevych, “Rheotaxis of spherical active particles near a planar wall”, *Soft Matter* **11**, 6613 (2015).
- [335] G. J. Elfring and J. F. Brady, “Active Stokesian Dynamics”, arXiv preprint [arXiv:2107.03531](https://arxiv.org/abs/2107.03531) (2021).
- [336] J. S. Lintuvuori, A. T. Brown, K. Stratford, and D. Marenduzzo, “Hydrodynamic oscillations and variable swimming speed in squirmers close to repulsive walls”, *Soft Matter* **12**, 7959 (2016).

- [337] F. Alarcón, C. Valeriani, and I. Pagonabarraga, “Morphology of clusters of attractive dry and wet self-propelled spherical particle suspensions”, *Soft Matter* **13**, 814 (2017).
- [338] Z. Shen, A. Würger, and J. S. Lintuvuori, “Hydrodynamic self-assembly of active colloids: chiral spinners and dynamic crystals”, *Soft Matter* **15**, 1508 (2019).
- [339] Z. Shen, A. Würger, and J. S. Lintuvuori, “Hydrodynamic interaction of a self-propelling particle with a wall”, *European Physical Journal E* **41**, 39 (2018).
- [340] N.-Q. Nguyen and A. J. C. Ladd, “Lubrication corrections for lattice-Boltzmann simulations of particle suspensions”, *Physical Review E* **66**, 046708 (2002).
- [341] J. D. Weeks, D. Chandler, and H. C. Andersen, “Role of Repulsive Forces in Determining the Equilibrium Structure of Simple Liquids”, *Journal of Chemical Physics* **54**, 5237 (1971).
- [342] J. de Graaf and J. Stenhammar, “Stirring by periodic arrays of microswimmers”, *Journal of Fluid Mechanics* **811**, 487 (2017).
- [343] T. C. Adhyapak and S. Jabbari-Farouji, “Ewald sum for hydrodynamic interactions of rigid spherical microswimmers”, *Journal of Chemical Physics* **149**, 144110 (2018).
- [344] J. F. Brady, R. J. Phillips, J. C. Lester, and G. Bossis, “Dynamic simulation of hydrodynamically interacting suspensions”, *Journal of Fluid Mechanics* **195**, 257 (1988).
- [345] I. Pagonabarraga and I. Llopis, “The structure and rheology of sheared model swimmer suspensions”, *Soft Matter* **9**, 7174 (2013).
- [346] P. Stärk, “Toward Swimming in Porous Networks: Interactions between Microswimmers and Obstacles”, Bachelor’s thesis (University of Stuttgart, 2018).
- [347] D. R. Noble and J. R. Torczynski, “A lattice-Boltzmann method for partially saturated computational cells”, *International Journal of Modern Physics C* **9**, 1189 (1998).
- [348] C. Burkard, “Investigating the Behaviour of Active Colloids at Interfaces Using the Squirmer Model and the Lattice Boltzmann Algorithm”, Bachelor’s thesis (University of Stuttgart, 2017).
- [349] J.-C. Desplat, I. Pagonabarraga, and P. Bladon, “LUDWIG: A parallel Lattice-Boltzmann code for complex fluids”, *Computer Physics Communications* **134**, 273 (2001).

- [350] D. M. Woolley, “Motility of spermatozoa at surfaces”, *Reproduction* **126**, 259 (2003).
- [351] A. Bukatin, I. Kukhtevich, N. Stoop, J. Dunkel, and V. Kantsler, “Bimodal rheotactic behavior reflects flagellar beat asymmetry in human sperm cells”, *Proceedings of the National Academy of Sciences* **112**, 15904 (2015).
- [352] E. Lauga, W. R. DiLuzio, G. M. Whitesides, and H. A. Stone, “Swimming in Circles: Motion of Bacteria near Solid Boundaries”, *Biophysical Journal* **90**, 400 (2006).
- [353] J. Elgeti, U. B. Kaupp, and G. Gompper, “Hydrodynamics of sperm cells near surfaces”, *Biophysical Journal* **99**, 1018 (2010).
- [354] H. Gadêlha, E. A. Gaffney, D. J. Smith, and J. C. Kirkman-Brown, “Nonlinear instability in flagellar dynamics: a novel modulation mechanism in sperm migration?”, *Journal of The Royal Society Interface* **7**, 1689 (2010).
- [355] D. Giacché, T. Ishikawa, and T. Yamaguchi, “Hydrodynamic entrapment of bacteria swimming near a solid surface”, *Physical Review E* **82**, 056309 (2010).
- [356] L. Alvarez, B. M. Friedrich, G. Gompper, and U. B. Kaupp, “The computational sperm cell”, *Trends in Cell Biology* **24**, 198 (2014).
- [357] G. Saggiorato, L. Alvarez, J. F. Jikeli, U. B. Kaupp, G. Gompper, and J. Elgeti, “Human sperm steer with second harmonics of the flagellar beat”, *Nature Communications* **8**, 1415 (2017).
- [358] D. Takagi, J. Palacci, A. B. Braunschweig, M. J. Shelley, and J. Zhang, “Hydrodynamic capture of microswimmers into sphere-bound orbits”, *Soft Matter* **10**, 1784 (2014).
- [359] S. Das, A. Garg, A. I. Campbell, J. Howse, A. Sen, D. Velegol, R. Golestanian, and S. J. Ebbens, “Boundaries can steer active Janus spheres”, *Nature Communications* **6**, 8999 (2015).
- [360] A. T. Brown, I. D. Vladescu, A. Dawson, T. Vissers, J. Schwarz-Linek, J. S. Lintuvuori, and W. C. K. Poon, “Swimming in a crystal”, *Soft Matter* **12**, 131 (2016).
- [361] J. Simmchen, J. Katuri, W. E. Uspal, M. N. Popescu, M. Tasinkevych, and S. Sánchez, “Topographical pathways guide chemical microswimmers”, *Nature Communications* **7**, 10598 (2016).
- [362] C. Kurzthaler and H. A. Stone, “Microswimmers near corrugated, periodic surfaces”, *Soft Matter* **17**, 3322 (2021).

- [363] M. N. Popescu, S. Dietrich, and G. Oshanin, “Confinement effects on diffusiophoretic self-propellers”, *Journal of Chemical Physics* **130**, 194702 (2009).
- [364] W. E. Uspal, M. N. Popescu, S. Dietrich, and M. Tasinkevych, “Self-propulsion of a catalytically active particle near a planar wall: from reflection to sliding and hovering”, *Soft Matter* **11**, 434 (2015).
- [365] A. Mozaffari, N. Sharifi-Mood, J. Koplik, and C. Maldarelli, “Self-diffusiophoretic colloidal propulsion near a solid boundary”, *Physics of Fluids* **28**, 053107 (2016).
- [366] A. Choudhary, K. V. S. Chaithanya, S. Michelin, and S. Pushpavanam, “Self-propulsion in 2D confinement: phoretic and hydrodynamic interactions”, *European Physical Journal E* **44**, 97 (2021).
- [367] Y. Wang, R. M. Hernandez, D. J. Bartlett, J. M. Bingham, T. R. Kline, A. Sen, and T. E. Mallouk, “Bipolar electrochemical mechanism for the propulsion of catalytic nanomotors in hydrogen peroxide solutions”, *Langmuir* **22**, 10451 (2006).
- [368] M. N. Popescu, S. Dietrich, M. Tasinkevych, and J. Ralston, “Phoretic motion of spheroidal particles due to self-generated solute gradients”, *European Physical Journal E* **31**, 351 (2010).
- [369] J. L. Moran and J. D. Posner, “Electrokinetic locomotion due to reaction-induced charge auto-electrophoresis”, *Journal of Fluid Mechanics* **680**, 31 (2011).
- [370] S. Ebbens, M.-H. Tu, J. R. Howse, and R. Golestanian, “Size dependence of the propulsion velocity for catalytic Janus-sphere swimmers”, *Physical Review E* **85**, 020401 (2012).
- [371] A. I. Campbell, S. J. Ebbens, P. Illien, and R. Golestanian, “Experimental observation of flow fields around active Janus spheres”, *Nature Communications* **10**, 1 (2019).
- [372] J. Hu, A. Wysocki, R. G. Winkler, and G. Gompper, “Physical sensing of surface properties by microswimmers—directing bacterial motion via wall slip”, *Scientific Reports* **5**, 9586 (2015).
- [373] W. E. Uspal, M. N. Popescu, S. Dietrich, and M. Tasinkevych, “Guiding catalytically active particles with chemically patterned surfaces”, *Physical Review Letters* **117**, 048002 (2016).
- [374] H. Ceylan, I. C. Yasa, and M. Sitti, “3D chemical patterning of micromaterials for encoded functionality”, *Advanced Materials* **29**, 1605072 (2017).

- [375] M. N. Popescu, W. E. Uspal, and S. Dietrich, “Chemically active colloids near osmotic-responsive walls with surface-chemistry gradients”, *Journal of Physics: Condensed Matter* **29**, 134001 (2017).
- [376] W. E. Uspal, M. N. Popescu, M. Tasinkevych, and S. Dietrich, “Shape-dependent guidance of active Janus particles by chemically patterned surfaces”, *New Journal of Physics* **20**, 015013 (2018).
- [377] V. Sharma, E. Azar, A. P. Schroder, C. M. Marques, and A. Stocco, “Active colloids orbiting giant vesicles”, *Soft Matter* **17**, 4275 (2021).
- [378] N. Desai, V. A. Shaik, and A. M. Ardekani, “Hydrodynamics-mediated trapping of micro-swimmers near drops”, *Soft Matter* **14**, 264 (2018).
- [379] A. Varma and S. Michelin, “Modeling chemo-hydrodynamic interactions of phoretic particles: A unified framework”, *Physical Review Fluids* **4**, 124204 (2019).
- [380] K. Schaar, A. Zöttl, and H. Stark, “Detention times of microswimmers close to surfaces: influence of hydrodynamic interactions and noise”, *Physical Review Letters* **115**, 038101 (2015).
- [381] A. Zöttl and H. Stark, “Simulating squirmers with multiparticle collision dynamics”, *European Physical Journal E* **41**, 61 (2018).
- [382] A. J. Goldman, R. G. Cox, and H. Brenner, “Slow viscous motion of a sphere parallel to a plane wall I — Motion through a quiescent fluid”, *Chemical Engineering Science* **22**, 637 (1967).
- [383] B. Cichocki and R. B. Jones, “Image representation of a spherical particle near a hard wall”, *Physica A: Statistical Mechanics and its Applications* **258**, 273 (1998).
- [384] F. Aurenhammer, “Voronoi diagrams—a survey of a fundamental geometric data structure”, *ACM Computing Surveys* **23**, 345 (1991).
- [385] T.-C. Lee, M. Alarcón-Correa, C. Miksch, K. Hahn, J. G. Gibbs, and P. Fischer, “Self-propelling nanomotors in the presence of strong Brownian forces”, *Nano Letters* **14**, 2407 (2014).
- [386] F. Rojas-Pérez, B. Delmotte, and S. Michelin, “Hydrochemical interactions of phoretic particles: a regularized multipole framework”, *Journal of Fluid Mechanics* **919**, A22 (2021).
- [387] K. Han, C. W. Shields IV, B. Bharti, P. E. Arratia, and O. D. Velev, “Active reversible swimming of magnetically assembled microscallop in non-Newtonian fluids”, *Langmuir* **36**, 7148 (2020).

- [388] K. Yasuda, M. Kuroda, and S. Komura, “Reciprocal microswimmers in a viscoelastic fluid”, *Physics of Fluids* **32**, 093102 (2020).
- [389] J. R. Gomez-Solano, A. Blokhuis, and C. Bechinger, “Dynamics of Self-Propelled Janus Particles in Viscoelastic Fluids”, *Physical Review Letters* **116**, 138301 (2016).
- [390] C. Li, B. Qin, A. Gopinath, P. E. Arratia, B. Thomases, and R. D. Guy, “Flagellar swimming in viscoelastic fluids: role of fluid elastic stress revealed by simulations based on experimental data”, *Journal of The Royal Society Interface* **14**, 20170289 (2017).
- [391] R. G. Larson, *The Structure and Rheology of Complex Fluids* (Oxford University Press, New York, 1999), ISBN: 978-0-19-512197-1.
- [392] S. M. Peker and S. S. Helvaci, *Solid-Liquid Two Phase Flow* (Elsevier Science, Amsterdam, 2008), ISBN: 978-0-444-52237-5.
- [393] R. B. Bird, P. J. Dotson, and N. L. Johnson, “Polymer solution rheology based on a finitely extensible bead-spring chain model”, *Journal of Non-Newtonian Fluid Mechanics* **7**, 213 (1980).
- [394] Y. Zhang, G. Li, and A. M. Ardekani, “Reduced viscosity for flagella moving in a solution of long polymer chains”, *Physical Review Fluids* **3**, 023101 (2018).
- [395] S. De, J. A. M. Kuipers, E. A. J. F. Peters, and J. T. Padding, “Viscoelastic flow simulations in model porous media”, *Physical Review Fluids* **2**, 053303 (2017).
- [396] G. Li and A. M. Ardekani, “Collective Motion of Microorganisms in a Viscoelastic Fluid”, *Physical Review Letters* **117**, 118001 (2016).
- [397] D. Toneian, G. Kahl, G. Gompper, and R. G. Winkler, “Hydrodynamic correlations of viscoelastic fluids by multiparticle collision dynamics simulations”, *Journal of Chemical Physics* **151**, 194110 (2019).
- [398] S. Sahoo, S. P. Singh, and S. Thakur, “Enhanced self-propulsion of a sphere-dimer in viscoelastic fluid”, *Soft Matter* **15**, 2170 (2019).
- [399] B. I. M. ten Bosch, “On an extension of Dissipative Particle Dynamics for viscoelastic flow modelling”, *Journal of Non-Newtonian Fluid Mechanics* **83**, 231 (1999).
- [400] A. Vázquez-Quesada, P. Español, R. I. Tanner, and M. Ellero, “Shear thickening of a non-colloidal suspension with a viscoelastic matrix”, *Journal of Fluid Mechanics* **880**, 1070 (2019).

- [401] J. R. C. King and S. J. Lind, “High Weissenberg number simulations with incompressible Smoothed Particle Hydrodynamics and the log-conformation formulation”, *Journal of Non-Newtonian Fluid Mechanics* **293**, 104556 (2021).
- [402] A. K. Townsend and H. J. Wilson, “Small- and large-amplitude oscillatory rheometry with bead-spring dumbbells in Stokesian Dynamics to mimic viscoelasticity”, *Journal of Non-Newtonian Fluid Mechanics* **261**, 136 (2018).
- [403] L. Giraud, D. d’Humières, and P. Lallemand, “A lattice-Boltzmann model for visco-elasticity”, *International Journal of Modern Physics C* **8**, 805 (1997).
- [404] L. Giraud, D. d’Humières, and P. Lallemand, “A lattice Boltzmann model for Jeffreys viscoelastic fluid”, *Europhysics Letters* **42**, 625 (1998).
- [405] I. Ispolatov and M. Grant, “Lattice Boltzmann method for viscoelastic fluids”, *Physical Review E* **65**, 056704 (2002).
- [406] H.-B. Li and H.-P. Fang, “Lattice Boltzmann simulation of transverse wave travelling in Maxwell viscoelastic fluid”, *Chinese Physics* **13**, 2087 (2004).
- [407] G. N. Frantziskonis, “Lattice Boltzmann method for multimode wave propagation in viscoelastic media and in elastic solids”, *Physical Review E* **83**, 066703 (2011).
- [408] X. Frank and H. Z. Li, “Complex flow around a bubble rising in a non-Newtonian fluid”, *Physical Review E* **71**, 036309 (2005).
- [409] X. Frank and H. Z. Li, “Negative wake behind a sphere rising in viscoelastic fluids: A lattice Boltzmann investigation”, *Physical Review E* **74**, 056307 (2006).
- [410] P. J. Dellar, “Lattice Boltzmann formulation for linear viscoelastic fluids using an abstract second stress”, *SIAM Journal on Scientific Computing* **36**, A2507 (2014).
- [411] J. Onishi, Y. Chen, and H. Ohashi, “A lattice Boltzmann model for polymeric liquids”, *Progress in Computational Fluid Dynamics, an International Journal* **5**, 75 (2005).
- [412] F. Osmanlic and C. Körner, “Lattice Boltzmann method for Oldroyd-B fluids”, *Computers & Fluids* **124**, 190 (2016).
- [413] S. Karra, “Modeling electrospinning process and a numerical scheme using Lattice Boltzmann method to simulate viscoelastic fluid flows”, Master’s thesis (Texas A&M University, 2007).

- [414] J. Su, J. Ouyang, X. Wang, B. Yang, and W. Zhou, “Lattice Boltzmann method for the simulation of viscoelastic fluid flows over a large range of Weissenberg numbers”, *Journal of Non-Newtonian Fluid Mechanics* **194**, 42 (2013).
- [415] R. B. Bird and J. M. Wiest, “Constitutive equations for polymeric liquids”, *Annual Review of Fluid Mechanics* **27**, 169 (1995).
- [416] T. N. Phillips and G. W. Roberts, “Lattice Boltzmann models for non-Newtonian flows”, *IMA Journal of Applied Mathematics* **76**, 790 (2011).
- [417] E. Aharonov and D. H. Rothman, “Non-Newtonian flow (through porous media): A lattice-Boltzmann method”, *Geophysical Research Letters* **20**, 679 (1993).
- [418] E. S. Boek, J. Chin, and P. V. Coveney, “Lattice Boltzmann simulation of the flow of non-Newtonian fluids in porous media”, *International Journal of Modern Physics B* **17**, 99 (2003).
- [419] J. Boyd, J. Buick, and S. Green, “A second-order accurate lattice Boltzmann non-Newtonian flow model”, *Journal of Physics A: Mathematical and General* **39**, 14241 (2006).
- [420] S. P. Sullivan, L. F. Gladden, and M. L. Johns, “Simulation of power-law fluid flow through porous media using lattice Boltzmann techniques”, *Journal of Non-Newtonian Fluid Mechanics* **133**, 91 (2006).
- [421] M. Yoshino, Y.-h. Hotta, T. Hirozane, and M. Endo, “A numerical method for incompressible non-Newtonian fluid flows based on the lattice Boltzmann method”, *Journal of Non-Newtonian Fluid Mechanics* **147**, 69 (2007).
- [422] O. Malaspinas, G. Courbebaisse, and M. Deville, “Simulation of generalized Newtonian fluids with the lattice Boltzmann method”, *International Journal of Modern Physics C* **18**, 1939 (2007).
- [423] Z. Ouyang, J. Lin, and X. Ku, “Hydrodynamic properties of squirmer swimming in power-law fluid near a wall”, *Rheologica Acta* **57**, 655 (2018).
- [424] D. Kehrwald, “Lattice Boltzmann simulation of shear-thinning fluids”, *Journal of Statistical Physics* **121**, 223 (2005).
- [425] A. Vikhansky, “Lattice-Boltzmann method for yield-stress liquids”, *Journal of Non-Newtonian Fluid Mechanics* **155**, 95 (2008).

- [426] R. Ouared and B. Chopard, “Lattice Boltzmann simulations of blood flow: non-Newtonian rheology and clotting processes”, *Journal of Statistical Physics* **121**, 209 (2005).
- [427] M. Ashrafizaadeh and H. Bakhshaei, “A comparison of non-Newtonian models for lattice Boltzmann blood flow simulations”, *Computers & Mathematics with Applications* **58**, 1045 (2009).
- [428] J. Bernsdorf and D. Wang, “Non-Newtonian blood flow simulation in cerebral aneurysms”, *Computers & Mathematics with Applications* **58**, 1024 (2009).
- [429] L. N. Carenza, G. Gonnella, A. Lamura, G. Negro, and A. Tiribocchi, “Lattice Boltzmann methods and active fluids”, *European Physical Journal E* **42**, 81 (2019).
- [430] K. J. Burns, G. M. Vasil, J. S. Oishi, D. Lecoanet, and B. P. Brown, “Dedalus: A flexible framework for numerical simulations with spectral methods”, *Physical Review Research* **2**, 023068 (2020).
- [431] H. Jasak, A. Jemcov, Z. Tukovic, et al., “OpenFOAM: A C++ library for complex physics simulations”, in *International Workshop on Coupled Methods in Numerical Dynamics*, Vol. 1000 (2007), pages 1–20, ISBN: 978-953-6313-88-4.
- [432] N. D. Waters and M. J. King, “Unsteady flow of an elastico-viscous liquid”, *Rheologica Acta* **9**, 345 (1970).
- [433] S.-C. Xue, R. I. Tanner, and N. Phan-Thien, “Numerical modelling of transient viscoelastic flows”, *Journal of Non-Newtonian Fluid Mechanics* **123**, 33 (2004).
- [434] K. S. Park and Y. don Kwon, “Numerical description of start-up viscoelastic plane Poiseuille flow”, *Korea-Australia Rheology Journal* **21**, 47 (2009).
- [435] I. Ginzbourg and P. M. Adler, “Boundary flow condition analysis for the three-dimensional lattice Boltzmann model”, *Journal de Physique II* **4**, 191 (1994).
- [436] K. Yapici, B. Karasozen, and Y. Uludag, “Finite volume simulation of viscoelastic laminar flow in a lid-driven cavity”, *Journal of Non-Newtonian Fluid Mechanics* **164**, 51 (2009).
- [437] R. G. Sousa, R. J. Poole, A. M. Afonso, F. T. Pinho, P. J. Oliveira, A. Morozov, and M. A. Alves, “Lid-driven cavity flow of viscoelastic liquids”, *Journal of Non-Newtonian Fluid Mechanics* **234**, 129 (2016).

- [438] S. Dalal, G. Tomar, and P. Dutta, “Numerical study of driven flows of shear thinning viscoelastic fluids in rectangular cavities”, *Journal of Non-Newtonian Fluid Mechanics* **229**, 59 (2016).
- [439] T.-W. Pan, J. Hao, and R. Glowinski, “On the simulation of a time-dependent cavity flow of an Oldroyd-B fluid”, *International Journal for Numerical Methods in Fluids* **60**, 791 (2009).
- [440] F. Habla, M. W. Tan, J. Haßberger, and O. Hinrichsen, “Numerical simulation of the viscoelastic flow in a three-dimensional lid-driven cavity using the log-conformation reformulation in OpenFOAM”, *Journal of Non-Newtonian Fluid Mechanics* **212**, 47 (2014).
- [441] B. Thomases and M. Shelley, “Emergence of singular structures in Oldroyd-B fluids”, *Physics of Fluids* **19**, 103103 (2007).
- [442] F. Pimenta and M. A. Alves, “Stabilization of an open-source finite-volume solver for viscoelastic fluid flows”, *Journal of Non-Newtonian Fluid Mechanics* **239**, 85 (2017).
- [443] P. Becherer, A. N. Morozov, and W. van Saarloos, “Scaling of singular structures in extensional flow of dilute polymer solutions”, *Journal of Non-Newtonian Fluid Mechanics* **153**, 183 (2008).
- [444] L. P. Fischer, T. Peter, C. Holm, and J. de Graaf, “The raspberry model for hydrodynamic interactions revisited. I. Periodic arrays of spheres and dumbbells”, *Journal of Chemical Physics* **143**, 084107 (2015).
- [445] K. D. Housiadas, “Steady sedimentation of a spherical particle under constant rotation”, *Physical Review Fluids* **4**, 103301 (2019).
- [446] K. D. Housiadas, “Improved convergence based on linear and non-linear transformations at low and high Weissenberg asymptotic analysis”, *Journal of Non-Newtonian Fluid Mechanics* **247**, 1 (2017).
- [447] A. Castillo, W. L. Murch, J. Einarsson, B. Mena, E. S. G. Shaqfeh, and R. Zenit, “Drag coefficient for a sedimenting and rotating sphere in a viscoelastic fluid”, *Physical Review Fluids* **4**, 063302 (2019).
- [448] M. A. Joens and J. W. Swan, “On the unsteady and lineal translation of a sphere through a viscoelastic fluid”, arXiv preprint [arXiv : 2106.07774](https://arxiv.org/abs/2106.07774) (2021).
- [449] O. S. Pak, L. Zhu, L. Brandt, and E. Lauga, “Micropropulsion and microrheology in complex fluids via symmetry breaking”, *Physics of Fluids* **24**, 103102 (2012).

- [450] J. P. Binagia and E. S. G. Shaqfeh, “Self-propulsion of a freely suspended swimmer by a swirling tail in a viscoelastic fluid”, *Physical Review Fluids* **6**, 053301 (2021).
- [451] N. C. Keim, M. Garcia, and P. E. Arratia, “Fluid elasticity can enable propulsion at low Reynolds number”, *Physics of Fluids* **24**, 081703 (2012).
- [452] J. A. Puente-Velázquez, F. A. Godínez, E. Lauga, and R. Zenit, “Viscoelastic propulsion of a rotating dumbbell”, *Microfluidics and Nanofluidics* **23**, 1 (2019).
- [453] J. P. Binagia, A. Phoa, K. D. Housiadas, and E. S. G. Shaqfeh, “Swimming with swirl in a viscoelastic fluid”, *Journal of Fluid Mechanics* **900**, A4 (2020).
- [454] K. D. Housiadas, J. P. Binagia, and E. S. G. Shaqfeh, “Squirmlers with swirl at low Weissenberg number”, *Journal of Fluid Mechanics* **911**, A16 (2021).
- [455] K. D. Housiadas, “An active body in a Phan-Thien and Tanner fluid: The effect of the third polar squirmering mode”, *Physics of Fluids* **33**, 043110 (2021).
- [456] C. Datt and G. J. Elfring, “A note on higher-order perturbative corrections to squirmering speed in weakly viscoelastic fluids”, *Journal of Non-Newtonian Fluid Mechanics* **270**, 51 (2019).
- [457] W. L. Murch and E. S. G. Shaqfeh, “Collective effects in the sedimentation of particles in a viscoelastic fluid”, *Physical Review Fluids* **5**, 073301 (2020).
- [458] S. Saad and G. Natale, “Diffusiophoresis of active colloids in viscoelastic media”, *Soft Matter* **15**, 9909 (2019).
- [459] W. F. Paxton, P. T. Baker, T. R. Kline, Y. Wang, T. E. Mallouk, and A. Sen, “Catalytically induced electrokinetics for motors and micropumps”, *Journal of the American Chemical Society* **128**, 14881 (2006).
- [460] M. E. Ibele, Y. Wang, T. R. Kline, T. E. Mallouk, and A. Sen, “Hydrazine fuels for bimetallic catalytic microfluidic pumping”, *Journal of the American Chemical Society* **129**, 7762 (2007).
- [461] A. Reinmüller, E. C. Oğuz, R. Messina, H. Löwen, H. J. Schöpe, and T. Palberg, “Colloidal crystallization in the quasi-two-dimensional induced by electrolyte gradients”, *Journal of Chemical Physics* **136**, 164505 (2012).

- [462] R. W. O'Brien and L. R. White, "Electrophoretic Mobility of a spherical colloidal Particle", *Journal of the Chemical Society, Faraday Transactions 2: Molecular and Chemical Physics* **74**, 1607 (1978).
- [463] M. von Smoluchowski, "Grundriß der Koagulationskinetik kolloider Lösungen", *Kolloid-Zeitschrift* **21**, 98 (1917).
- [464] E. Hückel, "Die Kataphorese der Kugel", *Physikalische Zeitschrift* **25**, 204 (1924).
- [465] D. C. Henry, "The Cataphoresis of Suspended Particles. Part I. The Equation of Cataphoresis", *Proceedings of the Royal Society, Series A: Containing Papers of a Mathematical and Physical Character* **133**, 106 (1931).
- [466] B. Sabass and U. Seifert, "Nonlinear, electrocatalytic swimming in the presence of salt", *Journal of Chemical Physics* **136**, 214507 (2012).
- [467] A. T. Woolley and R. A. Mathies, "Ultra-high-speed DNA sequencing using capillary electrophoresis chips", *Analytical Chemistry* **67**, 3676 (1995).
- [468] A. S. Mikheyev and M. M. Y. Tin, "A first look at the Oxford Nanopore MinION sequencer", *Molecular Ecology Resources* **14**, 1097 (2014).
- [469] I. Pagonabarraga, B. Rotenberg, and D. Frenkel, "Recent advances in the modelling and simulation of electrokinetic effects: bridging the gap between atomistic and macroscopic descriptions", *Physical Chemistry Chemical Physics* **12**, 9566 (2010).
- [470] L. Castellanos-Serra and E. Hardy, "Detection of biomolecules in electrophoresis gels with salts of imidazole and zinc II: a decade of research", *Electrophoresis* **22**, 864 (2001).
- [471] H. Schägger and G. von Jagow, "Tricine-sodium dodecyl sulfate-polyacrylamide gel electrophoresis for the separation of proteins in the range from 1 to 100 kDa", *Analytical Biochemistry* **166**, 368 (1987).
- [472] P. J. Blanche, E. L. Gong, T. M. Forte, and A. V. Nichols, "Characterization of human high-density lipoproteins by gradient gel electrophoresis", *Biochimica et Biophysica Acta – Lipids and Lipid Metabolism* **665**, 408 (1981).
- [473] S. Medina, J. Zhou, Z.-G. Wang, and F. Schmid, "An efficient dissipative particle dynamics-based algorithm for simulating electrolyte solutions", *Journal of Chemical Physics* **142**, 024103 (2015).

- [474] J. Smiatek and F. Schmid, “Mesoscopic simulations of electroosmotic flow and electrophoresis in nanochannels”, *Computer Physics Communications* **182**, 1941 (2011).
- [475] S. Frank and R. G. Winkler, “Polyelectrolyte electrophoresis: field effects and hydrodynamic interactions”, *Europhysics Letters* **83**, 38004 (2008).
- [476] S. Frank and R. G. Winkler, “Mesoscale hydrodynamic simulation of short polyelectrolytes in electric fields”, *Journal of Chemical Physics* **131**, 234905 (2009).
- [477] R. W. Lewis and R. W. Garner, “A finite element solution of coupled electrokinetic and hydrodynamic flow in porous media”, *International Journal for Numerical Methods in Engineering* **5**, 41 (1972).
- [478] S. A. Allison and Y. Xin, “Electrokinetic transport of rigid macroions in the thin double layer limit: A boundary element approach”, *Journal of Colloid and Interface Science* **288**, 616 (2005).
- [479] J. J. Hoyt and W. G. Wolfer, “Boundary element modeling of electrokinetically driven fluid flow in two-dimensional microchannels”, *Electrophoresis* **19**, 2432 (1998).
- [480] D. L. House, “Applications of the Boundary-element Method for Electrokinetics in Microfluidics”, PhD thesis (Vanderbilt University, 2012).
- [481] R. Schmitz and B. Dünweg, “Numerical electrokinetics”, *Journal of Physics: Condensed Matter* **24**, 464111 (2012).
- [482] S.-I. Jeong, J. Seyed-Yagoobi, and P. Atten, “Theoretical/numerical study of electrohydrodynamic pumping through conduction phenomenon”, *IEEE Transactions on Industry Applications* **39**, 355 (2003).
- [483] P. B. Warren, “Electroviscous transport problems via lattice-Boltzmann”, *International Journal of Modern Physics C* **8**, 889 (1997).
- [484] Y. Nakayama, K. Kim, and R. Yamamoto, “Simulating (electro) hydrodynamic effects in colloidal dispersions: smoothed profile method”, *European Physical Journal E* **26**, 361 (2008).
- [485] B. Rotenberg and I. Pagonabarraga, “Electrokinetics: insights from simulation on the microscopic scale”, *Molecular Physics* **111**, 827 (2013).
- [486] H. S. White and A. Bund, “Ion current rectification at nanopores in glass membranes”, *Langmuir* **24**, 2212 (2008).

- [487] W.-J. Lan, D. A. Holden, B. Zhang, and H. S. White, “Nanoparticle transport in conical-shaped nanopores”, *Analytical Chemistry* **83**, 3840 (2011).
- [488] G. Rempfer, S. Ehrhardt, C. Holm, and J. de Graaf, “Nanoparticle Translocation through Conical Nanopores: A Finite Element Study of Electrokinetic Transport”, *Macromolecular Theory and Simulations* **26**, 1600051 (2017).
- [489] S. Qian and S. W. Joo, “Analysis of self-electrophoretic motion of a spherical particle in a nanotube: effect of nonuniform surface charge density”, *Langmuir* **24**, 4778 (2008).
- [490] W. Wang, W. Duan, A. Sen, and T. E. Mallouk, “Catalytically powered dynamic assembly of rod-shaped nanomotors and passive tracer particles”, *Proceedings of the National Academy of Sciences* **110**, 17744 (2013).
- [491] T.-Y. Chiang and D. Velegol, “Localized electroosmosis (LEO) induced by spherical colloidal motors”, *Langmuir* **30**, 2600 (2014).
- [492] V. Mengeaud, J. Jossierand, and H. H. Girault, “Mixing processes in a zigzag microchannel: finite element simulations and optical study”, *Analytical Chemistry* **74**, 4279 (2002).
- [493] F. Bianchi, R. Ferrigno, and H. H. Girault, “Finite element simulation of an electroosmotic-driven flow division at a T-junction of microscale dimensions”, *Analytical Chemistry* **72**, 1987 (2000).
- [494] F. Yang, S. Qian, Y. Zhao, and R. Qiao, “Self-diffusiophoresis of Janus Catalytic Micromotors in Confined Geometries”, *Langmuir* **32**, 5580 (2016).
- [495] G. Giupponi and I. Pagonabarraga, “Colloid Electrophoresis for Strong and Weak Ion Diffusivity”, *Physical Review Letters* **106**, 248304 (2011).
- [496] B. Rotenberg, I. Pagonabarraga, and D. Frenkel, “Dispersion of charged tracers in charged porous media”, *Europhysics Letters* **83**, 34004 (2008).
- [497] A. Obliger, M. Jardat, D. Coelho, S. Bekri, and B. Rotenberg, “Pore network model of electrokinetic transport through charged porous media”, *Physical Review E* **89**, 043013 (2014).
- [498] S. Reboux, F. Capuani, N. Gonzales-Segredo, and D. Frenkel, “Lattice-Boltzmann Simulations of Ionic Current Modulation by DNA translocation”, *Journal of Chemical Theory and Computation* **2**, 495 (2006).

- [499] V. Lobaskin, B. Dünweg, M. Medebach, T. Palberg, and C. Holm, “Electrophoresis of Colloidal Dispersions in the Low-Salt Regime”, *Physical Review Letters* **98**, 176105 (2007).
- [500] N. Garbow, M. Evers, T. Palberg, and T. Okubo, “On the electrophoretic mobility of isolated colloidal spheres”, *Journal of Physics: Condensed Matter* **16**, 3835 (2004).
- [501] M. Medebach and T. Palberg, “Electrophoretic mobility of electrostatically interacting colloidal spheres”, *Journal of Physics: Condensed Matter* **16**, 5653 (2004).
- [502] T. Palberg, M. Medebach, N. Garbow, M. Evers, A. B. Fontecha, H. Reiber, and E. Bartsch, “Electrophoresis of model colloidal spheres in low salt aqueous suspension”, *Journal of Physics: Condensed Matter* **16**, 4039 (2004).
- [503] P. H. Wiersema, A. L. Loeb, and J. T. G. Overbeek, “Calculation of the electrophoretic mobility of a spherical colloid particle”, *Journal of Colloid and Interface Science* **22**, 78 (1966).
- [504] J. de Graaf, T. Peter, L. P. Fischer, and C. Holm, “The raspberry model for hydrodynamic interactions revisited. II. The effect of confinement”, *Journal of Chemical Physics* **143**, 084108 (2015).

The electronic version of this dissertation contains internet links to the referenced sources, where available. They may be accessed from the above bibliography by clicking on the journal, book title, or university for articles, books, and theses, respectively. Most of these links refer to Digital Object Identifiers (DOIs), which should enable long-term access. A small number of references is not available through the DOI system, so their links point to their websites instead. If any of these websites are no longer available by the time the reader attempts to access them, please refer to the Internet Archive’s Wayback Machine¹ for copies that were archived at the time this dissertation was written.

¹<https://web.archive.org/>

Acknowledgments

This thesis would not have been possible without the support of the following people.

I thank **Christian Holm** for accepting me as a doctoral student. He gave me the freedom to explore and take my project into unexpected directions, and he suggested new ideas to consider and people to talk to whenever I got stuck.

I am grateful to **Joost de Graaf**, who agreed to be my co-advisor over a distance, first from Edinburgh and then from Utrecht. I greatly benefited from his deep knowledge on active matter and appreciated the many discussions we had about my work and science in general, as well as his tireless commenting of my manuscripts.

Further thanks go to my students, **Cameron Stewart**, **Christian Burkard**, and **Philipp Stärk**, for the trust they placed in me by choosing to do their bachelor/master theses with me and for jump-starting some of the projects that I ended up working on for my own doctoral thesis. More thanks go to my colleagues, in particular **Ashreya Jayaram**, **Christoph Lohrmann**, **Florian Weik**, **Georg Rempfer**, **Kai Szuttor**, **Patrick Kreissl**, and **Rudolf Weeber**, for the many discussions about soft matter physics and software development, as well as science and everything else. I am grateful to **Henri Menke** for help with the typesetting, to **Claudia Lemke**, **Henriette Patzelt**, **Meike Kreidler**, and **Simone Blümlein** for help with all administrative matters, and to **Frank Huber** for help with computing matters.

I thank **Christian Godenschwager**, **Christoph Rettinger**, **Florian Schornbaum**, **Harald Köstler**, **Markus Holzer**, **Martin Bauer**, **Sebastian Eibl**, and **Ulrich Rüde**, who developed the `waLBerla` software and supported me in using and extending it.

I am grateful to my parents, **Daniela Kuron** and **Johannes Kuron**, and my brothers, **Stephan Kuron** and **Oliver Kuron**, for supporting me throughout my studies.

I thank the Deutsche Forschungsgemeinschaft (DFG) for funding the largest part of my doctoral studies through the SPP 1726 “Microswimmers: from single particle motion to collective behavior” program. I also thank the other projects’ principal investigators and students, in particular **Clemens**

Acknowledgments

Bechinger, Kai Qi, Mihail Popescu, Peer Fischer, Roland Winkler, and **William Uspal**, for the inspiring presentations and valuable discussions at and beyond the annual meetings.

The final thanks go to the many other people not yet listed with whom I have discussed my work over the years and who have provided valuable comments and inspired new ideas. These include **Alexander Chamolly, Jens Harting, Nicholas Rivas,** and **Ulf Schiller**, but this list is by no means complete.

Zusammenfassung

Mikroschwimmer faszinieren die Menschen, seit man Bakterien erstmals unter dem Mikroskop gesehen hat. Erst mit der Entwicklung der Mikrohydrodynamik fast drei Jahrhunderte später waren Physiker in der Lage, die einzigartigen Herausforderungen, die die Umgebung eines Mikroorganismus an seine Bewegung stellt, zu beschreiben und zu würdigen. Es wurde festgestellt, dass das Schwimmen auf solchen Längenskalen völlig anders funktioniert als das, was ein menschlicher Schwimmer gewohnt ist: Es gleicht eher dem Versuch, durch Honig oder ein Gewirr von Seilen zu schwimmen, als durch ein Wasserbecken. Theoretische Modelle wurden entwickelt, um die Komplexität der Biologie in einfache Mathematik zu abstrahieren.

Das Feld gewann an Fahrt, als man erkannte, dass künstliche Mikroschwimmer eine Fülle von Anwendungen in Technik und Medizin haben könnten. Nach den bahnbrechenden Experimenten von Paxton et al., deren Bimetall-Nanostäbchen sich durch katalytische Zersetzung von Wasserstoffperoxid fortbewegen, bald gefolgt von Howse et al. mit katalysatorbeschichteten, nicht-leitenden Mikrokugeln, entwickelten Dutzende anderer Gruppen ihre eigenen Mikroschwimmer, die in den unterschiedlichsten Umgebungen schwammen. Dabei wurden auch kollektive Effekte beobachtet, die bisher nur von makroskopischen Skalen bekannt waren, wie etwa Turbulenz oder Schwarmverhalten. Neue Antriebsarten wurden schneller entwickelt als das theoretische Verständnis darüber gewonnen werden konnte, wie effizient oder warum überhaupt sie funktionieren. Einige Leute argumentierten sogar, dass ein natürlicher Mikroschwimmer wie *Escherichia coli*, kombiniert mit den Werkzeugen der modernen Gentechnik, ein einfacheres, besser kontrollierbares Modell darstellen und mehr Einblick in das Mikroschwimmen geben würde als jedes seiner künstlichen Pendanten.

Es ist schwierig und zeitaufwendig, einen hochdimensionalen Parameterraum in Experimenten zu erforschen, und nicht immer sind alle relevanten Größen direkt messbar. Ein Bottom-up-Modell kann hier Abhilfe schaffen, sobald die relevanten physikalischen Phänomene — wie Diffusion, Hydrodynamik oder Wärmeleitfähigkeit — identifiziert worden sind. Die charakteristische Eigenschaft eines Bottom-up-Modells ist, dass es nur physikalische Parameter enthält — wie Diffusionskoeffizienten, Viskosität oder Wärmekapazität — und keine Modellierungsparameter wie Oberflächenpotentiale

oder effektive Ladungen. Ein solches Modell kann ein detaillierteres Bild von dem geben, was im Experiment vor sich geht, und erlaubt es, Aspekte wie Elektrostatik oder Hydrodynamik selektiv ein- und auszuschalten, um ihre relative Signifikanz zu bestimmen. Es kann auch eingesetzt werden, um eine Antriebsmethode auf Effizienz oder Geschwindigkeit in einer bestimmten Umgebung zu optimieren. Analytische Theorie kann diese Modelle oft nur für einfache Systeme oder in grober Näherung lösen, liefert aber mathematische Ausdrücke, die eine Frage für einen großen Parameterbereich vollständig beantworten. Die Stärke von Computersimulationen liegt dagegen in ihrer Fähigkeit, komplexe Mehrkörperprobleme und beliebige Randbedingungen zu behandeln. Folglich gehen theoretische und rechnergestützte Ansätze oft Hand in Hand, um das Verständnis von Mikroschwimmern zu fördern, so wie auch von vielen anderen Bereichen der Physik.

In dieser Dissertation werden verschiedene Modelle zur Untersuchung von Mikroschwimmern vorgestellt, validiert und angewendet, wobei der Schwerpunkt auf der Entwicklung von Gitteralgorithmen liegt. Die Modelle sind auf biologische Schwimmer wie Bakterien anwendbar, aber auch auf künstliche Schwimmer, die durch chemische Reaktionen angetrieben werden. Das verbindende Thema ist eine komplexe Fluidumgebung, die von Newton'schen Einkomponentenflüssigkeiten über Elektrolytlösungen bis hin zu viskoelastischen Medien reicht, die durch beliebige Geometrien fließen. Ein besonderer Schwerpunkt liegt auf der Auflösung der Oberfläche eines jeden Schwimmers, da der Vortrieb, auch „Phorese“ genannt, von einer dünnen Flüssigkeitsschicht um sie herum ausgeht. Die Auflösung des Antriebsmechanismus ist notwendig, um hydrodynamische Wechselwirkungen mit Hindernissen und anderen Schwimmern genau zu untersuchen. Sie ist auch eine Voraussetzung für die Untersuchung von Taxis, der Ausrichtung in einem äußeren Feld wie z.B. einem Nährstoffgradienten. In ähnlicher Weise können phoretische Wechselwirkungen untersucht werden, z.B. wenn ein Schwimmer die Spur wahrnimmt, auf der ein anderer Schwimmer bereits den Treibstoff aufgebraucht hat, und ihr ausweicht.

Die Auflösung des Antriebs stellt eine Herausforderung dar, da sie den erforderlichen Rechenaufwand deutlich erhöht. Andere Methoden wie Multi-Particle Collision Dynamics oder Finite Elemente wurden bereits für diesen Zweck verwendet, leiden aber unter unphysikalischen Effekten oder sind nicht effizient genug, um instationäres Verhalten zu simulieren. Dieses offene Problem wird durch die in der vorliegenden Arbeit entwickelten neuen Berechnungsmethoden angegangen. Sie werden so konzipiert, dass sie allgemein genug sind, um auch auf andere Arten von Flüssigkeiten und sogar auf Bereiche der Physik der weichen Materie jenseits der aktiven Materie angewendet werden zu können. Die Methoden basieren auf Gitter-Boltzmann (LB), das

für zeitabhängige Probleme mit komplexen Randbedingungen gut geeignet ist. Die Berücksichtigung ionischer gelöster Stoffe und viskoelastischer Spannung erfolgt über die Finite-Volumen-Methode (FV), die sich ideal für die Untersuchung von Problemen eignet, die auf Erhaltungssätzen basieren. Neuartige Schemata für bewegte Randbedingungen erlauben die Auflösung der Schwimmer auf dem Gitter ohne Neugenerierung des Gitters, wenn diese sich bewegen. Ein Sub-Grid-Schema wird eingesetzt, um Artefakte zu glätten, die entstehen, wenn Gitterzellen zwischen flüssig und fest umgewandelt werden. Außerdem wird in dieser Arbeit ein einfaches analytisches Fernfeldmodell verwendet, um eine Erklärung für die Mobilitätsumkehr von einfachen Schwimmern an Hindernissen zu finden — ein Verhalten, das zuvor zwar beobachtet, aber nicht allein durch die Hydrodynamik erklärt wurde.

Die Entwicklung dieser Gittermethoden erlaubte es mir, einige von der Literatur bislang offen gelassene Fragen zu beantworten, was zu vier Hauptergebnissen führte, von denen jedes in einem eigenen Kapitel vorgestellt wird. Das erste Ergebnis ist für einen Squirmer, ein einfaches, aber lehrreiches Modell für Mikroschwimmer, das eine effektive Oberflächengeschwindigkeit auf einer Kugel verwendet, um den Selbstantrieb zu beschreiben. Das Lösen der Strömung um den Squirmer herum ist mit der LB-Methode relativ einfach, erfordert jedoch eine unerwartet feine Gitterauflösung, um die physikalischen Strömungsfelder und das Schwimmverhalten mit ausreichender Genauigkeit zu erfassen. Die Genauigkeit des LB-Modells wird anhand von vier grundlegenden hydrodynamischen Tests demonstriert, zwei für die Fernfeldströmung und zwei, bei denen das Nahfeld genau aufgelöst werden muss, wozu LB bis hinunter zur Gitterauflösung in der Lage ist. Es wird eine hervorragende Übereinstimmung mit Ergebnissen gefunden, die mit anderen hydrodynamischen Lösern in den gleichen Geometrien erzielt wurden, und es wird die minimale Auflösung ermittelt, die erforderlich ist, um diese Übereinstimmung zu erreichen.

Das zweite Thema wurde durch eine unerwartete Mobilitätsumkehr inspiriert, die in einigen der LB-Squirmer-Simulationen beobachtet wurde. Bei selbstgetriebenen Teilchen wurde experimentell gezeigt, dass sie kugelförmige Hindernisse umkreisen und sich entlang ebener Wände bewegen können. Eine theoretische und numerische Untersuchung dieses Verhaltens wird für einen Squirmer durchgeführt, der mit flachen und gekrümmten Oberflächen wechselwirkt. Die Hydrodynamik wird mit Hilfe der hydrodynamischen Spiegelladungsmethode angenähert, die im Fernfeld exakt ist; der LB-Löser wird verwendet, um zu bestätigen, dass die Vorhersagen aus dem Fernfeld gültig bleiben, wenn auch die Strömungen im Nahfeld berücksichtigt werden. Das Fernfeldmodell sagt drei verschiedene Verhal-

tensweisen voraus: Umkreisen/Gleiten, Streuung und Schweben, wobei das Umkreisen bei geringerer Krümmung wie aus dem Experiment bekannt bevorzugt wird. Überraschenderweise sagen die Fernfeldberechnungen auch ein rückwärtsgerichtetes Umkreisen/Gleiten für ausreichend starke Pusher voraus. Dies wird durch Flüssigkeitsrezirkulation im Spalt zwischen dem Squirmer und dem Hindernis verursacht, was zu starken Kräften führt, die der Vorwärtsbewegung entgegenwirken. Der Effekt kann auf das Quadrupolmoment des Squirmers zurückgeführt werden. Diese Ergebnisse geben Einblick in einen möglichen Mechanismus der Mobilitätsumkehr, der allein durch hydrodynamische Wechselwirkungen mit einer Oberfläche vermittelt wird.

Das dritte Hauptthema betrifft viskoelastische Flüssigkeiten. Damit ist es auf viele biologische Flüssigkeiten anwendbar, die zusätzlich zu den dissipativen Eigenschaften, die in Newton'schen Flüssigkeiten zu finden sind, auch elastische Eigenschaften aufweisen. Beispiele hierfür sind der Verlust der Zeitreversibilität durch einen Memory-Effekt sowie eine Kopplung zwischen Translation und Rotation. Computermodelle können uns helfen, viskoelastische Strömungen zu verstehen, sind aber oft in der Handhabung komplexer Strömungsgeometrien und suspendierter Teilchen eingeschränkt. Einige bauen unphysikalische Zusatzterme in die konstitutiven Gleichungen ein; andere erfordern, dass Spannungsrandbedingungen bekannt sind, was bei beliebig geformten festen und beweglichen Rändern nicht von vornherein der Fall ist. Der in dieser Arbeit vorgestellte LB-Löser für Oldroyd-B-Fluide vermeidet diese Mängel, wodurch er sich ideal für die Simulation von kolloidalen Suspensionen in beschränkten Geometrien eignet. Die Methode wird unter Verwendung mehrerer rheologischer Standardaufbauten validiert: instationäre Poiseuille-Strömung, stetige Scherströmung, die Lid-driven Cavity und die Four-Roll Mill. Zusätzlich wird ein einzelnes sedimentierendes Kolloid untersucht, um das neue Schema mit bewegten Randbedingungen zu verifizieren; auch hier findet sich eine gute Übereinstimmung mit der Literatur. Translations-Rotations-Kopplung, eine wichtige Eigenschaft für viskoelastischen Medien, wird für zwei starr verbundene Kugeln demonstriert. Dieses schneemannartige Gebilde wird durch ein von außen angelegtes Drehmoment gedreht, was nur in viskoelastischen Flüssigkeiten zu einer linearen Bewegung führt. Der Squirmer wird erneut verwendet, um die Anwendbarkeit der Methode auf Mikroschwimmer zu zeigen, stößt aber auch an die Grenzen von Oldroyd-B. Oldroyd-B wird unphysikalisch für elastische Relaxationszeiten jenseits einer bestimmten Grenze. Der Ansatz in der vorliegenden Arbeit ist jedoch so konzipiert, dass es einfach ist, den Algorithmus auf andere konstitutive Gleichungen zu erweitern, wie z.B. Giesekus oder FENE-P, die nicht unter derartigen Problemen leiden.

Das vierte Thema befasst sich mit Kolloiden, die in Elektrolytlösungen suspendiert sind. Dabei wird ein Schema mit bewegten Randbedingungen eingeführt, das demjenigen für viskoelastische Flüssigkeiten ähnelt. Die Bewegung von ionischen Solvaten und geladenen Teilchen unter dem Einfluss eines elektrischen Feldes und die daraus resultierende hydrodynamische Strömung des Lösungsmittels sind in der Physik der weichen Materie allgegenwärtig. Der gelöste Stoff und die Strömung werden durch gekoppelte Differentialgleichungen beschrieben, die zusammen als elektrokinetische Gleichungen bezeichnet werden; ihre Randbedingungen definieren das spezifische zu betrachtende Problem. Es existierte schon vorher eine gitterbasierte Methode zum Lösen dieses Gleichungssystems, die auf der Kopplung von LB und FV basiert; diese erlaubte jedoch keine Teilchenkopplung. Die wichtigsten Bestandteile der neuen Methode mit beweglichen Randbedingungen sind die Massen- und Ladungserhaltung für die Solvate und ein Glättungsschema zur Minimierung von Diskretisierungsartefakten. Die Leistungsfähigkeit des Algorithmus wird durch die Simulation der Elektrophorese von geladenen Kugeln in einem externen Feld demonstriert. Für eine einzelne Kugel wird dies mit dem äquivalenten elektroosmotischen (mitbewegten) Problem verglichen, wobei sich herausstellt, dass die Instantangeschwindigkeit im ersteren Fall um nur 2% vom stationären Wert im letzteren Fall abweicht und die zeitlichen Artefakte der Diskretisierung ebenfalls in dieser Größenordnung liegen.

Das Forschungsgebiet der aktiven Materie hat sich seit Beginn meiner Arbeit an dieser Dissertation im Jahr 2016 stark verändert. Die Entwicklung und das Verständnis des Antriebs und des Verhaltens von künstlichen Mikroschwimmern war eine der zentralen Fragen, die die Wissenschaft auf dem Gebiet der aktiven Materie in den davorliegenden zehn Jahren beschäftigte. Meine Arbeit zur Elektrokinetik sollte einen Beitrag zu diesem Forschungszweig leisten, wobei sie gleichzeitig auch für die Bereiche Katalyse und bioreaktive Strömungen relevant ist. Eine umfassende Antwort auf die offenen Fragen zum selbst-diffusiophoretischen und selbst-elektrophoretischen Antrieb steht leider noch aus, wobei das Haupthindernis im unzureichenden Verständnis der beteiligten chemischen Reaktionen zu liegen scheint. Noch bevor die Forschung an künstlichen Mikroschwimmern begann, war jedoch bereits klar, dass ein Großteil des Verhaltens von Schwimmern auf großen Skalen unabhängig von der jeweiligen Antriebsmethode ist. So konnten unabhängig von diesen Details wichtige Erkenntnisse über das Mikroschwimmen gewonnen werden, z.B. durch die Untersuchung ihres Schwarmverhaltens oder ihrer Wechselwirkung mit Oberflächen. Infolgedessen hat sich mein eigenes Interesse auf einfachere Modelle verlagert, was einem schon länger bestehenden Trend in der Forschergemeinschaft folgt. Dennoch bleibt die

Elektrokinetik im Bereich der aktiven Materie relevant, weil der chemische Antrieb zu emergenten Phänomenen führt, die nicht universell sind oder die von den einfacheren Modellen nicht erfasst werden. In jüngerer Zeit hat sich der Fokus der Fachgemeinschaft auf biologische, bio-kompatible und bio-inspirierte Schwimmer verlagert, woran meine Arbeit über Squirmer anknüpft. Die Forschung an diesen Schwimmern hat mehr medizinische Relevanz und liefert direkte Einblicke in die Biologie. Als weitere Folge ist das Interesse an viskoelastischen Flüssigkeiten aufgrund ihrer Verbreitung in der Natur stark angestiegen. Ihre komplexere Rheologie eröffnete neue Verhaltensweisen von Schwimmern, z.B. weil sie ihnen ermöglicht, dem Scallop-Theorem auszuweichen. Die Kombination der Simulationsmethoden für Viskoelastizität, Elektrolyte und chemische Reaktionen, die ich in dieser Arbeit vorstelle, wird ein wertvolles Werkzeug für die Untersuchung von biologischen und künstlichen Mikroschwimmern in einem breiten Spektrum von Fluidumgebungen darstellen.

Erklärung

Ich habe diese Dissertation selbständig verfasst. Alle verwendeten Quellen wurden angegeben.

Frickenhausen, den _____

Michael Johannes Kuron